An investigation on the formation and occurrence of spiral grain and compression wood in radiata pine (*Pinus radiata* D. Don.)

A thesis submitted in partial fulfilment
of the requirements for the degree of

Doctor of Philosophy
In Plant Biotechnology

at the

School of Biological Sciences
University of Canterbury

by

Jimmy Thomas

UC
UNIVERSITY OF CANTERBURY
Te Whare Wānanga o Waitaha
CHRISTCHURCH NEW ZEALAND

2014

Acknowledgements

I would like to submit my praise to “The almighty” who enabled me to carry the umbrella of education up to this level.

I am immensely grateful and indebted to **Dr David Collings**, School of Biological Sciences, University of Canterbury, Christchurch, New Zealand, who guided and helped me through out in this long journey of research, by all possible means with great understanding and patience. I feel proud and fortunate to have him as my Principal Supervisor without whose timely helps, fruitful discussions and invaluable advises at various stages, this thesis could not have made in to the present shape and content.

I’m thankful to the Associate Supervisors, Dr Ashley Garrill, Dr Shakti Singh Chauhan, and Dr Hema Nair, former Associate Supervisor for their support and guidance. Many thanks are due to Professor John Walker, Dr Luis Apiolaza along with Dr Chauhan who provided the clonal sample materials for this study and valuable suggestions for improvements. I acknowledge Dr Brian Butterfield for his advices on preparing a manuscript.

I express my deep sense of gratitude to Manfred Ingerfeld, who was always ready to help me at anytime, especially in the early confocal microscopy lab.

Thanks are also due to the technicians of the department who never hesitated to help me, - Matt Walters (imaging and processing); Graeme Bull (Microtomy, Histology); Neil Andrews (SEM imaging); Graeme Young and John Scott (IT support); Dave Rutherford (Electrical) and Nick Etheridge (wood work); Selwyn Cox, Nicky Judson, Elizabeth Fitzgerald, Nicole Lauren-Manuera, and Penny Moore (Admin). Special thanks to Alan Woods for making a rotating stage for the confocal microscope. I thank Allen Mitchell and Andrew McNaughton of the Otago University, Dunedin for X-ray tomography and technical advice, M/s Wood Quality Initiative, a forest industry consortium based in Rotorua, New Zealand for providing several unpublished data on resin canals

I’m grateful to Scion, Rotorua, New Zealand for the generous fellowship provided.

My sincere thanks are also due to Mr MK Balagopalan Nair, Mr Sunny Sebastian and Mr Mohanachandran Nair, former Directors and Mr Rajagopal Narayanapanicker, Director, Department of Processing and Product Development, The Rubber Board, Government of India for granting leave from job for pursuing this study; Mr Tomson Francis, Mechanical Engineer & Mr Umasankar, Assistant Engineer for taking care of the Laboratory in my absence.

I thank my colleagues in the Central Wood Testing Laboratory Mrs Jayasree, Mrs Suseela, Mr Anil Kumar, and Mr Ajith Kumar for their help and co-operation during this study.

I offer my heartiest respects to my most affectionate parents who taught me the lesson of “LOVE TO ALL” & DEVOTION TO WORK”. I appreciate the understanding, patience and support of my loving wife, Sonia and dear kids (Tom, Tia and Tait) who have always been a source of inspiration to me. And it is because their sacrifice and blessing that I would gather impetus to achieve my target.

5th September 2014..... **JIMMY THOMAS**

Table of Contents

Chapter 2. Automated quantification of compression wood in wood cross sections by image analysis

Chapter 5. 3-dimensional visualisations and measurements of spiral grain in young *Pinus radiata* wood by image reconstruction

Abstract

Radiata pine (*Pinus radiata*) is the most important plantation tree in New Zealand forestry, and factors that reduce the quality of wood cause significant economic loss. Two of the most important of these issues are compression wood and spiral grain. Compression wood is a type of reaction wood, formed when a tree moves away from the vertical, and is characterised by biochemical and structural changes within the wood that reduce its quality and value. Spiral grain, however, is the alignment of the wood grain in a helix around the tree's axis and away from the vertical. Again, this reduces the structural qualities of the wood and thus its value. Spiral grain and compression wood are notorious for their deleterious effect on the quality of wood produced and are very important for the forest industry due to the huge economic loss they cause. The demand for reliable tools to evaluate these wood quality issues in clonal planting material at an early stage, within 3 years of germination rather than at 8 to 15 years as in current practise, is of ever increasing importance from plant breeders and other industry stake holders.

Therefore this research was undertaken with an overall aim to develop quick, easy and reproducible techniques to evaluate young radiata pine clones (up to 3 years old) based on compression wood content and presence of spiral grain. This is important because a shortened breeding cycle could provide significant economic benefits to the forest industry. The incidence of these commercially important wood quality parameters has been studied in this thesis in research conducted on young trees (1 to 3 years old). The research described in this thesis used a variety of different imaging approaches to investigate wood structure, including polarised light and confocal microscopy, and X-ray tomography and circular polarised light scanning. The images achieved have been analysed using a range of different software, including Photoshop, ImageJ and Matlab bringing a quantification approach to the imaging.

Compression wood was quantified in young clonal material using images collected with a commercial document scanner, and processed using image analysis tools available in Photoshop. An easy, reliable and robust, automatic image analysis protocol was successfully developed and tested for the detection and quantification of compression wood in these young trees. This new technique to detect and quantify compression wood was based on the thresholding of the blue channel of the scanned RGB image as this was demonstrated to contain the greatest image contrast. Development of this new technique may reduce the waiting time for screening clonal planting materials based on compression wood content.

To understand the organisation of the grain at a cellular level within these young trees, confocal microscopy techniques were utilised. The cell wall characteristics and fluorescence properties of compression wood in comparison with normal wood were investigated using a new cellulose specific dye, pontamine fast scarlet 4B. Staining protocols for this dye for confocal microscopy were optimised, and the potential of measuring the microfibril angle of the S1 and S3 layers of the pontamine treated opposite wood was demonstrated through either direct observations of these layers, or through the property of bifluorescence where the dye is excited only when aligned parallel to the polarisation of the incident light.

Despite extensive work with confocal microscopy, this technique proved to be unsuitable for investigations of spiral grain because although it provided cellular detail, imaging was limited to the surface layers of sections, and the area over which observations were required was prohibitive. Instead of confocal microscopy, the incidence of spiral grain in young stems was investigated in two completely new ways. Resin canals, which are formed from the same cambial initials as the tracheids and which align with the grain, were used as a proxy to demonstrate the grain changes. A novel technique, using circular polarised light and a professional flatbed scanner, was developed to image whole serial transverse sections of the young stems to detect the resin canals. Using ImageJ, the number and location of resin canals was measured on vertical controls, and trees that had been rocked and leaned. The number and frequency of resin canals were less in tilted trees, especially in compression wood, compared to the higher number of canals formed in the rocked trees. More importantly, a combination of serial sectioning and this approach allowed a 3-dimensional view of the orientation of resin canals inside a stem to be generated with ImageJ, and the angles of these canals could be measured using Matlab.

The resin canals were oriented with a left-handed spiralling near the stem surface whereas the canals near to the pith were nearly straight, consistent with previous observations of the development of spiral grain in radiata pine. However, it was observed that while vertical trees had a symmetric pattern of grain and grain changes around the stem, this was not the case in tilted trees. In these, the opposite wood often had severe spiral grain visible through formation of twist whereas the compression wood formed on the lower side had bending. Consistent with this, grain associated with compression wood was significantly straighter than in opposite wood. This hitherto unknown link between the incidence of compression wood and spiral grain was investigated and explained on the basis of the characteristics of resin canals in these types of wood. X-ray micro-tomography was also used to investigate resin canals in the stubs from which serial sections were collected. The 3D reconstructions of the resin canals showed exactly the same patterns as observed by polarised light scanning.

Abbreviations

CLSM	confocal laser scanning microscopy
CW	compression wood
FAA	formaldehyde - acetic acid - alcohol
IAA	indole-3-acetic acid
MFA	microfibril angle
MOE	modulus of elasticity
MOR	modulus of rupture
NW	normal wood
OW	opposite wood
P4B	pontamine fast scarlet 4B
SEM	scanning electron microscopy
FFT	fast Fourier transform

List of Figures

List of Tables

List of Movies

Movie 1 Rocking trees undergoing the simulated wind treatment on a purpose-built rocking mechnism

Movie 2 3-dimensional visualisation of spiral grain through image reconstructions followed by detection of canals in the serial transverse section images.

Chapter 1

The incidence of compression wood and spiral grain in *Pinus radiata* and their impact on wood quality

1.1 Introduction

The role of plants and plant-derived products, especially wood, in human life is immense. The timber for human utilisation is produced from the wood of either softwoods (gymnosperms, including the pines) or hardwoods (angiosperms, the flowering plants). This timber, however, can be of different quality. Wood quality is a broad term that describes the suitability of a particular species for a specific use. Density, moisture content, shrinkage, stiffness and the presence of knots, compression wood and spiral grain are some of the important parameters determining wood quality (see section 1.5).

Radiata pine (*Pinus radiata*) is the most important softwood plantation species in New Zealand and the timber produced from this tree can suffer from several different wood quality problems. These include the presence of compression wood and spiral grain, and these issues are highly problematic for the New Zealand forestry industry. In this thesis, methods for the early detection of compression wood and spiral grain in young trees have been investigated, as these might enable plant breeders and policy makers to more rapidly assess good and bad trees and clones for the next generation of planting. Novel imaging techniques are also used. The cell wall features of compression wood are presented, in comparison with normal wood, through visualisation with a new cellulose-labelling dye, pontamine, and confocal microscopy. Novel imaging techniques based on circular polarised light and X-ray tomography, along with 3-dimensional rendering techniques, are also presented to visualise and quantify resin canals and spiral grain.

1.2 The tracheid cell wall

In gymnosperms, tracheids are the major conducting and supportive cell element and constitute over 90% of the total wood volume (Brändström, 2001). Each tracheid has a well defined cell wall structure. The formation, development and organisation of the different layers of the cell wall in radiata pine tracheids is highly complex, both at the structural and biochemical levels (reviewed in Donaldson, 2008; Plomion et al., 2001). Wood cells that develop into xylem originate in the vascular cambium, and transform through cell expansion, cell wall thickening and lignification before their programmed cell death. During this journey, a variety of physical and chemical changes occur. Once cell expansion is completed, polysaccharides such as cellulose and hemicelluloses, lignin, cell wall proteins and other minor soluble (flavonoids (stilbenes and tannins), and terpenoids) and insoluble compounds are deposited or formed within the secondary wall (Plomion et al., 2001).

1.3 Organisation of the tracheid cell wall

The tracheid cell wall is composed of two main but separate regions, the primary and secondary walls, in which the former disappears with cell maturity to form the compound middle lamella, and the latter develops in to three separate layers (Figure 1.1b).

i) The middle lamella is the first layer formed after the cell differentiation and is the cementing layer that marks the junction between adjacent tracheids. This layer is amorphous and is composed of pectic substances that are insoluble in water and to which lignin is added during cell differentiation. The middle lamella region contains no cellulose microfibrils and ranges in thickness between 0.5 and 1.5 µm (Walker and Butterfield, 1993).

ii) The primary wall is the outermost of the cell wall layers, and is highly elastic and thin (about 0.1 µm). However, its thickness is reduced to as little as 0.03 µm in mature secondary wall making it extremely hard to distinguish. Hence, the primary wall is often considered combined with the middle lamella and known as compound middle lamella (Walker and Butterfield, 1993; Wiedenhoeft and Miller, 2005).

iii) The secondary wall has 3 distinct layers which are structurally and functionally different (Figure 1.1b). The outermost layer, S1, is the thinnest among the secondary walls (0.1 to 0.35 µm) comprising less than 10% of the total cell wall thickness. The S2 layer, the middle layer of the secondary wall, is the thickest and most important layer considering its role in providing mechanical support to the tracheid and the tree as a whole. The thickness of this layer varies between 1 to 10 µm which is about 75 to 85% of the total wall thickness. This highly-lignified layer is made up of cellulose embedded in a matrix of lignin and hemicellulose. The innermost layer of the secondary wall is the S3 layer that, where present, is adjacent to the lumen. In radiata pine, the S3 layer is considerably more lignified than the S2 layer (Donaldson, 1987). This lignin-rich layer is very thin (0.5 to 1.1 µm) but forms a barrier between the lumen and the rest of the cell wall. Early wood tracheids are thinner-walled than latewood tracheids as they contain a thinner S2 layer (Walker and Butterfield, 1993).

The lumen is the cavity inside the tracheid which carries all the nutrients from the roots to leaf and the processed food back to the cells. The lumen surface is lined with a wax like coating to make an extremely thin ‘warty layer’.

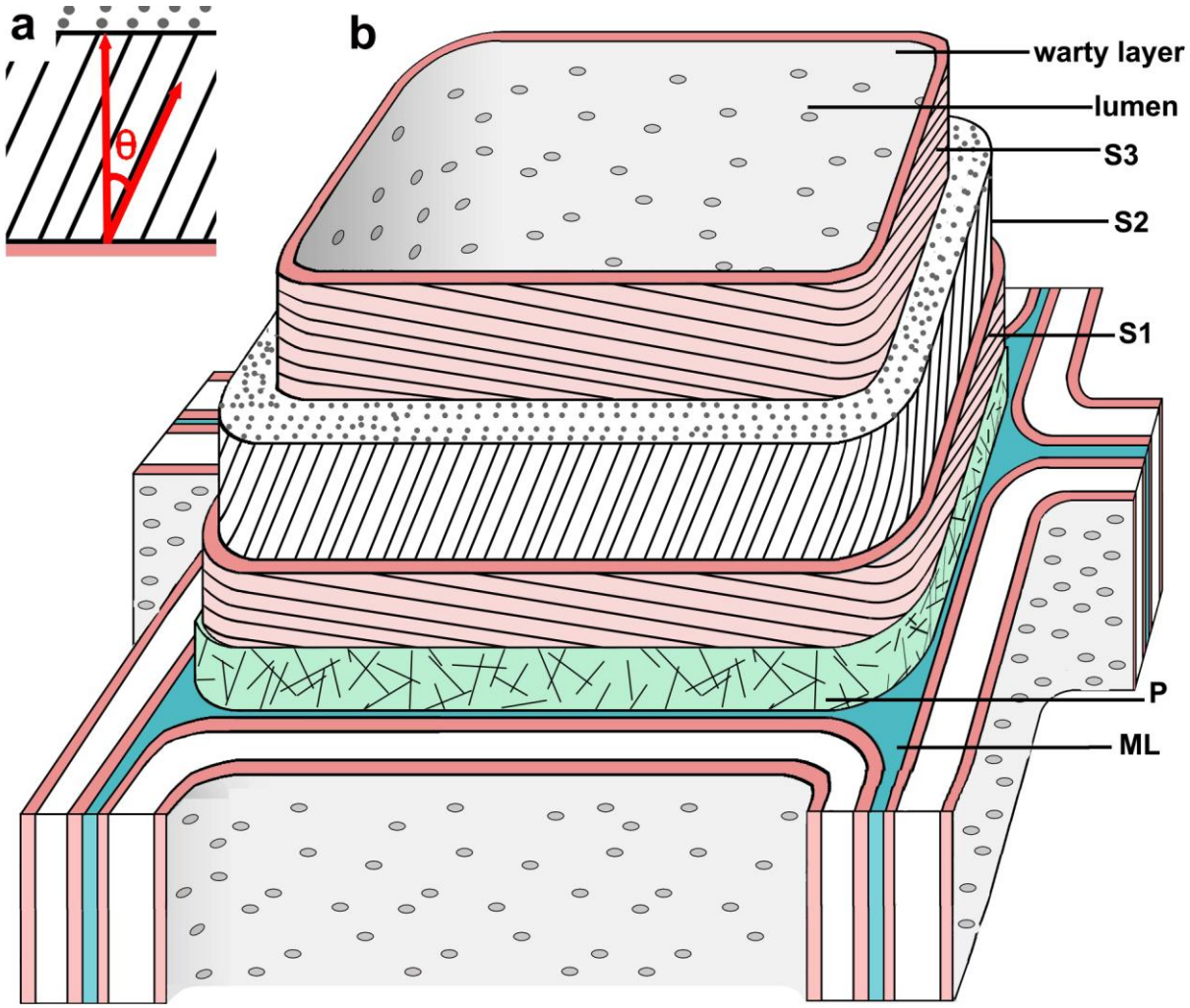

Figure 1.1 Organisation of cell wall layers in a tracheid.

a. The angle formed between the microfibrils of the S2 layer and the cell's axis is denoted as θ.

b. ML - middle lamella, P - primary wall, S1 - outer layer of secondary wall, S2 - middle layer of secondary wall, S3 - inner layer of secondary wall, lumen - the cavity inside the tracheid, and warty layer - the lining ion the lumen surface.

(Originally image drawn by David Collings, and subsequently customised by JT.)

1.4 The importance of microfibril angle

Each cell wall layer is made up of bundles of cellulose microfibrils oriented at an angle to the tracheid axis. The angle between the orientation of the cellulose microfibrils and the tracheid longitudinal axis is called the microfibril angle (MFA) (Figure 1.1a). In addition to the variation between the different layers of the cell wall (Figure 1.1b), the microfibril angle varies within and between tracheids of different wood types, with a tracheid's position in the tree, with species and with locality. It is the differences in organisation of cellulose microfibrils within the different wall layers that define many of the physical and mechanical properties of wood, and of timber cut from the wood. The microfibril angle, especially of the S2 layer, is considered the major parameter influencing certain physical and mechanical properties such as the stiffness and strength of the wood as a whole.

In the S1 layer, the cellulose microfibrils are oriented nearly perpendicular to the tracheid axis (Abe and Funada, 2005) creating large microfibril angles (Kollmann and Cote, 1984; Walker and Butterfield, 1993). In the S2 layer, the microfibrils are very closely packed enabling the tracheids to bear the weight and stress acting on the cells (Booker and Sell, 1998). The typical range of microfibril angle variation in the S2 layer is between 0 and 60^0 (Donaldson and Xu, 2005). The microfibrils in the S3 layer have a parallel arrangement with a less strict order and the angle ranges between 60 and 90^0. The microfibril angle of mild compression wood (defined in section 1.7) is about 5^0 higher than opposite wood, meaning that the microfibrils run in a more transverse direction, while in severe compression wood the microfibril angle is about 8^0 more than that of the opposite wood (Donaldson, 2008). Understanding the organisation of the microfibrils in the different cell wall layers is critical for investigating wood quality.

1.5 Wood quality in radiata pine

Radiata pine is one of the most widely planted and commercially important softwood plantation species in the world, and it is currently the most extensively planted conifer species in New Zealand, Australia and Chile (Cown, 1999; Gapare et al., 2007). In New Zealand, it constitutes about 90% of the country's plantation forests. Radiata pine has many desirable properties for a variety of general purpose uses. This timber saws easily with high lumber recovery, is very easy to kiln dry to achieve uniform moisture content and has excellent treatability with preservatives to comply with all durability levels. Its medium density, even texture and good machinability make it particularly suitable for joinery, mouldings and turnery, and considerably better than many other temperate conifers of similar density. It compares favourably with other similar species in routing, finger jointing, sanding, fastening

characteristics, paper making properties and veneering (Cown, 1999). Furthermore, problems like severe malformation, internal decay and growth stresses, which are associated with other common species, are rare in radiata pine.

1.6 Wood variability in radiata pine

The use of radiata pine as a fast growing plantation species has many problems. Some of these problems are associated with the shortening of the rotation of the trees which, in New Zealand, are harvested as young as 27 years old. This results in a substantial variability in wood quality, both between trees and within a tree (Cown, 1999; Cown and Hanslett, 1996). Variability in radiata pine timber occurs for multiple reasons. For example, wood density, the most important wood property of any tree, shows wide radial and axial variation within a tree, and shows significant variation between trees from different stands, sites and environmental conditions.

Another pronounced wood quality issue related to the immature trees is the high proportion of corewood (also known as juvenile wood). These different types of wood are explained in Table 1.1. In New Zealand, the term corewood is more commonly used as it aptly describes its position in a tree. In *Pinus radiata*, corewood is the wood found within 10 growth rings from the central pith, and thus is formed in the first 10 years of growth. The morphology and chemical composition of corewood are significantly different from compression wood (Yeh et al., 2005). This corewood causes problems during processing and utilization as it has wider growth rings, lower density, and shorter tracheids. It also has a higher microfibril angle, higher longitudinal shrinkage, a higher presence of compression wood and more pronounced spiral grain (Cown et al. 1991; Zobel and Sprague, 1998). Corewood's properties, however, often result in dimentional instability such as shrinking when the timber is dried. Such changes in shape are highly undesireable in timber to be used for construction. Also, the presence of a high amount of non-durable sapwood, which is prone to stains, fungal and termite attacks, requires preservative treatment for practically all purposes, especially in tropical export markets. The occurrence, causes and related features of two of these quality issues, compression wood and spiral grain, are of particular importance to radiata pine considering the various aspects of tree growth, processing, utilisation and the commercial value of this wood species in New Zealand.

The intention of this study is to develop a better understanding on how compression wood and spiral grain are associated with young stems of *Pinus radiata* at a cellular level, and to develop suitable tools to detect and quantify these. In the remainder of this introduction, the vast literature concerning these wood quality parameters will be discussed in separate sections.

Table 1.1 Important differences between wood types.

Wood type	Distribution	Appearance	Physical features	Cell shape	Wall chemistry and microanatomy
Normal wood		Circular cross section, pith at the centre, light colour sapwood and darker heartwood.	Nominal levels of shrinkage, density, moisture content, strength	Tracheids with an angular to rectangular cross sectional shape.	S2 wall uniformly thick & lignified, S1 & S3 present. S2 microfibrils arranged parallel to axis with orthogonally arranged S1 and S3 microfibrils.
Reaction wood	Angiosperms (tension wood) and gymnosperms (compression wood)	Tissues formed as result of the mechanical stress due to reasons like gravity, wind or snow.	Light and less stiff tension wood forms on the upper side. Highly dense, heavy and tough compression wood forms on the lower side.	Eccentric cross section in both the tension and compression wood.	Higher cellulose and lower lignin content in tension wood. Higher lignin and lower cellulose content in compression wood.
Compression wood	Gymnosperms	Eccentric cross section, pith move upwards, new darker coloured compression wood tissues form on underside.	Higher longitudinal shrinkage. Lower radial, tangential and volumetric shrinkage. Low moisture content	Rounded tracheids with thicker cell walls, narrow lumen and inter-cellular spaces. Tracheids are also shorter.	Highly lignified S2L region. S3 mostly absent. Inner S2 with helical thickening or checks. reduced cellulose content. Large S2 microfibril angle ~50^0.

Table 1.1 continued

Tension wood	Angiosperms	Eccentric cross section, pith move downwards, new light coloured tension wood tissues form on upper side. Woolly appearance when fresh sawn.	High tensile strength when dry but very low when green.	Presence of cellulose-rich gelatinous layer in the fibers.	Lack of lignification but rich in cellulose. Microfibrils arranged almost parallel to fibre axis in the fibers.
Opposite wood		Wood formed, opposite to the compression or tension wood.	Similar to normal wood.	Similar to normal wood.	Similar to normal wood.
Juvenile wood or core wood	Angiosperms and gymnosperms	The wood in the first ten growth rings.	Low density, less latewood. High longitudinal shrinkage. Growth stresses create processing defects.	Short and thin tracheids/fibres with thin walls and large lumens.	Higher lignin and lower cellulose. large microfibril angle and spiral grain angle

Table 1.1 continued

Sapwood	Angiosperms and gymnosperms	Wood inside between the cambium and the heartwood	Lighter coloured, moistened, physiologically active part of the tree	Tracheids/fibres with an angular to rectangular cross sectional shape.	Contains stored food materials, water
Heartwood	Angiosperms and gymnosperms	Surrounding near to the pith, usually darker than the sapwood.	darker coloured, heavy, and dry, cells are dead and matured.	Tracheids/fibres with an angular to rectangular cross sectional shape.	Contains extractives, minerals

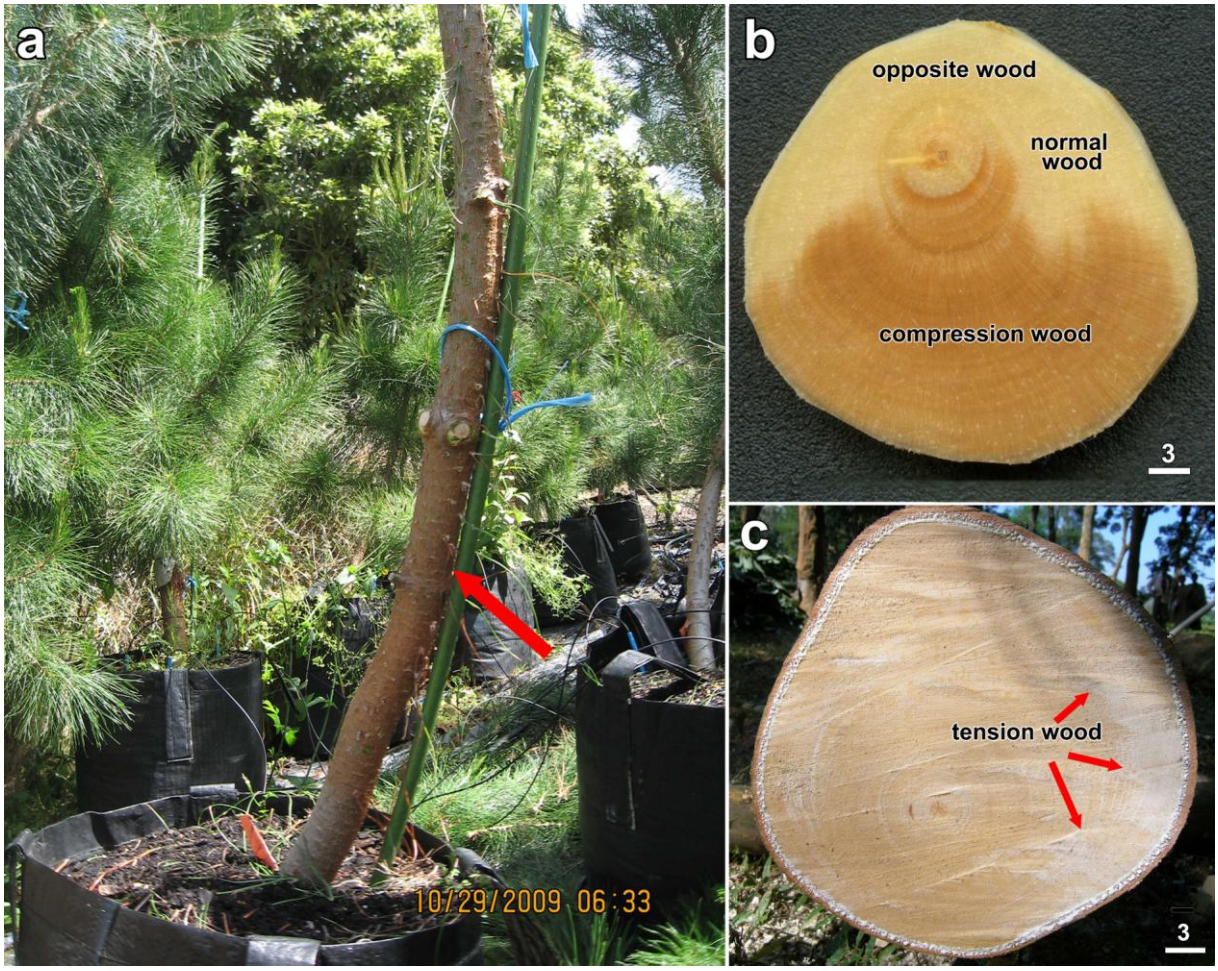

Figure 1.2 Reaction wood forms as result of bending.

a. A two year old radiata pine tree in a controlled bending experiment.

b. Transverse section cut from the arrowed location in the tree in **a**, showing darker-coloured compression wood formed on the lower side of the bending.

c. Transverse section of a rubber tree (*Hevea brasiliensis*), an angiosperm, showing the formation of lighter-coloured tension wood on the upper surface. The tree rotated through 90^{o} after felling. The white dots around the tree's perimeter are latex.

Scale bar in **b** = 3 mm and bar in **c** = 3 cm.

1.7 Compression wood

The general habit of trees is to grow upright. However, when this natural tendency is disturbed, either through mechanical disruption of the main trunk or through the growth of side-branches, trees develop reaction wood as a response (Table 1.1) (Low, 1964). In angiosperms, tension wood forms on the upper side of leaning stems (Figure 1.2c). Tension wood fibres have an additional cellulose-rich layer called the 'G-layer' that has a very low microfibril angle which contributes to a very high longitudinal shrinkage and many undesirable characters. In gymnosperms, however, reaction wood is called compression wood and forms on the underside of leaning stems (Figure 1.2a, b) (Boyd, 1977; Sundberg et al., 1994; Timell, 1986).

1.7.1 Physical, chemical, anatomical and ultrastructural characteristics of compression wood

Compression wood is substantially different from normal wood in its physical appearance, gross features and anatomical properties. Normal wood tracheids are characterised by thin cell walls, uniform lignin distribution and cross sectional shape. Mild compression wood tracheids showed lignification of the outer part of the S2 layer (S2L). Cell shape starts changing from polygonal or angular to round, creating intercellular spaces in the corners between the cells. Certain specific ultrastructural and chemical features are also associated with the presence of compression wood. At a larger scale, timber containing compression wood has eccentric pith, higher density (specific gravity), darker colour, lower permeability to liquids, lower fibre saturation point, lower radial and tangential shrinkage with significantly higher longitudinal shrinkage than the normal wood. Lower modulus of elasticity (stiffness) and tensile strength, and higher compressive strength are also associated with compression wood. Moreover, compression wood is also denser and more brittle than normal wood, fracturing more readily (Gardiner and MacDonald, 2005).

At the cellular level, compression wood differs from normal wood by the presence of intercellular spaces between individual tracheids, by tracheids being rounded and shorter than normal wood, by a uniform cell wall thickness both in early and in latewood (Toit, 1963), and by a larger microfibril angle in the S2 layer and lack of S3 layer (Harris, 1977; Timell, 1986). A thicker S1 region, highly lignified S2L region, presence of helical cavities in the inner S2 region and a lack of S3 regions are some of the ultrastructural features associated with compression wood.

At the ultrastructural level, compression wood has increased lignin but lower cellulose contents (Toit, 1963). A major chemical difference between normal and compression wood is in the uniformity of distribution of lignin among the wall layers. Compression wood is characterised by higher lignin and galactan contents while the quantity of cellulose and galactoglucomannan are lower than normal wood. While lignin and the content of galactosyl residues increase with the severity of compression wood, the content of mannosyl, glucosyl and arabinosyl residues decrease (Nanayakkara et al., 2005). In compression wood, the outer parts of the S2 layer becomes more heavily lignified and are collectively referred to as the S2L layer. In mild compression wood, this S2L is restricted to cell corners but in severe compression wood, it extends around tracheids and is more extensively lignified than the middle lamellae (above 70%) (Donaldson et al., 2004). Lignin in compression wood is also chemically different as it contains increased amounts of *p*-hydroxyphenyl (H units), derived from the monolignol *p*-coumaryl alcohol, compared to normal wood (Fukushima and Terashima, 1991; Li and Chapple, 2010; Nanayakkara et al., 2009). The modifications in compression wood lignin are revealed by changes in the fluorescence emission spectrum (Donaldson et al., 2010). These spectral differences arise from the fact that secondary wall lignin contains a higher percentage of phenolic –OH groups whereas the middle lamella lignin has a higher molecular weight and oxygen content (Donaldson, 2001). It is these structural differences that result in the physical characteristics of compression wood.

1.7.2 Compression wood in different species

Compression wood is typical of branches and leaning stems, and is present in all conifer species where it occurs in a range of gradations from normal wood through mild to severe compression wood (Burdon, 1975; Nicholls, 1982; Yumoto et al., 1983). It can be found at any position in the tree, but particularly near the pith. Yumoto et al. (1983) made a detailed study on the gradation of compression wood in young trees of white spruce (*Picea glauca*) and classified different types of compression wood based on microscopic features from normal wood through mild to severe compression wood. Elaborate and comprehensive reviews of compression wood formation in conifers were made by Cote and Day (1965), Duncker and Warensjö (2005), Timell (1983, 1986) and Westing (1965).

1.7.3 Compression wood in *Pinus radiata*

In radiata pine, around 15% of the total volume of radiata pine produced may be compression wood in some form (Timell 1986). Compression wood is most commonly found in the juvenile wood, partly because of the high rate of growth in this region of the stem (Burdon, 1975; Harris, 1977). Based on a study on compression wood in different clones of radiata pine growing at different sites, Burdon (1975) found that compression wood is more pronounced near ground level, and that straight trees contained little compression wood. In crooked trees, however, compression wood was abundant. These differences occurred regardless of the genotype. Many studies have reported a decrease in compression wood severity with height of the tree (Burdon, 1975; Cown, 1973; Harris, 1977). As in other trees, compression wood in radiata pine has wider growth rings, a reddish or brownish colour and little differentiation between early and latewood. Higher density, lower moisture content and lower fibre saturation point are also associated with compression wood (Cown et al., 2003). In transverse sections, compression wood tracheids have a rounded appearance with thicker cell walls and are surrounded at their corner by intercellular spaces. These tracheids are shorter in length, and have a higher lignin concentration in the wall layers and middle lamella, as found in other gymnosperms. Compression wood in radiata pine has an abnormally high microfibril angle (S2 layer cellulose microfibrils up to 72) (Donaldson and Burdon, 1995) leading to higher longitudinal shrinkage, but with lower than normal radial, tangential and volumetric shrinkage values (Cown et al., 2003; Donaldson et al., 2004). Donaldson and Turner (2001) found that compression wood percentage and distribution, microfibril angle, and microfibril angle gradient had a significant influence on the occurrence of distortion and suggested the need for further research to clarify the role of compression wood on dimensional (in)stability on anatomical and chemical levels in *Pinus radiata*.

Compression wood is chemically different from normal and opposite wood especially by higher lignin and lower cellulose contents. The presence of higher lignin content in the S2L region is characteristic of compression wood. The difference in chemical composition in compression wood is also associated with the distribution of the components (Cown et al., 2003; Donaldson, 1991; Donaldson et al., 1999). In radiata pine, changes in lignin distribution seem to be characteristic of the mildest forms of compression wood, with reduced lignification of the middle lamella representing the earliest change observed from normal wood (see section 1.7.1).

1.7.4 Environemental and genetic factors affecting compression wood formation

Although numerous different theories have been postulated concerning the formation of compression wood, a comprehensive explanation of the mechanism remains unclear (Burgert et al., 2006). Early theories related the combined forces of tension and compression stresses in the trunk, the effects of wind, development of branches on only one side, difference in the intensity of sunlight available to different sides of the trunk and radial pressure of the bark to account for compression wood development, but these ideas have generally been proved invalid (Toit, 1963). Similarly, various studies have been conducted on the distribution and the role of lignin in compression wood formation (Bamber, 2001; Kukkola et al., 2008; Saito and Fukushima, 2005; Yoshizawa et al., 1993). Bamber (2001) established that, contrary to the prevailing view, lignin is not involved in generating growth stress in compression wood. However, the severity of compression wood is positively correlated with a higher lignin concentration which is thought to provide better compressive strength to the stem to stay upright.

Several studies on the influence of site quality on compression wood formation were inconclusive (Burdon, 1975; McLaren, 2002). Among the different silvicultural factors, thinning and spacing had shown little effect on the compression wood formation. Studies on thinning practices showed that compression wood formation after thinning is directly related to the rate of growth and up to 20% of the wood formed after thinning was compression wood (Cown, 1974a; 1974b; Cown et al., 2003; Harris, 1977). Higher compression wood content was reported in trees planted with more spacing (Cown et al., 2003) and further studies on the same stands revealed that faster grown stems had about twice the level of compression wood as slower-grown stems. Shelbourne (1968) showed that the tendency to generate compression wood was inherited.

Of more relevance physiologically are the role(s) played by plant hormones. Extensive studies have been conducted to determine the role(s) of growth substances such as the naturally occurring auxin, indole-3-acetic acid (IAA), on the formation of compression wood (Christopher and Phelps, 1986; Funada et al., 1990; Sundberg et al., 1994; Wilson et al., 1989; Yamaguchi et al., 1980). Timell (1986), in his classical review, noted that high concentrations of exogenous IAA stimulate compression wood formation in vertical stems that would not otherwise form compression wood. In rooted stem cuttings of Douglas fir (*Pseudotsuga menziesii*), Christopher and Phelps (1986) induced the formation of new xylem cells as compression wood through the application of IAA for three weeks. In a similar experiment on 7 year old Douglas fir branches, Wilson et al. (1989) also found that the

occurrence of compression wood correlated with presence of IAA. Similarly, Funada et al. (1990), based on the experiments on 6 year old Japanese cedar (*Cryptomeria japonica*) trees, suggested that the induction and continuation of compression wood formation are associated with a high concentration of endogenous IAA. They also opined that the IAA-induced ethylene, another plant growth hormone, might be involved in the formation of compression wood. In radiata pine, compression wood formation induced by the application of IAA has been confirmed (Cown et al., 2003). These works suggest that plant hormones, especially IAA, have an important role in the formation of compression wood.

1.7.5 Effect of compression wood on strength and processing

Microfibril angle in the S2 layer of the secondary wall is believed to control many mechanical properties including stiffness (Cave, 1968; 1969). Due to the high microfibril angle of the compression wood tracheids, compression wood greatly reduces the strength of sawn timber, enhances the longitudinal shrinkage and causes significant distortion and instability on drying (Cown et al., 1996; Johanson, 2002; Nyström, 2002). It results in wooliness on sawn surfaces, and causes other undesirable attributes (Donaldson and Turner, 2001; Harris, 1977). Several studies have been conducted to explore the effect of presence of compression wood on timber properties. Its abnormal shrinkage properties create dimensional instability in service. Dhubhain et al. (1988) found that Sitka spruce (*Picea sitchensis*) planks containing compression wood have a lower stiffness, whereas Perem (1958) found that compression wood in red pine (*Pinus resinosa*) and white spruce lowers timber strength and reduces toughness. Warensjö et al. (2002) found that the distribution of compression wood in sawn timber influences the direction and size of bow and spring. Sawn wood containing excessive compression wood is undesirable because of the low value and the handling problems it may cause during processing and utilisation. Higher lignin content contributes to high level of hardness and brittleness to the wood which makes its handling difficult during wood working operations like drilling, turning, and planing. To minimize waste production and unnecessary material handling of the wood products, compression wood should be detected and rejected at an early stage of processing.

1.7.6 Detection and quantification of compression wood

The accurate detection of compression wood is problematic because of the gradation between normal wood, and mild and severe compression wood. Measurement of compression wood on disc surfaces is now carried out largely using image-processing techniques, based on the darker colour of compression wood (Nyström and Kline, 2000; Pont et al., 2007). Various other methods also have been investigated for the detection of compression wood, but these

have not generally been successful. For example, Nyström and Kline (2000) tested an automatic compression wood detection method that compared a colour camera and X-ray scanning, and concluded that X-ray scanning would not be useful in detecting compression wood in green southern yellow pine (*Pinus sp*.) lumber. Similarly, Moell and Fujita (2004) attempted to detect compression wood in radiata pine and Sitka spruce transverse section micrographs by using a Fast Fourier Transform (FFT) method and succeeded in detecting severe compression wood whereas the detection of mild compression wood was not satisfactory. Warensjö et al. (2002) were unsuccessful in modelling the distribution of compression wood only from external log geometry and but did conclude that compression wood content on the end of a log is a good indicator of compression wood inside.

However to evaluate young radiata pine clones on the basis of compression wood content in their cross section discs, a new quick, easy, reliable and robust method was required. None of the existing techniques was either suitable or available for the present study and a new methodology based on image analysis was therefore developed.

1.8 Spiral grain

Spiral grain refers to an inclination of the grain direction away from the tree's axis and is a natural feature in most tree species (Cown et al., 1991; Lausberg, 1997). It occurs in stems when the tracheids in gymnosperms, or the fibres in angiosperms, systematically have the same inclination away from the stem's axis. The tracheids and fibres thus describe a spiral, or more correctly, a helix (Cown et al., 1991; Harris, 1989; Northcott, 1957).

Spiral grain in trees is a normal condition of growth, emerging from a variety of normal growth patterns, and occurs both in gymnosperms and angiosperms, in trees of different ages from saplings to mature trees, and in plantation and naturally growing forest trees (Harris, 1981; 1989; Houkal, 1982; Kubler, 1991; Lowery, 1966; Northcott, 1957). Practically no tree, either at the individual or species level, seems to be completely free from spiral grain and, therefore, no tree will be entirely straight-grained throughout its stem. Spiral grain also occurs in roots and branches (Koslowski and Winget, 1963). Moreover, spiral grain can be observed in living trees through the pattern of the bark, and can be readily observed on dead trees, including electricity poles, as checks or cracks that appear along the grain (Figure 1.3a-d).

In conifers, the grain angle typically follows a predetermined pattern (Danborg, 1994b; Harris, 1989). This pattern, called the LR pattern for left-to-right, is for a maximum of left-handed spirality close to the central pith when the tree is young, and then a gradual decrease towards the bark, sometimes changing to a right-handed spiral in the outer rings (Danborg, 1994b;

Elliott, 1958; Harris, 1989; Noskowiak, 1963; Pape, 1999). This is the reverse of the RL (right-to-left) pattern in which the innermost parts of the tree have right-handed spiral grain which changes to left-handed in the outermost part (Skatter and Kucera, 1998). In many LR-patterned trees, the right-handed growth never occurs (Danborg, 1994b; Eklund et al., 2003; Gjerdrum et al., 2002; Harris, 1989).

Although the presence of spiral grain is considered to be a defect from a timber utilisation point of view, spiral grain must also be considered as a natural property of trees, which provides enhanced strength to withstand external forces such as wind and may allow more equitable distribution of water and nutrients (see section 1.8.7). Hence, it is beneficial to the trees. This duality arises from the fact that what people perceive as being useful and deleterious qualities in timber may not be relevant biologically for the tree itself, whereas wood properties important to the tree may be detrimental for their use by people as timber. To a certain extent, the same also holds true for compression wood. The higher than normal wood density and longitudinal shrinkage, but lower fiber saturation point, permeability, radial and tangential shrinkage typical of compression wood also contribute to keeping trees to stay upright because although compression wood has a lower modulus of elasticity and tensile strength, it does have higher compressive strength (Gardiner and MacDonald, 2005). However, these properties that are good for wood function in the living tree cause severe utilisation issues such as distortion, non-destructive uniform shrinkage and swelling when the wood is used as timber.

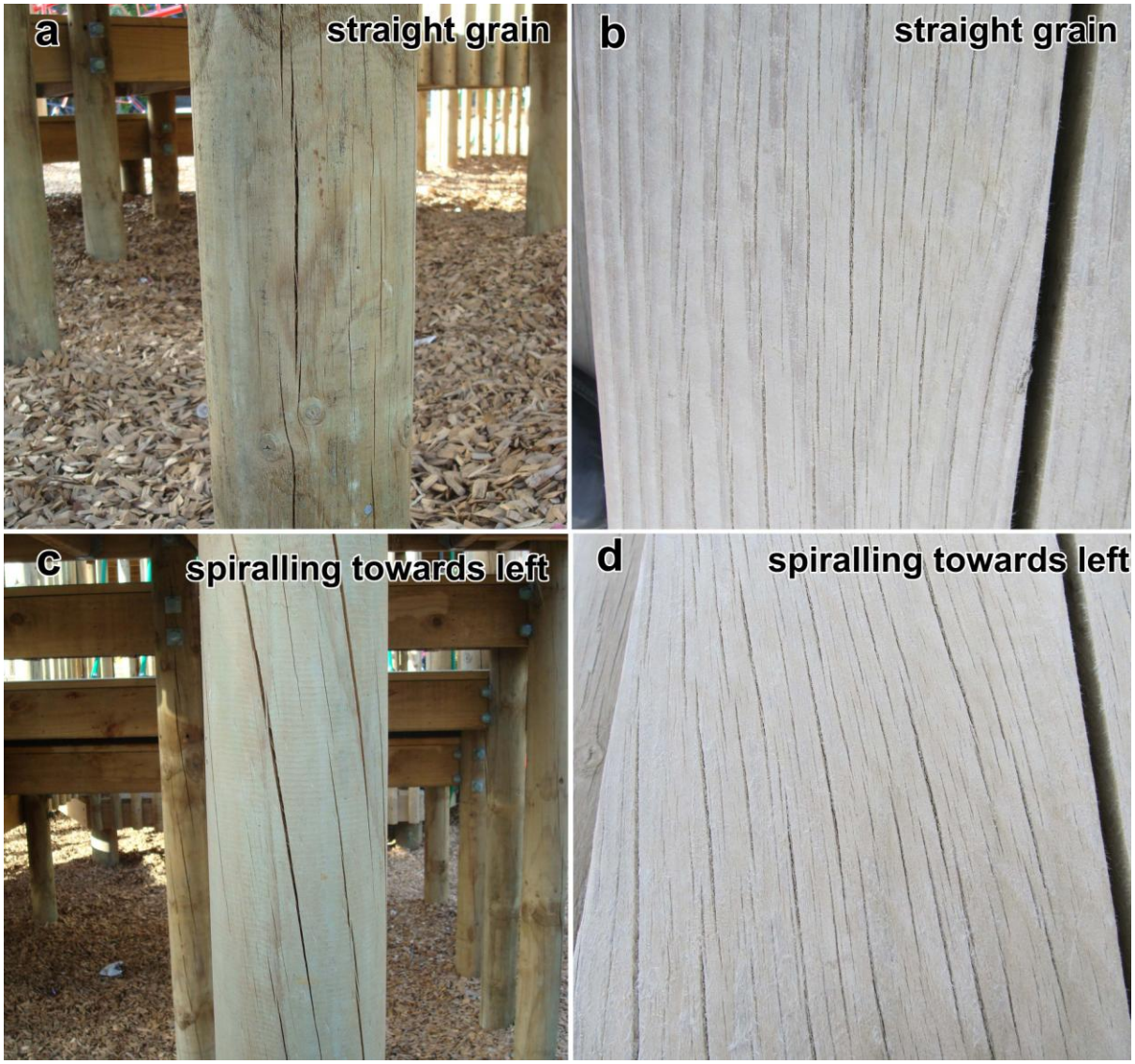

Figure 1.3 Spiral grain can be visible externally through surface checks and cracks.

a. Straight grain in this radiata pine pole was visible through surface cracks.

b. Straight grain present in a plank.

c. Left-handed spiralling present in a pole.

d. Leftward grain present in a plank.

1.8.1 The deleterious effects of spiral grain on timber properties

While spiral grain may be the natural growth state for trees (Northcott, 1957), it is considered by timber users and foresters to be a defect, and is one of several wood characteristics that influence the utility and acceptability of timber in the market (Raymond, 2002; Thinley et al., 2005). These issues occur because spiral grain

1) has a detrimental effect on the strength, seasoning and machining properties of timber (Noskowiak, 1963),

2) leads to a reduction in strength properties of timber (Cown et al., 1991; Dinwoodie, 2000; Gindl and Teischinger, 2002; Kollmann and Cote, 1984; Skatter and Kucera, 1997; Tsehaye, 1995),

3) has a negative effect on the surface smoothness (Harris, 1989; Sepúlveda, 2001),

4) and, most importantly, is a major cause of drying defects, especially twist in different pine species. Wood with a spiral grain angle of 5^{o} has approximately double the longitudinal shrinkage of straight-grained timber (Harris, 1965; Lausberg, 1997). This has been reported from New Zealand in radiata pine (Haslett et al., 1991), and in South Africa in from several other plantation species (Caribbean, loblolly, lodgepole, maritime, ponderosa pines - *P. caribaea, P. taeda, P. contorta, P. pinaster* and *P. ponderosa* respectively) (Sorensson et al., 1997). Similar reports also exist for Sitka and Norway spruce (*P. sitchensis* and *P. abies*) (Danborg, 1994a). Wood with spiral grain has a remarkable tendency to twist in dried sawn timber through anisotropic shrinkage (Balodis, 1972; Harris, 1965) (Harris, 1989; Ormarsson and Cown, 2005; Ormarsson et al., 1998; Ormarsson et al., 1999; Sepúlveda, 2001; Thinley et al., 2005; Tsehaye and Walker, 1996) which may result in the downgrading in quality or the rejection of large proportions of sawn boards (Balodis, 1972; Johansson et al., 2001; Kliger, 2001).

The economic losses due to spiral grain are considerable (Eklund and Sall, 2000; Harris, 1989; Skatter and Kucera, 1997). Cown et al. (1996) estimated that over 90% of the drying problem in *Pinus radiata* is related to twist which is related to both diameter and spiral grain. Tarvainen (2005) estimated that between 10 to 12% of wood produced in saw mills across the Europe was rejected due to distortion caused by spiral grain, which is equivalent to a devaluation of about €1 billion per annum. During the 1990s, it was also estimated that spiral grain devalued radiata pine logs entering New Zealand saw mills by NZ$100 million per year (Sorensson and Lausberg, 1996).

1.8.2 The presence of spiral grain in different species

Most northern hemisphere conifer species exhibit the LR spiral grain pattern (Harris, 1989) whereas southern hemisphere species have been reported to show the RL pattern (Balodis, 1972; Harding and Woolaston, 1991; Harris, 1989). This difference may reflect systematic differences in wind direction in the hemispheres or, more, likely, the fact that in the southern hemisphere the sun tracks through the northern sky in an anti-clockwise direction whereas in the northern hemisphere this is reversed (Harris, 1989).

Most research has been conducted on northern hemisphere species. Importantly, these species, including radiata pine, keep their original LR pattern even when grown in the southern hemisphere (Cown et al. 1991; Skatter and Kucera, 1998). This demonstrates that the differences between the LR and RL patterns must be controlled genetically through some unknown mechanism (see section 1.8.4), and that the overall pattern is not controlled by the environment.

The incidence of spiral grain is controlled at a genetic level in numerous species. Lowery (1966) studied spiral grain in four different conifer species (lodgepole pine, western larch (*Larix occidentalis*), Douglas fir (*Pseudotsuga menziesii*), Engelmann spruce (*Picea engelmannii)*) and found that each species has its own characteristic distribution pattern of spirality. In both Sitka (Brazier, 1967) and Norway spruce, spiral grain was more pronounced in faster growing trees (Danborg, 1994b). Extensive studies of Sitka spruce have demonstrated that grain angles aligned left and decreased from the pith and outwards and with height (Hansen and Roulund, 1998) and that almost no interaction was present between the genotype of the tree and the environment, suggesting that the spiral grain in Sitka spruce is under genetic control (Hansen and Roulund, 1997).

1.8.3 Spiral grain in *Pinus radiata*

Spiral grain has been extensively investigated in radiata pine by researchers in New Zealand and elsewhere, because its presence causes problems for the forestry industry. However, radiata pine shows some spiral grain characteristics that are unusual when compared to other pine species. Cown and colleagues (Cown et al., 1991) presented detailed studies of the variations in spiral grain in 25 year-old radiata pine trees grown in New Zealand. They found strong radial and vertical patterns of spiral grain formation with a substantial individual tree effect. Grain near the pith is aligned almost vertically, but left-handed spiral grain develops in the youngest growth ring reaching a maximum in the second or third ring. The most pronounced deviations from vertical were in the inner 10 growth rings (corewood) where the

left-handed deviation averaged 4.7^{o} which is sufficient to cause significant processing and utilisation problems (Cown et al., 1991). After achieving this maximum, the grain angle decreases slowly to approach zero by about the ninth year and thereafter the grain angle rarely exceed 2^{o} which can be either left- or right-handed. A similar pattern was reported by Chattaway (1959) after examining 13 to 30 year old trees grown in Australia. Significantly, Walker and Butterfield (1995) also observed that spiral grain is a property of corewood and is seldom severe outside this zone. Hence, radiata pine differs from many other softwoods where spiral grain is predominantly a feature of the outer wood of old trees (Cown et al., 1991; Harris, 1989; Skatter and Kucera, 1998). In radiata pine, spiral grain also tends to increase above breast height (Burdon et al., 2004; Cown et al., 1991; Dumbrell and McGrath, 2000; Tian et al., 1996; Walker and Butterfield, 1995) but there appears to be no or only limited correlation between growth rate and grain angle (Cown and McConchie, 1981a; Dumbrell and McGrath, 2000; Fielding, 1967). The reduced rotation times for radiata pine prevalent in the New Zealand forestry industry (harvesting below the age of 30 years) mean that the presence of significant amounts of spiral grain in the corewood can be highly problematic.

1.8.4 Environmental stimuli and spiral grain

Various factors have been suggested to cause spiral grain in trees. Early researchers attributed spiral grain to various environmental factors including gravity, day light, the direction of the sun's movement through the sky (different in the northern and southern hemispheres), the phases of the moon, snow, wind, altitude, soil, and temperature (reviewed in Eklund and Sall, 2000; Harris, 1989; Mattheck, 1991; Noskowiak, 1963). Even the Earth's rotation has been linked to twist in trees (Harris, 1989).

The role of the environment in generating spiral grain has been extensively tested, with few clear links ever established. Thus, Rault and Marsh (1952) could not find any effect of temperature on spiral grain in chir pine (*Pinus roxburghii*) grown in South Africa while Champion (1924) and Rault and Marsh (1952) could not find any effect of soil conditions on the development or severity of spiral grain. Although silvicultural factors like stand density (Rault and Marsh, 1952), early pruning and thinning contributed to the severity of spiral grain through higher growth rate, these could not be linked to spiral grain formation in Norway spruce stands owing to the large between tree variation in spiral grain (Pape, 1999). The role of growth rates is also equivocal: Elliott (1958) found spiral grain formation is related to slow growth in Douglas fir (*Pseudotsuga menziesii*) and western hemlock (*Tsuga heterophylla*) whereas faster growth rate was found responsible for spiral grain in radiata pine (Jacobs, 1935), *Pinus roxburghii* (Rault and Marsh, 1952) and in *Picea sitchensis* (Brazier, 1967).

Perhaps the best characterised environmental factor is the wind. Several early researchers (Cahn, 1931; Howard, 1932; Wentworth, 1931) considered prevailing wind as the causative factor for spiral grain formation. However the wind theory was questioned and rejected by Herrick (1932), Jacobs (1935) and Jacot (1931). They suggested age could be the contributory factor to the change in direction and magnitude of spiral grain by citing less spiral grain in old and mature trees. More recently, both Eklund and Sall (2000) and Skatter and Kucera (1997, 1998) have argued that spiral grain forms as a response to the torque generated by wind, and that the direction of the spirals depended on crown asymmetry and prevailing winds.

1.8.5 The genetics of spiral grain

As discussed above, northern hemisphere pines grown in the southern hemisphere retain their LR growth pattern demonstrating that spiral grain must be controlled at the genetic level. Direct evidence for this has also been obtained. Champion (1924), in a classic long-term study of spiral grain formation in chir pine *(Pinus roxburghii)*, established that spiral grain is a 'hereditary' characteristic and that is transmitted according to Mendelian laws. Kadambi and Dabral (1955) also observed that spiral grain is an inherited characteristic in chir pine, and subsequently, based on a detailed review of the spiral grain literature, Noskowiak (1963) also concluded that spiral grain is controlled genetically. Many other investigations also show a strong genetic control of the spiral grain (Hansen and Roulund, 1997, 1998; Harris, 1989; Kubler, 1991; Pape, 1999; Tian et al., 1996) although these widely-held views were challenged by Eklund and Sall (2000) and Skatter and Kucera (1997,1998) who argued that spiral grain is formed in response to wind torque, and that the direction of the spirals depended on crown asymmetry and prevailing winds.

Genes associated with spiral grain have not been identified. However, as it is believed that spiral grain formation is coupled with the cell divisions taking place in the cambial region (Harris, 1989) (see subsequent sections), and as spiral grain formation may be linked to plant hormones like auxin and ethylene (Eklund et al., 2003; Zagorska-Marek, 1986), genes associated with the formation or breakdown of hormones, or in their detection and signalling pathways might be linked to spiral grain generation. Eklund et al. (2003) concluded that ethylene regulates the extend of spiral grain angle formation in Norway spruce and balsam fir (*Abies balsamea*) whereas Zagorska-Marek (1986) concluded that auxin was important based on experiments that showed the orientation of fusiform initials that form parallel to auxin flow.

1.8.6 Mechanisms of spiral grain development

The functions of spiral grain, and the pathways that lead to its development in trees, have always fascinated researchers. Most evidence suggests that spiral grain develops during cell division and maturation within the vascular cambium, the meristematic tissue from which wood develops, and much effort in the past half century has been put into elucidating the mechanism(s) involved. There are three cell division-related processes which are believed to allow for the development of spiral grain (Eklund et al., 2003; Hejnowicz and Marek, 1974).These are:

1) Spiral grain angle is related to the frequency of pseudo-transverse divisions of the vertically-aligned cambial cells (Bannan, 1966; Hejnowicz, 1980; Kubler, 1991; Larson, 1994). The cells within the vascular cambium divide lengthwise in a periclinal manner (parallel to the surface of the plant) to form new xylem and phloem cells. However, as the tree increases in diameter, new cambial initials are required because the perimeter of the cambium has increased. The anticlinal divisions (perpendicular to the trunk surface) that form these new initials do not occur along the full length of the cell, but instead are pseudo-transverse. This means that the division plane forms at an angle across the cell, and results in two cells that are somewhat shorter than the original cambial initial. If the pseudo-transverse divisions occur more often in one direction than the other, then this might change the orientation of the cambial initials and thus the grain.

2) Another process involved is the imperfect periclinal divisions and the cell differentiations that accompany those divisions (Savidge and Farrar, 1984).

3) Intrusive growth can occur in either cambial initials (within the cambium) or in developing xylem cells. Intrusive growth means that the pointed tips of the cells undergo elongation, sliding in between already existing cells. If the opposite ends of the cell elongate in slightly different directions, this will generate a net rotation of the cell which results in a change in the angle between the stem axis and the cell.

There is some evidence to support the concepts listed above, all of which may contribute to the generation of spiral grain (Eklund et al., 2003). The most widely accepted view of spiral grain formation is that the pseudo-transverse cell divisions that occur during anticlinal (multiplicative) division in the vascular cambium, and the subsequent intrusive growth of the daughter cells, is biased to the left or to the right thus generating new cells at a slightly different angle to the previously formed cells (Kohl, 1933; Larson, 1994). Jura et al. (2006)

demonstrated through their studies on the cambial dynamics that intrusion of the elongating initial is taking place along tangential walls of adjacent fusiform initials and their immediate derivatives. This new concept also suggests a new mechanism for 'elimination of initials'. According to Schulgasser and Witztum (2007) development of the growth stresses and the formation of spiral grain are just two aspects of the same process occurring throughout the cambial zone during cell maturation. This approach was apparently proposed by Kohl (1933) and given strong support by Hejnowicz and co-workers (Hejnowicz, 1961; Hejnowicz and Romberger, 1979).

Based on girdling experiments in *Pinus radiata* saplings, Harris (1969) explained the development of spirality in terms of spiral flow of metabolites induced by the phyllotaxy of the vascular supplies to the short shoots as a contributory or determining factor. In subsequent studies, Harris (1973, 1981) concluded that ''the direction of pseudo-transverse division is thought to be symptomatic of differential growth rather than a primary cause of spiral grain'' and suggested that differential sideways growth of cell tips after periclinal division played a dominant role.

Some researchers have also suggested that a rapid change in the orientation of cambial cells may take place either as a result of intrusively growing cell ends twisting in one direction (Preston, 1949), or as a result of imperfect periclinal divisions (Savidge and Farrar, 1984). However, these authors did not explain the way in which those events might influence the inclination of cells (Włoch et al., 2002). Bannan (1966) suggested that the formation of spiral grain is related to the anticlinal divisions of the cambium cells and intrusive growth of the cell tips. He concluded that among the different types of morphogenetic events, the major contributing factor to the changing orientation of cambium initials leading to spiral grain formation is the pseudo-transverse division.

There have also been suggestions that link the formation of spiral grain to the microtubule cytoskeleton inside cells, through their link to the alignment of cellulose within the cell wall. In elongating and maturing cells of the roots of *Arabidopsis thaliana*, microtubules reorient from transverse to forming a helix with consistent handedness (Liang and Baskin, 1996). As it is also known that mutations in the protein tubulin that polymerizes to form microtubules can result in the generation of spiralling growth within the root and other elongating tissues (Thitamadee et al., 2002, Ishida et al., 2007), a link between microtubules and the generation of spiral grain has also been suggested (Liang and Baskin, 1996).

1.8.7. The functions of spiral grain

Many theories have been proposed on the functions of spiral grain in trees, and as to why spiral grain is so prevalent in different tree species. These have typically focussed on engineering and hydrological concepts. Kubler (1991) suggested that spiral grain benefits the trees mainly by redistributing the water and nutrients laterally within the trees with lopsided root systems. The reported relationships between environmental conditions and spiral grain provide some support for this supply hypothesis. This concept was supported by the modelling experiments of Leelavanichkul and Cherkaev (2004) in spiral grain-prone Ponderosa pine (*Pinus ponderosa*) which considered trunk morphology as a result of optimisation of a mechanical construction, and concluded that spiral grain developed to equally transport of water and nutrients to the branches and not for mechanical reasons. However, Kubler (1991), Noskowiak (1963), Skatter and Kucera (1997) and Wentworth (1931) all theorised that spiral grain might act as a contributor to increasing stability by dissipating the stresses formed in trees in areas with strong prevailing winds.

1.8.8 Methods for detecting and measuring spiral grain

Spiral grain can be observed on dead trees, dried logs, posts and utility poles through the drying checks on the surface (Figure 1.3), and through observation of bark inclination on standing trees or logs with bark (Chiu and Lee, 1993; Kliger, 2001). However, spiral grain measurements on the surface are not reliable as the magnitude and direction of spiral grain inside the wood likely to be different (Noskowiak, 1963; Rault and Marsh, 1952). Therefore, methods are required that measure spiral grain internally.

Spiral grain has been measured using a wide variety of approaches and tools. The traditional method for measuring grain angle is radial splitting (Brazier, 1967; Harris, 1989) which involves accurate splitting of a wood disc across its diameter to get grain angle measurements which are in turn converted in to spiral grain index using a simple formula. However, this splitting method has been found to be inaccurate for some trees and gives poor correlations with several other methods (Rauchfuss and Speer, 2006). Mechanical measurements of spiral grain can also be made by scribe instruments that score along a wood surface, running with the grain (Danborg, 1994b), by wire insertion into vessels (Kanai et al., 1996), through the injection of ink and observations of its transmission (reviewed in Harris, 1989) and through serial tangential sectioning.

Many non-destructive methods (that do not require sectioning or splitting of the timber) have also been developed to measure spiral grain. These approaches have included:

1) soft X-rays in wood discs of *Acacia mangium* (Ogata et al., 2003), X-ray computed tomography of whole logs (Sepúlveda, 2001), and X-ray diffraction (Silviscan technology) in Norway spruce logs (Buksnowitz et al., 2008),

2) near infra-red spectroscopy of small blocks of larch (*Larix decidua*) (Gindl and Teischinger, 2002),

3) microwave spectroscopy of lumber (Schajer and Orhan, 2006),

4) measurements of electrical capacitance in Douglas fir planks (McDonald and Bendsten, 1986; Samson et al., 1993), and the slope of grain indicator, a non-contact device that made measurements based on the dielectric constant of wood (McLauchlan et al., 1973; Samson, 1984),

5) using the tracheid effect where the light conducting properties of the tracheids are used to measure fibre orientation on Norway spruce planks (Nyström, 2003; Nyström and Grundberg, 2002),

6) confocal microscopy of transverse wood sections in *Hopea odorata* in which image analysis techniques were used to measure grain (Ogata and Fujita (2005), and,

7) mathematical modelling using green heartwood density and knot volume as input variables obtained from an industrial log scanner (Sepúlveda et al., 2002a).

These methods provide the compound inclination angle of tracheids and fibres, and information concerning the gross organisation of the wood, and define the average value of the grain. They do not, however, distinguish variations in grain angle at the cellular level and might be of little use in understanding how spiral grain may develop. This information would, however, be critical for developing theories about how spiral grain develops because it is at cellular level where the incremental change in tracheid orientation that generate spiral grain develop.

1.9 The scope and structure of the thesis.

The major aims of this research were to develop quick, easy and reproducible techniques to evaluate young radiata pine clones (up to 3 years old) based on compression wood content and the presence of spiral grain. Reduced breeding cycle could provide significant economic benefits for forest industry. The objectives were met by conducting experiments to:

- Develop software-assisted automated techniques to quantify compression wood in transverse sections.

- Characterise pontamine fast scarlet 4B (a cellulose specific fluorescent dye) with regards to normal and compression wood tracheids.

- Develop simple image acquisition and processing techniques to analyse resin canal properties in transverse sections of trees that had been subjected to tilting and rocking treatments, and to determine the potential of using these data for evaluating the young trees.

- Develop image processing methods to create the 3D visualisation of the organisation of resin canals and study the incidence of spiral grain, and to verify the potential of computed X-ray tomography as a tool to study spiral grain in wood.

Spiral grain and compression wood are, each in their own different way, a significant cause of decreased wood quality. Due to this, they have been subject to a large amount of research which is unfortunately mostly descriptive. While much is known about their prevalence in different species and under different conditions, and while many suggestions have been made as to their causes, little progress has been made in understanding how they develop, how they are organised within the stem and, more importantly, how they are connected each other. In fact, most research has not been interested on the growth of the trees, but in how spiral grain and compression wood relate to timber as a product. However, without an understanding of their organisation within the stem, efforts at mitigating spiral grain and compression wood defects through breeding and silviculture can only meet with limited success.

In this study, young radiata pine trees were investigated. These were from one to three years old and, in many cases, had been deliberately leaned to induce the formation of compression wood. In **chapter 2** of this thesis, the development of an easy and reliable image processing tool based on a Photoshop routine is described. This tool was used to evaluate and screen a large population of young clonal planting material for compression wood content, and showed that different clonal populations responded to tipping by generating small but significantly different amounts of compression wood. Development of this compression wood detection technique may contribute to the reduction in waiting time for screening clonal planting materials to find ‘potential winners’ and ‘certain losers’.

A newly-characterised, cellulose-specific dye, pontamine fast scarlet 4B, has been successfully used to visualise and study the cell wall organisation in normal and compression wood. The use of pontamine as a cell wall stain, along with imaging of lignin autofluorescence,

has revealed much information about the fluorescence properties of the different cell wall regions of radiata pine tracheids. This has been described in **Chapter 3.**

As part of a larger study in which the rocking of trees was used to mimic the effects of wind, axial resin canals present in complete serial transverse sections were measured using image analysis of methods on images collected with a professional flatbed scanner using circular polarised light. **Chapter 4** describes how the results achieved in this study run counter to previous investigations of rocked trees. More importantly, **Chapter 5** describes how, after extensive image processing of serial sections, the orientation of the resin canals could be reconstructed 3-dimensionally to visualise spiral grain at the cellular level for the first time. These observations were confirmed using X-ray microtomography of the same wood, with this approach allowing investigation of the internal organisation of tracheids and resin canals. The results confirmed a possible link between the development of spiral grain and compression wood, with grain angle being lower in areas of compression wood.

Chapter 6 discusses the salient features of the research undertaken during this study and summarises the conclusions.

Chapter 2

Automated quantification of compression wood in wood cross sections by image analysis

Some material from this chapter has been published. See Chauhan et al. (2013).

2.1 Introduction

This chapter concerns the automated detection and quantification of compression wood in cross sections of 2 to 3 year old radiata pine trees being screened as part of a larger investigation of selective breeding techniques. Using image analysis tools available in the Adobe Photoshop CS4 programme (version 11.0.1, Adobe Systems, San Jose, CA USA), an automated routine was developed exclusively for this purpose, which will be detailed in the following sections. The new method was verified by comparing automated results with a manual detection on the same samples and it was found to be comparable in accuracy but significantly faster than manual detection. Even though an attempt to evaluate certain radiata pine clones on the basis of compression wood content in them was made, the primary aim of the entire exercise was to verify the new, automated technique developed.

2.1.1 Radiata pine in New Zealand

Forestry is the third largest industry in New Zealand. As the most popular and widely planted tree species in New Zealand, radiata pine holds an important role in the forestry sector, in particular, and the economy of the country in general. However, a reduction in the rotation age (the frequency of harvesting) of radiata pine to below 30 years has contributed to variable and reduced wood quality, with the incidence of compression wood being a major concern. Currently, a variety of clones of *Pinus radiata* are under commercial cultivation and these produce wood of variable quality.

Quick and accurate screening of clonal populations to select the good clones for future plantations, and to avoid the poor ones, is of paramount importance for a tree breeder. Traditionally, such a screening and selection of clones take place between the ages of 8 to 15 years for trees with a rotation period of about 30 years. This has created a considerable delay and contributed to higher expenses (Chauhan et al., 2013). For solid wood applications, the selection of clones has been based mainly on the basis of wood density. Recently, however, breeders have started to use quick and easy methods such as portable acoustic devices to evaluate large number of trees belonging to various clones at the sapling age, so as to reduce the generation interval (Apiolaza et al., 2011; Apiolaza et al., 2008; Chauhan et al., 2013). Portable devices such as Fakopp-2D and Woodspec have been used to non-destructively measure the acoustic velocity in standing trees and logs.

Because the acoustic velocity in wood is directly related to the wood density and the elastic modulus by the following equation

$$E = \rho V^2$$

where V is the acoustic velocity, E is the axial elastic modulus and ρ is the wood density (Chauhan and Walker, 2006), measuring the acoustic velocity allows direct measurements of stiffness and wood density.

Such early selection for wood quality needs rapid and reliable methods of wood quality assessment of a large breeding population. As this PhD research is a part of the ongoing research for ranking radiata pine genotypes on the basis of physical properties of their normal wood, comparison of genotypes based on the amount of compression wood formed would be another interesting outcome.

2.1.2 Quantification of compression wood

2.1.2.1 Existing techniques

In this section, only non-destructive methods for the detection of compression wood are discussed, with these primarily using image analyses. All other methods are discussed elsewhere (section 1.7.6).

Almost all softwood logs contain some compression wood, although some radiata pine clones are more prone to the incidence of compression wood than others. The importance of properly detecting and segregating compression wood during the processing of logs is extremely high for the successful running of the processing industry, and correct segregation of logs is of paramount importance. Being non–destructive and real time, image analysis techniques are popular in the timber industry for variety of purposes such as to detect various log characteristics including taper and defect localisation. Several attempts have been made to apply such processes to the automated detection of compression wood.

One of the earliest attempts to use digital image analysis for the automatic classification of compression wood was conducted by Andersson and Walter (1995). They developed an algorithm that used a supervised maximum likelihood classification to discriminate compression wood in colour images of thin wood discs photographed with a colour CCD camera. Even though this method could discriminate normal and mild compression wood in the images, accurate detection of severe compression wood was not achieved. In a different approach, Moell and Fujita (2004) suggested an image processing method for directly analysing tracheid and lumen shape over an entire confocal microscope image to detect

compression wood using a Fast Fourier Transform (FFT) technique. Their method was reportedly successful in detecting severe compression wood but the detection of mild compression wood was not satisfactory.

In a further approach, Duncker and Spiecker (2009) developed a method to detect compression wood on wood cross sections of Norway spruce by a technique called hyper-spectral image analysis. Wood cross section images were recorded with reflected light with an imaging spectrograph capable of simultaneously measuring the optical spectrum and spatial location of an object surface. An image processing routine was then used to detect and classify compression wood from the spectral properties. They reported an overall accuracy of 91%. The detection and classification of compression wood was done by a 'Spectral Angle Mapper algorithm', which compared the standardised spectrum of each pixel with reference spectra stored in a digital spectral library. Hyper-spectral image analysis was used to classify the wood cross sections to severe, moderate and normal compression wood and cracks/background. As it is difficult to set up these spectral analysis systems, and as the required reference spectra are not readily available, this approach has limited applicability beyond the Norway spruce trees used by Duncker and Spiegler. Moreover, its suitability for analysing young stems in which growth rings are not strongly visible remqains untested.

Nyström (1999, 2002) attempted different non-destructive methods to detect compression wood in Norway spruce and southern yellow pine sawn timbers. The methods were spectral and colour scanning, X-ray scanning and tracheid effect. Spectral scanning utilised many narrow wavelength bands to detect minute differences in the colour of normal and compression wood and the colour scanner utilised the spectral difference in light reflecting from normal and compression wood surfaces. X-ray scanning used the difference in density between normal and compression wood; and the tracheid effect scanning utilised the light scattering properties of the tracheids. Even though density differences between the normal and compression wood were considered as an indicator of compression wood, the influence of moisture content on density masked the differences. This suggested that X-ray scanning was not useful for detecting compression wood in green (undried) timber. Their results, however, confirmed the potential of colour scanning and the tracheid effect for compression wood detection.

Image analysis was also used by Warensjö et al. (2002) for compression wood detection to examine the correlation between compression wood content in log cross sections and the external log geometry. By measuring compression wood using an image analysis software

‘Compression wood Analysis 1.0’, this study found that compression wood content in the wood cross section is a good indicator for the compression wood inside the log.

There have also been several attempts to quantify compression wood with methods that are not fully automated and which require manual inputs from an operator. Wernsdörfer et al. (2004) attempted to identify and measure compression wood in digital images of Norway spruce log cross sections. Colour images were collected with an ordinary digital camera under uniform conditions before being processed using Photoshop tools like ‘lasso’ and ‘magic wand’ to detect the stem cross section and compression wood content. This method involved intense manual operations which can be subjective and time consuming. Similarly, Pont et al. (2007) developed a semi-automated method using image processing which examined the 3D distribution of compression wood in cross sections of radiata pine. The main drawback of this method was the operator-assisted selection of the threshold value which is detrimental in delineating compression wood and annual ring which is subjective due to the possible operator bias in judging and selecting compression wood or non-compression wood areas. And more recently, Selig et al. (2012) attempted to develop an automated method to detect and delineate compression wood tracheids using digital image analysis of fluorescent microscopic images to compute the compression wood content. Their method envisaged automatically segmenting the tracheids into lumen and different cell wall regions, based on lignin autofluorescence, and thereby differentiate between normal and compression wood tracheids. In this method, the detection of various fiber wall regions compared well with manual segmentation, but discriminating the boundary between the lumen and the cell wall was not successful.

2.1.2.2 Why do we need a new compression wood detection technique?

Many of the methods described in the previous section were either based on a limited number of samples, achieved only a limited success rate or used specialised equipment not generally available. Moreover, the methods were designed for detecting compression wood on sawn surfaces or on logs of large cross section area where knots and other wood defects need to be considered. In some of these methods, operator assistance was required to define or select the compression wood area. This can be a major source of error in detection as manual detection can be subjective (Selig et al., 2012). Besides, operator interference in selecting the deciding parameter (e.g. threshold) denies equal treatment to all samples in selecting compression wood.

Aiming at improving the wood quality of radiata pine wood and the tools available for selecting trees, a series of trials comprising different pine clones was established by the School of

Forestry at the University of Canterbury (Apiolaza et al., 2011; Apiolaza et al., 2008; Chauhan et al., 2013; Sharma, 2013). The overall aim of these experiments was to evaluate the clones based on specific wood quality parameters, including compression wood, to find the 'potential winners' (best clones) and 'certain losers' at a very young age (2-3 years). Thus, the waiting period for screening the clones could be minimised which is more economical than maintaining trials for up to 15 years.

However, such early selection of clones requires a rapid, reliable and robust method to detect and quantify the compression wood content on the basis of uniform criteria with minimal, subjective operator assistance. At present, there is a dearth of methods suitable to evaluate large numbers of wood cross sections from small trees of age less than 3 years. This chapter describes the evolution of image processing tools in Photoshop to generate a powerful automated protocol for batch processing images to measure compression wood. The development of a suitable automated detection technique for quantifying compression wood in wood cross sections of 2-3 year old radiata pine clonal samples was invaluable for the early evaluation and screening of these clones for the future plantations. The method is, however, only suitable to discriminate between the compression wood and the normal wood without separating in to different grades of compression wood.

2.1.3 Objectives

The research described in this chapter had 3 objectives. These were:

1) Using image analysis techniques to develop a quick, easy and reproducible method suitable for detecting and quantifying compression wood on young stem cross sections of 2-3 year old pine trees.

2) Automating this image processing technique in a manner that was suitable for batch processing.

3) Verify the new software-assisted image analysis tool against manual detection, using data collected from 2 year old radiata pine clones on the basis of the quantity of compression wood detected on their stem cross sections.

2.2 Materials and methods

2.2.1 Sources of plant material

The experimental wood specimens used in this study were sourced from two year old radiata pine plants from three different trials raised at different locations in Christchurch, Canterbury, New Zealand. The various letter and number codes used to describe the clones are used to hide the actual clonal identification which is proprietary information. Precise identity information was not required for this current study.

2.2.2 Growing trees and induction of compression wood

As part of a large wood quality screening programme run by the School of Forestry, University of Canterbury, Christchurch, wood from three different clonal trials was used to develop and improve screening protocols for compression wood. In the first set of samples (trial 1), a progeny trial comprising 4 different radiata pine clones (A, K, W and F) was established in Amberley, near Christchurch (43.15^0S 172.73^0E) in spring 2007 . These trees were planted in the ground (Figure 2.1a). Two leaning strategies were used to induce compression wood in these stems. After two months, the trees belonging to clones 'W' (9 trees) and 'F' (9 trees) were leant at an angle of approximately 35^0 from the vertical axis to induce compression wood, and were tied on to a stick kept at this angle (Figure 2.1b). The upper portion of the tree above the leaning was left free to reorient and grow vertically. In late autumn 2008, and at the age of around 6 months, the trees of clones 'A' (12 trees) and 'K' (6 trees) were leant in the same way. In late autumn 2009, trees of 'A' and 'K' were destructively sampled for various analyses, whereas 'W' and 'F' trees were cut in spring 2009, at the age of two years. These differences in treatment contributed the variability in compression wood formation between the different clones in this trial. Uniform compression wood was formed on the lower side of the leaning stems of the clones 'W' and 'F' (Figure 2.2a), whereas the compression wood initially formed in the trees of clones 'A' and 'K' was random as a result of their free standing in the first six months but was then found on the lower side of the stem (Figure 2.2b).

A second set of samples (trial 2) derived from trees belonging to 5 clones (F, I, K, O, and S) that were raised at the University of Canterbury farm in Christchurch (43.5^0S, 172.6^0E) under similar conditions but planted in 100 litre planter bags (Figure 2.1c). Six months after planting, trees were tilted in the same way as described above (Figure 2.1d). These plants were harvested in early spring 2009.

Figure 2.1 Growth of radiata pines for screening.

a. Vertical tree before leaning in trial 1.

b. A leaned tree from trial 1.

c. Vertical tree in a planter bag before leaning in trial 2.

d. A leaned tree in trial 2.

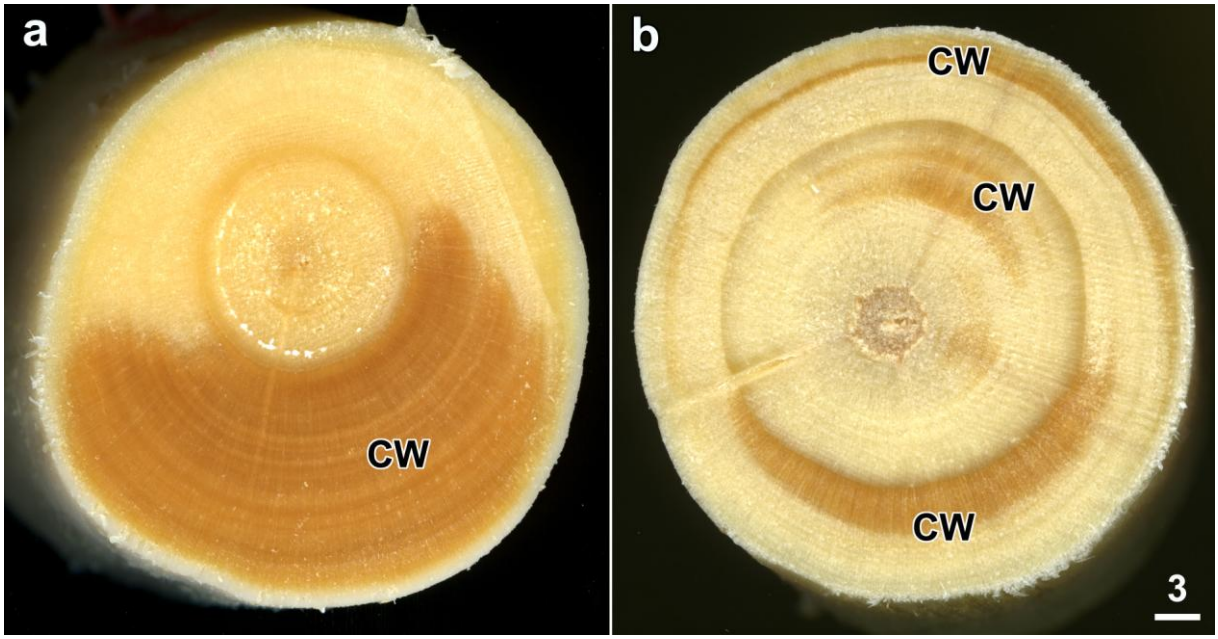

Figure 2.2 Scanned wood cross sections that demonstrate compression wood (CW).

a. Compact compression wood (CW) formed during trial 1 due to continuous leaning in clone 'W'.

b. Diffuse compression wood (CW) formed in clone 'K' due to a longer period of vertical growth during the initial stages of trial 1.

Scale bar in **b** = 3 mm for **a** and **b**.

A third clonal trial (trial 3) that included more clones and replicates was developed with uniform treatments and reduced environmental variability. Plants were grown at Harewood in the outskirts of Christchurch (43.49^0S, 172.54^0E). Growth uniformity was achieved by planting the seedlings in 100 litre planter bags with uniform soil quality and watering conditions to eliminate any influence of soil and moisture on wood quality. Twenty different clones of radiata pine with 35 replicates each were planted in August 2009 and, after 2 months and when the seedlings were established, the young stems were forcibly leant at an angle of approximately 25^0 to produce compression wood. These trees were harvested in July 2011 for wood quality assessment.

2.2.3 Preparation of wood discs for compression wood quantification

Sample trees had their branches and needles removed (Figure 2.3a,b) and were felled at stump height with a hand saw. A longitudinal scoring line was drawn on the lower side of the leaning stem to mark the direction of lean. For the analysis of the first clonal trial, discs

(approximately 25 mm long and stem diameter 20 - 40 mm) were cut from three height levels (bottom, middle and top) (Figure 2.3c) with a tungsten carbide-tipped saw blade to obtain a smooth surface suitable for imaging. Tree and clone number and the lower side of the stem were marked on the top surface of the discs with an indelible marker pencil. These discs were debarked, cleaned and fixed in formaldehyde / acetic acid / alcohol fixative (FAA; 10% (v/v) formaldehyde, 5% (v/v) acetic acid and 50% (v/v) ethanol) (Thomas et al., 2013). Samples from the second and third clonal trials were prepared in the same way except that discs were only collected from the base of the tree where the actual bending had occurred.

2.2.4 Phloroglucinol labelling of lignin

Phloroglucinol (1, 3, 5-trihydroxybenzene) was used to detect the increased lignin present in compression wood in wood cross sectional discs (Chaffey, 2002). A 0.1% (w/v) phloroglucinol solution was prepared by mixing 0.1 g phloroglucinol in 100 ml ethanol (95% (v/v) and 16 ml concentrated hydrochloric acid. Several drops of this test solution were applied to the cross sections which rapidly developed a visibly more intense red stain for lignin where compression wood was present.

2.2.5 Scanning of wood discs with reflected light

Wood discs kept in FAA were washed in water and blotted with a tissue paper to remove excess liquid before scanning. Wet cross section discs belonging to the same clone were placed together on a professional flatbed scanner table (Epson Perfection V700 Photo, Auckland, New Zealand) (Figure 2.3d). Discs were scanned with identical scanning conditions using reflected light (48 bit colour and 1200 dpi) and saved as TIFF images without any compression or scale changes by using a unique file name that denoted clone, tree and height position.

Several methods were used to improve the consistency of scans. First, a rainbow-coloured strip of plastic was placed along with the samples as a colour reference for the scanner. This colour strip helped the scanner software to keep the ‘white balancing’ of the images uniform irrespective of the variation in the colour of the wood samples. Second, the room lights were dropped and the scanner was covered with a dark cloth to reduce background light. And third, because the sides of discs that were cut unevenly were sometimes visible in scans and could confound automatic analyses, discs were surrounded by elastic hair ties (either black or brown) (The Warehouse, Riccarton, New Zealand).

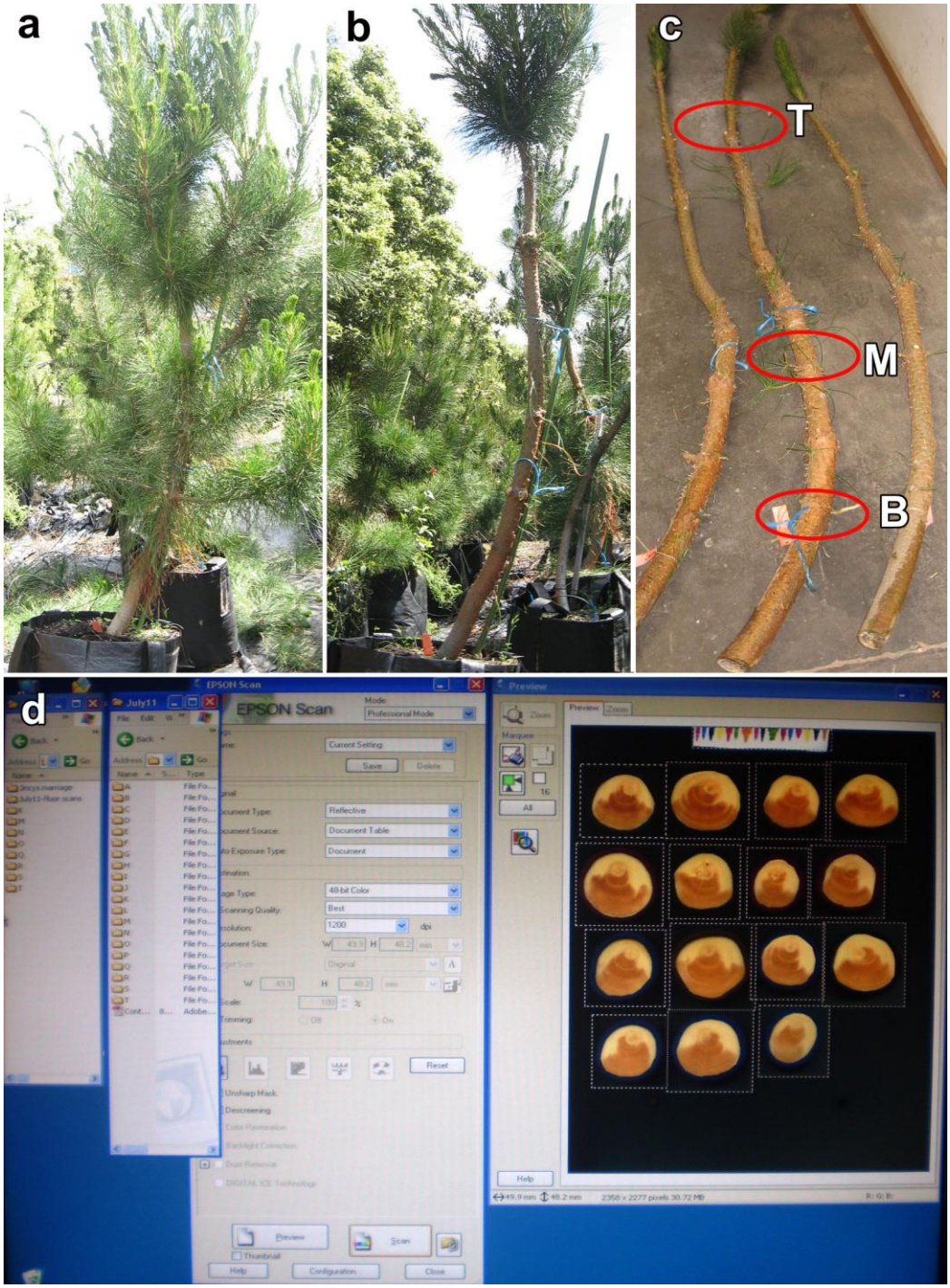

Figure 2.3 Harvesting of radiata pine samples.

a. A sample tree from trial 2 ready for compression wood evaluation.

b. The needles were removed from the stem.

c. Sample discs were cut at three heights at the top (T), middle (M) and bottom (B) of the stem.

d. A screen shot showing the set-up for reflected light scanning.

2.2.6 Automatic quantification of compression wood

Image analysis was used for the detection and quantification of compression wood in digital images of the wood discs. I used the popular, user-friendly yet powerful image processing software, Photoshop CS4 Extended (version 11.0.1, Adobe Systems, San Jose, CA, USA) for this purpose. As manually detecting the compression wood content was not feasible considering the large number of images involved, the aim was to develop an automated protocol suitable for batch processing the entire collection of images in a single run. In Photoshop, this is controlled by the 'Actions' menu. Moreover, manual detection is subjective leading to operator bias and non-uniform treatments whereas an automatic technique is (or should be) reproducible by uniformly processing all samples in a more reliable and non-subjective way. Full details of the developed protocols are described in the Results section.

2.2.7 Manual detection of compression wood

The newly developed automatic compression wood detection method using the batch processing tool in Photoshop was initially verified by the visual colour difference between opposite and compression wood. Manual detection of the compression wood was also competed in Photoshop using the 'lasso' tool to select areas of compression wood.

2.2.8 Fluorescence scanning

The wood discs were also scanned with an epifluorescence scanner (Storm 840, Molecular Dynamics, CA, USA). This system was often used in molecular biology and biochemistry to scan DNA, RNA and protein gels until it was replaced with more modern gel-doc systems that work with transmitted fluorescence. Compression wood generates higher fluorescence when excited with a suitable wavelength, owing to the presence of higher amount of lignin than the normal wood and to the different excitation and emission spectra of compression wood lignin (Donaldson et al., 2010; Thomas et al., 2013). With the Storm scanner, sample cross sections were imaged with blue excitation (450 nm) to collect the fluorescence emission with a 520 nm long pass filter at 254 dpi (100 µm per pixel), the highest available resolution (Figure 2.4).

In a later experiment to evaluate the use of fluorescence to detect compression wood, 60 µm-thick transverse sections of 10 month old radiata pine trees were imaged with a Leica DFC 310 FX digital camera connected to a stereo-fluorescence microscope (model MZ 10F Fluo, Leica Microsystems, Heerbrugg, Switzerland). Sections were excited by blue light (about 450 - 490 nm) and green fluorescence (510 nm and above) was collected to image the compression wood content. These samples were also scanned by a newer epifluorescence scanner (Typhoon FLA 9500, GE Healthcare and Life Sciences, Piscataway, NJ USA) recently

acquired by the University of Otago, School of Medicine at Christchurch Hospital, and used with the assistance of Dr Mark Hampton. Images were collected at 2540 dpi (10 µm per pixel) using excitation at 473 nm and with emission collected with 510 LP filter. Fluorescence with 532 nm excitation with 575 LP emissions (orange and red) was also collected.

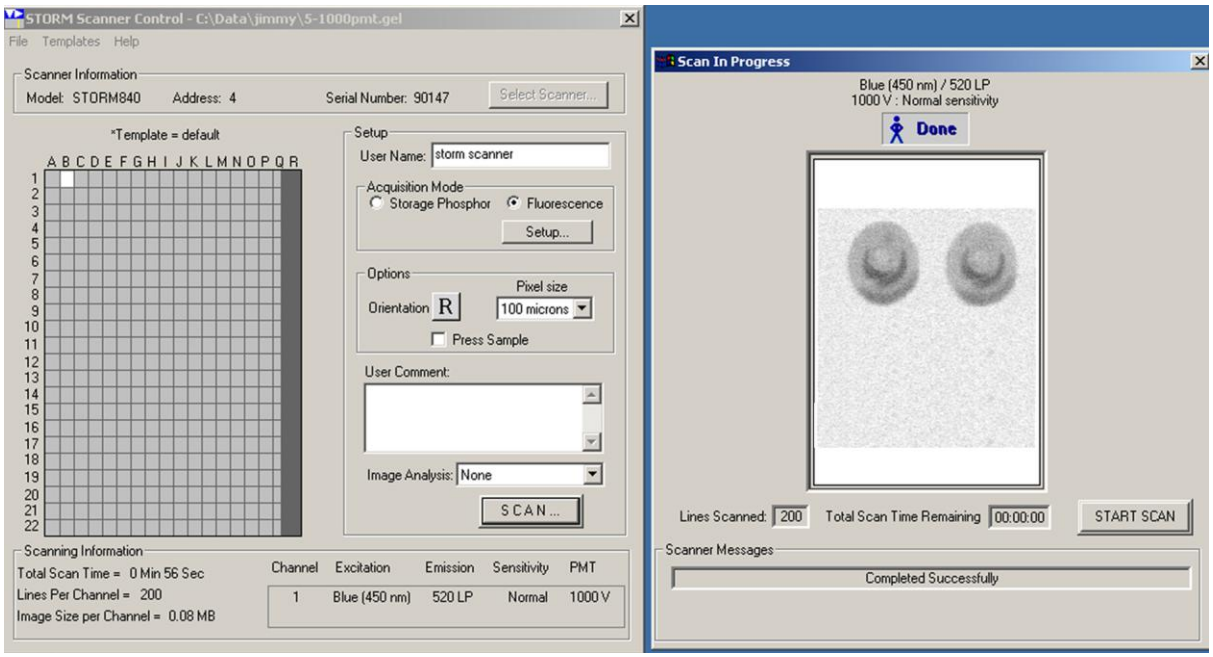

Figure 2.4 The set-up for the Storm fluorescence scanner. This used blue light excitation (450 nm) and collected fluorescence at wavelengths greater than 520 nm. Two wood discs are shown on the preview screen 9at right) that contain bands of compression wood.

2.3. Results

2.3.1 Developing a protocol for detecting and quantifying compression wood

Using samples from clonal trial 1, an automatic detection routine was developed in Photoshop to detect and quantify compression wood on wood cross sections. This technique has many image processing steps (Figure 2.5) including:

1) Measuring the total image area,

2) Detection, separation and area measurement of the background in the image,

3) Detection of the wood cross section and its area measurement, and,

4) Detection and measurement of compression wood area inside the wood cross section.

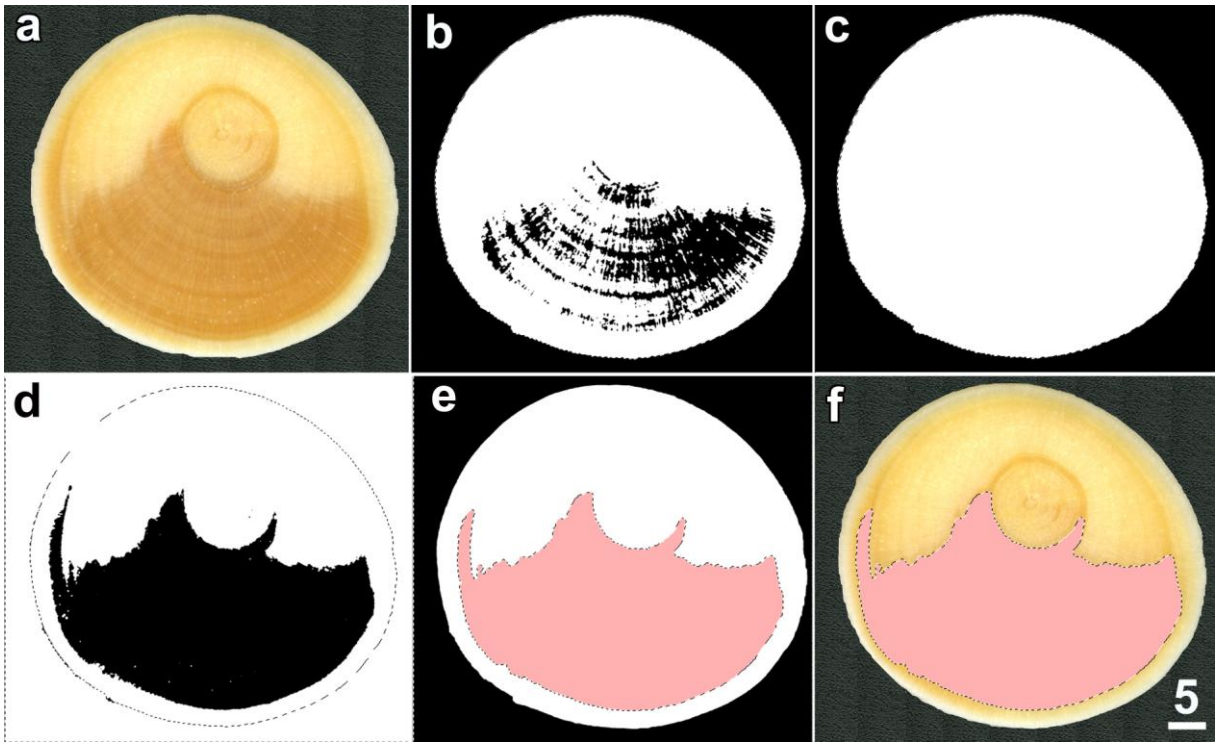

Figure 2.5 Major image processing stages involved in the automated detection of compression wood.

a. The scanned wood cross section image.

b, c. Detection and separation of the wood cross section.

d-f. Detection and separation of compression wood, with this indicated in pink and superimposed in the original scan (**f**).

Scale bar in **f** = 5 mm for all images.

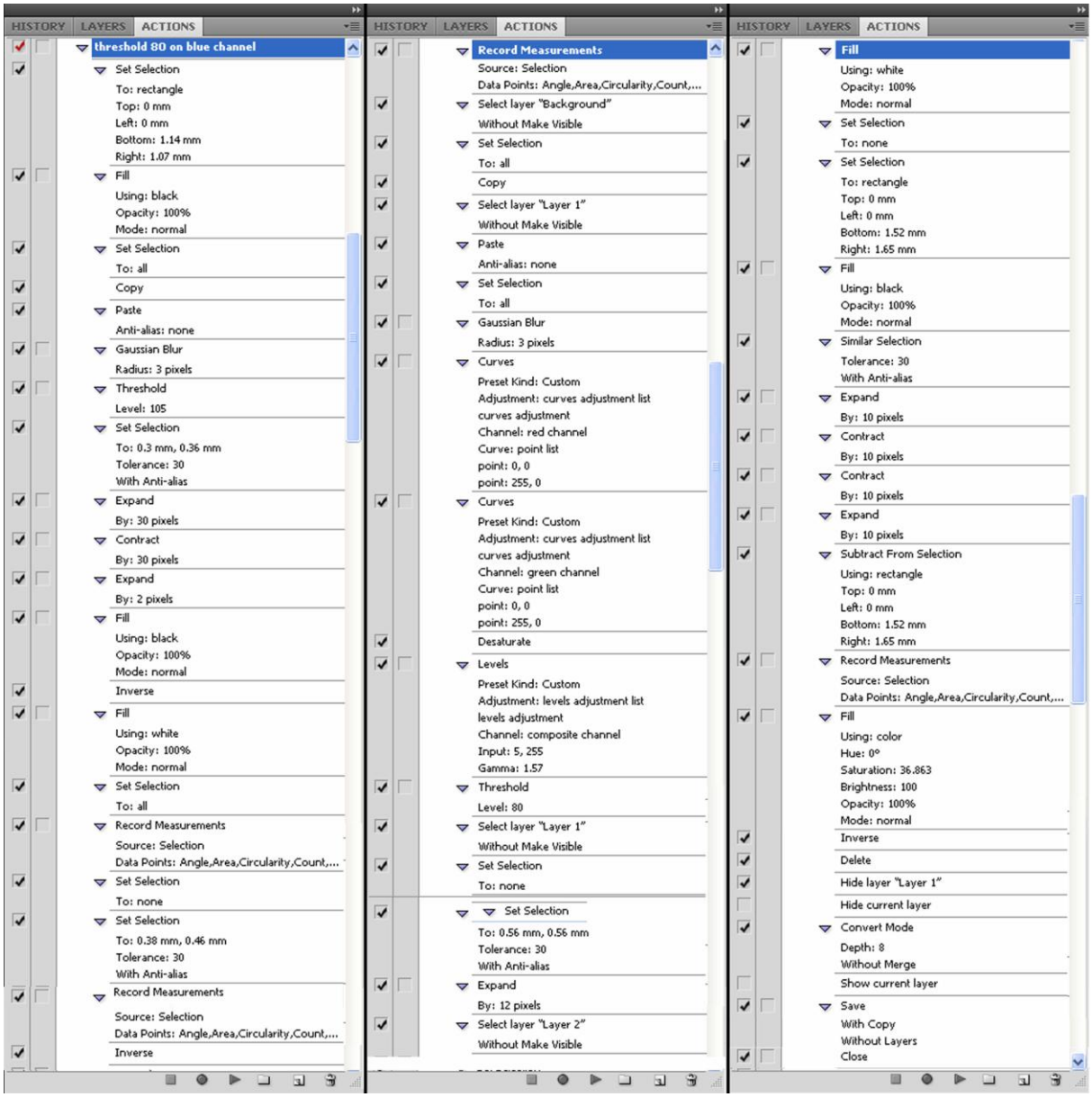

Figure 2.6 The automated procedure for compression wood detection. A combined screen shot of the image processing steps in Photoshop involved in the compression wood detection protocol 6. The procedure began at the top left of the list and ended 55 steps later at the lower right.

To achieve each of these tasks, a series of image processing steps were used that were arranged and recorded together under the 'Actions' menu in Photoshop (Figure 2.6).The first step in the image processing was to select and measure the total image area (Figure 2.5a). Image thresholding was then used to define and separate the wood cross section relative to the background leading to the area measurements of the background and the wood cross section (Figure 2.5b,c). Being darker than normal wood, compression wood was identified using a separate image thresholding (Figure 2.5d). Compression wood regions were smoothed and gaps filled in by serial image expansion (image dilation) and contraction (image erosion), and the areas of compression wood was then measured in pixels (Figure 2.5e). From the above measurements, the quantity of compression wood as a percentage of the wood cross section area was calculated. Batch processing was undertaken in which various image analysis steps saved in 'Actions' were executed on all the images identically and sequentially. This set of image processing steps was named as 'Protocol 1'. Data was then exported to MS Excel for analysis.

2.3.2 Manual verification of the image analysis protocol 1

This automatic compression wood detection method by batch processing using the 'Actions' command in Photoshop was verified manually on all the images in the first clonal trial by using the lasso and fill tools to select and measure areas in Photoshop. Compression wood area measured by the automatic image analysis procedure with Photoshop was in good agreement with the manual detection and quantification using available Photoshop tools with a higher correlation coefficient ($R^2 = 0.88$) (Figure 2.7).

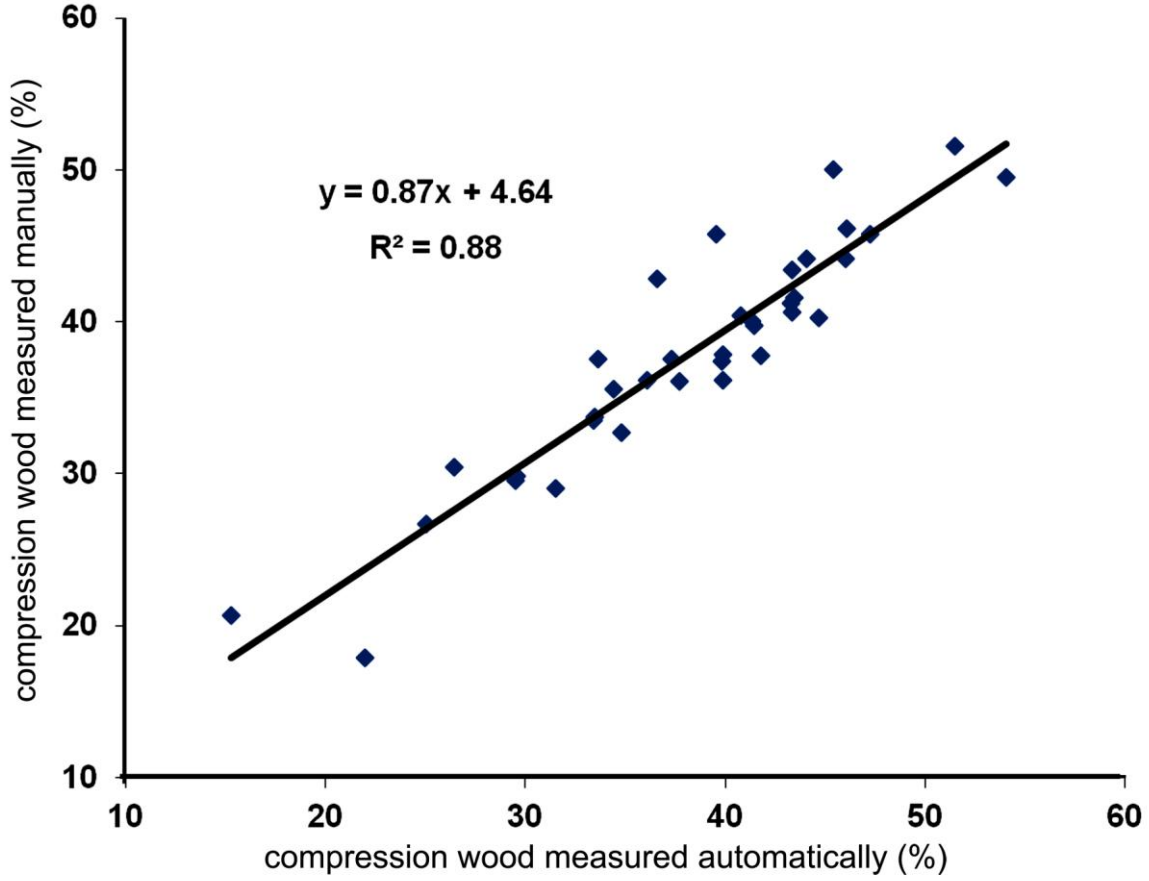

Figure 2.7 Automated detection of compression wood correlated well with manual detection. The batch processing of cross section images with Photoshop using protocol 1 was compared to manual detection using the lasso tool in Photoshop.

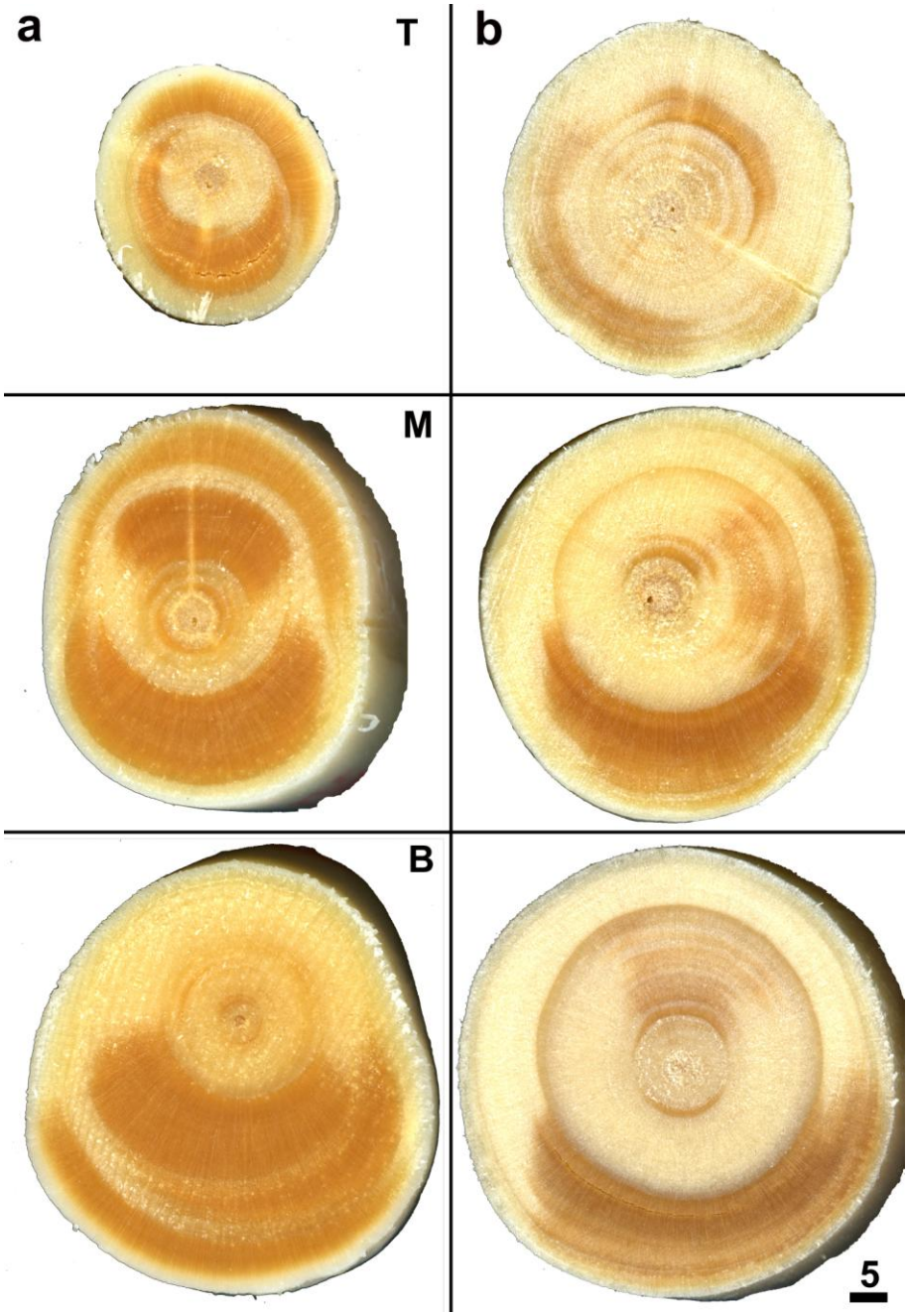

Figure 2.8 Patterns of compression wood formed during the two different leaning treatments in trial 1. Samples are shown from three different heights, the top (T), middle (M) and bottom (B) sampling positions. Scale bar in **b** = 5 mm for all images.

a. Continuously leaned tree (clone F).

b. Trees which were straight initially and leaned later (clone A).

2.3.3 Evaluation of clones (trials 1 & 2) with protocol 1

The propensity to form compression wood varies between clones and, as a result, the nature and quantity of compression wood formed in different clones of radiata pine trees is also different (Burdon, 1975; Timell, 1986). The main aim of this pilot study was to develop tools to quickly evaluate large clonal trials at the age of less than three years based on the compression wood content on the cross sections.

The variations in the pattern of compression wood formed are shown in Figure 2.8. The significantly higher compression wood content in clones 'F' (Figure 2.8a) and 'W' (not shown) was due to the formation of compact compression wood from early in growth because of the continuous leaning whereas the lower compression wood content in clones 'A' (Figure 2.8b) and 'K' (not shown) were initially grown vertically and only then tilted. These lower compression wood values did not mean that the clones were better than the others, forming less compression wood. This was proved in the second trial where clone 'K' had much higher levels of compression wood.

Trends were still evident in the analyses of compression wood in trial 1 (Figure 2.9, Table 2.1). Among the four clones analysed, clone 'W' had the highest and clone 'A' had the lowest compression wood content at the site of bending (the bottom level) (45.3% and 31.9% respectively) whereas clones 'F' and 'K' had intermediate values (39.1% and 33.8%).

Table 2.1 Average compression wood, as a percentage of wood cross sectional area, in the samples of trial 1

clone	A		K		F		W	
n	12		6		9		9	
	auto	man	auto	man	auto	man	auto	man
Top	13.2	16.0	20.7	25.7	20.1	24.2	21.7	22.9
	(2.0)	(2.0)	(3.4)	(3.7)	(2.2)	(2.6)	(5.0)	(3.2)
Middle	23.2	25.4	22.5	26.3	31.9	30.0	36.1	33.4
	(2.2)	(1.6)	(2.4)	(3.0)	(3.9)	(3.6)	(1.4)	(1.4)
Bottom	31.9	32.5	33.8	35.7	42.2	39.1	45.3	45.3
	(1.7)	(2.0)	(3.9)	(3.2)	(1.8)	(1.6)	(1.0)	(1.4)

Values in parentheses are standard error.

Auto = automatic image detection using protocol 1. Man = manual detection.

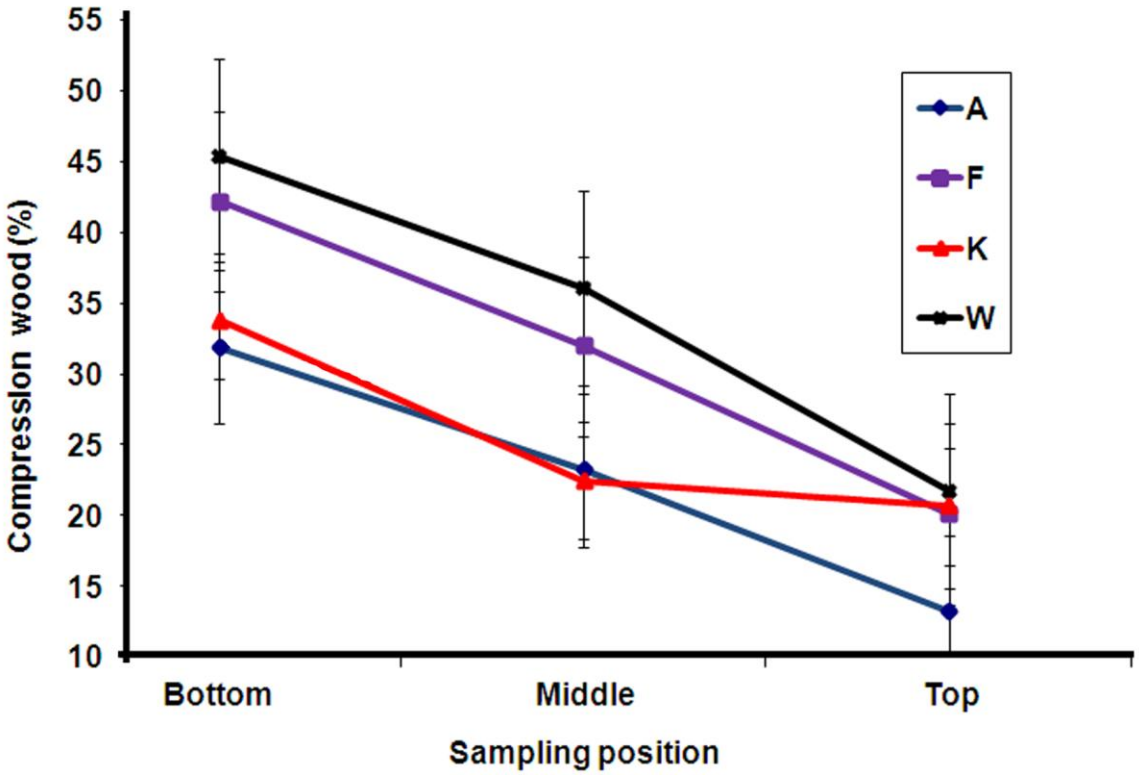

Figure 2.9 Axial and clonal variation of compression wood among four clones in trial 1. Values are means of 6 to 12 samples with standard errors.

In mature trees, the highest quantity of compression wood is formed just around the region of bending, and higher up in the stem, compression wood severity is reduced (Burdon, 1975; Cown and McConchie, 1981b). To test whether this is also true in young stems, the analysis of compression wood in trial 1 included samples from 3 different height levels. As expected, the bottom discs had maximum compression wood and the top discs had the minimum compression wood area (Figure 2.9). As the compression wood content at the bottom level was the highest in all the trees analysed (Table 2.1), only samples from bottom level were collected in subsequent trials.

The automated detection protocol 1 was then run with the five clones analysed in the second trial. The patterns (Figure 2.10) and quantity of compression wood (Table 2.2) formed in these five clones were similar. Among these, clone ‘S’ had the highest and clone ‘K’ had the lowest compression wood content (Table 2.2), with the difference in compression wood content between these clones being significant. The average area of compression wood in these discs of clones ‘S’ and ‘K’ were 59.1% and 52.7% respectively. Moreover, there was good agreement between automatic and manual detection of compression wood (R^2 = 0.79, Figure 2.11).

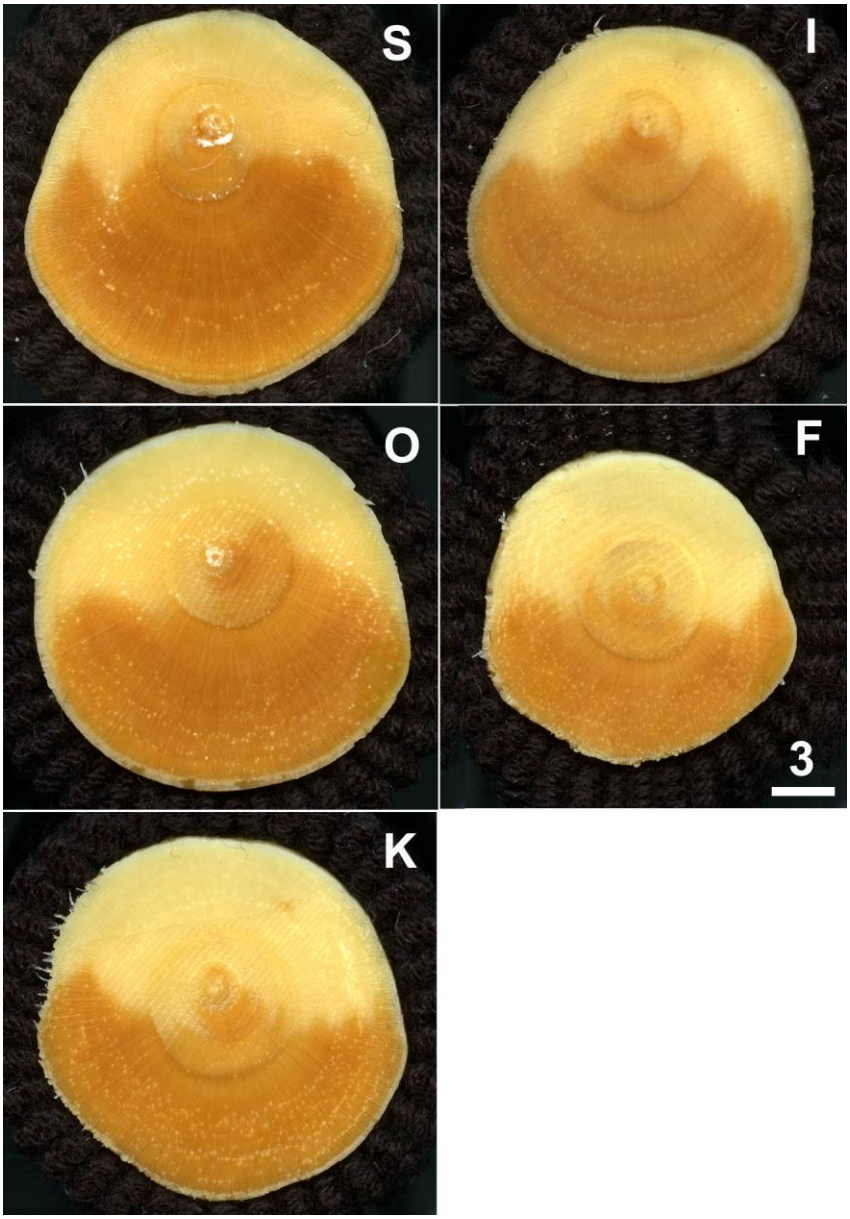

Figure 2.10 Scanned wood cross sections of trial 2 showing compact compression wood formed in 5 clones (S, O, K, I and F) due to continuous leaning.

Scale bar in **F** = 3 mm for all images.

.

Table 2.2 Average areas of compression wood formed in trial 2 clones

clone	F		I		K		O		S	
n	13		14		14		14		11	
	Auto	Man	Auto	Man	Auto	Man	Auto	Man	Auto	Man
mean	55.6	55.5	56.6[#]	56.5	52.7	54.7	56.8[#]	58.4	59.1[#]	61.0
SEM	1.1	0.9	1.2	0.7	1.4	1.0	1.1	0.8	1.2	1.0

[#] Automatic detection values significantly different from clone 'K' (the sample with the lowest compression wood content) at $P < 0.05$ (Student's T-test).

Auto = automatic compression wood detection using protocol 1, Man = manual detection.

The samples in trials1 and 2 were only subsets of large populations being screened for future planting, and the measurement of compression wood content in these samples was only one of the many wood quality traits being considered (Chauhan et al., 2013; Sharma, 2013). Moreover, sampling in these trials was aimed more for the development of methods, rather than for screening the clones, as there were considerable variations in sample treatments (section 2.2.2).

2.3.4 The basic protocol 1 failed with trial 3 samples

The newly-developed image analysis protocol was used to detect and quantify the compression wood content in the third trial of clonal samples. This trial comprised of 700 trees with 35 replicates from 20 different clones. Among these replicates, there was substantial variability in the scanned images in contrast and colour of the compression wood. The initially-developed detection protocol used a global threshold value to distinguish compression wood from rest of the wood. Wood with colour values above this threshold value was scored as normal wood, whereas areas darker than this set value were scored as compression wood. As the colour of compression wood was uniform in the initial set of samples, this protocol worked in trials 1 and 2. It did not, however, cope with the increased colour variability in the larger trial 3. Comparison against manual detection showed that protocol 1 failed badly, with two separate trends within the data set (Figure 2.12). The first was a subset of samples that showed good correlation between automatic and manual detection (red line). A second subset (horizontal black line), however, no correlation between automatic and manual detection

indicating that there was a very poor automatic discrimination of compression wood. This means that protocol 1 worked for a subset of images but failed badly for others. A better compression wood detection method was required to process these images (trial 3).

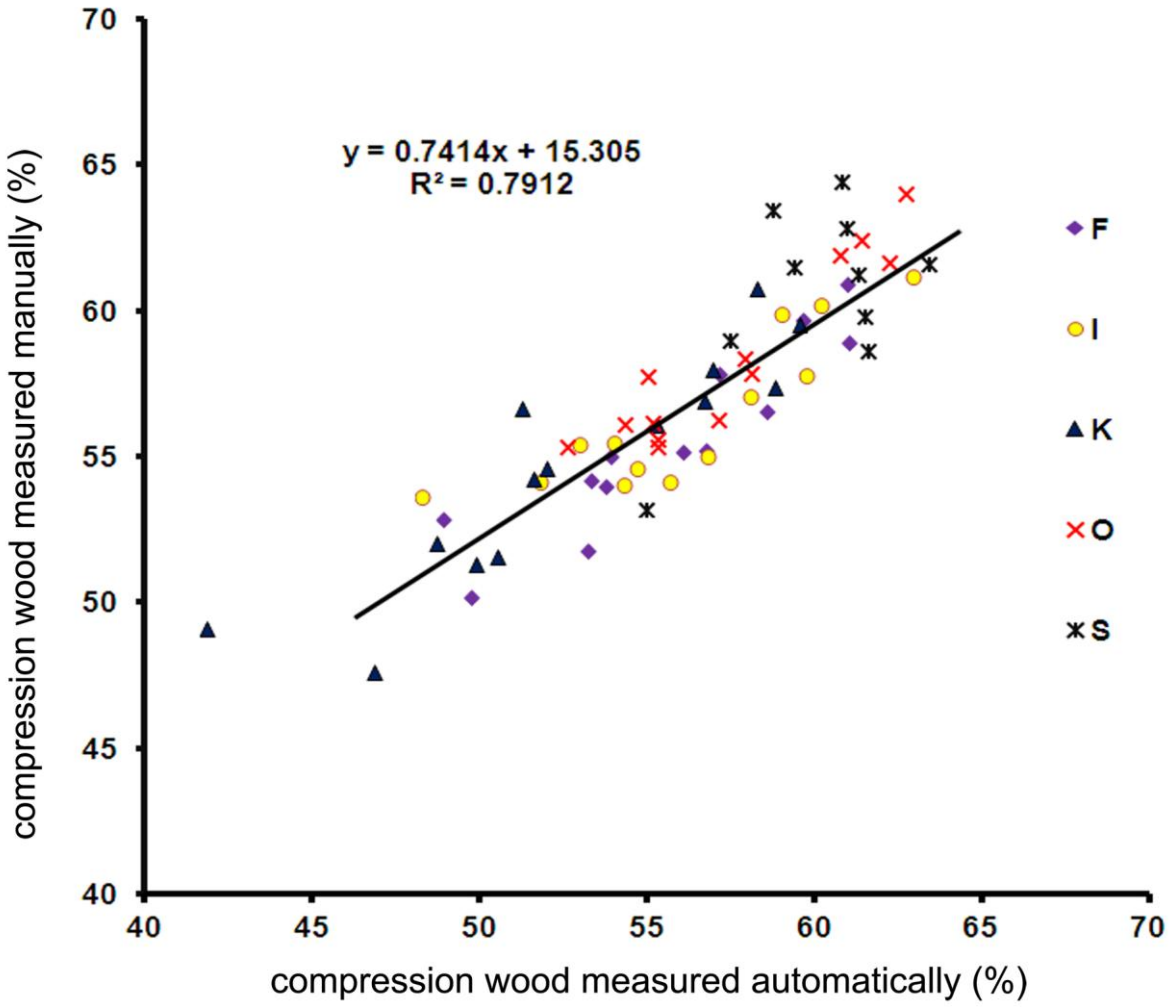

Figure 2.11 Automated detection of compression wood in trial 2 clones correlated well with manual detection. The batch processing of cross section images with Photoshop using protocol 1 was compared to manual detection using the lasso tool in Photoshop for the 5 different clones (F, I, K, O and S).

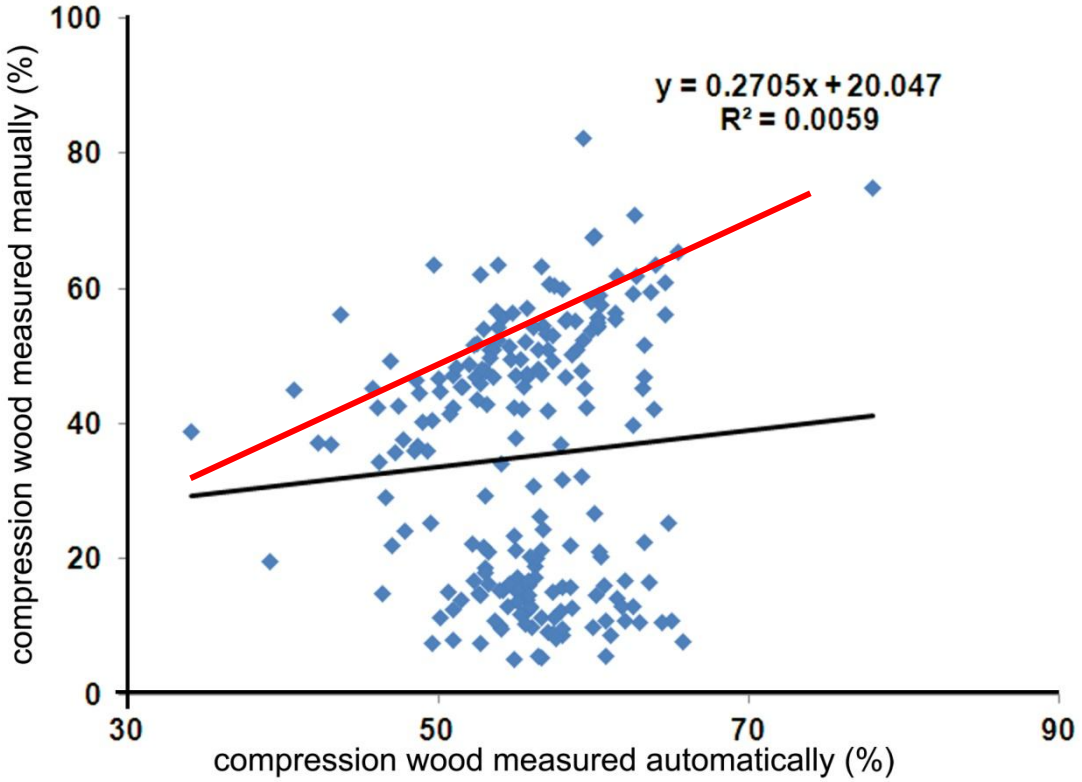

Figure 2.12 The initial compression wood detection protocol failed in trial 3 samples. Protocol 1, which was successful with the first two trials, failed badly with the third set of 20 clones containing 700 samples. When a subset of images were compared, the correlation between automatic and manual detection was very poor with $R^2 = 0.006$. However, two separate trends within the data set could be seen. The first is a horizontal line (black) which showed no correlation between automatic and manual detections while the second is a line (red line) which shows a very high correlation. In other words, protocol 1 worked for a subset of images but failed badly for others.

2.3.5 Developing better protocols

The main problem in trial 3 was that detection of mild compression wood areas was difficult because the threshold value required to discriminate between normal and compression wood varied between samples and clones. It was, therefore, necessary to make suitable changes in the protocol enabling it to detect all areas of compression wood in the stem cross section. Several different approaches were attempted to assess compression wood in samples that had variable colour, and these are described briefly in the following sections. To compare the efficiency of these detection methods, an arbitrary four point scaling system was introduced (Figure 2.13).

Score = 1: An accurate to near accurate detection of both the cross section and the compression wood by the automatic protocol.

Score = 2: Acceptable detection with only minimal errors in either compression wood detection or the detection of cross sectional area.

Score = 3: Poor, unacceptable detection due to wrong cross section or compression wood detection or both.

Score = 4: The poorest and most unacceptable detection of compression wood or cross section or both.

2.3.5.1 Compression wood detection by using different thresholds

Thresholding of the images was the determining factor in detecting and separating both the cross section and compression wood from rest of the image. However, the thresholding approach with existing values failed due to wide variations in both the colour of the wood and the colour of the compression wood among various clones. The failure was in detecting the mild compression wood as the applied threshold value (180) corresponded to severe compression wood. Moreover, it was found that a threshold value which discriminated mild compression wood in some clones (images) corresponded to the incorrect selection of normal wood in others (Figure 2.13).

Using the 4 point measurement scheme, the standard protocol devised for trials 1 and 2 gave an average score of 3.21 for the nearly 700 replicates. This was deemed unacceptable (Table 2.3, protocol 1). For a decreased threshold value of 165, which showed promise in random samples, the overall average score was 2.66 with individual clone average ranging from 2.21 to 3.26 (protocol 2) while for a threshold value 173, the overall average score was 2.54 with individual clone average ranging from 2.11 to 2.97 (protocol 3).

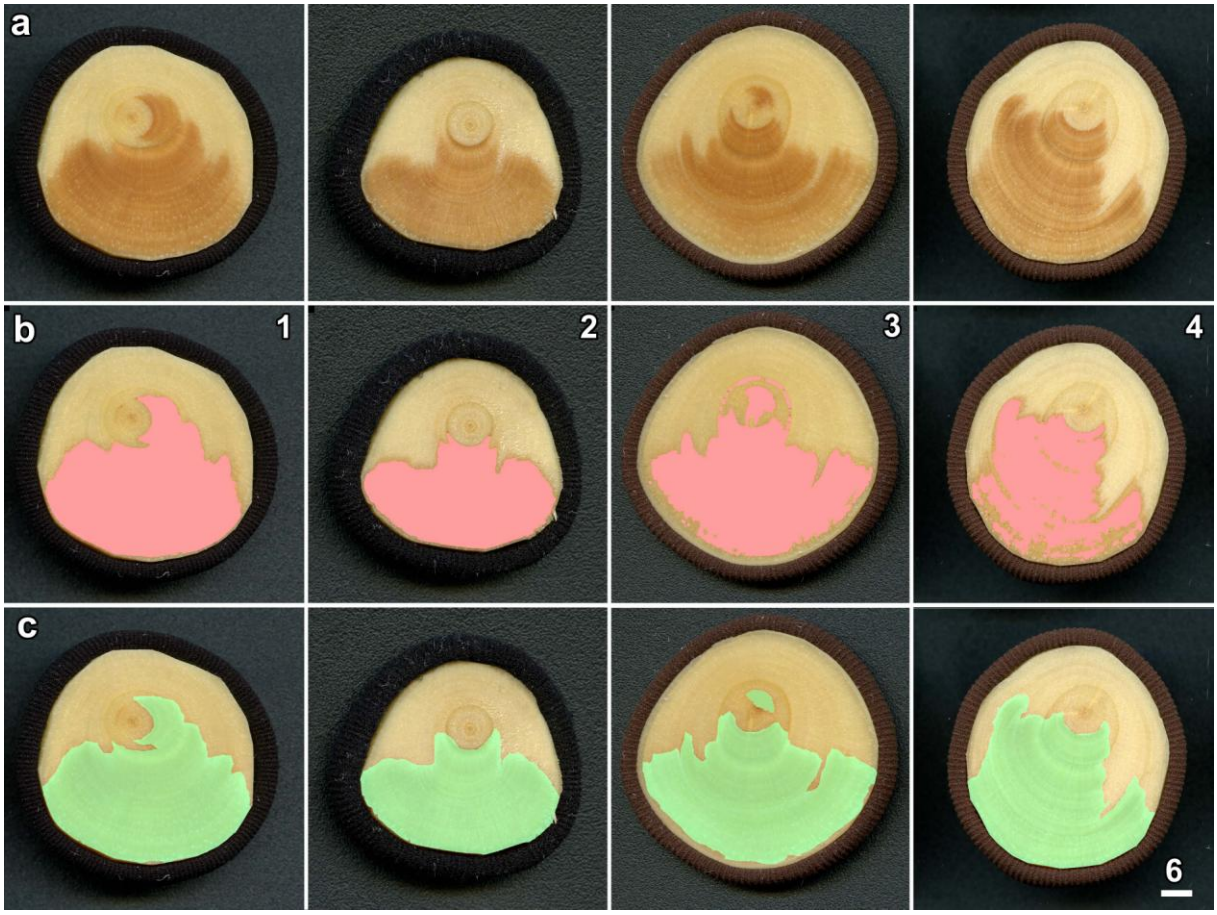

Figure 2.13 The four point scaling method for comparing the automatic and manual compression wood detection.

a. Actual images.

b. Automatic detection of compression wood (pink). A score of 1 = accurate detection 2 = near-accurate; acceptable detection; 3 = poor, unacceptable detection; 4 = very poor, unacceptable detection.

c. Manual detection with compression wood shown in green.

Bar in **c** = 6 mm for all images.

However, the net result of using a global threshold to detect compression wood was always that either normal wood or compression wood was missed in some samples. Thus, the use of a global threshold value to define compression wood appears to be impossible.

2.3.5.2 Compression wood detection by defining compression wood colour

A 24-bit colour image is a combination of three colour channels (red (R), green (G) and blue (B)). For a white image, the RGB values are 255, 255 and 255 while for black, the values are 0, 0 and 0. To define compression wood on the basis of the colour values, severe and mild compression wood areas in randomly selected images were analysed. RGB values for the severe compression wood areas, which were darker in colour, were found to average R = 166, G = 113 and B = 46 while for mild compression wood they were R = 235, G = 189 and B = 100. The Photoshop protocol was then modified to detect the compression wood areas lying in between these upper and lower limits. All the images were then processed and each resulting image scored against the original image. The average score based on compression wood colour detection ranged between 1.91 to 2.83 with an overall average of 2.29 (Table 2.3, protocol 4). With this method, however, the darker coloured pith was also detected as compression wood due to the similarity in colour.

Table 2.3 Comparison of compression wood detection methods during Trial 3

Clone	protocol 1	protocol 2	protocol3	protocol 4	protocol 5	protocol 6
12	-	2.86	2.49	1.91	1.51	1.74
13	-	2.26	2.49	2.09	1.51	1.49
15	3.14	2.71	2.57	2.63	2.29	2.49
17	-	2.57	2.20	2.83	2.03	1.94
18	-	2.59	2.50	2.06	2.00	1.53
19	-	2.77	2.71	1.94	2.03	1.63
20	-	2.80	2.63	2.09	1.97	1.66
23	-	2.21	2.50	1.79	1.32	1.77
24	-	2.76	2.44	2.18	1.85	1.62
25	-	2.94	2.71	2.66	1.89	1.71
28	-	2.54	2.31	2.14	2.11	1.63
30	-	2.49	2.29	2.51	1.77	1.66
31	3.26	2.50	2.44	2.76	2.26	2.03
34	-	2.69	2.91	2.14	1.66	1.91
36	3.36	2.29	2.11	2.34	1.63	1.34
37	-	2.66	2.54	2.29	2.03	1.83
38	3.21	2.76	2.88	2.00	2.06	2.24
41	2.14	2.83	2.71	2.34	1.94	2.43
43	-	2.61	2.36	2.39	1.76	1.79
45	3.17	3.26	2.97	2.77	2.63	2.77
mean	3.21	2.66	2.54	2.29	1.91	1.86
n	6	20	20	20	20	20
SEM	0.04	0.06	0.05	0.07	0.07	0.08

Scores given to the automated detection of compression wood by six different image analysis methods on each image on a scale from 1 to 4, where:

1 = perfect to near perfect detection.

2 = acceptable detection with minimal errors.

3 = unacceptable due to major errors.

4 = not acceptable detection.

Numbers highlighted in green = lowest score in each protocol while numbers highlighted in yellow are the highest score in that protocol. Not all samples were screened with protocol 1.

2.3.5.3 Compression wood detection by defining the normal / opposite wood

The detection of opposite wood was also attempted with an approach based on colour values, similar to the previous attempt of detecting compression wood. This assumed that opposite wood would have uniform colour and appearance. For defining the opposite wood, three different colour ranges were used. They were R = 255, G = 208 and B = 111; R = 253, G = 238 and B = 188; and R = 167, G = 161 and B = 138. After incorporating these values into the protocol, all 694 replicates were reprocessed and scored against the original images (Table 2.3, protocol 5). The average score for clones ranged between 1.32 to 2.63 with an overall average of 1.91. Most samples were, therefore, scored with either a 1 or a 2 and this was a significant improvement over previous approaches. However, there were problems associated with this detection as well. Detection of pith was the major issue due to colour similarity with the compression wood, notably with mild compression wood. Mild compression wood, which was properly defined in some images, was incorrectly identified as either pith or opposite wood in many other images.

2.3.5.4 Compression wood detection by processing the blue channel of an RGB image

While normal wood is pale and slightly yellow in colour, compression wood is distinctly darker and brownish. Comparison of the average colour values for both types of wood showed large variations, most notably in the blue channel. This was demonstrated by viewing the individual colour channels for a scanned image, both in colour and as adjusted black and white images for each colour. Much greater contrast was present within the blue channel images (Figure 2.14). Therefore, the detection protocol was modified to remove the red and green channels from each image, and to detect compression wood based on thresholding the blue channel with a values of 80. This provided better detection across the samples. All the samples were processed with the modified protocol and scored against the original images (Table 2.3, protocol 6). The average score for the clones ranged between 1.34 to 2.77 with an impressive overall average of 1.86. The problem of detection of pith as compression wood was much lower with this protocol. Most samples were, therefore, scored with either a 1 or a 2 and this was a significant improvement over other approaches. Overall, problems associated with this detection protocol were reduced. As this became the preferred method for detecting compression wood, the protocol was manually verified in 6 clones by using the ‘lasso’, ‘fill’ and ‘select and measure areas’ tools in Photoshop. A high positive correlation between the automated and the manual detection methods (R^2 = 0.81) was obtained (Figure 2.15).

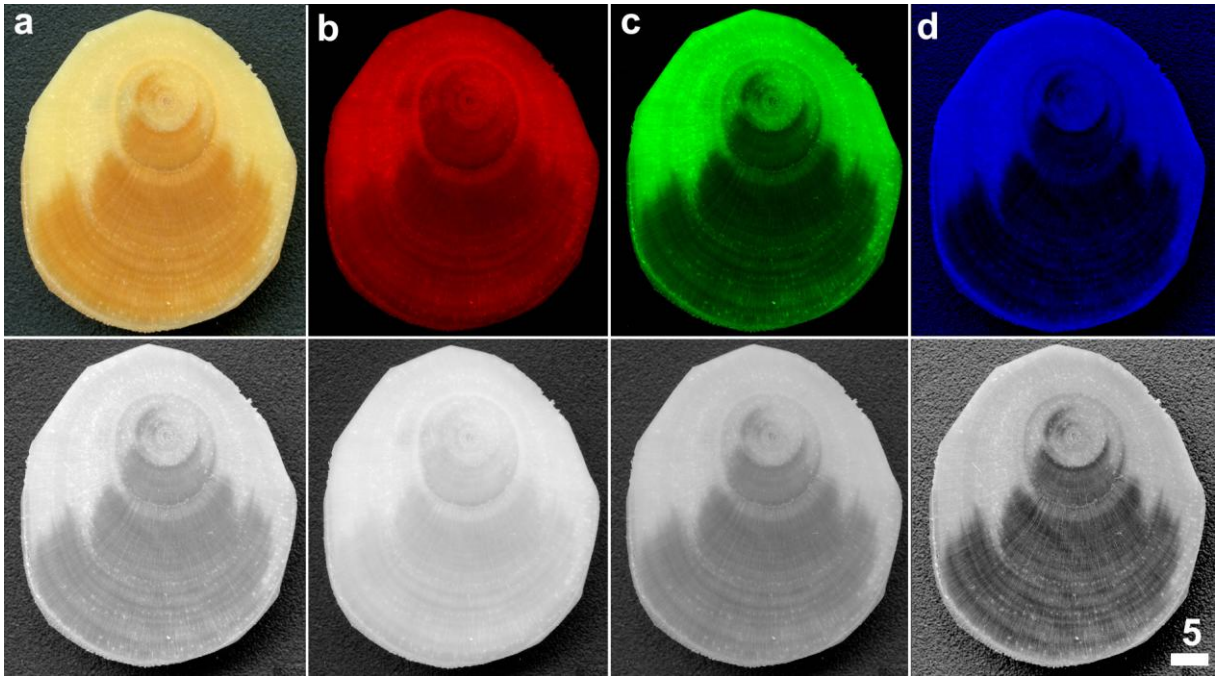

Figure 2.14 The advantage of detecting compression wood using the blue channel of an RGB image. Colour images (top panel) and corresponding de-saturated, contrast-adjusted images (bottom panel) showing compression wood on the lower side of the stem.

a. RGB colour image.
b. The red channel.
c. The green channel.
d. The blue channel.

Scale bar = 5 mm for all images.

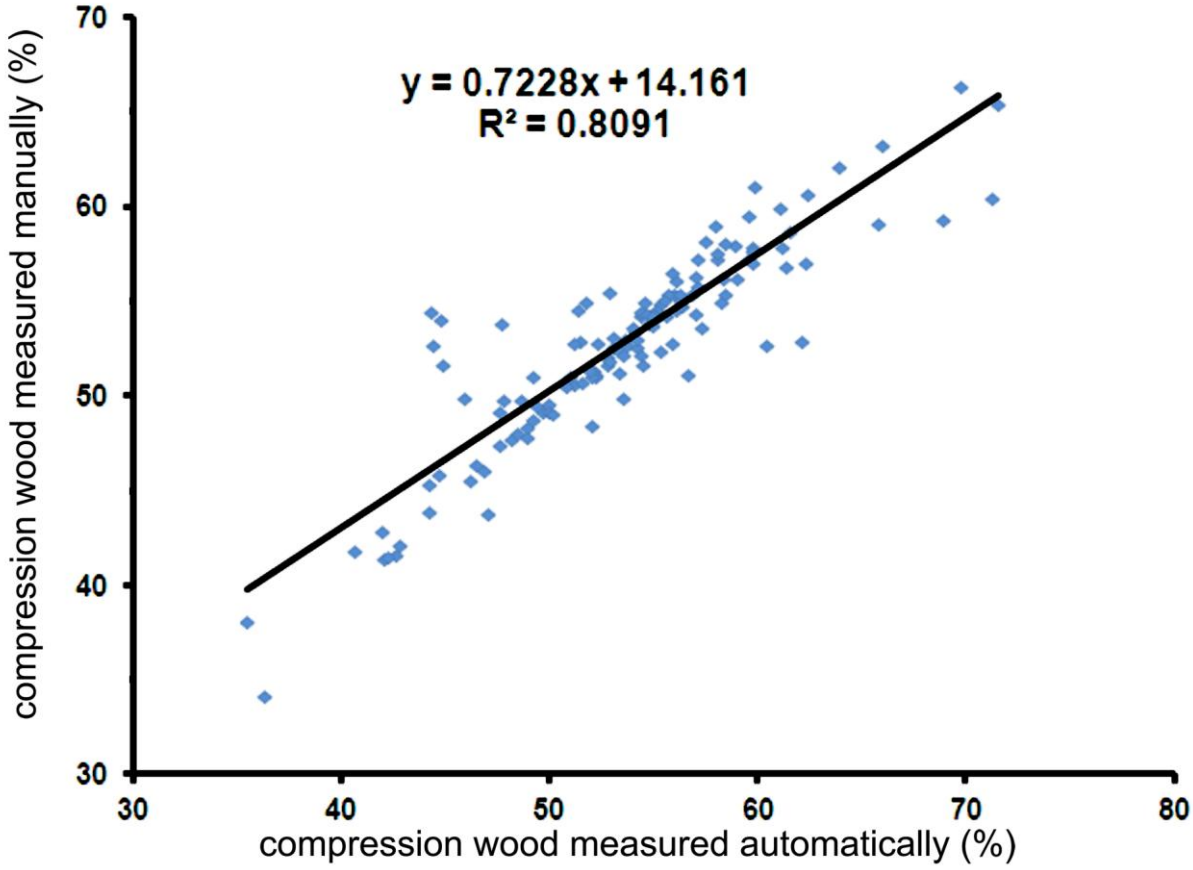

Figure 2.15 Automated compression wood detection protocol using thresholding of the blue channel compared to manual measurement. Measurements showed a high positive correlation between automatic and manual detection of compression wood for a subset of the 20 clones in trial 3.

2.3.6 Compression wood content among 20 clones

Cross section images of all samples (694 trees) belonging to the 20 different clones were analysed using images thresholded in the blue channel using batch processing (Table 2.3, protocol 6).

Table 2.4 Scores given to the automated detection of compression wood by protocol 6 which used thresholding of the blue channel.

clone	n	score = 1	score = 2	score = 3	score = 4
12	35	20	8	3	4
13	35	25	4	5	1
15	35	7	6	20	2
17	35	13	13	7	2
18	34	25	3	3	3
19	35	22	6	5	2
20	35	23	2	9	1
23	35	18	10	4	3
24	34	21	6	6	1
25	35	20	6	8	1
28	35	22	6	5	2
30	35	21	7	5	2
31	34	15	5	12	2
34	35	19	3	10	3
36	35	27	5	2	1
37	35	17	10	5	3
38	34	9	10	13	2
41	35	9	5	18	3
43	33	9	3	18	3
45	35	5	7	14	9
total	694	347	125	172	50
%	100	50	18.01	24.78	7.20

Table 2.5 Compression wood content in 700 trees belonging to 20 different clones from trial 3

Clone	n	Compression wood (%)
12	35	46.9 ± 1.8
13	35	52.8 ± 1.2 #
15	35	49.2 ± 1.6
17	35	50.9 ± 1.1
18	34	54.2 ± 1.5 #
19	35	49.9 ± 1.2
20	35	55.3 ± 1.2 #
23	35	55.4 ± 1.4 #
24	34	53.4 ± 0.9 #
25	35	54.2 ± 1.0 #
28	35	50.5 ± 0.9 #
30	35	48.2 ± 1.4
31	35	49.9 ± 1.5
34	35	52.1 ± 1.3 #
36	35	50.0 ± 0.9
37	35	53.1 ± 0.9 #
38	34	53.5 ± 1.0 #
41	35	49.0 ± 1.2
43	33	49.8 ± 1.0
45	35	47.9 ± 1.8
average		51.3 ± 1.2
SEM		0.57
maximum		55.4 ± 1.8
minimum		46.9 ± 0.9

Significantly different from clone '12' (lowest compression wood content) at $P < 0.05$ (Student's T-test).

Compression wood was determined with the automated Photoshop protocol using the thresholding of the blue channel (protocol 6) approach. Values are averages ± standard errors. Clones with less than average compression wood content are highlighted in green and above average values are highlighted in yellow.

Out of the 20 clones evaluated, 10 of them had more than 20 ‘score 1s’ (Table 2.4) and another four clones had 15 or more ‘score 1s’. The major cause of inaccuracies remained determining the border between the compression wood and normal wood.

Among the 20 clones evaluated, average compression wood content in clones varied between 46.9% to 55.4% with an overall average of 51.31% (Table 2.5). Clone ‘23’ recorded the highest clone average compression wood content (55.4%) which was closely followed by clone ‘20’ (55.3%), while clone ‘12’ had the lowest (46.9%). 11 clones (clone numbers 12, 15, 17, 19, 28, 30, 31, 36, 41, 43 and 45) had their compression wood content less than that of the overall average whereas 9 clones (clone numbers 13, 20, 23, 24, 25, 34, 37 and 38) had higher than average compression wood content. In conclusion, although the final selection of a clone for rejecting or selecting for future planting would be based on many quality parameters, compression wood content was likely to be one of them.

2.3.7 Fluorescence scanning

Detection of compression wood in the discs was also attempted using a Storm 840 fluorescence scanner. This scanner detected lignin fluorescence (Donaldson et al., 2010; Thomas et al., 2013) using excitation at 450 nm (blue light) and collecting fluorescence at wavelengths longer than 520 nm (green light). Scanned sections clearly visualised areas of compression wood (Figure 2.16c) that matched reflected light scans (Figure 2.16a, b) although there were subtle differences. It was found that fluorescence scanning with blue light provided a much better segregation of compression wood, especially what is likely to be mild compression wood (Figure 2.16c). Although this wood was not confirmed at that time as mild compression wood, this seems probable based on the darker than normal wood colour. Being younger, chance of forming annual rings is low and the arcs visible could be mild compression wood.

There were, however, several major limitations with using the Storm scanner to automatically detect compression wood. First, the imaging had comparatively low resolution (the pixel size was 100 µm corresponding to 254 dpi). Second, signal levels were very low and only marginally above background. Third, the Storm scanner was old (circa 1995) and unreliable. And finally, when thresholded, areas of mild compression wood were not well discriminated from normal wood. Hence, these images were not suitable for automated image analysis leading to compression wood detection.

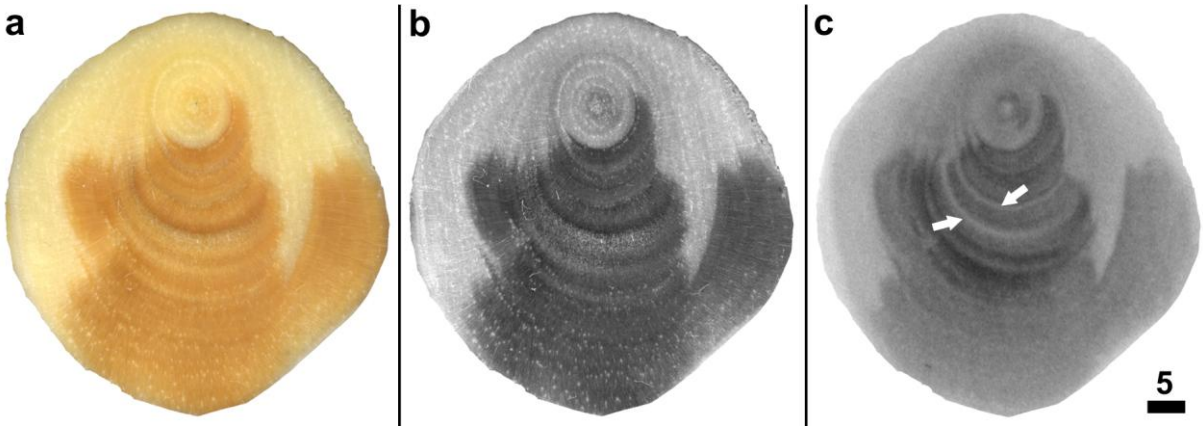

Figure 2.16 Comparing reflected light and fluorescence scans of compression wood samples. Scale bar = 5 mm.

a. A stem cross section imaged with reflected light.

b. Unsaturated version of the blue channel of the image in **a**.

c. The same cross section imaged with 450 nm excitation light collecting fluorescence at wavelengths longer than 520 nm. White arrows indicate bands that might be regions of mild compression wood, distinct from surrounding normal wood and severe compression wood.

Two further experiments, conducted after the completion of the analysis of trials 1, 2 and 3, demonstrated that fluorescence imaging holds considerable promise for the automated detection of compression wood. In stereo-fluorescence microscope images of 60 µm-thick transverse sections of young radiata pine trees collected with blue light excitation (450 nm), compression wood was clearly visible (Figure 2.17d). Similarly, epifluorescence images collected using a Typhoon scanner (a new version of the Strom scanner) with excitation at 472 (Figure 2.17a) and 532 nm (Figure 2.17b) also demonstrated lignin fluorescence. Interestingly, the overlay image (Figure 2.17c) showed that the images were not fully congruent, with the bands of compression wood appearing yellow against a more green background. This demonstrated that fluorescence, or a ratio of the fluorescence signals from different excitation wavelengths, might be used to discriminate between normal and compression wood.

Hence, fluorescence in general and excitation with blue light in particular, is a powerful tool to detect and segregate compression wood from rest of the image.

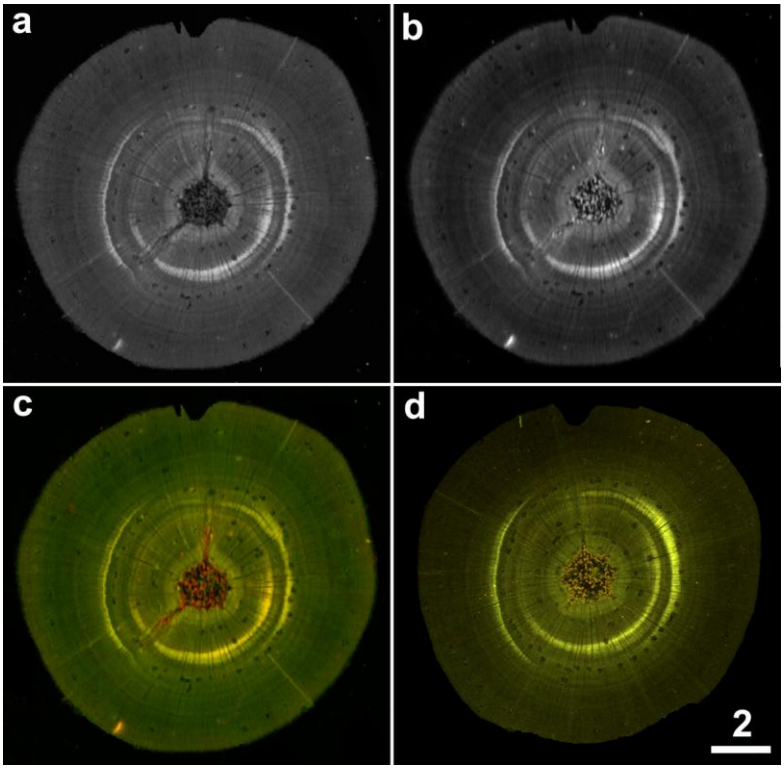

Figure 2.17 Fluorescence imaging of a 60 µm-thick wood transverse section with suitable wavelengths clearly detect the compression wood in it. Scale bar in **c** = 2 mm for all images.

a. Fluorescence on the typhoon scanner with 472 nm excitation and with 510 LP emission (green).

b. Fluorescence with 532 nm excitation and with 575 LP emission (orange and red).

c. An overlay of the two fluorescence images, with panel **a** in green and panel **b** in red. The compression wood fluoresced more strongly in the yellow and red part of the spectrum.

d. A different section from the same tree that was imaged with stereo fluorescence microscope with blue excitation and green fluorescence. The overall pattern was very similar to the scanned image.

2.4 Discussion

2.4.1 Developing a protocol for detecting and quantifying compression wood

A new, automated image analysis protocol using the popular yet powerful software, Photoshop, was developed to analyse large number of wood cross section images belonging to various clones. This new protocol was intended to automatically detect and quantify the compression wood content as a percentage of the stem cross section area. Detection of compression wood area can also be done manually by using similar tools in Photoshop. However, manual detection is always subjective leading to operator bias and inconsistent detection due to unequal treatment (Selig et al., 2012).

Demand for timber for a variety of purposes is ever increasing and there is a growing interest in early evaluation of clonal planting materials (Apiolaza et al., 2011). In large-scale clonal evaluation trials, the availability of quick and reliable tools is of utmost importance to save time and money (Chauhan et al., 2013). To evaluate the different clones on the basis of compression wood content, a batch processing technique was needed which could process all the images in a group uniformly, using the same criteria. Batch processing has the advantage of applying the same protocol to all images without any subjective operator interference. In the initial set of trial 1 and trial 2 clones, the thresholding approach on the RGB images (protocol 1) successfully separated both the wood cross section and the compression wood parts from the rest of the image with a reasonable accuracy (R^2 = 0.88) in comparison with the manual technique (Figure 2.7).

While thresholding the image was successful in detecting the compression wood in the initial set of clones, the larger number of clones and replicates in trial 3 came with a large variation in wood colour. Due to this colour variation, the different threshold values tried all failed to detect compression wood in all samples (protocols 2 and 3). In these failed analyses, in a comparison with auto and manual methods, two separate trends within the data set could be seen (Figure 2.12). The first is a horizontal line (black) which showed no correlation between automatic and manual detections while the second is a line (red line) which shows a very high correlation. In other words, protocol 1 worked for a subset of images but failed badly for others. After extensive trials that compared varying the threshold, analysis of colour and detection of opposite wood, a method based on the thresholding of the blue channel of RBG images evolved.

An important point that needs to be mentioned here is that these protocols were aimed for batch processing of cross section images to detect, segregate and quantify compression wood in them. Different global threshold values were used for different aspects of this purpose. The first thresholding resulted in detection and separation of the wood cross section from the rest of the image. In later stages of the different protocols, a second global threshold value was used to detect the compression wood inside the wood cross section. As discussed above, compression wood detection in some images was inaccurate because of differences in wood colour between clones. Depending on wood colour, each image would have an optimal threshold value for detecting compression wood which might be different from the global threshold value used. This means that if the protocol resulted in poor compression wood detection in any image, improvements might be made by optimising the threshold manually. Such operator assistance has been used in methods described by authors such as Wernsdörfer et al. (2004) as 'automated detection techniques' that are not in fact fully automated. Such operator assistance would, however, be useful wherever perfect compression wood detection is required. Nevertheless, in such cases, the uniformity of selection of compression wood and the rapid processing capacity would then be lost. Even without manual assistance, this protocol 6 provided excellent results as automated detection correlated well with manual detection in a subset of images ($R^2 = 0.81$).

In this study, detecting compression wood by defining the colour of either the compression wood or the normal / opposite wood was found to be troublesome because in most cases, the pith and neighbouring areas were also detected. This process also incorrectly identified the boundary between the normal and mild compression wood in many images. This was a major issue previously identified by Nyström (1999, 2002). Considerable improvements in detection were, however, possible when image thresholding was based solely on the blue channel of the colour scan. This protocol was found to be the most reliable and robust method to detect and quantify the compression wood content on stems cross section images. The average score for clones ranged between 1.34 to 2.77 with an overall average of 1.86. Out of the 694 images processed, 347 (50%) and 125 (18%) were scored as 1 and 2 respectively to give a combined acceptable detection efficiency of 68%.

Being a natural product, no two sections of wood will have completely identical colour because of the involvement of many different cell wall components. For example, the colour values of the normal wood from different clones were found to vary and although the red channel values varied over a small range (~220 to 255), the corresponding blue channel values were lower and more varied (~80 to 155). In compression wood, the red channel was again more stable (~175 to 200) while the blue channel varied more extensively (~40 to 80). This suggested that

the blue channel is somehow more linked to the wood colour, especially to the colour of compression wood. The quantity and nature of lignin present in compression wood is different from that contained in the normal and opposite wood (Nanayakkara et al., 2005; Timell, 1986; Yeh et al., 2006) and it is well documented that lignin content, which is higher in compression wood, absorbs blue light (Donaldson and Bond, 2005; Donaldson et al., 2010; Duncker and Spiecker, 2009; Thomas et al., 2013) (Figure 2.14).

The wood samples were fixed in FAA immediately after cutting and the reflected light scans were completed after the samples were washes and while the wood was wet.. This rapid screening turned out to be important, because the wetness of the cross cut surface ensured that the true colour of wood was detected, and this facilitated the accuracy of compression wood detection with the methods based on the blue channel. Nyström and Kline (2000) also observed this effect and mentioned that colour scanning with a RGB camera worked well for detecting compression wood in the fresh state but that it was less accurate upon drying.

2.4.2 Limitations of the automated methods and future developments

Optimal detection of stem cross section and compression wood by image analysis depends on many factors. These include factors relating to sample preparation, including smoothness of the wood cross section, straightness of cutting, and the presence of foreign materials (dust, lint, and resin). Wood properties, such as colour variations between normal, opposite and various forms of compression wood (mild and severe), are also equally important. Ensuring identical imaging conditions is of utmost important as it can create inaccurate detection and segregation of compression wood. In this new technique all the sample discs were scanned at identical conditions to keep consistency.

Thresholding the image is a popular but simple image processing technique to delineate the objects of interest in an image. In this new Photoshop-based protocol, several different thresholding steps were used. A low threshold value to detect and separate the wood transverse section from the rest of the image was initially applied. At a later stage, another image thresholding was run to detect and segregate the compression wood from the rest of the wood. These threshold values, especially the initial one which detects and separates the wood cross section, play the most critical role in the overall detection protocol as they pave the way to the subsequent compression wood detection and accurate area measurements. In trial 3, in which the variability in wood colour was much higher, both the thresholding steps in protocol 1 were ineffective. This failure is not particularly surprising as detecting compression wood based on wood colour has previously been tried and has not been completely successful. For example, Andersson and Walter (1995) were successful only in estimating the

mild and total compression wood content while the automatic method proposed by Moell and Fujita (2004) was only good for detecting the severe compression wood. As observed by Wernsdörfer et al. (2004), these findings point to certain weaknesses in detection accuracy by three band colour value analysis in which an operator has to define the reference regions in every image. Thresholding the blue channel of the RGB image has shown an acceptable success rate and has the potential of segregating compression wood from rest of the image with a better contrast. In comparison to previous similar image based compression wood detection methods, this new technique has comparable accuracy (81%). However, the detection accuracy can be enhanced considerably by selecting a suitable threshold value manually.

2.4.3 Can compression wood be detected by fluorescence?

The results obtained by imaging of the stem cross sections with 450 nm excitation light suggest that fluorescence imaging can detect compression wood distribution in wood transverse sections, notably mild compression wood. Interestingly, the severity of compression wood is more profoundly visible in these images than the three channel (RGB) images or the blue channel image (Figure 2.16). Moreover, even the mild form of compression wood is clearly delineated in these images in a clearer manner than in the RGB images (Figure 2.16c). However, due to the poor image quality generated by the existing fluorescent scanner when the samples in trial 1 to 3 were prepared, no quantification of compression wood in these images could be made. Subsequent images collected using the Typhoon scanner with 473 (Figure 2.18a) and 532 nm (Figure 2.18b) excitation confirmed the usefulness of these excitation wavelengths in detecting compression wood in wood transverse section images. This is also consistent with what is known about compression wood lignin. The use of violet to blue excitation (405 nm to 488 nm) generates maximum autofluorescence emission from the lignin-rich compression wood (Donaldson, 2001; Donaldson et al., 2010; Duncker and Spiecker, 2009) and has also be confirmed in section 3.3.2 of this thesis.

2.4.4 Evaluation of clones based on compression wood content

In the samples belonging to the first trial, the consistently lower quantity of compression wood in clones ‘A’ and ‘K’ was due to the differences in the leaning treatment rather than having a biological cause. Some systematic differences were, however, observed between the clones. At each height, clone ‘F’ had less compression wood than clone ‘W’, despite being treated in the same way. In trial 2, however, clone ‘F’ was intermediate between clone ‘S,’ which had maximum compression wood, and clone ‘W’ which had the lowest compression wood content. However, the quantification of compression wood in trials 1 and 2 was aimed at method

development, rather than screening, and provided stepping stones for developing suitable protocols for evaluating the larger trial 3.

The overall aim of this multi-party project was to rank genotypes on the basis of their mechanical properties of their normal wood. One of the major objectives of these ongoing experiments was to develop suitable, easy, quick, reliable and robust tools to evaluate clonal planting materials at an early stage of growth (Chauhan et al., 2013). Compression wood content in the transverse section was one of the major quality traits for selecting or rejecting a clone from future experiments and plantations. Accurate detection and quantification of compression wood was therefore considered important to achieve this goal. As detailed in the preceding sections, after extensive attempts, 'thresholding in the blue channel method' (protocol 6) was used to measure compression wood.

In this more extensive trial 3, more clones and more trees were evaluated for compression wood content. Average compression wood in these 20 clones varied from 46.9% to 55.4% with an overall average of 51.3% (Table 2.5). Among the clones evaluated, clone 12 had the lowest average compression wood which was 46.9% while clone 23 had the highest (55.4%). Compression wood in 11 of the 20 clones was significantly higher than that present in clone '12'. The remaining 9 clones with low compression wood content might also be considered for the next level of screening. Other wood quality traits would also be then considered before making any such decision. The clones with higher compression wood might also be re-evaluated with due consideration to such quality traits. The major advantage of this type of early screening is the early availability of a suitable decision on the future of these trees which in other way can save money for the breeding companies.

2.5 Conclusions

1) Automated, accurate detection and quantification of compression wood in young wood cross section images is possible with batch processing using Photoshop.

2) Young stems could be evaluated for compression wood content and clones of potential winners and definite losers could be quickly selected for the future planting.

3) Batch processing of the blue channel of transverse section images provided a reliable, robust and quick way of detecting compression wood with an acceptable level of accuracy. Lack of operator assistance avoids any subjective defining of compression wood

4) Fluorescence imaging might also prove to be an important way of detecting compression wood in samples, as it clearly delineates the normal and compression wood.

Chapter 3

Visualising cell wall organisation in radiata pine tracheids with pontamine fast scarlet 4B

Some of the material in this chapter has been published. See Thomas et al. (2013).

In this chapter, Figures 3.10, 3.15, 3.16, 3.17 and 3.18 are reprinted from Thomas et al. (2013) and some of the text of this chapter has been modified from the same paper.

3.1 Introduction

This chapter discusses the cell wall properties of normal and compression wood tracheids in radiata pine, as documented by the confocal laser scanning microscope with a new cellulose-specific fluorescent dye, pontamine fast scarlet 4B (P4B). Understanding cell wall organisation is critical for investigations of both compression wood and spiral grain, and fluorescence microscopy using suitable cell wall stains is a popular technique to study the wall structure. More importantly, P4B shows promise as a dye that labels to the microfibrils in the S1 and S3 regions of the secondary wall. As the incidence of spiral grain is closely associated with the orientation and arrangement of cellulose microfibrils in different regions of the tracheid secondary wall, such investigations were thought to be critical for understanding spiral grain development.

Unless specifically stated to the contrary, wherever tracheids or cell walls are referred to in this chapter, the source of the material is radiata pine.

3.1.1 The tracheid cell wall and its biochemistry

Tracheids, the major cell elements in gymnosperms, have a complex wall organisation, with variations in chemical composition, microfibril orientation and developmental processes associated with the different layers of the wall (reviewed in sections 1.1 to 1.4). Tracheid cell walls are composed of three main polysaccharides (cellulose, hemicellulose and pectins), a polyphenolic polymer (lignin) and proteins. Cellulose is an insoluble, hydrophilic and crystalline polymer of β-(1-4)-linked glucose that forms cellulose microfibrils. These are the most basic building unit of the cell walls, throughout the entire plant kingdom. Cellulose is the most abundant biopolymer comprising about 40 to 50% of the total plant biomass. Cellulose microfibrils are 2 - 5 nm in diameter, can extend several micrometers in length, and exhibit high tensile strength. This allows cell walls to withstand turgor pressures up to 1 MPa. Hemicelluloses are non-cellulosic cell wall polysaccharides present in a variety of structural types and are the third most abundant biopolymer. They are β-(1-4)-linked carbohydrate polymers with extensive side-chains of various sugars which include xylans, mannans, glucomannans and xyloglucans (Atalla, 2005; Scheller and Ulvskov, 2010; Walker and Butterfield, 1993). Within the wall, hemicellulose is less well ordered than the cellulose microfibrils and forms a cross-linked network enmeshing the cellulose. Pectins are water soluble, complex polysaccharides present mainly in the middle lamella and primary walls and are rich in galacturonic acid. Pectins make up the middle lamella, which holds cells together. Pectins are major components of the primary cell walls of gymnosperms, although they are probably not the only component controlling primary wall expansion during growth.

The major non-polysaccharide component of the secondary cell wall is lignin. Lignin is a complex, hydrophobic, phenolic, 3-dimensional polymer that provides the mechanical strength to cell walls and tree stems, and water proofing the inner layer of the conducting xylem. Lignin provides compressive strength to the cell walls, whereas cellulose provides tensile strength. Lignin is the second most abundant polymer in nature forming about one third of terrestrial woody biomass (Donaldson, 2001). Lignin is also structurally diverse. It forms through the production of mono-lignols in the cytoplasm of secondary wall-forming cells, and the movement of these molecules into the cell wall where they are enzymatically oxidised to phenolic radicals which polymerise (Donaldson, 2001; Li and Chapple, 2010). Lignin surrounds all the cellulose microfibrils to provide rigidity and binds to and cross-links hemicelluloses to reinforce the cell wall. Thus, the cellulose microfibrils of the cell wall are embedded in a matrix of hemicellulose, lignin and cell wall proteins. As described by Booker and Sell (1998), cellulose microfibrils in the cell wall act like steel rods in reinforced concrete, while hemicellulose acts like the cement and cross-links with lignin which plays the role of rock and the sand filler.

Lignification varies between the different layers of the tracheid wall, and between tracheids of different wood types. In normal wood, lignin is most prominent in the compound middle lamella region (lignin concentration is about 50%) whereas lignin concentration in the S2 layer is only about 20% (Donaldson, 2001; Walker and Butterfield, 1993). However, due to the high volume of the secondary wall, the total amount of lignin there is much higher than in the lignin-rich but relatively thin middle lamella. The S3 layer is also lignified to about 53% (Donaldson, 1987).

3.1.2 Functions of different wall layers

The secondary cell wall of the tracheid is composed of 3 different layers (see section 1.3 and Figure 1.1). Each cell wall layer, irrespective of its thickness, has defined roles in plant cell wall architecture. The S1 layer strengthens the cell wall by limiting any radial expansion of the S2 layer and helps prevent the tracheids from collapsing while under longitudinal compression (Booker and Sell, 1998; Donaldson, 2008). Inside this, the S2 layer comprises most of the thickness of the secondary wall and has low angle microfibrils running along the cell's axis. The S2 microfibril angle determines the compressive strength, longitudinal stiffness and the longitudinal shrinkage of wood, with the increased microfibril angles found in juvenile wood contributing to lower stiffness and poorer timber quality (reviewed in Donaldson, 2008). The S3 layer is characterised by high lignin content which enables it to resist swelling and collapse of the wall due to water potential and prevents crack propagation. It is also believed that the

S3 layer plays important roles in permeability, wood preservative absorption and in decay resistance.

The structure and properties of the S2 layer, including the variation and organisation of microfibrils, have received much attention from researchers. This is partially due to the thickness of the S2 layer compared to the relatively thin S1 and S3 layers and to the major role of S2 layer in controlling the critical wood properties such as stiffness and shrinkage. However, there exists a dearth of knowledge on the S1 and S3 layer properties. This is due to the difficulty in measuring these comparatively thin layers (Brändström, 2001; Donaldson, 2008). However there are certain differences in these wall organisations among wood types. The anatomical, physical and chemical characteristics of tracheids in compression wood are significantly different from the normal wood tracheids (see section 1.7.1). Physically, compression wood tracheids are thick walled, semi- to completely circular in cross section and have small, intercellular spaces in the corners between cells.

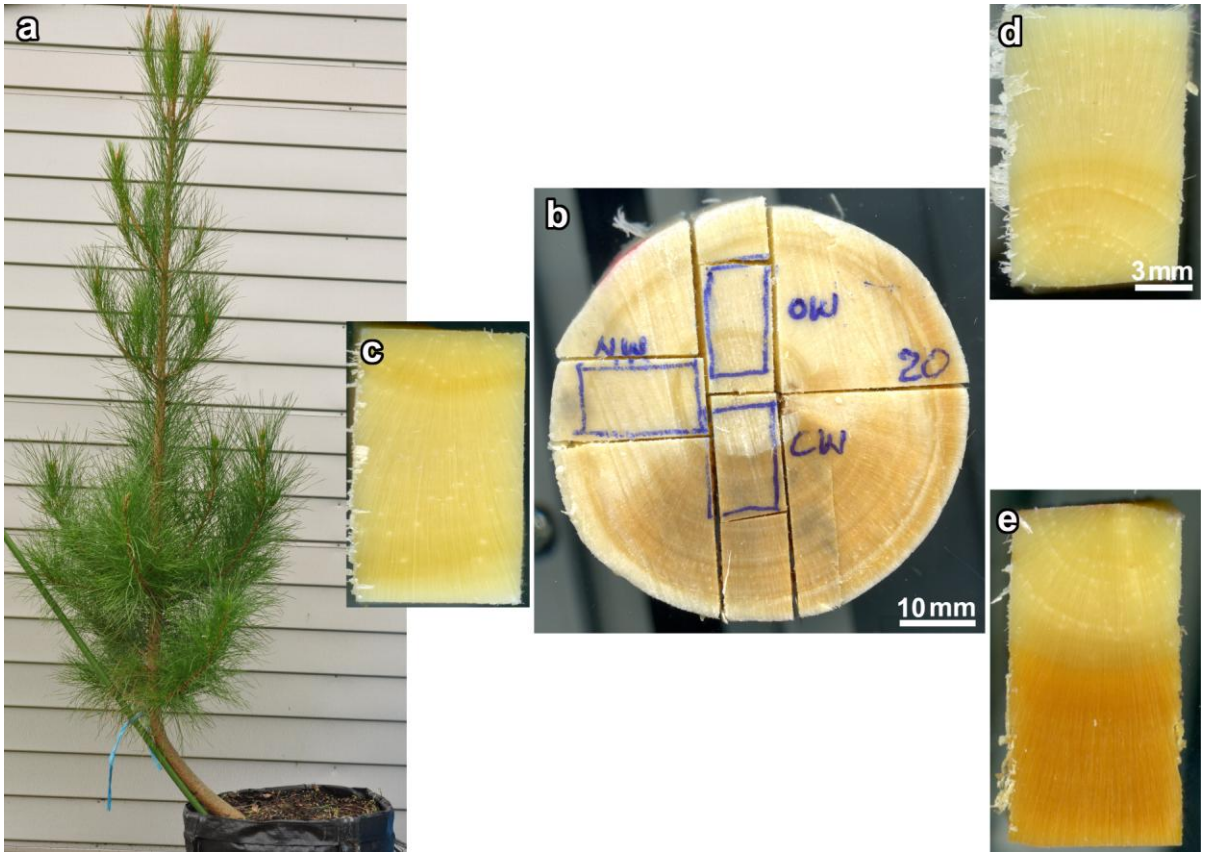

Figure 3.1 Isolation of different wood sections from two year-old pine trees.

a. The tree was forcibly bent to induce compression wood on the lower side of the lean.

b. Cross sectional disk marked with the locations of normal wood (NW), compression (CW) and opposite wood (OW) in preparation for microtome sectioning.

c. Normal wood.

d. Opposite wood found on the upper side of the stem.

e. Compression wood formed on the lower side of the stem.

Bar in **d** = 3 mm for **c**-**e**; bar in **b** = 10 mm for **b.**

3.1.3 Fluorescence studies on cell walls

Many different microscopic approaches have been used to investigate the structural organisation of the tracheid cell wall (Abe and Funada, 2005) including fluorescence (reviewed in (Donaldson, 2008). Autofluorescence, primarily induced by UV and short wavelength excitation of lignin, has been extensively used to characterise wall structure and formation, especially in relation to the development of compression wood (Donaldson et al., 1999), and has been quantified during tracheid development where spectral variations from different types of wood (normal wood versus mild and severe compression wood) have been detected (Donaldson et al., 2010). Fluorescent dyes including safranin (Bond et al., 2008), acriflavin and basic fuchsin (Donaldson and Bond, 2005) have also been used to investigate lignin localisation.

However, to understand the deposition and organisation of cellulose within the wall, different strategies are required. Different fluorescent dyes exist that label cellulosic wall components. These include calcofluor white, also known as fluorescent brightener (Sauter et al., 1993) and Congo red (Verbelen and Kerstens, 2000). These stains are, however, neither specific in labelling cellulose nor ideal for cellulose localisations. Congo red, which binds more strongly to xyloglucan than cellulose (Anderson et al., 2010; Wood, 1980), is also a well-characterised protein stain (Prentø, 2009), and has been used to label chitin in both fungi (Slifkin and Cumbie, 1988) and crustaceans (Michels and Büntzow, 2010). Calcofluor too has low discrimination for cellulose over other cell wall polysaccharides (Anderson et al., 2010; Verbelen and Stickens, 1995).

3.1.4 Pontamine fast scarlet 4B and pine cell walls

P4B is a red dye traditionally used in the textile industry for staining cloth and fabrics (Bedrick, 1968). The dye was initially introduced for the fluorescent labelling of fungal and oomycelial cell walls (Hoch et al., 2005), and was used to label newly synthesised cellulose microfibrils in the primary wall of living *Arabidopsis thaliana* roots (Anderson et al., 2010). According to Anderson and colleagues, P4B showed a greater specificity than calcofluor for cellulose, as opposed to other cell wall components such as xyloglucan, callose and pectin, and its fluorescence output was significantly increased by the inclusion of 150 mM NaCl or KCl in the buffer solution. More recently, Sun et al. (2011) used confocal microscopy to demonstrate that a secreted fungal endoglucanase bound parallel to P4B-labelled cellulose in *Arabidopsis* seedlings. The dye has also been used in numerous other recent studies involving the cell

wall of *Arabidopsis* (Anderson et al., 2012; Lampugnani et al., 2013; Landrein et al., 2013; Liu et al., 2013; Park et al., 2011; Voiniciuc et al., 2013; Wang et al., 2011).

In this study, it was initially investigated whether P4B could be used to label the secondary cell walls of radiata pine tracheids. Although the preliminary results showed some significant differences to Anderson et al. (2010), it was confirmed that P4B is an excellent stain for labelling cellulose in pine tracheids, notably for the S1 and S3 layers and that it shows a higher specificity in labelling than either Congo red or calcofluor. It is also demonstrated that, like Congo red, P4B exhibits polarisation-dependent fluorescence (bifluorescence), although it does this more strongly.

3.1.5 Objectives

The research described in this chapter had 3 objectives. These were:

1) Developing and optimising a suitable protocol for staining and confocal microscopy, and characterising the dye, P4B with regards to radiata pine tracheids.

2) Comparing the fluorescence properties of P4B with the traditional dyes such as safranin, calcofluor white and Congo red.

3) Exploring the potential of observing and measuring the microfibril angle of S1 and S3 layers by confocal microscopy of P4B-stained tracheids.

3.2 Materials and Methods

3.2.1 Sample preparation

Discs (stem diameter 20 - 40 mm, 25 mm in length) were cut from 2 year old radiata pine trees (Figure 3.1), some of which had been artificially leaned for 6 - 12 months, and preserved in formaldehyde / acetic acid / alcohol fixative (FAA; 10% (v/v) formaldehyde, 5% (v/v) acetic acid, and 50% (v/v) ethanol). Wood blocks (10 mm by 10 mm) containing either compression and opposite wood were prepared from the same growth ring and used for sectioning (Figure 3.1). Blocks were washed in warm water (30^0C, 15 min) and 60 µm-thick transverse or longitudinal sections cut with a sledge microtome (Reichert, Vienna, Austria). During sectioning, the wood block was kept wet. Sections were washed in warm distilled water and dried on a filter paper for several seconds before staining.

3.2.2 P4B staining

P4B (Hoch et al., 2005; Thomas et al., 2013) was purchased from the Sigma-Aldrich Rare Chemical Library (Sigma-Aldrich, St Louis, MO, USA; catalogue number S479896, CAS number 3441-14-3). This product was discontinued in 2012, but Direct Red 23 (Sigma-Aldrich; catalogue number 212490, CAS number 3441-14-3) was found to be an identical chemical and to provide similar labelling (see section 3.3.6).

Initial experiments aimed to optimise the staining compared to the traditional stains. For P4B, four different concentrations, 0.01, 0.05, 0.1 and 0.2% (w/v) were tried with different staining time (5, 30 and 120 min) to find the optimum stain solution concentration and staining time. Once the concentration and staining time were optimised, the effect of NaCl on fluorescence, as reported in Anderson et al. (2010), was tested by preparing 0.1% (w/v) P4B in either distilled water or 150 mM NaCl. Sections were also stained with P4B (0.1% (w/v)) for various times (5 min, 30 min, 2 h and 12 h) at different pH values (approximately 5, 7 and 9) and temperatures (room temperature, 35^0C and 45^0C) to assess variations in dye uptake. Except where noted, sections in subsequent experiments were stained for 5 min in 0.1% (w/v) P4B. Stained samples were blotted on filter paper to remove excess stain and mounted in glycerol. In all cases, slides were sealed with nail polish and viewed as early as possible to avoid leaching of stain.

3.2.3 Staining with other fluorescent dyes

Calcofluor white and Congo red were purchased from Sigma-Aldrich while safranin was sourced from Nice Microscopy (Kochi, India). Sections were stained in either Congo red (0.1%

(w/v) in 50% ethanol) or calcofluor white (0.01% (w/v) in distilled water with a few drops of 1 M NaOH) for 5 min, blotted on filter paper to remove excess stain and mounted in glycerol. Safranin (2% (w/v)) was prepared by dissolving 5 g ferric alum in 100 ml distilled water with gentle heating, followed by the addition of safranin (2 g) and glycerol (14 ml) and filtering. Sections were dipped in safranin for several seconds, blotted on filter paper to remove excess stain and washed in distilled water before being mounted in glycerol. In all cases, slides were sealed with nail polish and viewed as early as possible to avoid leaching of stain.

3.2.4 Confocal microscopy

Confocal laser scanning microscopy (model TCS SP5, Leica Microsystems, Wetzlar, Germany) used a 63X NA1.3 glycerol immersion lens and excitation at 405, 488, 561 and 633 nm (violet, blue, green and red lasers respectively). Fluorescence on the SP5 system was collected in user-defined wavelength bands. 405 nm excitation light was used to collect lignin autofluorescence and calcofluor white fluorescence between 420 and 480 nm, and 561 nm excitation to collect P4B, safranin, and Congo red fluorescence between 570 and 650 nm. However, lignin autofluorescence in calcofluor white-stained material was generated at 488 nm, with fluorescence collected between 500 to 580 nm. To reduce cross-talk between lignin and the different dyes, images were collected using sequential line scanning with only a single excitation wavelength and the corresponding fluorescence collected at any one time. Concurrent transmitted light images were also collected using brightfield optics and, wherever appropriate, colour transmitted light images were generated by combining transmitted light images collected concurrently with the 488, 561 and 633 nm lasers (Wiltshire and Collings, 2009). Separate brightfield and polarised light images were collected using a cooled CCD camera (model DFC310FX, Leica).

3.2.4.1 Spectral scanning

Being a new dye for the pine cell wall studies, the spectral properties of P4B were measured to determine the best excitation and emission wavelengths. Emission spectral data (lambda scanning) were collected from P4B-labelled and unlabelled control samples of opposite and compression wood. These spectra were generated with 405, 488, 561 and 633 nm excitation, and with emission ranges from 420 to 700 nm, 500 to 700 nm, 572 to 700 nm and 640 to 700 nm respectively. Scans used a 10 nm wide window and 4 nm step size. Identical collection settings were used for all samples, and spectra were averaged for the entire image field of two separate preparations, rather than specific regions of individual cells. Fluorescence emission spectra from safranin-treated opposite and compression wood were also collected using similar wavelength settings.

3.2.4.2 Modulation of the polarisation of excitation light

In P4B-stained sections, it was observed that within individual tracheids, only specific cell wall layers / regions parallel to the direction of excitation light fluoresced and that the same walls did not fluoresce when placed at an angle of 90^0 to the excitation light. Fluorescence emission of any material is dependant on the amount of light (energy) absorbed. Therefore, only the walls / regions parallel to the incident light will absorb energy and excite to generate fluorescence emission. This property, known as 'bifluorescence', was earlier reported in samples labelled with dyes such as Congo red and calcofluor white (Jang, 1998; Verbelen and Kerstens, 2000).

The inbuilt 'scanfield rotation' function in the Leica confocal system is capable of diverting the orientation of the field of view scanned by the excitation laser light by up to +/- 100^0. This is typically used to frame the object being scanned. Scanfield rotation also modifies the polarisation of the incident light, and allows excitation with different polarisations thereby modulating the fluorescence output of polarisation-dependent dyes such as P4B. In these experiments, however, the scanfield rotation function was not used. This function caused a variable, wavelength-dependent modulation of the polarity of the excitation lasers that was difficult to control. For example, using a scanfield rotation of 45^0 did not rotate the polarisation of all the excitation lasers by 45^0, but by some other value.

Therefore, to determine these polarisation effects, it was instead necessary to replace the standard Leica confocal galvo-stage with a graduated, circular and rotatable stage that had been removed from a polarisation microscope. This was attached to the standard microscope stage so that rotation of the circular stage occurred around the axis of the microscope lens. An insert in the circular stage allowed the specimen location to be adjusted. In this configuration, the polarisation of the incident light could be manipulated by precisely rotating the circular stage, while keeping the same focal plane and the cells of interest within the field of view, with specimen rotation corrected in Adobe Photoshop CS4 (version 11.0.1, Adobe Systems, San Jose, CA USA).

3.2.5 Correlative scanning electron microscopy

Scanning electron microscopy (SEM) was used to correlate the cell regions of interest found by confocal microscopy. For SEM, small blocks of opposite and compression wood were boiled in water (10 min) to soften the wood, and trimmed by hand with a new, single-edged razor blade for each surface (Butterfield and Meylan, 1980). The blocks were mounted on stubs, gold-coated under vacuum (2 min, 10 nm) (Emitech K 550X sputter coater) and imaged

with an SEM (Leica, model S440). The last section removed from the block, a mirror image of the surface, was P4B-labelled and viewed by confocal microscopy to correlate fluorescence and SEM images. The fluorescence image was reversed in Photoshop to match the SEM image.

3.2.6 Delignification of cell walls

Fluorescent images of delignified wood were collected to study the effect of lignification on P4B labelling of the S2 layer. Wood blocks (7 x 4 x 2 mm) were cut by hand with a single-edged razor and delignified in a 1:1 solution (v/v) of glacial acetic acid (JT Baker, Phillipsburg, NJ USA) and 30% (v/v) hydrogen peroxide (BDH Laboratory Supplies, Poole, England) (85^0C, 4 h), cooled and washed extensively in distilled water (Donaldson et al. 2010). As the blocks were extremely soft, they were allowed to dry on filter paper (1 h). Blocks were then stained in 0.1% (w/v) P4B (10 min) and imaged without further sectioning. Unstained blocks were also imaged as controls. Experiments were also conducted to find whether the extended staining time or higher dye temperature could improve the S2 labelling of P4B. For this, 60 µm-thick sections were stained with P4B (0.1% (w/v)) for 5 min and 12 hour at room temperature and at 45^0C and compared with the delignified sections for assessing the improvement in S2 layer labelling.

3.2.7 Measurements of tracheid dimensions

Measurement of tracheid and cell wall dimensions involved imaging the wood cross sections with the Leica confocal microscope and subsequent image processing. 60 µm-thick sections from normal, opposite and compression wood of two year old radiata pine trees (Figure 3.1) were imaged with the confocal microscope using a 20X NA 0.7 immersion lens and excitation at 405 nm (violet) light to capture the lignin autofluorescence (420 - 480 nm). Large format images (2048 x 2048 pixels) were collected which covered a field of view of 775 x 775 µm providing a resolution of 378 nm / pixel. These images were oriented with the outer surface of the tree towards the top of the image and the pith on the bottom (Figure 3.2a). Photoshop was used to identify and measure the tracheid dimensions (Figure 3.2b). Using the ‘quick selection’ tool, 20 tracheids were selected per image (Figure 3.2a), avoiding adjoining tracheids, and tracheids adjacent to resin canals or ray cells. The selected cells were numbered using the ‘count tool’ and the image was processed with a pre-defined ‘Actions’ tool in which the following commands were recorded:

‘expand’ = 4 pixels then ‘contract’ = 4 pixels (this smooths the shape of the tracheids, and eliminates outliers).

'fill' = grey colour at 50% visibility.

'measure' = area, perimeter, height (radial lumen diameter), width (tangential lumen diameter) and circularity of the lumen.

The circularity index measurement made by Photoshop is defined as follows:

Circularity Index, CI = 4π (Area / Perimeter^2)

where the area and perimeter had been measured directly. The resultant measurements were saved as an Excel file. Manual measurements were made of the radial and tangential dimensions of the tracheid with the 'ruler' tool in Photoshop, and saved in to Excel file (Figure 3.2c). Wall thicknesses in the radial and tangential directions were measured by the following formulae:

Radial wall thickness, WT (R) = [TD (R) - LD (R)]/2

Tangential wall thickness, WT (T) = [TD (T) - LD (T)]/2

where LD (T) = tangential lumen diameter, LD (R) = radial lumen diameter, TD (T) = tangential tracheid diameter and TD (R) = radial tracheid diameter.

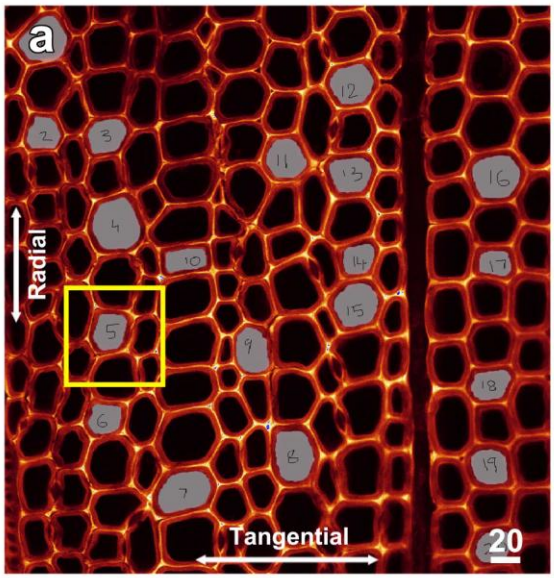

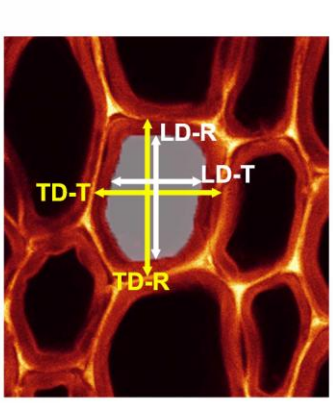

c

Wood ty	LD-R	LD-T	LD-Av	L-Ar	TD-R	TD-T	TD-Avg	WT-R	WT-T	WT_Av	circularity	perimeter
NW	µm	µm	µm	sq.µm	µm	µm	µm	µm	µm	µm	µm	µm
1	31.42	30.11	30.77	743.16	37.75	36.22	36.98	3.16	3.05	3.11	0.83	105.76
2	24	21.38	22.69	400.74	27.71	24.22	25.97	1.85	1.42	1.64	0.81	78.92
3	25.75	24.44	25.09	486.44	29.46	29.68	29.57	1.85	2.62	2.24	0.83	85.93
4	38.4	30.55	34.48	914.23	43.42	36.44	39.93	2.51	2.95	2.73	0.84	117.11
5	26.62	21.38	24	451.69	32.08	24.87	28.48	2.73	1.75	2.24	0.81	83.55
6	22.26	21.38	21.82	385.03	27.06	27.06	27.06	2.4	2.84	2.62	0.82	76.65
7	31.42	33.6	32.51	795.3	34.26	39.06	36.66	1.42	2.73	2.07	0.82	110.43
8	37.53	24.87	31.2	756.3	46.26	30.77	38.51	4.36	2.95	3.65	0.81	109.22
9	33.6	20.95	27.28	571.67	38.19	24.22	31.2	2.29	1.64	1.96	0.81	94.59
10	17.89	25.75	21.82	375.22	22.26	32.73	27.49	2.18	3.49	2.84	0.81	78.46
11	28.8	25.75	27.28	572.19	34.48	30.33	32.4	2.84	2.29	2.56	0.86	91.21
12	29.68	27.93	28.8	627.94	34.48	34.48	34.48	2.4	3.27	2.84	0.85	96.42
13	26.18	27.06	26.62	560.62	32.29	32.73	32.51	3.05	2.84	2.95	0.84	91.53
14	22.26	20.07	21.17	368.99	27.28	24.87	26.07	2.51	2.4	2.45	0.84	74.31
15	32.29	27.93	30.11	703.36	37.09	35.35	36.22	2.4	3.71	3.05	0.86	101.59
16	31.86	30.55	31.2	780.21	38.4	37.09	37.75	3.27	3.27	3.27	0.86	106.66
17	18.98	20.51	19.75	324.04	23.35	26.62	24.98	2.18	3.05	2.62	0.84	69.71
18	22.26	25.53	23.89	438.36	25.97	28.58	27.28	1.85	1.53	1.69	0.82	82.09
19	26.18	23.13	24.66	500.73	32.95	28.8	30.88	3.38	2.84	3.11	0.87	85.21
20	23.13	22.69	22.91	417.88	29.02	29.02	29.02	2.95	3.16	3.05	0.85	78.67
Avg	27.53	25.28	26.4	558.71	32.69	30.66	31.67	2.58	2.69	2.63	0.83	90.9
Min	17.89	20.07	19.75	324.04	22.26	24.22	24.98	1.42	1.42	1.64	0.77	69.71
Max	38.4	33.6	34.48	914.23	46.26	39.06	39.93	4.36	3.71	3.65	0.87	117.11
SD	5.721	3.921	4.262	172.41	6.356	4.657	4.724	0.67	0.66	0.54	0.03	13.76
SE	1.279	0.877	0.953	38.552	1.421	1.041	1.056	0.15	0.15	0.12	0.01	3.08

Figure 3.2 Measurement of cell dimensions using Photoshop.

a. A typical transverse section image of normal wood where 20 tracheids were selected randomly. Double headed arrows show the radial and tangential directions.

b. Enlarged view of the yellow box in **a** showing how tangential (TD-T) and radial (TD-R) tracheid diameters (yellow arrows) were measured along with the tangential (LD-T) and radial (LD-R) lumen diameters (white arrows).

c. Replica of the Excel sheet used for calculating and reporting the cell dimensions.

LD-T = tangential lumen diameter,

LD-R = radial lumen diameter,

TD-T = tangential tracheid diameter,

TD-R = radial tracheid diameter,

WT-R = radial wall thickness,

WT-T = tangential wall thickness.

Bar in **a** = 20 µm for **a**.

3.3 Results

For the analysis of cell wall structure, as well as of autofluorescence and cell wall labelling with dyes such as safranin and P4B, 60 µm-thick transverse sections were cut by microtoming FAA-fixed stems of 2 year old pine trees that had been leaned to induce compression wood on the lower side. This allowed a direct comparison by confocal microscopy of compression wood with opposite wood in the same tree formed at the same stage of the annual growth ring (Figure 3.1).

3.3.1 Anatomical features of normal and compression wood

Dimensional measurements of various cell and cell wall parameters were collected from normal, opposite and compression wood sourced from two year-old radiata pine stems (Table 3.1). The cell walls of normal and opposite wood tracheids were much thinner than the cell walls of compression wood tracheids (Figure 3.3), and within individual tracheids, the tangential walls were significantly thicker than radial walls in all the three wood types. (By definition, the radial wall is the wall parallel to the radial surface of the wood whereas the tangential wall is the wall perpendicular to the radial wall.) The average thickness of tangential walls in normal wood was 3.02 µm whereas these walls were significantly thicker in compression wood at 5.65 µm. Radial wall thickness in normal wood was 2.61 µm and the corresponding compression wood tracheids were significantly thicker (4.93 µm). The overall tracheid diameter (average of radial and tangential diameters) was similar in both normal and compression wood (25.7 to 26.3 µm). The lumen diameter and lumen area were, however, higher in normal and opposite wood compared to compression wood. These cell dimensions were similar to previous observations (Donaldson and Lausberg, 1998; Schimleck and Evans, 2001). The circularity index, which is the measure of an object's closeness to a circle, was significantly higher in compression wood indicating that these lumens were rounder (Figure 3.3h). Loss of the original shape of the opposite wood cells to form round compression wood tracheids lead to the presence of intercellular spaces, which is a characteristic feature of the severe compression wood. These observations reiterate the fact that normal/opposite wood and compression wood tracheids are not only different in chemical properties but in their physical shape and dimensions.

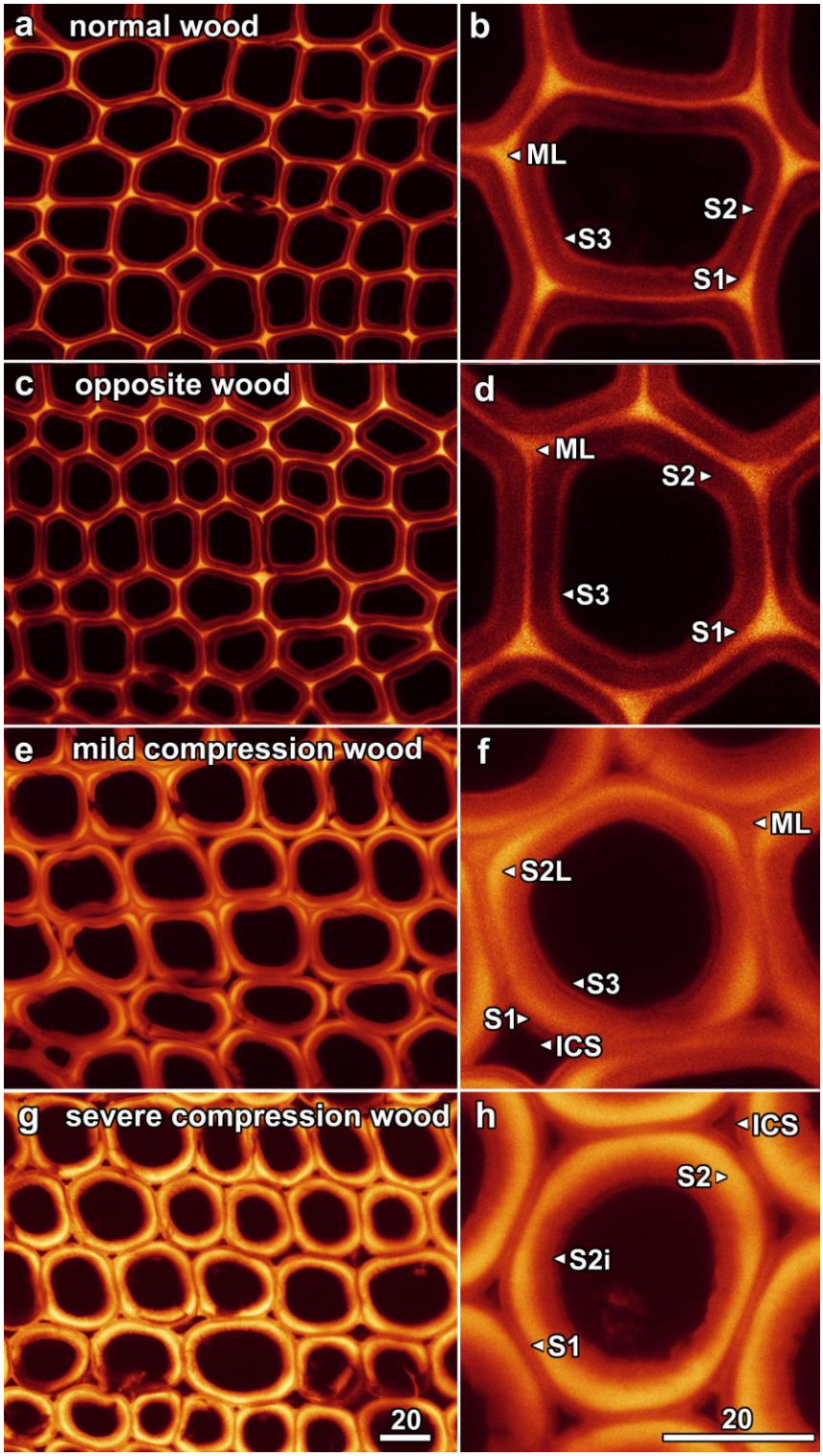

Figure 3.3 Autofluorescence from different wood types, and different cell wall layers. Single confocal optical sections were collected using 405 nm excitation, and are shown at low (**a**, **c**, **e** and **g**) and high magnification (**b**, **d**, **f** and **h**).

a,**b.** Normal wood tracheids were characterised by thin cell walls, uniform lignin distribution and tracheid cross section with a polygonal shape. Autofluorescence

was strongest from the lignin rich middle lamellae (ML) and much weaker from the S3 layer. The S1 and S2 layers did not produce much lignin autofluorescence.

c,**d.** Opposite wood tracheids were similar in appearance and fluorescence to normal wood tracheids.

e,**f.** Mild compression wood tracheids showed lignification of the outer part of the S2 layer (S2L), with this lignin preferentially found in the cell corners. Cell shape changed from polygonal to round, and the wood was characterised by the presence of inter-cellular spaces (ICS) between the cells.

g,**h.** In severe compression wood, the thick-walled tracheids developed a strong circular band of lignin in the S2 layer, although the inner part of the S2 layer (S2i) showed less lignification.

Bar in **g** = 20 µm for **a**, **c**, **e** and **g**; bar in **h**= 20 µm for **b**, **d**, **f** and **h**.

Table 3.1 Tracheid dimensional variation among wood types.

	Tracheids			Tracheid cell wall thickness			Tracheid lumen	
	Diameter (μm)	Perimeter (μm)	Circularity index[1]	Radial (μm)	Tangential (μm)	Average (μm)	Diameter (μm)	Area (μm^2)
Normal wood	25.7 ± 2.2	71.1± 8.8	0.814 ± 0.010	2.61 ± 0.20 *	3.02 ± 0.23	2.82 ± 0.22	20.1 ± 2.3	356 ± 87
Opposite wood	23.7 ± 0.4	63.8 ± 1.0	0.815 ± 0.011	2.50 ± 0.16 *	3.05 ± 0.29	2.78 ± 0.22	18.1 ± 0.3	271 ± 11
Compression wood	26.3 ± 0.9	53.6 ± 2.7	0.856 ± 0.009#	4.93 ± 0.17 *#	5.65 ± 0.08 #	5.29 ± 0.11 #	15.8 ± 0.8	205 ± 22

Values reported are mean +/- standard error for n = 20 cells each from 18 different specimens.

# indicates significantly different from the normal wood at $P < 0.05$, Student's T-test.

* indicates significantly different between radial and tangential dimensions at $P < 0.05$, Student's T-test.

[1] Mathematically, the circularity index (CI) measures how closely an object is shaped to a circle and is defined as follows:

$$CI = 4\pi (Area / Perimeter^2).$$

3.3.2 Autofluorescence varies with wavelengths and wood type

Just as normal, opposite and compression wood were different in their anatomical features, their fluorescence properties were also different (Figure 3.3). This was evident from the intrinsic fluorescence (autofluorescence) of the different cell wall regions which fluoresced differently when different excitation lasers were used. This autofluorescence derives from lignin which, when stimulated with suitable excitation light, fluoresces. Therefore, the autofluorescence was much stronger from compression wood due to the higher amount of lignin present in its S2 layer (Figure 3.3g,h). Autofluorescence from opposite and compression wood was collected with 405, 488 and 561 nm excitation (Table 3.2). 405 nm light was found to be the best excitation wavelength to obtain autofluorescence (Figure 3.4a), while 561 nm produced hardly any autofluorescence (Figure 3.4c) in comparison to weak fluorescence with 488 nm (Figure 3.4b). Thus, the 405 nm laser was used for collecting the lignin autofluorescence in all subsequent experiments, with the one exception of when the 405 nm-excited dye calcofluor white was imaged (see section 3.2.4). In normal and opposite wood, lignin in the middle lamella region fluoresced strongly with the excitation of 405 nm light (Figure 3.3a-d). No other wall region fluoresced strongly except the slightly weaker S3 region. However, in compression wood, the S2L region around the round tracheids fluoresced more strongly than other regions of the wall and the normal wood (Figure 3.3).

Table 3.2. Variation of fluorescence intensities with wavelength and staining solution.

Excitation (nm)		Lignin autofluorescence				P4B fluorescence			
		In distilled water		In 150 mM NaCl		In distilled water		In 150 mM NaCl	
		Emission peak (nm)	Intensity	Emission peak (nm)	Intensity	Emission peak (nm)	Intensity	Emission peak (nm)	Intensity
405	Opposite wood	472	29.6	468	27.5	460	31.8	464	30.8
	Compression wood	480 *	55.4	480 *	53.8	468 *	56.5	472 *	52.2
488	Opposite wood	540	10.1	548	5.2	584	14.0	584	34.3
	Compression wood	542 *	15.3	552 *	11.9	576 **	15.9	576 *	27.1
561	Opposite wood	584	3.0	584	2.7	584	13.4	584	35.1
	Compression wood	584	3.9	592 *	3.8	584	8.1	584	18.8

* Indicates spectral shift to a longer wavelength in compression wood.

** Indicates spectral shift to a shorter wavelength in compression wood. In this case, the shorter wavelength likely represent a significant contribution from lignin autofluorescence as well as P4B fluorescence.

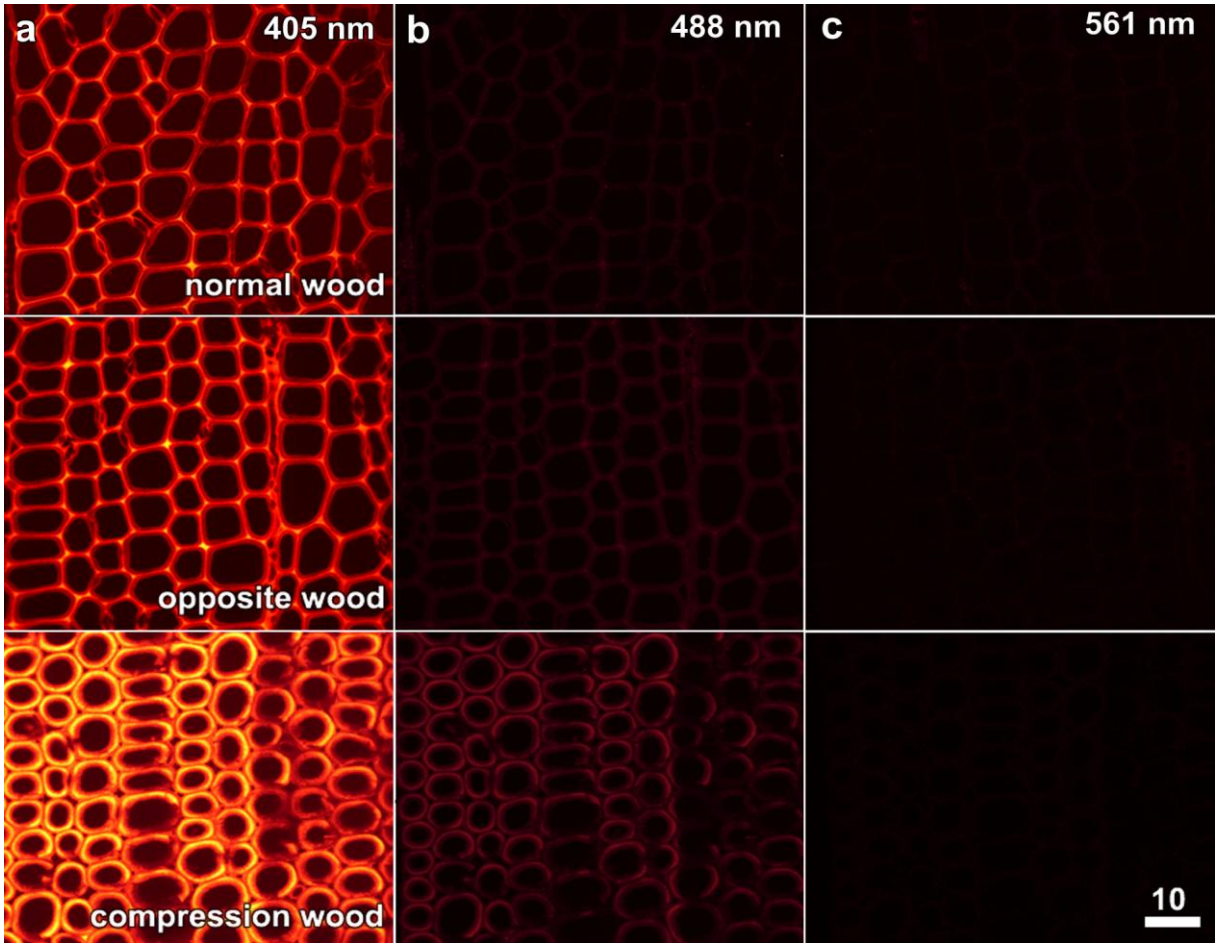

Figure 3.4 Autofluorescence varied in wood types with different excitation wavelengths. When using identical image collection conditions for 3 different excitation wavelengths (405, 488 and 561 nm), autofluorescence was much stronger from lignin-rich compression wood. 405 nm light was found to be the best excitation wavelength to obtain autofluorescence while 561 nm light produced hardly any autofluorescence in comparison to a weak fluorescence with 488 nm light.

a. Normal wood.

b. Opposite wood.

c. Compression wood.

Bar in **c** = 10 µm for all images.

3.3.3 Safranin fluorescence

Safranin, Congo red and calcofluor white are popular cell wall-staining dyes that have been used for various wood cell wall studies. These could be described as 'traditional dyes' owing to their long-term usefulness and popularity among researchers. While safranin is considered to be a lignin-binding dye, calcofluor white and Congo red are generally described as "cellulose-labelling" or "cellulose-binding" dyes. Analysis, however, demonstrates that their labelling is more specific to the β-glucans (Anderson et al., 2010; Verbelen and Kerstens, 2000).

Fluorescence emission spectra from safranin-treated opposite and compression wood were collected using 405, 488, and 561 nm excitation and with emission ranges from 420 to 700 nm, 500 to 700 nm and 572 to 700 nm respectively (Figure 3.5). 405 nm excitation generated hardly any fluorescence in normal (Figure 3.5a), opposite (Figure 3.5b) and compression wood (Figure 3.5c).

Overall fluorescence generated by 488 nm excitation in normal (Figure 3.5e) and opposite wood (Figure 3.5f) was considerably higher than the 405 fluorescence but was less than fluorescence from the compression wood (Figure 3.5g). With 561 nm excitation, safranin-treated normal (Figure 3.5i), opposite (Figure 3.5j) and compression wood (Figure 3.5k) fluoresced much more strongly than with either of the other excitation wavelengths. In normal and opposite wood, fluorescence from the lignin-rich middle lamella and the S3 regions was conspicuous while in compression wood the fluorescence was mainly from the S2L region. Spectral analysis showed that for 405 nm the emission peak was 568 nm, and for 488 and 561 nm maximum emission was at 576 nm (Figure 3.5d,h,l).

3.3.4 Optimising P4B labelling of the tracheid cell wall

Anderson et al. (2010) reported that P4B (0.01%) labels developing cellulose microfibrils in the primary cell walls of living *Arabidopsis thaliana* roots without inhibiting growth, but that 0.1% P4B significantly retarded growth. Moreover, they reported that fluorescence emissions peaked at wavelengths longer than 620 nm with the highest fluorescence recovered with red light excitation (633 nm), and that fluorescence improved when dye was dissolved in a 150 mM salt solution. As the excitation and emission wavelengths reported by Anderson et al. (2010) were different from those reported by Hoch et al. (2005), fluorescence emission spectra were measured for different excitation wavelengths for 0.01, 0.05, 0.1 and 0.2% P4B, dissolved either in deionised water or 150 mM NaCl, for both compression and opposite wood.

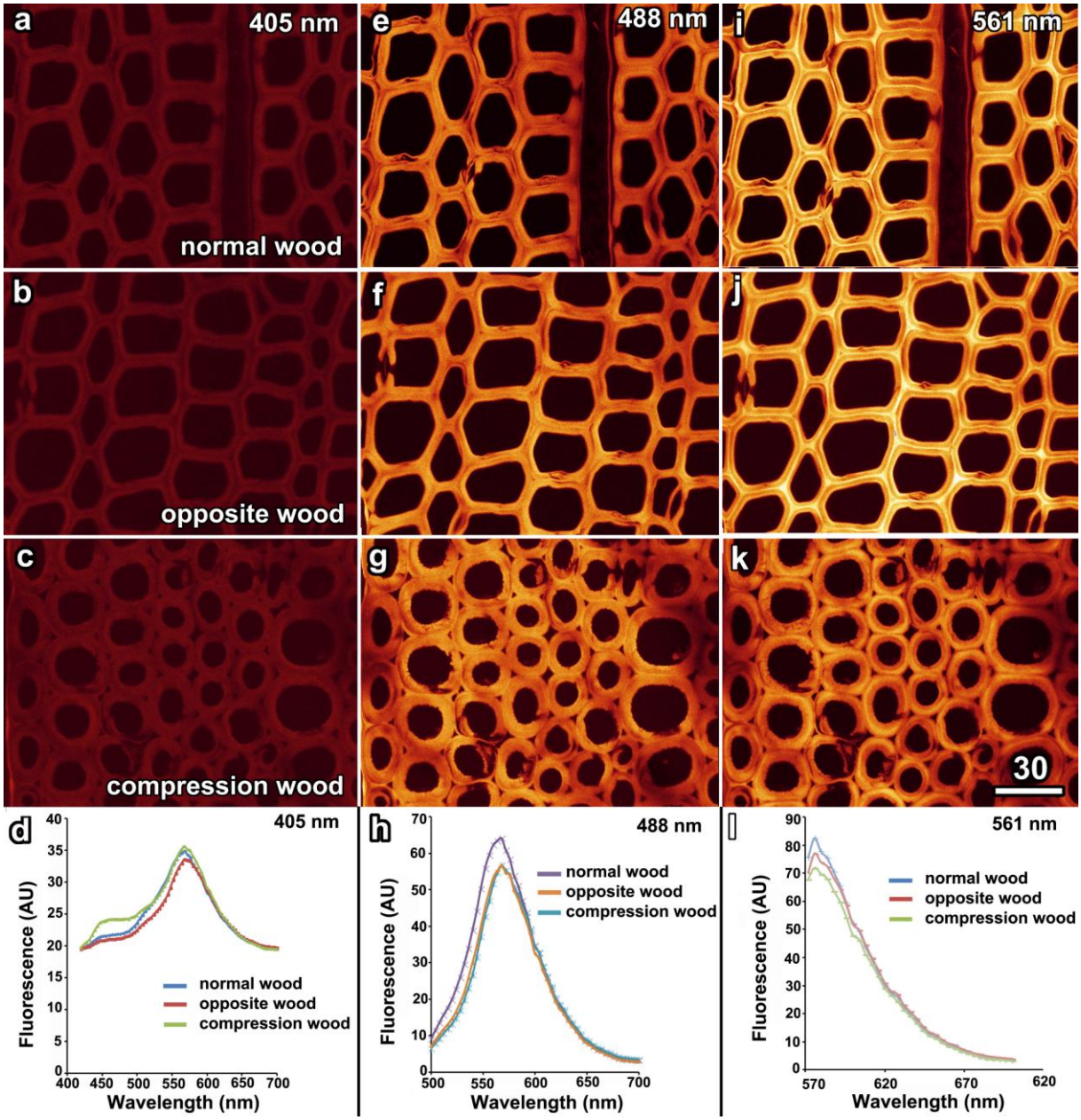

Figure 3.5 Safranin fluorescence varied in wood types with different excitation wavelengths. When using identical image collection conditions for 3 different excitation wavelengths (405 nm (**a**-**d**), 488 nm (**e**-**h**) and 561 nm (**i**-**l**)), safranin fluorescence was much stronger from lignin-rich compression wood. 561 nm light was found to be the best excitation wavelength to obtain safranin fluorescence while 405 nm light produced hardly any fluorescence in comparison to a weak fluorescence with 488 nm light.

a,e,i. Normal wood.

b,f,j. Opposite wood.

c,g,k. Compression wood.

Bar in **k** = 30 µm for all images.

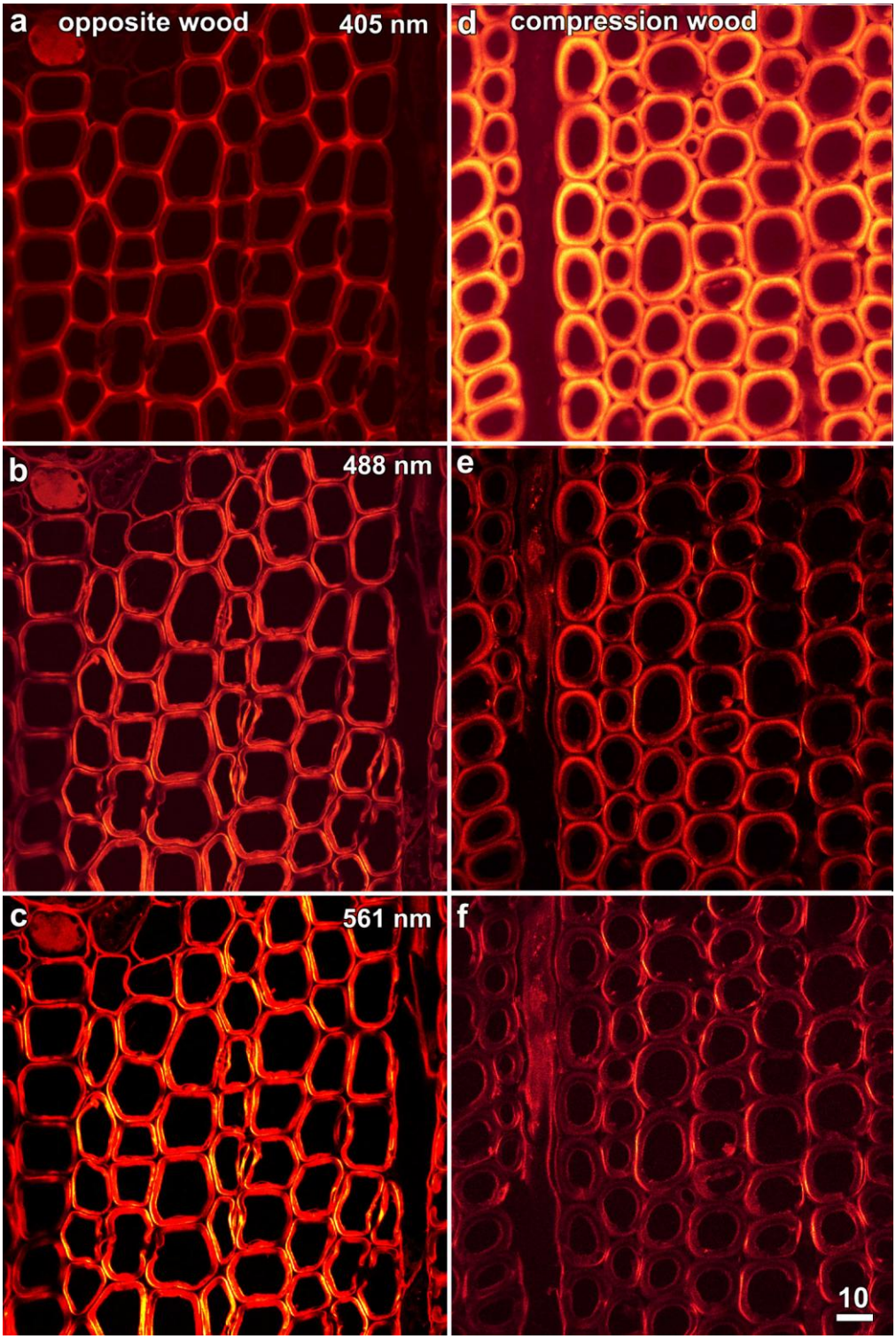

Figure 3.6 P4B fluorescence varied with different excitation wavelengths and wood types. Three different excitation wavelengths (405, 488 and 561 nm) were used to excite P4B-labelled samples. Identical image collection settings were used at each wavelength. P4B fluorescence was optimum when excited with 561 nm light. 488 nm light also generated some

P4B fluorescence, but with a mix of autofluorescence while only autofluorescence was generated by 405 nm excitation.

a-c. Opposite wood.

d-f. Compression wood.

Bar in **f** = 10 µm for all images.

3.3.4.1 Finding a suitable excitation wavelength

P4B-labelled compression and opposite wood were excited with 405, 488 and 561 nm light. 405 nm excitation generated only lignin autofluorescence in opposite (Figure 3.6a) and compression wood (Figure 3.6d). Although excitation of P4B at 488 nm generated fairly strong fluorescence in compression wood (Figure 3.6e), this excitation wavelength was not used because it also generated some lignin autofluorescence (Figure 3.6b,e). With 561-nm excitation, P4B-treated opposite (Figure 3.6c) and compression wood (Figure 3.6e) fluoresced much brighter, and showed characteristic patterns (see section 3.3.5) unrelated to lignin autofluorescence. However, when red excitation at 633 nm was used, no P4B fluorescence was seen (see section 3.3.4.4).

3.3.4.2 Optimising the P4B concentration

In the experiments by Hoch et al. (2005) labelling fungal cell walls, a 0.1% P4B solution was prepared in water. However, Anderson et al. (2010) who tested the elongation of living *Arabidopsis* roots with different P4B concentrations ranging between 0.0001 to 0.1%, conducted their imaging experiments with a 0.01% solution as this did not reduce plant growth. In this set of experiments in which labelling of the fixed secondary walls of radiata tracheids was investigated (and in which keeping cells alive and growing was not an issue), experiments were conducted to determine a suitable dye concentration. Several P4B solutions (0.01, 0.05, 0.1 and 0.2%) were tested. Normal, opposite and compression wood sections were excited with 561 nm light. In all the three wood types, 0.1% dye generated better overall fluorescence (Figure 3.7) with characteristic labelling patterns (see section 3.3.5). Although fluorescence was observed in samples labelled with 0.01 and 0.05% P4B, their fluorescence intensity was low and the characteristic S1 and S3 labelling patterns were not clearly seen. Moreover, the labelling pattern in the compression wood (Figure 3.7c) was also different and resembled the fluorescence generated with 488 nm light. P4B fluorescence was also low when the wood was labelled with 0.2% dye (Figure 3.7d), although the reason(s) for this effect remain unclear. Therefore, the dye concentration was kept at 0.1% for subsequent experiments.

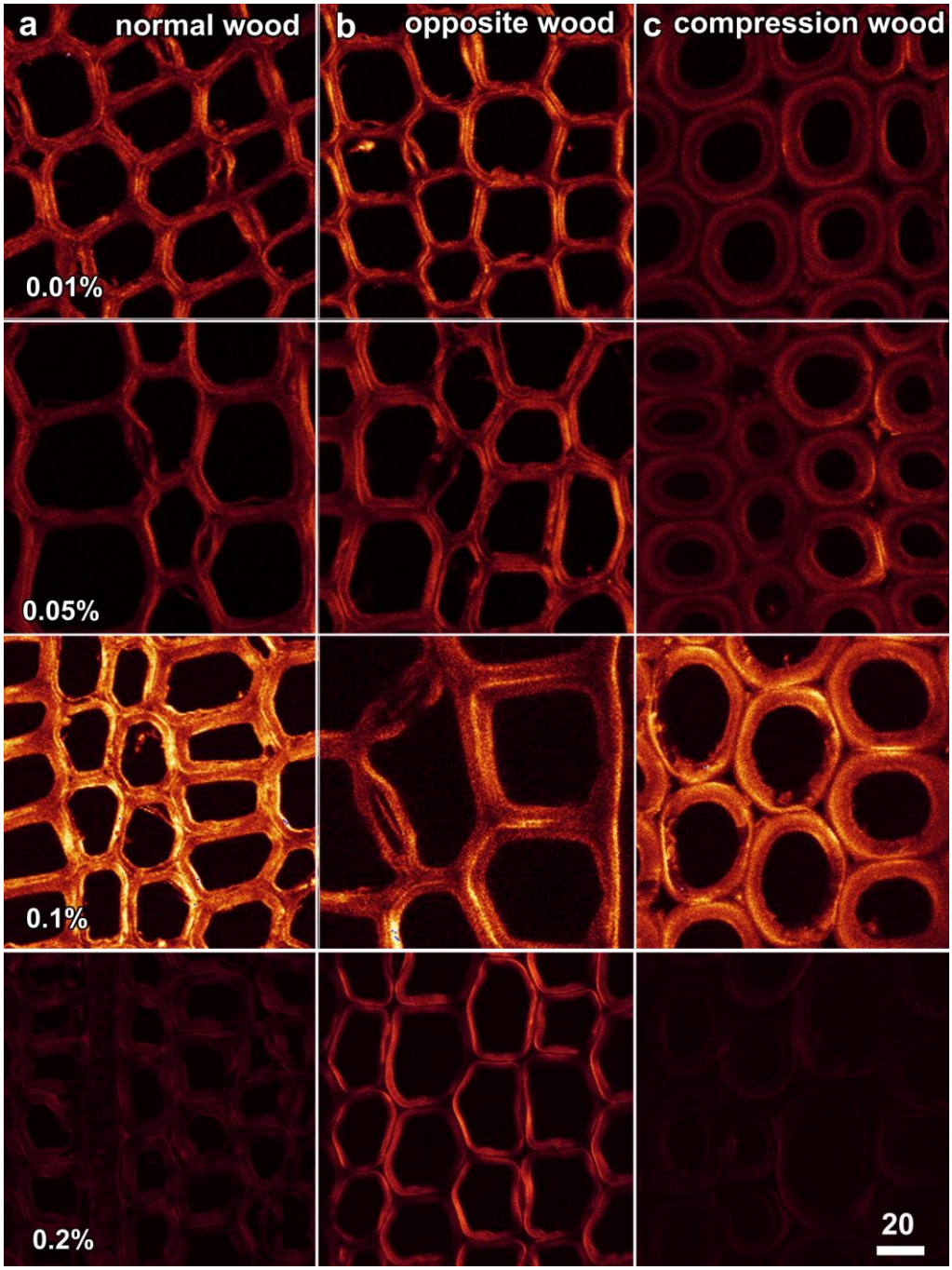

Figure 3.7 Differential P4B fluorescence among wood types and dye concentrations. Identical confocal excitation (561 nm) and emission settings were used for all images so that comparisons of labelling intensity could be made. P4B was tested at 0.01, 0.05, 0.1 and 0.2% (w/v).

a. Normal wood.

b. Opposite wood.

c. Compression wood.

Bar in **c** = 20 µm for all images.

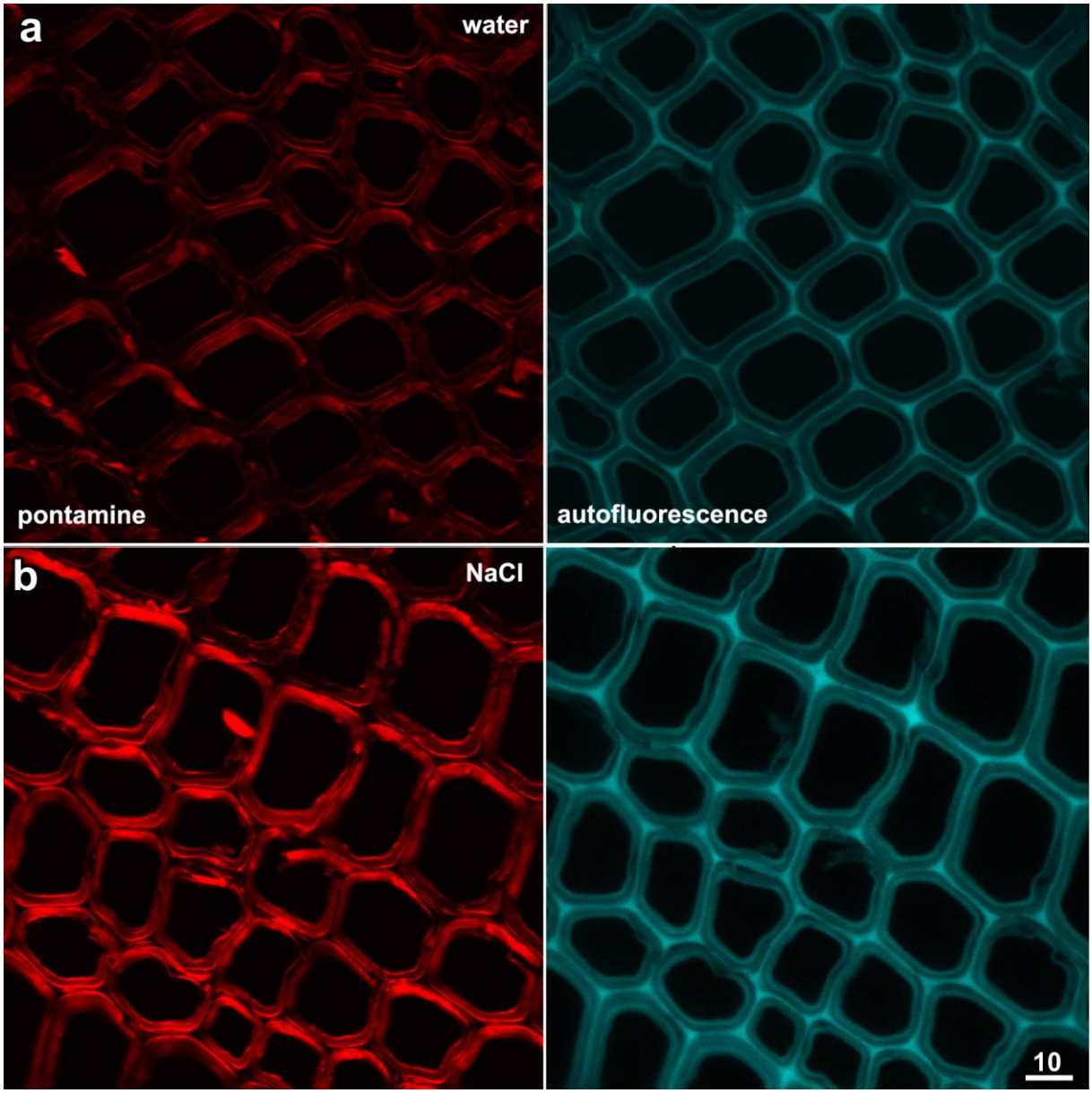

Figure 3.8 P4B fluorescence from opposite wood was improved by the inclusion of 150 mM NaCl in the staining solution.

- **a.** P4B prepared in distilled water, showing P4B fluorescence excited at 561 nm (left) and concurrent lignin autofluorescence excited at 405 nm (right).
- **b.** Improved P4B fluorescence when staining was conducted in the presence of 150 mM NaCl. P4B and lignin autofluorescence were collected using similar images settings to panel **a** to allow comparison of image intensities. While NaCl improved P4B labelling, it did not affect the lignin autofluorescence.

Bar in **d** = 10 µm for all images.

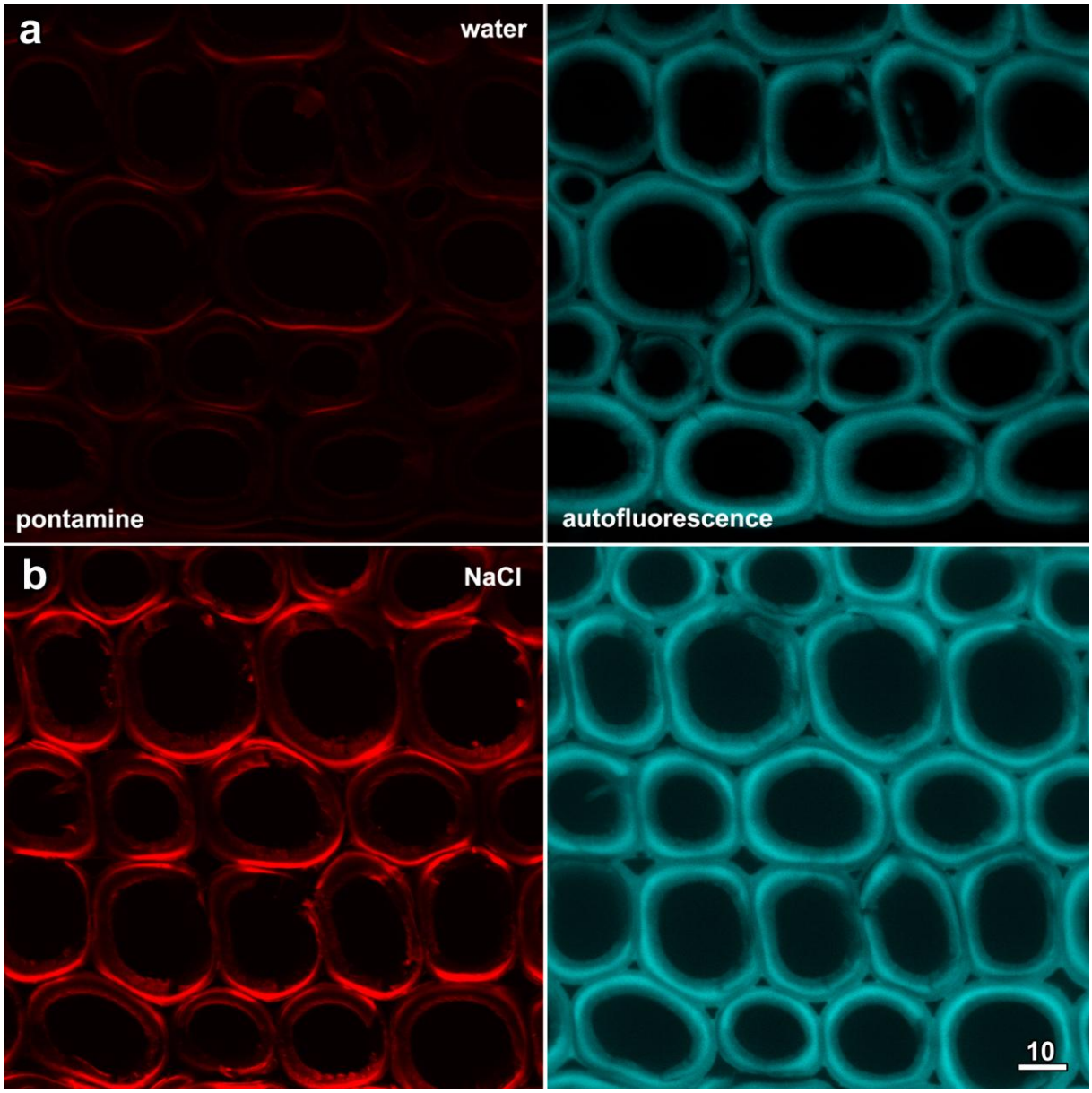

Figure 3.9 P4B fluorescence from compression wood was improved by the inclusion of 150 mM NaCl in the staining solution.

a. P4B prepared in distilled water, showing P4B fluorescence excited at 561 nm (left) and concurrent lignin autofluorescence excited at 405 nm (right).

b. Improved P4B fluorescence when staining was conducted in the presence of 150 mM NaCl. P4B and lignin autofluorescence were collected using similar images settings to panel **a** to allow comparison of image intensities. While NaCl improved P4B labelling, it did not affect the lignin autofluorescence.

Bar in **d** = 10 µm for all images.

3.3.4.3 The effect of salt on P4B fluorescence and spectra

The addition of 150 mM NaCl to the staining solution increased fluorescence for both opposite (Figure 3.8) and compression wood (Figure 3.9) and for both 488 and 561-nm excitation. This increase in fluorescence was quantifiable, and emission peaks were two to threefold higher (Table 3.2). These differences were also clearly evident in wavelength scans. 405 nm excitation caused autofluorescence from lignin in opposite wood, and increased fluorescence from heavily-lignified compression wood. The strongest emission occurred at about 460 nm and was unaffected by the presence of salt (Figure 3.10a,d). The addition of 0.1% P4B did not modify this autofluorescence emission peak, but in opposite wood, the presence of salt did result in a shoulder at 580 nm (asterisk, Figure 3.10a). By comparison, excitation with 488 nm light showed autofluorescence with a peak at 550 nm (arrow, Figure 3.10b,e), and a distinct P4B emission peak at 580 nm (asterisk). Autofluorescence from 561-nm excitation was negligible and there was strong P4B fluorescence peaking at 580 nm from both opposite (Figure 3.10c) and compression wood (Figure 3.10f). However, P4B fluorescence was generally lower from compression wood than opposite wood even though lignin autofluorescence was higher. All subsequent experiments used 0.1% P4B in 150 mM NaCl, and used excitation at 561 nm with emission collected from 570 - 650 nm.

3.3.4.4 P4B does not excite with red light

Despite the observations of Anderson et al. (2010) suggesting that P4B can be best excited with 633 nm (red) light, only very weak fluorescence was observed from P4B-stained wood samples using this excitation (Figure 3.11). While autofluorescence and 561 nm-excited fluorescence were present in the sample (Figure 3.11a,b), no signal was detected when red excitation (633 nm) was used (Figure 3.11c). This was quantified by line traces through the cell walls. While the different walls were clearly visible with autofluorescence and green-excited P4B, no signal was detected with red excitation (Figure 3.11d).

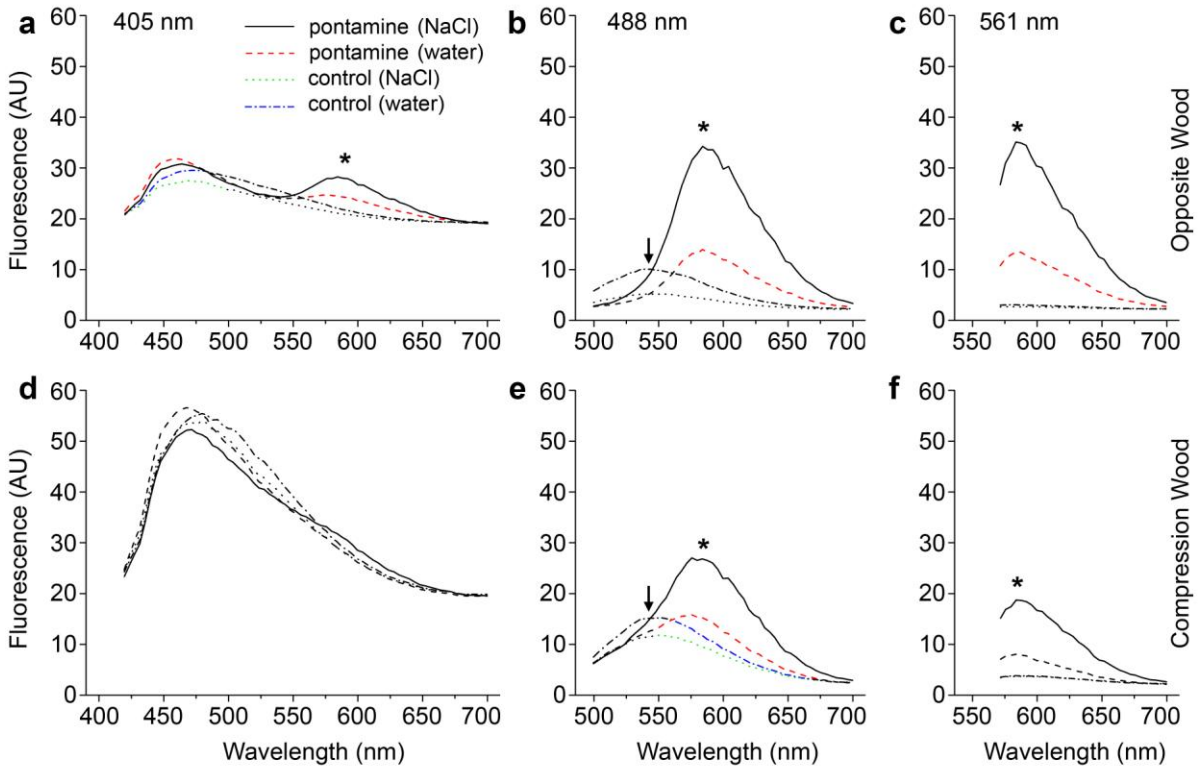

Figure 3.10 Confocal spectral scanning of different wood types. Wood was stained with 0.1% P4B in either 150 mM NaCl or deionised water and compared to control samples treated with distilled water or 150 mM NaCl. Excitations used were violet (405 nm), blue (488 nm) and green light (561 nm). Wavelengths scans were recorded using similar collection settings so that direct comparisons could be made between spectra.

a-**c.** Opposite wood.

d-**f.** Compression wood.

P4B showed a fluorescence peak at 580 nm using both blue and green excitation, but only weakly with violet excitation (asterisks), and this peak was significantly increased by the addition of NaCl. Autofluorescence peaked at 460 nm with violet excitation and 550 nm with blue excitation (arrows, **b**,**e**) at a shorter wavelength than P4B. AU = arbitrary units.

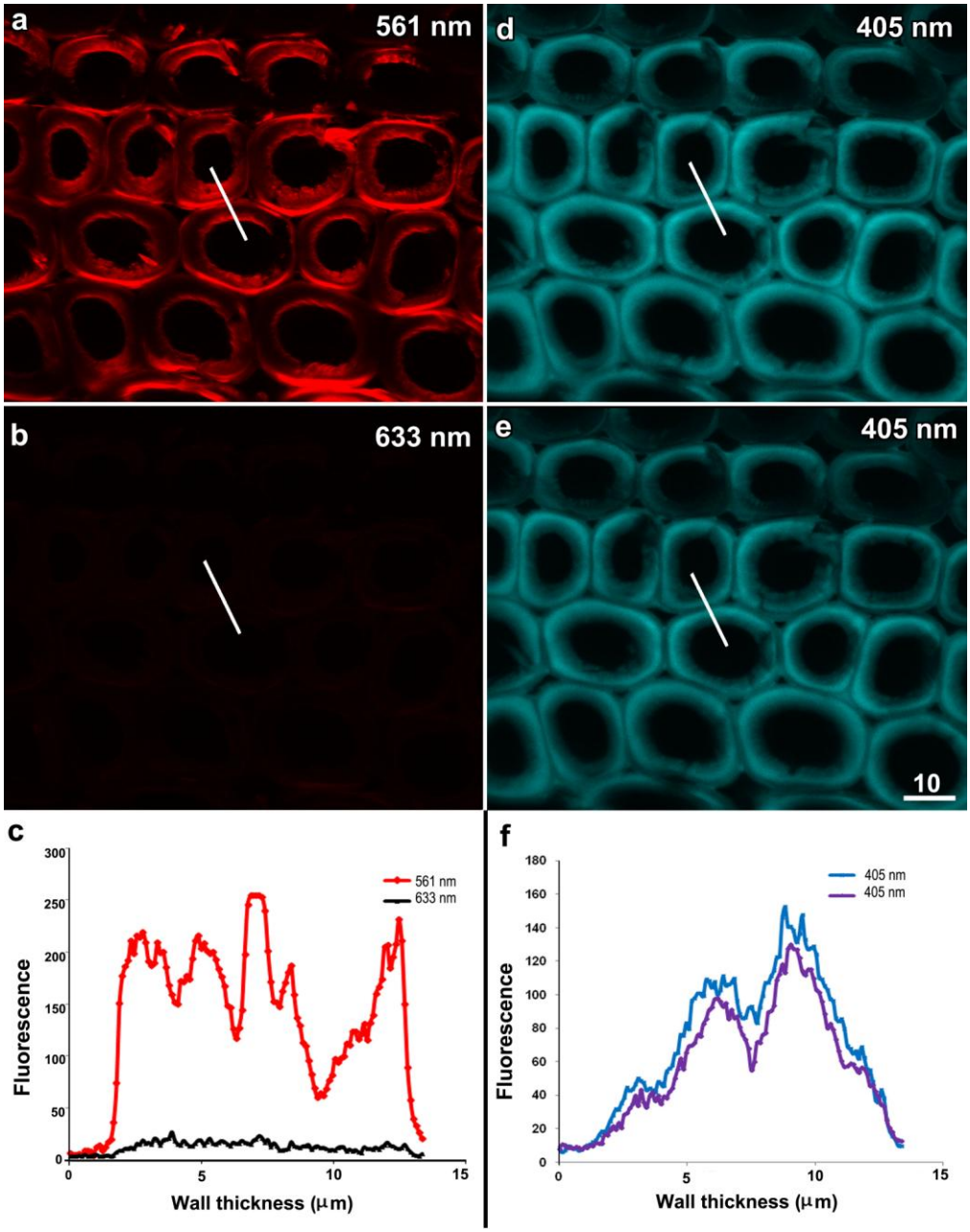

Figure 3.11 Comparing P4B fluorescence with 561 nm and 633 nm excitation; red light does not excite P4B. Intensity profiles were recorded along the lines shown in the micrographs.

- **a**, **b.** P4B fluorescence with 561 nm (at 31% laser power) and 633 nm (at 100% laser power) respectively.
- **d**, **e.** Concurrently collected lignin autofluorescence with 405 nm.
- **c**, **f.** Intensity profiles demonstrated that P4B fluoresced much stronger with 561 nm light. Lignin autofluorescence remained constant between scans.

Bar in **e** = 10 µm for **a, b, d** and **e**.

3.3.4.5 Optimising the staining time

Experiments were also conducted to determine the optimal P4B staining time. P4B stained sections were imaged with sequential scanning at 405 and 561 nm, recording lignin autofluorescence from 420 to 480 nm along with P4B fluorescence from 570 to 650 nm. While lignin autofluoresced from the middle lamella of opposite wood (Figure 3.12a) and from the thickened S2L layer of compression wood (Figure 3.12b), P4B fluorescence localised to distinct bands in both opposite and compression wood. The differential staining of the various cell wall layers may reflect that these layers have different permeabilities to P4B. To test this, opposite and compression wood samples stained for varying lengths of time (5 min to 120 min) were imaged. Using identical imaging conditions the staining patterns were compared, and there was no difference in labelling patterns in opposite or compression wood (Figure 3.12a, b). When quantified, there was only a marginal increase in P4B fluorescence intensity with time, and the slight variations in autofluorescence intensity (e.g. Figure 3.12b, 30 min) were not significant (Table 3.3). Subsequent experiments used 5 min staining. Further variations in staining time and conditions, including delignification and temperature of the dye solution were also tested in an attempt to enhance the S2 layer labelling. These dye uptake experiments will be discussed separately in section 3.3.9.

Table 3.3. Increasing staining times increase P4B intensity.

	Opposite wood (n = 3) [1]		Compression wood (n = 3) [1]	
Time (min)	P4B [2]	autofluorescence [3]	P4B [2]	autofluorescence [4]
5	187 ± 9	144 ± 12	151 ± 12	179 ± 6
30	207 ± 4	120 ± 8	138 ± 8	147 ± 9
120	221 ± 4 *	144 ± 9	160 ± 7	156 ± 5

* Different to the 5 min sample, $p < 0.05$, t-test.

[1] Three independent slices measured, with 15 separate cells averaged to calculate the value for each slice.

[2] P4B intensity measured in the S1 layer.

[3] Autofluorescence intensity for opposite wood measured in the corners of the middle lamella.

[4] Autofluorescence intensity for compression wood measured in the S2L region.

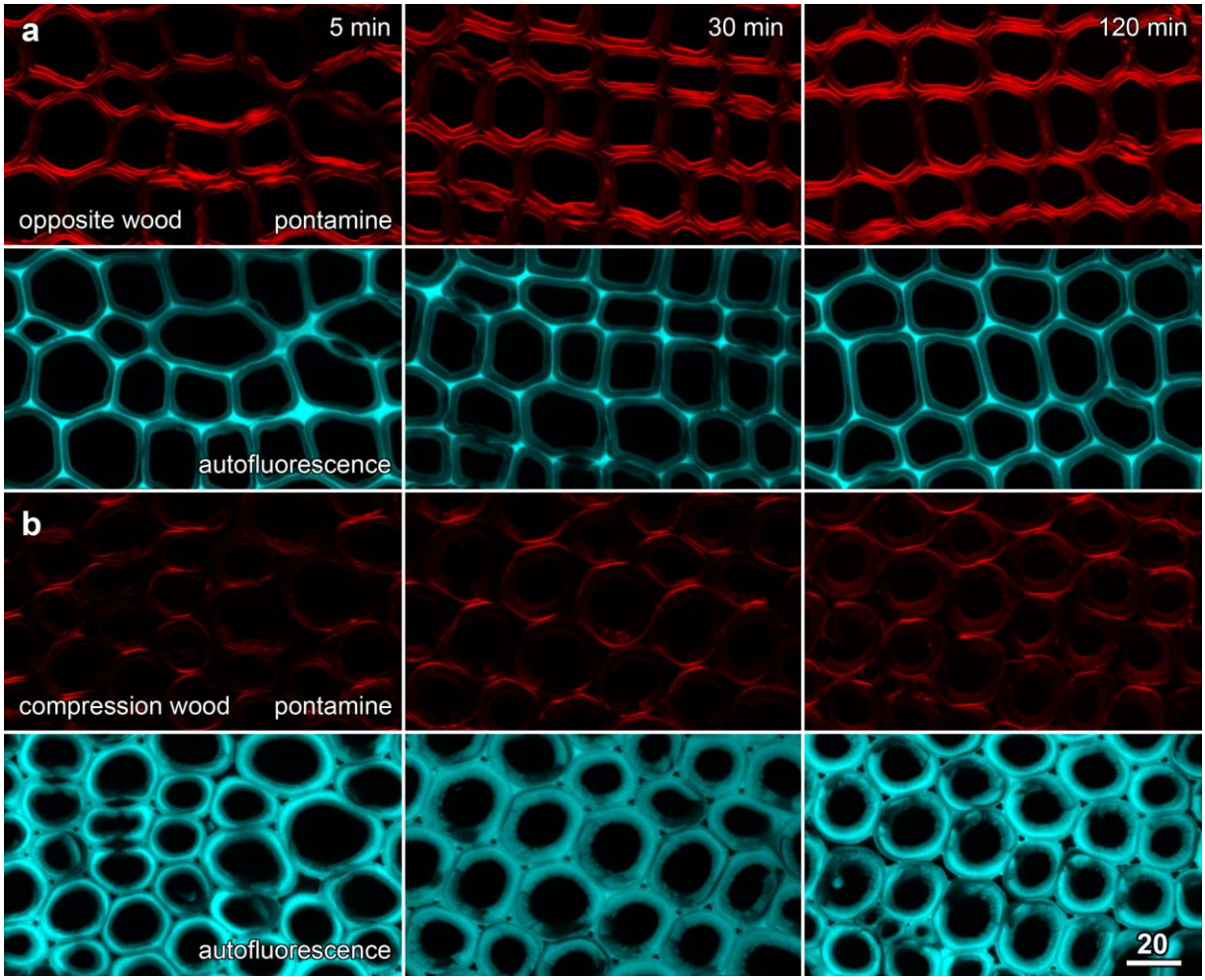

Figure 3.12 Increased P4B staining times did not modify P4B staining intensity or labelling patterns. Wood sections were stained for varying lengths of time and imaged under identical conditions using excitation at 561 nm for P4B and 405 nm for autofluorescence.

a. Opposite wood.

b. Compression wood.

Bar in **b** = 20 µm for all images.

3.3.4.6 Direct Red 23, a replacement for pontamine fast scarlet 4B

P4B is a red dye traditionally used in the textile industry (Bedrick, 1968) whose use with plant and fungal cell walls has been limited (Anderson et al., 2010; Hoch et al., 2005; Knight and Sutherland, 2011; Sun et al., 2011). P4B was initially sourced from Sigma-Aldrich Rare Chemical Library but by 2012, this supply had been exhausted. Direct Red 23, a chemical with the same molecular formula, weight and characteristics (Figure 3.13a, b) was also available from Sigma-Aldrich although surprisingly, these two chemicals were initially not cross-referenced within the company's catalogue. Wood stained with 0.1% (w/v) Direct Red 23 gave similar labelling patterns and fluorescent properties to P4B, both in opposite and compression wood (Figure 3.13c,d).

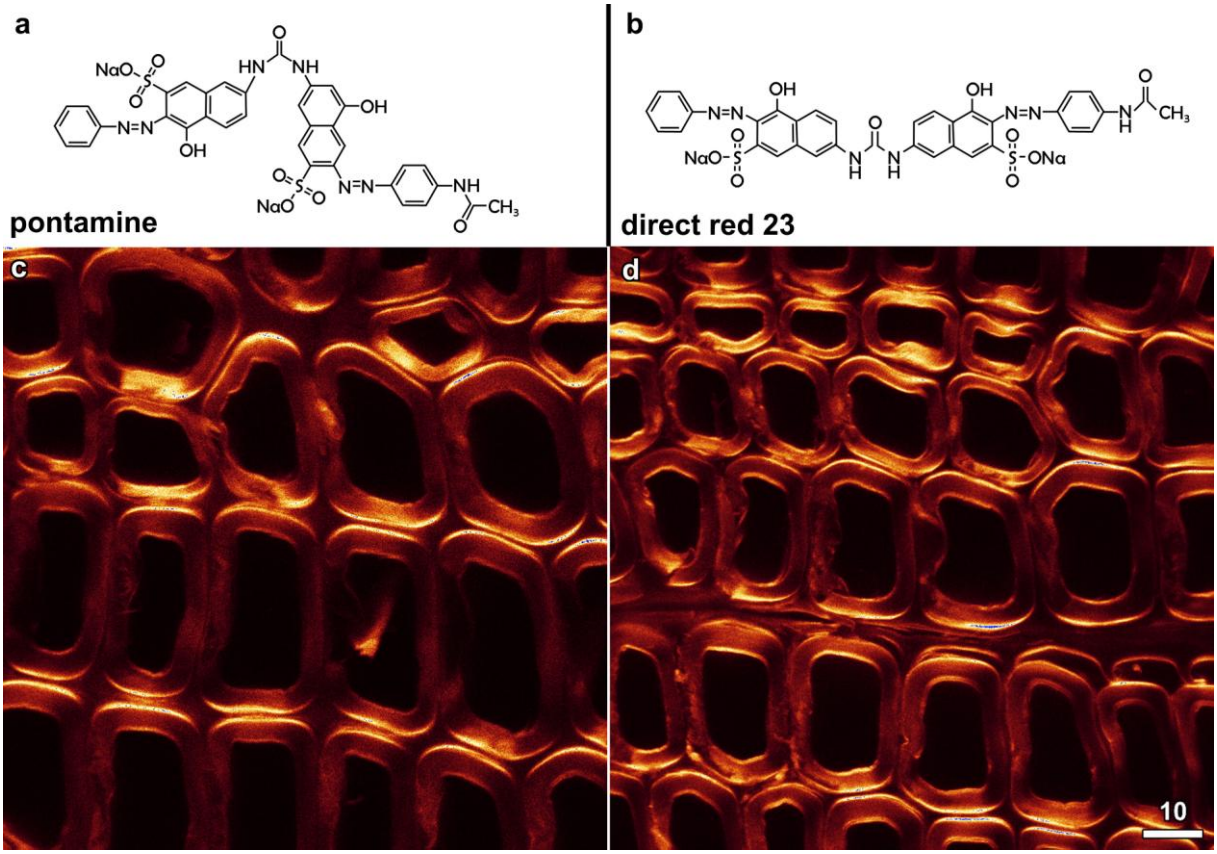

Figure 3.13 Direct Red 23 provides a suitable alternative for P4B. Direct red staining gave similar fluorescence labelling intensities and patterns to P4B.

a, **b.** The chemical structures for P4B (**a**) and Fast Red 23 (**b**) modified from the structures shown in the Sigma-Aldrich website.

c, **d.** Labelling of cells walls in opposite wood by P4B (c) and Fast Red 23 (d).

Bar in **d** = 10 µm for **c** and **d**.

3.3.5 P4B stains the S1 and S3 cell walls

The localisation of P4B fluorescence from both opposite and compression wood was analysed with sequential scanning at 405 and 561 nm, recording lignin autofluorescence from 420 to 480 nm along with P4B fluorescence from 570 to 650 nm, and observed that P4B showed a localisation pattern distinct from that of lignin and other characterised cell wall stains (Figure 3.14). In opposite wood, lignin autofluoresced in the middle lamella, and also in a weaker band on the lumen side of the S2 layer (Figure 3.14a,b, middle panel).

By contrast, P4B fluorescence was found in a narrow band immediately adjacent to the middle lamella and also in a similar narrow band, again on the lumen side of the S2 layer (Figure 3.14a, left panel). Overlay images (Figure 3.14a, right panel with P4B in red and lignin in cyan) suggested that the autofluorescence and P4B bands in S2 layer near to the lumen were not congruent. This was confirmed using line intensity traces which demonstrated that the inner P4B band was located marginally inside the band of lignin autofluorescence (Figure 3.14e,f). These line traces also showed that the band adjacent to the middle lamella was approximately 500 nm in width, with the band next to the tracheid lumen about 1 µm in thickness.

In compression wood, lignin autofluorescence was strongest from the S2L layer and not from the middle lamella while P4B fluorescence was generally weaker than in opposite wood but again derived from two bands adjacent to the middle lamella and internal to the S2L (Figure 3.14c). Line intensity profiles demonstrated that the P4B layer adjacent to the tracheid lumen was at the inner margin of the S2L region showing lignin autofluorescence, and that the bands were similar in width to those found in opposite wood (Figure 3.14g,h). Under similar imaging conditions, P4B-free controls showed only limited red fluorescence in opposite (Figure 3.14b and compression wood (Figure 3.14d).

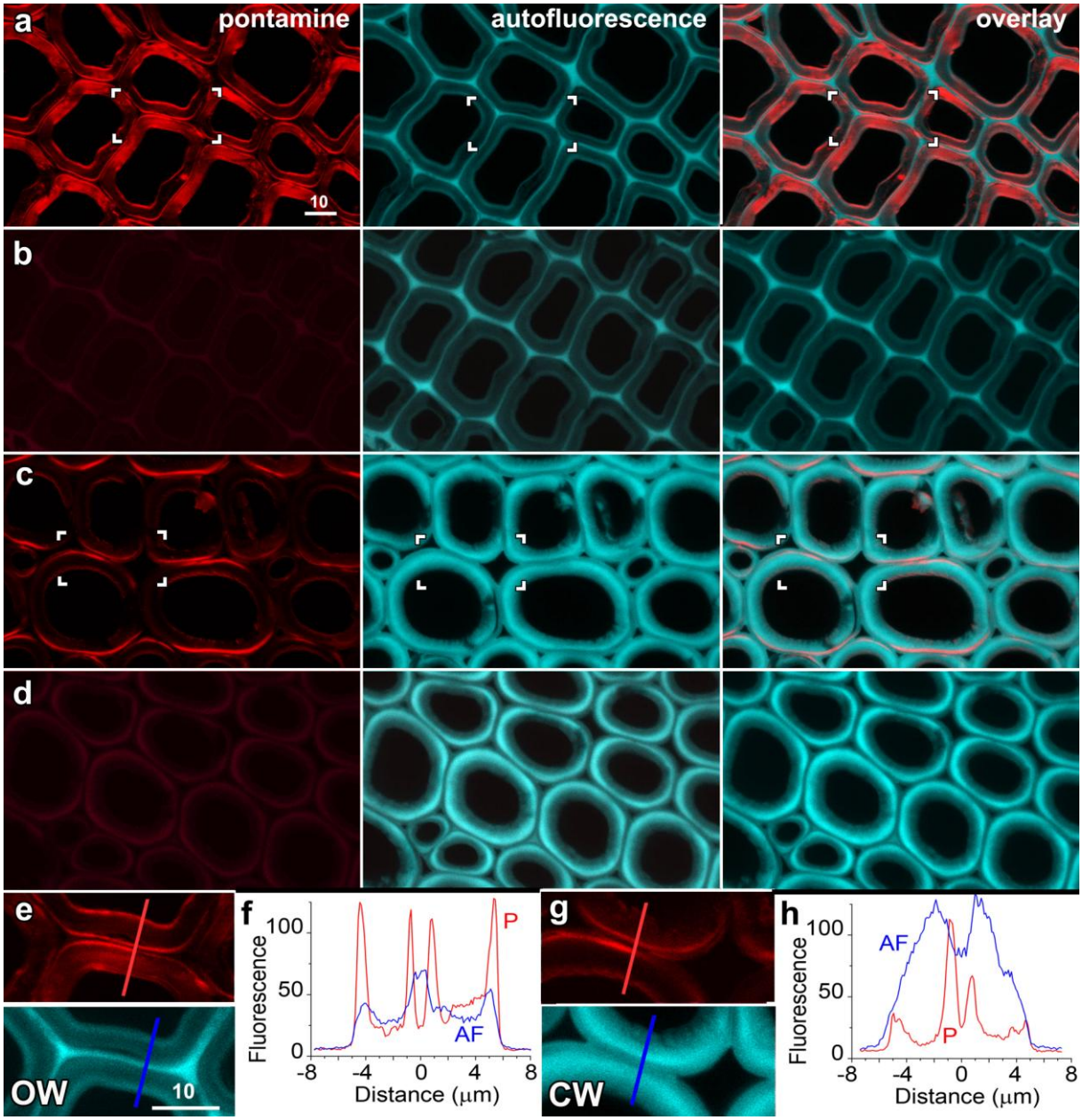

Figure 3.14 P4B stains the S1 and S3 wall regions. Lignin autofluorescence (middle column, and cyan in overlay at right) and P4B fluorescence (left column, and red in overlay) are shown as single confocal optical sections.

a. Opposite wood.

b. Opposite wood unstained control.

c. Compression wood.

d. Compression wood unstained control.

e,**g.** Enlargements of the boxed regions in **a** and **c**, showing P4B and lignin fluorescence for opposite (**e**, OW) and compression wood (**g**, CW).

f,**h.** Line scans for opposite and compression wood (at locations indicated in **e**,**g**) with P4B (P) in red and lignin autofluorescence (AF) in blue.

Bar in **a** = 10 µm for **a**-**d**; bar in **e** = 10 µm for **e**,**g**.

3.3.5.1 Correlative microscopy

Confocal fluorescent images of opposite and compression wood were correlated with scanning electron micrographs of the same cells (from opposite faces of a single cut of the same block) to confirm where P4B labelled in the wall (Figure 3.15). Low magnification cross sections of SEM and fluorescence images of the same cells (Figure 3.15a,c) confirmed that identical cells were imaged. Higher magnification images of the individual cells (Figure 3.15b,d) showed the compound middle lamella (M) and the S1, S2 and S3 layers in opposite wood (Figure 3.15b, left) and M, S1 and S2L regions in compression wood (Figure 3.15d, left). Similar high magnification confocal images confirmed P4B fluorescence from the S1 and S3 regions in opposite wood (Figure 3.15b, middle), and S1 and inner S2 fluorescence in compression wood (Figure 3.15d, middle), that made concentric bands that matched with the corresponding SEM images. Concurrent images of autofluorescence (Figure 3.15d, right) showed increased lignin in the S2L region of compression wood. Therefore, the two bands of P4B labelling are attributed to the S1 and S3 layers of opposite wood, and the S1 and inner S2 layers of compression wood. This is consistent with previous observations by polarised light (Frey-Wissling, 1976; Wardrop and Dadswell, 1953) and electron microscopy (Butterfield and Meylan, 1980; Maurer and Fengel, 1991).

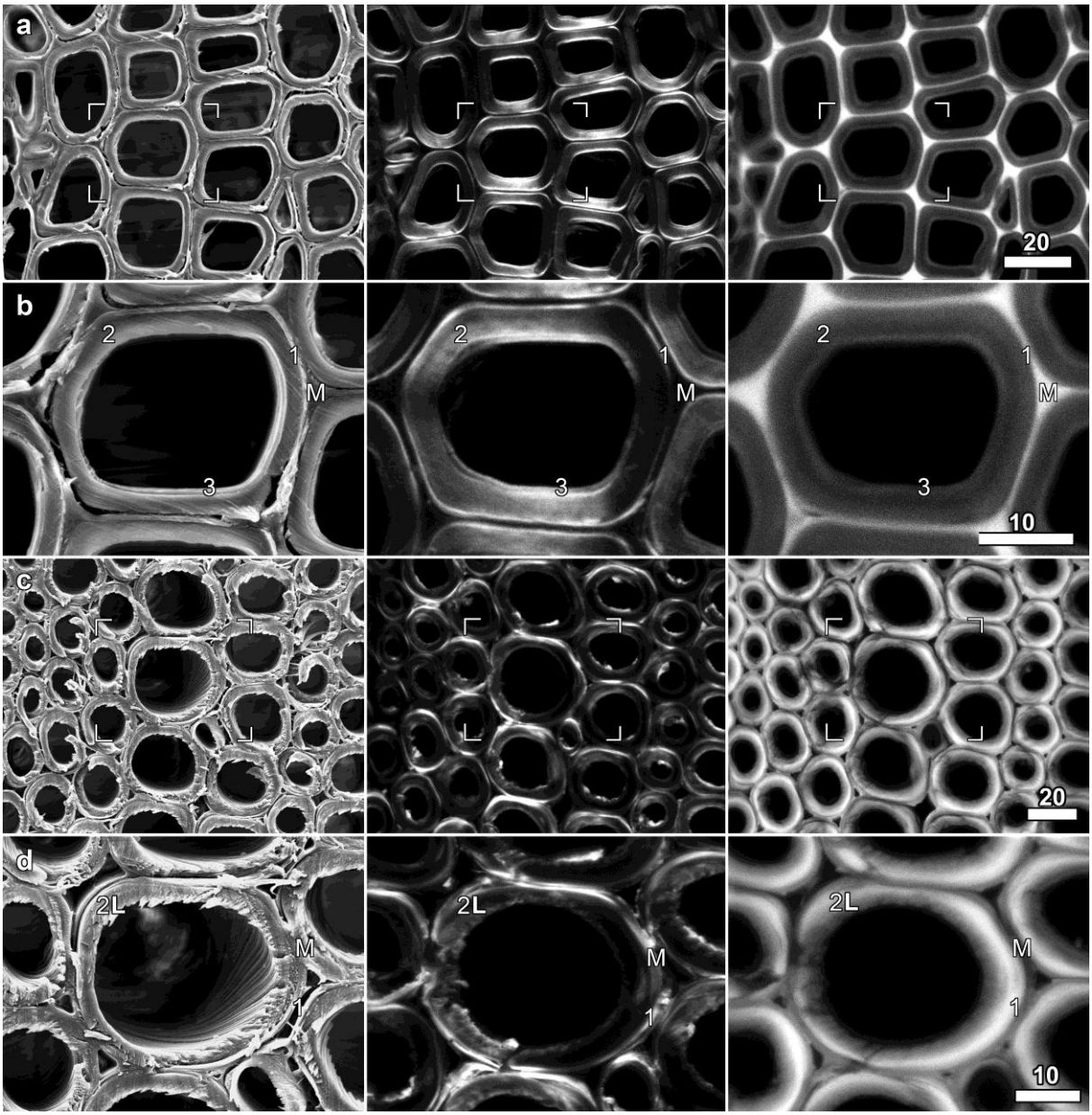

Figure 3.15 Correlative microscopy confirmed the location of P4B fluorescence in the cell wall. Samples were imaged by scanning electron (left column), and confocal microscopy of P4B labelling and lignin autofluorescence (middle and right columns). Images were collected from opposite faces of a single cut. Low magnification (**a**,**c**), and the individual cells (boxed in **a**,**c**) at higher magnification (**b**,**d**).

- **a**, **b.** Opposite wood. Distinct wall layers were visible in electron micrographs including the middle lamella (M) and the S1, S2 and S3 layers (1,2 and 3 respectively),
- **c**, **d.** Compression wood. Distinct wall layers were visible including the S2L region of compression wood (2L).

Bars in **a**,**c** = 20 µm; bars in **b**,**d** = 10 µm.

3.3.5.2 P4B staining is bifluorescent

One notable feature of P4B staining is that specific cell wall regions within individual tracheids fluoresced more brightly than others. For example, in Figure 3.14a the radial walls (lower and upper walls) of mature tracheids fluoresced more strongly. This spatial variation in fluorescence suggested that P4B was bifluorescent, with the intensity of light absorption by the dye, and thus of fluorescent emissions, being determined by the orientation of the cell wall-bound dye molecules relative to the polarisation of the light used for excitation (Frey-Wissling, 1976). This effect has previously been observed in Congo red where ordered arrays of cellulose microfibrils present Congo red towards the excitation light in a regular pattern, and where the analysis of fluorescence intensities derived from different excitation polarisations have revealed the microfibril angle within the walls of various plants (Jang, 1998; Suslov et al., 2009; Verbelen and Stickens, 1995).

It was first demonstrated that absorbance of light by P4B-stained walls is polarisation dependent. When viewed with brightfield optics, tracheid walls in opposite wood were evenly labelled (Figure 3.16a), and images recorded with a CCD camera were identical when the sample was rotated through 90^{o} using a rotatable stage (Figure 3.16b). When viewed with plane polarised light, however, cell walls that were parallel to the orientation of the polarised light absorbed more strongly and appeared to be redder than cell walls perpendicular to the light. Thus, when the sample was rotated through 90^{0}, the pattern of staining changed from the radial to tangential walls (Figure 3.16c,d). When an analyser was used to select polarised light after transmission through the sample, walls parallel to the filter appeared red (Figure 3.16e,f) although this labelling would likely be confounded, in part, by birefringence of the cell walls themselves. This patterning was also apparent using polarisation optics when the polariser and analyser are crossed to cause extinction of background light (Figure 3.16g,h).

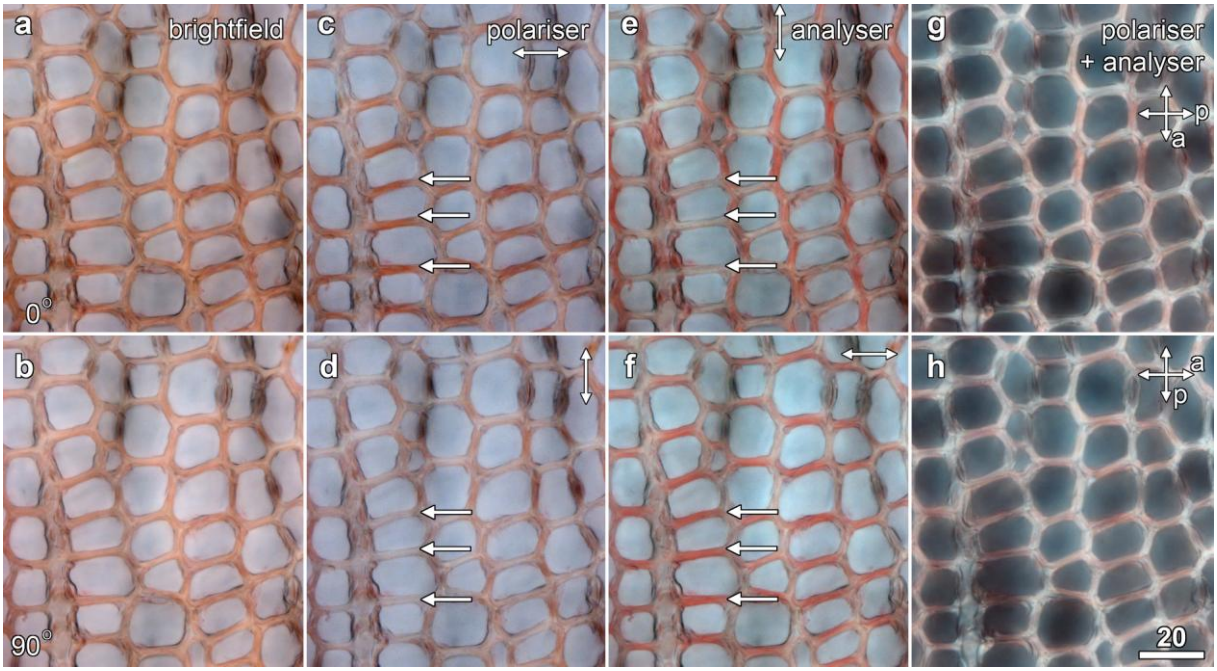

Figure 3.16 P4B-stained opposite wood showed polarisation-dependent colours. The sample was photographed in one orientation (top row), and re-photographed after rotation through 90° with this image rotation corrected in the figure (bottom row).

a,**b.** Brightfield optics.

c,**d.** Incident light polarised (direction indicated with arrows).

e,**f.** Transmitted light polarised with analyser.

g,**h.** Polariser and analyser crossed to extinction.

Bar in **h** = 20 µm for all images.

The bifluorescence of P4B in opposite wood was then investigated by confocal microscopy, and compared to observations of bifluorescence generated by Congo red and calcofluor white (Figure 3.17). As it was not possible to effectively rotate the polarisation of the excitation lasers on the confocal microscope, measurements of bifluorescence were made by rotating samples on the stage through 90^0, with careful attention paid to keeping identical focal planes. P4B labelled radial walls when the stage was oriented at 0^0 and tangential walls were labelled when oriented at 90^0, clearly demonstrating bifluorescence (Figure 3.17a). Corresponding lignin autofluorescence images, however, were identical which is emphasised in the overlay image where identical cyan and red signals sum to give a grey-scale image (Figure 3.17b). Bifluorescence was also seen in P4B-stained compression wood (Figure 3.17c).

These experiments were extended to look at opposite wood stained with 0.1% Congo red (Figure 3.17d) and 0.01% calcofluor white (Figure 3.17e). Both dyes showed labelling of the S1 and S3 layers, and bifluorescence. However, increased labelling in the S2 layer was observed with these dyes, which suggests that P4B labelling is more specific than Congo red or calcofluor.

This was confirmed by quantifying fluorescence patterns from the different stains, and measuring axiality ratios (Suslov et al., 2009). This ratio was defined as the fluorescence intensity collected when the excitation light was polarised parallel to the radial walls divided by the intensity when excitation was parallel to the tangential walls. Autofluorescence measured from line intensity scans through the middle lamella was unaffected by sample rotation, with the ratios between 1 and 1.20 confirming a lack of bifluorescence. For the cell wall-staining dyes, however, axiality ratios measured from the intensity scans through the S3 layer ranged between 2 and 4, confirming bifluorescence (Table 3.4). Further, the axiality ratio was highest for P4B verifying that P4B labelling is more specific than the other dyes.

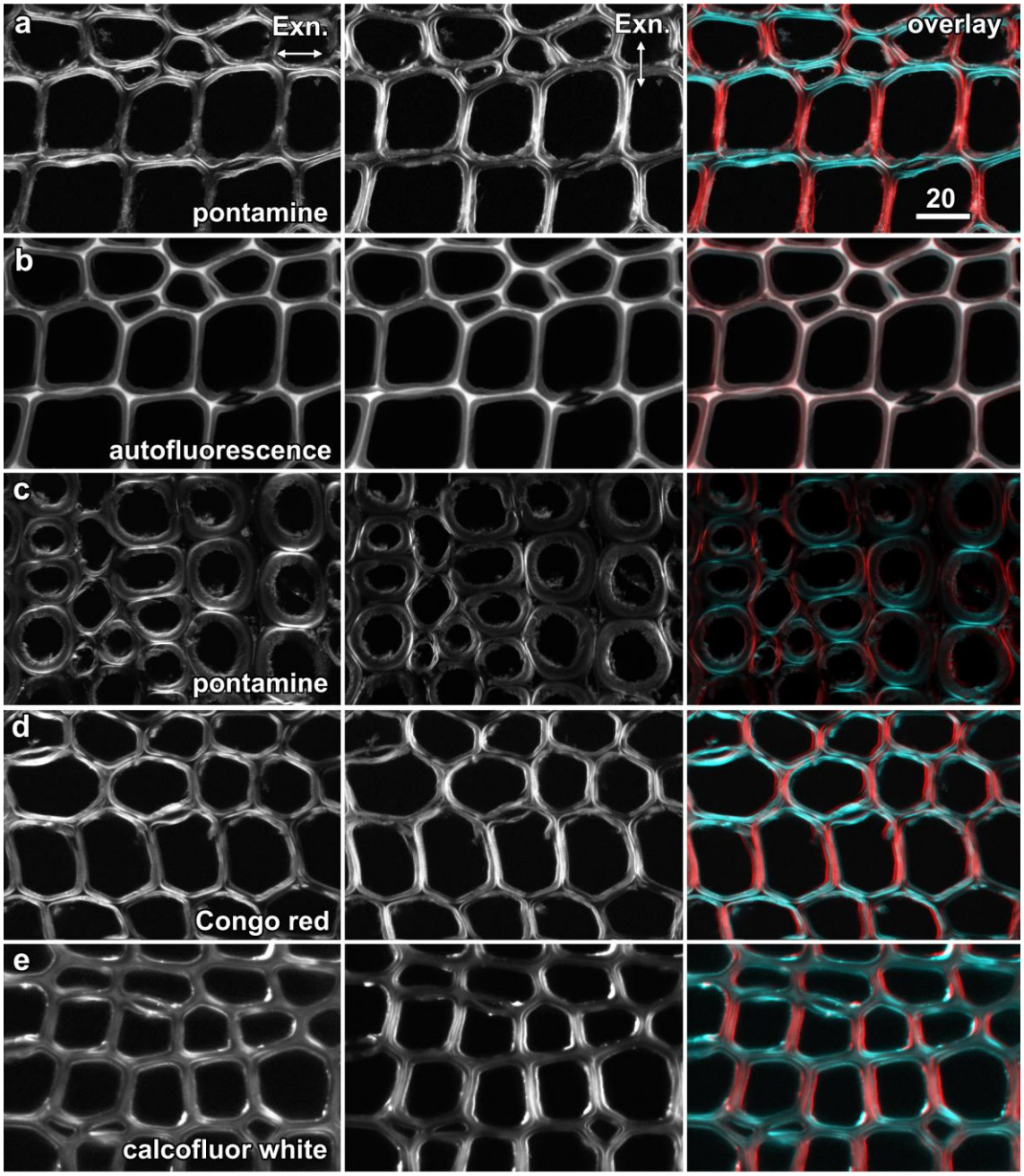

Figure 3.17 P4B is bifluorescent. Laser excitation (Exn.) in the horizontal (left, cyan in overlay) and vertical planes (centre, red in overlay). Areas of equal intensity (a lack of bifluorescence) appear white in the overlay.

a. P4B demonstrating strong bifluorescence in opposite wood.

b. Lignin autofluorescence, collected concurrently with the images in **a**, was not bifluorescent.

c. Compression wood also showed bifluorescence.

d. Congo red demonstrated weak bifluorescence in opposite wood.

e. Calcofluor white demonstrated weak bifluorescence in opposite wood.

Bar in **a** = 20 µm for all images.

Table 3.4. Axiality ratios measured for cell wall stains.

	n [1]	Dye ratio [2]	Autofluorescence ratio [3]
P4B	4	3.92 ± 0.32	1.17 ± 0.07
Congo red	4	2.02 ± 0.22	1.03 ± 0.06
calcofluor white	3	3.05 ± 0.36	1.14 ± 0.01

[1] Replicate slices; averaged ratios were calculated for 20 or more cell walls per slice, and averaged.

[2] Ratio of fluorescence emissions from a single location with excitation polarisation rotated through 90^{o}. Values measure from centre-weighted line traces along the radial axis of sections, measuring intensities in the S3 layer.

[3] Ratio of fluorescence emissions within the middle lamella with excitation polarisation rotated through 90^{o}.

3.3.5.3 P4B stains unlignified cell walls

The poor P4B labelling of the S2 layer in opposite and compression wood was investigated and found to be, in part, due to the presence of increased lignification. Line intensity scans (Figure 3.14f,h) demonstrated that locations with strong P4B labelling such as the S1 layer contained reduced lignin. This correlation was confirmed in three specific cases where cell walls have reduced levels of lignin. As tracheids matured after their formation in the vascular cambium, their secondary walls were lignified, initially from the cell corners and then progressively through the compound middle lamella and the inner S2 layer (Atalla, 2005; Donaldson, 2001) (Figure 3.18a). During lignification, P4B labelling changed from an even pattern throughout the wall to the distinct pattern found in mature tracheids (Figure 3.18a inset). Moreover, colour transmitted light images showed that the developing tracheids stained red whereas comparatively little staining was present in mature cells (Figure 3.18a) although staining was inconsistent with the equal levels of fluorescence visible in all cells. Ray cells which contained little lignin autofluorescence were also imaged but with extensively labelled with P4B labelling (Figure 3.18c). Similar observations were made in the unlignified parenchyma cells surrounding resin canals (Figure 3.18c, arrow in inset). Controls demonstrated that the red staining and fluorescence were dependent on P4B in the cambium, ray cells (Figure 3.18b) and in the parenchyma cells adjacent to resin canals (Figure 3.18d).

3.3.6 Changes in microfibril angle around bordered pits

A pit is a recess in the secondary wall which opens to the lumen to provide inter-cell exchange of liquids between adjacent cells. Usually, a pit on one cell (tracheid) has a matching complimenting pit on the adjacent cell to make a ‘pit pair’. Bordered pits connect the longitudinal tracheids through pit cavity towards the cell lumen. Many studies have reported that there are local variations in microfibril angle around bordered pits (Anagnost et al., 2002; Sedighi-Gilani et al., 2005; 2006). Sedighi-Gilani et al. (2005) noted that the microfibril angle of the radial tracheid wall was highly non-uniform and had a near circular form of arrangement around the bordered pits. These variations in microfibril angle should, therefore, be observable with P4B bifluorescence.

In Figure 3.19a-d, confocal optical sections show 3 bordered pits that lay almost parallel to the polarisation of the excitation laser resulting in good, but varying, P4B fluorescence (arrowheads). As the pit aperture opens, the fluorescence varied dramatically among these optical sections, which were 2 µm apart, due to the variation in microfibril angle around the aperture. These observations, covering a depth of 6 µm, confirmed that the microfibril angle around the pits varies, which is consistent with previous reports (Anagnost et al., 2002; Sedighi-Gilani et al., 2005; 2006). They also revealed that the S1 and S3 layers of the pit border show similar fluorescence to the tracheid wall.

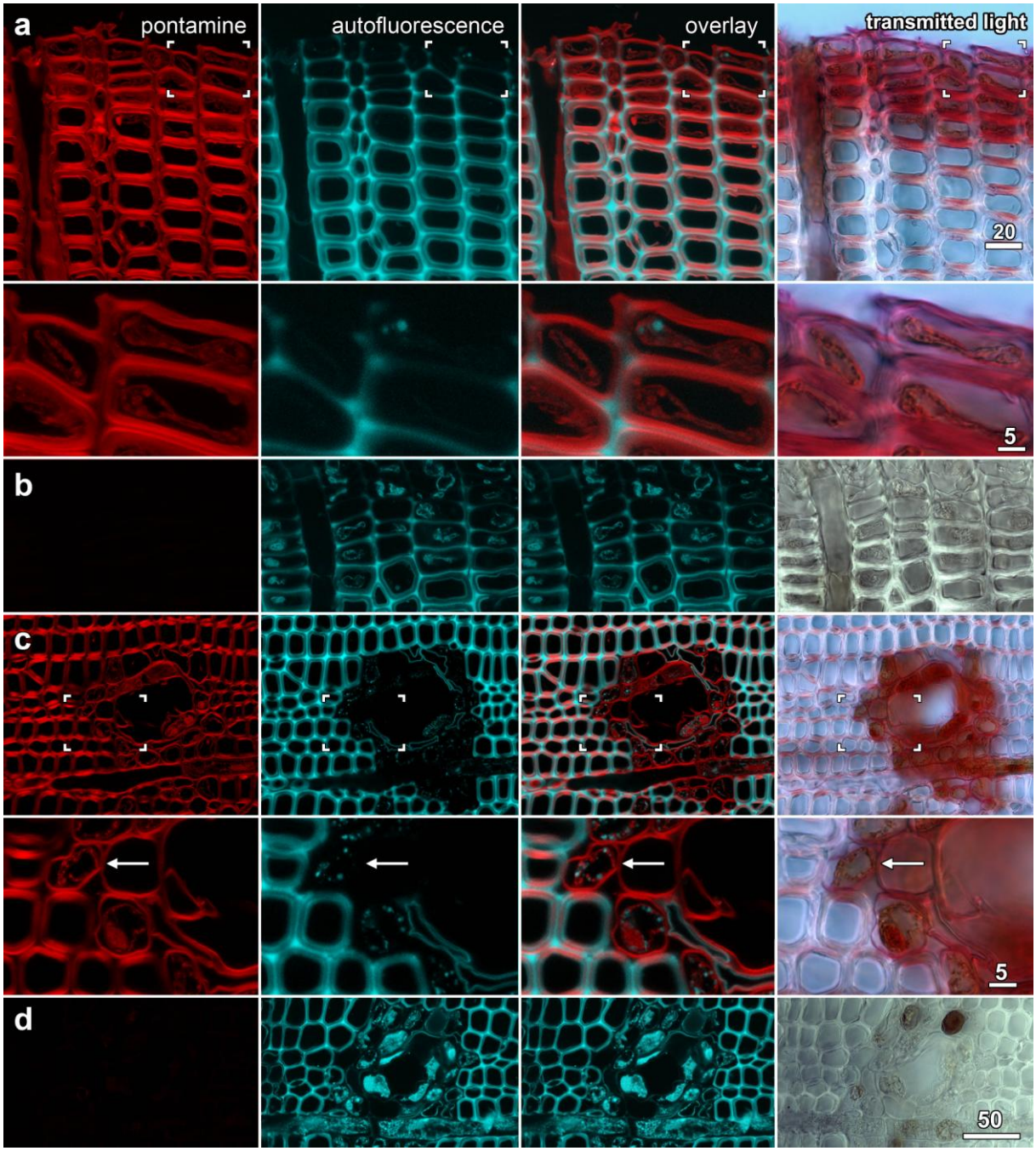

Figure 3.18 P4B fluorescence and staining was reduced by the presence of lignin. Images show confocal optical sections of P4B fluorescence (left column, red in overlay) and lignin autofluorescence (second column, cyan in overlay), and colour transmitted light images (right column).

a. P4B-stained cambial section. Inset shows the boxed region at a higher magnification.

b. An unstained cambial section.

c. A resin canal in a P4B-stained section, with the inset showing the boxed region at a higher magnification. Two adjacent walls stained in their entirety with P4B are indicated (arrows).

d. An unstained section through a resin canal.

Bar in **a** = 20 µm for **a**,**b** with bar in inset = 5 µm; bar in **d** = 50 µm for **c**,**d** with bar in inset = 5 µm.

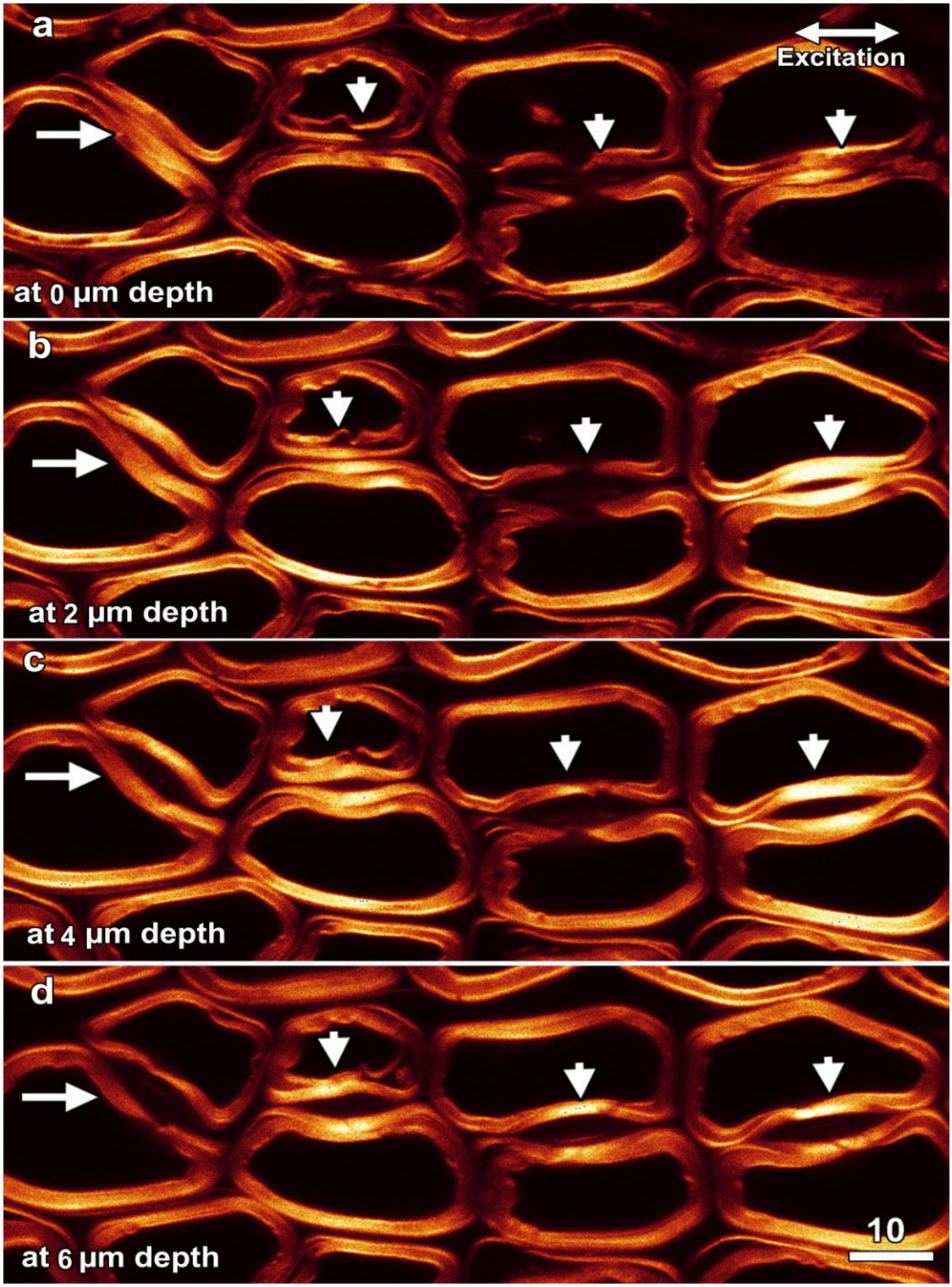

Figure 3.19 The organisation of cellulose microfibrils changed around bordered pits, which is evident from differential P4B labelling. Three bordered pits (arrow heads) which were nearly parallel to the incident light show varying P4B labelling due to the variation of microfibril angle around the pit border. A fourth pit at an angle about 45^0 (arrow) shows reduced fluorescence proving the importance of incidence angle.

a. At the sample surface.

b. At a depth of 2 µm into the sample.

c. At a depth of 4 µm into the sample.

d. At a depth of 6 µm into the sample.

Bar in **d** = 10 µm for all images.

3.3.7 Observing and measuring microfibril orientation

Because P4B shows bifluorescence, it can be used to measure the orientation of cellulose microfibrils in the different cell wall layers. This approach has previously been used with the dye Congo red to measure average cellulose orientation in the primary wall of expanding plant organs (Suslov et al., 2009; Verbelen and Kerstens, 2000; Verbelen and Stickens, 1995) and the secondary cell walls of tracheids (Bergander et al., 2002; Jang, 1998; Sedighi-Gilani et al., 2005). However, as P4B gives better staining of the S1 and S3 layers, notably in opposite wood, P4B was investigated to determine whether it could be used to measure the microfibril angle in these wall layers. This approach was first attempted in compression wood where the angle of the cellulose microfibrils in the inner S2 layer of compression wood tracheids matches the angle of the striations in this layer. Thus, the angle of the cellulose microfibrils can be determined indirectly by determining the angle of the striations of the inner S2 layer (Figure 3.20).

Direct measurements of the striations in two cells (labelled 1 and 2 in Figure 3.20a) showed microfibril angles for these two cells of 44^0, while a clockwise rotation of the sample on the microscope stage caused an initial increase in fluorescence in cell 1 and a decrease for cell 2 (Figure 3.20b,c). When plotted, fluorescence intensities for the cells gave the expected sinusoidal distribution, and the equation of best fit gave microfibril angles of 37^0 and 40^0 for cells 1 and 2 respectively matching the direct observations (Figure 3.20d). This conforms to the equation:

$$F = A \cos^2 (P - \theta) + F_{min}$$

where F is fluorescence intensity, A is the amplitude of intensity variation, P is the angle of incident/excitation polarisation, θ is the phase angle and a measure of the microfibril angle, and F_{min} is the background fluorescence (Bergander et al., 2002; Jang, 1998).

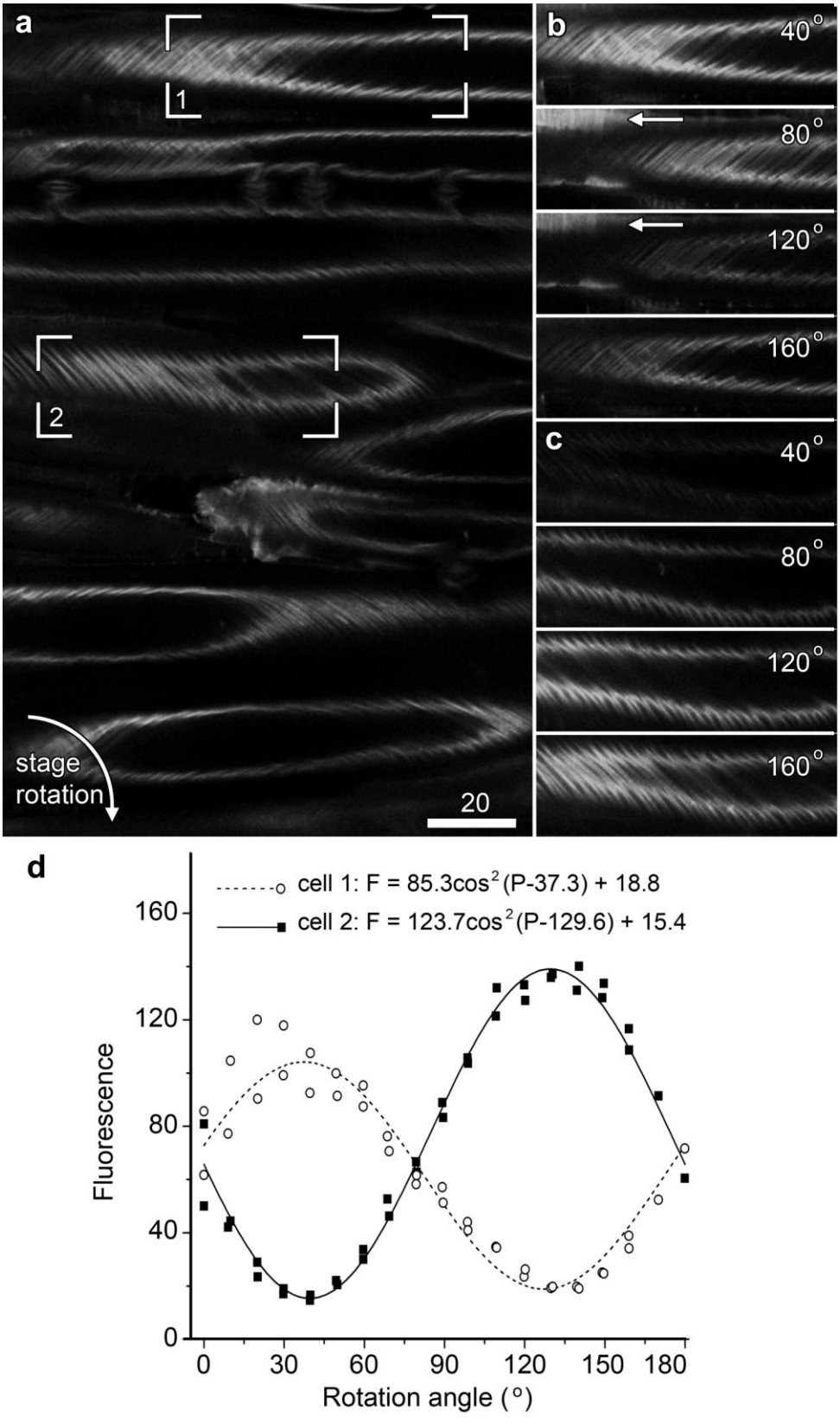

Figure 3.20 Measurements of P4B bifluorescence confirm direct observations of microfibril angle in compression wood.

a. A single confocal optical section of a longitudinal section in which the striations of the inner S2 layer were readily visible. Their orientation is known to correspond to the S2 microfibril angle. Two cells (boxed; 1 and 2) were studied further.

b,c. The longitudinal section was rotated through 180^{o}, as indicated by the arrow in **a**, with images recorded every 10^{o}. Images were aligned manually, and the boxed cells shown at four further rotations. The focal plane varied slightly between images because of the manual rotation mechanism. Arrows in **b** indicate transversely aligned microfibrils in the S1 layer of this cell.

d. Fluorescence from the cells was quantified from line intensity traces along the cells' lengths, measuring the average staining intensity (F) of the microfibril bundles. Microfibril angle varied with the incidence angle, P.

Bar in **a** = 20 µm for **a-c**.

3.3.8 P4B fluorescence is incident angle dependent

P4B fluorescence, however, was also visible from the S1 layer of compression wood and can be used to investigate the organisation of cellulose in that layer. The transverse organisation of the S1 layer was observed when the sample was rotated into a suitable orientation (Figure 3.20b, arrows) and investigated further. Compression wood was imaged and optical sections at different depths were recorded through the walls between two adjacent tracheids. The inner S2 layers of the adjacent cells show striations (bundled microfibrils) in opposed directions (Figure 3.21a), but in the gap between the striations, transverse cellulose was present (overlay in Figure 3.21a). Imaging in the vertical plane (XZ sectioning though image reconstruction) confirmed that this transverse cellulose lay in the S1 layer (Figure 3.21b). It was also observed that the S2 striation pattern was visible in lignin autofluorescence (Figure 3.21a middle column).

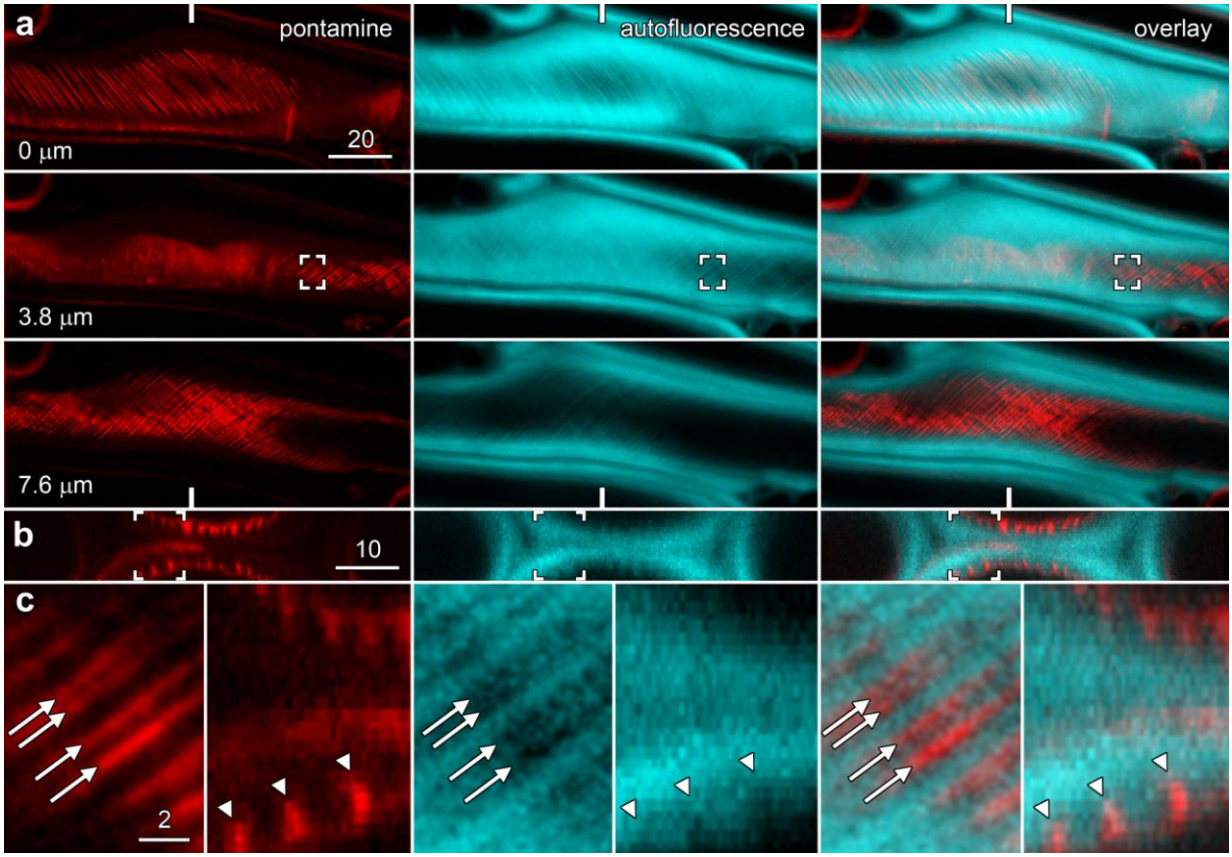

Figure 3.21 The organisation of the S1 layer was visible in longitudinal sections of compression wood.

a. Optical sections collected with concurrent imaging of P4B (red) and autofluorescence (cyan) at different heights within compression wood revealed striations running in one direction (top image), transversely-oriented microfibrils in the S1 layer (central image, at a depth of 3.8 µm compared to the top image) and striations running in the reverse direction adjacent to the lumen of a second tracheid (lower image).

b. Computer-generated cross section through the tracheids in the plane boxed in **a**. The S1 layer observed in **a** was confirmed to lie between the inner S2 striations, although individual S1 layers from the two tracheids were not resolved.

c. Enlargement of the regions boxed in **a** (left) and **b** (right). The striations visible in the autofluorescence images were out of phase with the P4B striations, and lay in between the bands stained with the dye. In the cross section, the P4B-labelled striations matched regions showing reduced lignin autofluorescence (arrow heads).

Bar in **a** = 20 µm, **b** = 10 µm and in **c** = 2 µm.

However, the banding in the lignin and P4B images were out of phase, so that a band of lignin fluorescence was observed between the P4B striations (Figure 3.21c arrows). When scanned in the z-direction, it was apparent that the lignification was present at the base of the striation ridges (Figure 3.21b & 3.22c arrowheads).

The angle dependence of the P4B fluorescence from the S2 layer was evident through the differential fluorescence seen in images collected at different incident angles (0 to 180^0, Figure 3.22a-e). However, the angle of excitation had no effect on lignin autofluorescence which was similar at different incident angles (Figure 3.22f). A similar effect was seen in the wall layers of opposite wood as it was rotated although no S2 striations were present (Figure 3.23).

3.3.9 Why don't the S2 microfibrils fluoresce?

It was established that in transverse sections, P4B labels the cellulose microfibrils in the S1 and S3 layers in opposite wood, and the S1 and inner S2 regions in compression wood (Figure 3.14). However, the labelling in the S2 layer in transverse sections of both opposite and compression wood was negligible. Possible reasons for this effect could include:

Accessibility: Microfibrils in S2 region are closely arranged to form a highly dense lignin-cellulose matrix (Booker and Sell, 1998; Walker and Butterfield, 1993). It is possible that the dye molecules are unable to access the cellulose microfibrils for any effective labelling. Evidence for this argument includes the reduced labelling of P4B in highly lignified compression wood wall layers compared to the latewood tracheids in the opposite wood region. The higher labelling by P4B of the cambial cells, and the parenchyma cells in rays and resin canals that have lower levels of lignification, supports this argument (Figure 3.18). By comparison, the cellulose microfibrils are more loosely arranged in S1 and S3 layers providing opportunity for the dye molecules to label the cellulose microfibrils.

Penetrability: Due to the dense lignification and higher thickness of the S2 layer compared to the S1 and S3 layers, the complex lignin-cellulose-hemicellulose matrix hinders penetration of the dye molecules and binding with the cellulose microfibrils. This argument is subtly different from (but related to) the accessibility issue described in point 1.

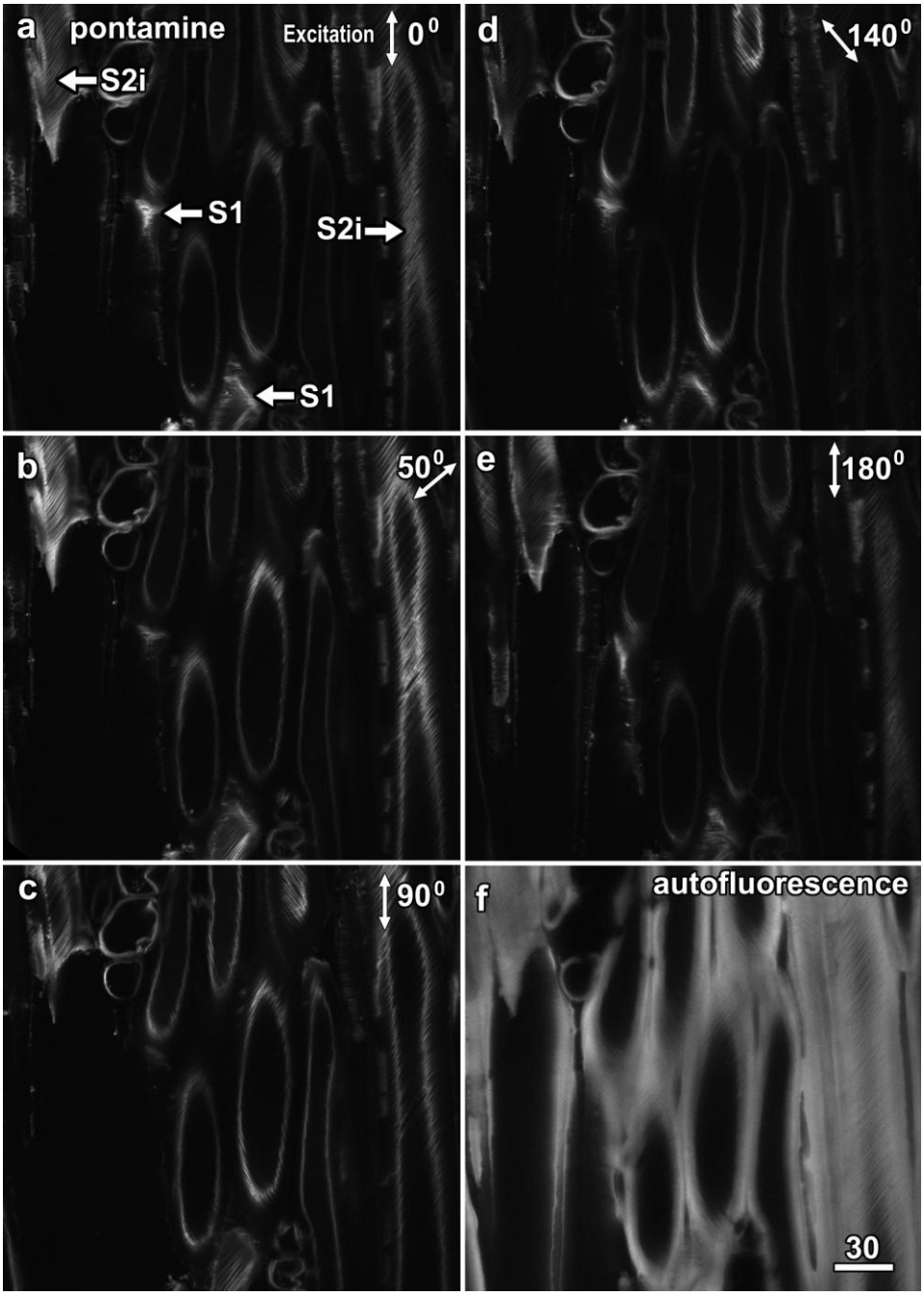

Figure 3.22 P4B fluorescence was dependent on the polarisation angle of the excitation light. Only the microfibrils oriented parallel or near parallel to the excitation light showed P4B labelling in compression wood.

a-e. Variations in P4B fluorescence due to stage rotation angles of 0^o, 50^o, 90^o, 140^o and 180^o that modified the relative polarity of the excitation light.

f. Autofluorescence collected concurrently was independent of incident angle. Only the image collected at 0^o is shown.

Bar in **f** = 30 µm for **a**-**f**.

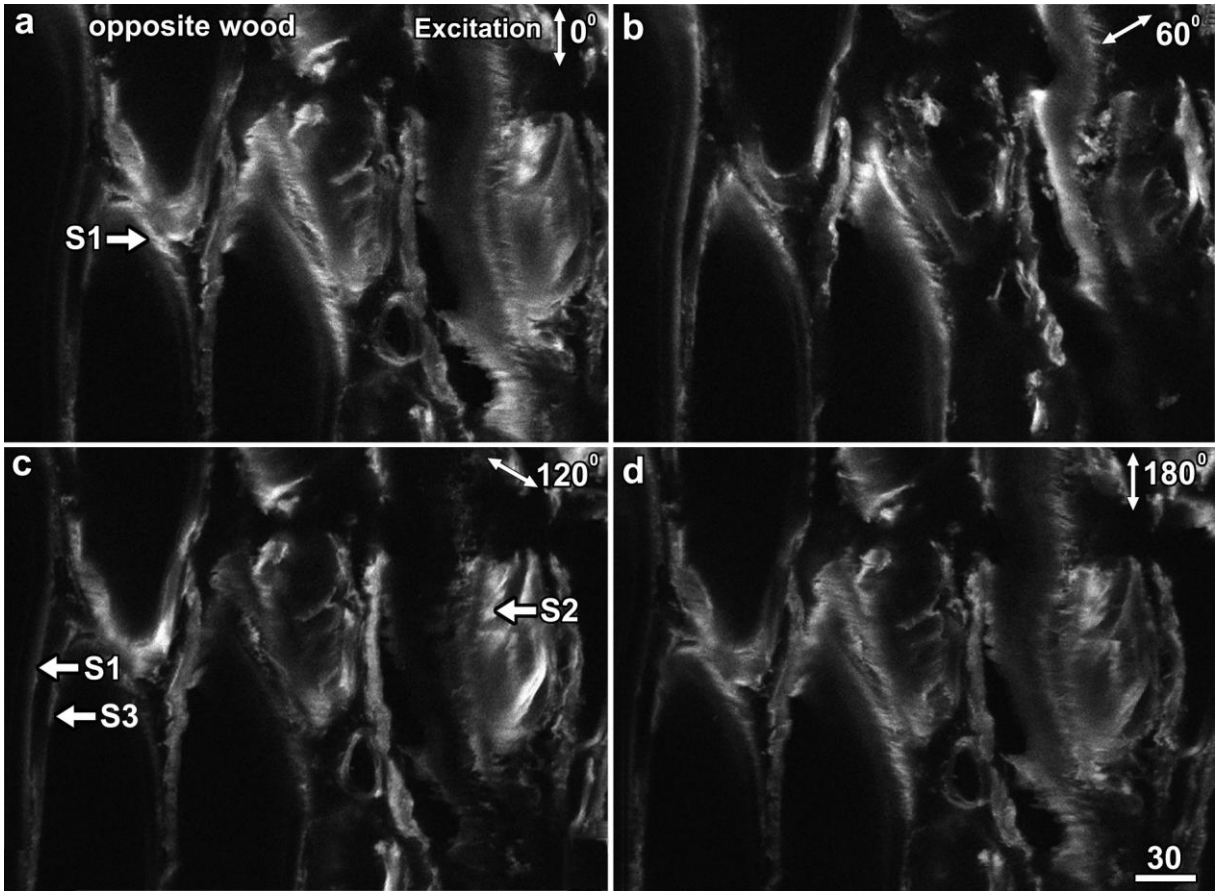

Figure 3.23 P4B fluorescence in S1 layer microfibrils was dependent on the polarisation angle of the excitation light. Only the microfibrils oriented parallel or near parallel to the excitation light showed P4B labelling in opposite wood.

a-d. Variations in P4B fluorescence due to stage rotational angles of 0^o, 60^o, 120^o and 180^o that modified the relative polarity of the excitation light.

Bar in **d** = 30 µm for **a**-**d**.

Microfibril angle: In opposite wood tracheids, the cellulose microfibrils in the S1 and S3 layers are arranged nearly orthogonal to the microfibrils in the S2 layer which in turn lie nearly parallel to the tracheid length (Booker and Sell, 1998) (Figure 1.1b). However the S2 microfibrils in compression wood can have an angle of up to 50^0. As P4B is bifluorescent, only the microfibrils parallel to the excitation light properly excite and fluoresce. In cross sections, the S2 microfibrils which run in a near vertical direction can only show limited fluorescence.

To determine whether higher lignification prevents P4B labelling of the S2 layer, the effects of cell wall delignification with glacial acetic acid and hydrogen peroxide on P4B labelling were investigated in both transverse (TS) and tangential longitudinal sections (TLS) of opposite and compression wood. These experiments revealed that wall lignification is not the only reason why P4B fails to label the S2 layer (Figure 3.24, 3.25). In transverse sections, opposite wood control sections showed both P4B labelling on to S1 and S3 layers (Figure 3.24a) and lignin autofluorescence (Figure 3.24b). In delignified samples, there was hardly any lignin autofluorescence (Figure 3.24h) and the increased P4B labelling was in similar patterns to controls, although the delignification process had caused some cell separation and enhanced labelling of the S2 layer (Figure 3.24g).

Because of the complex, bifluorescent nature of P4B's labelling, and the preferential fluorescence from microfibrils parallel to the polarisation of light, P4B labelling in longitudinal sections were also investigated in control and delignified material. Reconstructed transverse sections were calculated (Figure 3.24d,f,j,l) from optical stacks that had been collected with 0.5 µm steps through longitudinal sections where the cell axis was parallel with (Figure 3.24c,i) and perpendicular to the polarisation of the excitation laser (Figure 3.24e,k). In reconstructions through the opposite wood cells in which the S2 layer was parallel to laser polarisation, fluorescence from S1 and inner S2/S3 wall regions were seen in controls (Figure 3.24d) whereas the delignified sample showed strongly enhanced S2 fluorescence although this was not resolvable into individual microfibrils (Figure 3.24j). However, in reconstructions through cells where the S2 layer was perpendicular to the laser polarisation, only the inner S2/S3 regions were strongly fluoresced in controls (Figure 3.24f). The labelling in delignified samples however was strongly from the S2 regions as seen in the controls (Figure 3.24l).

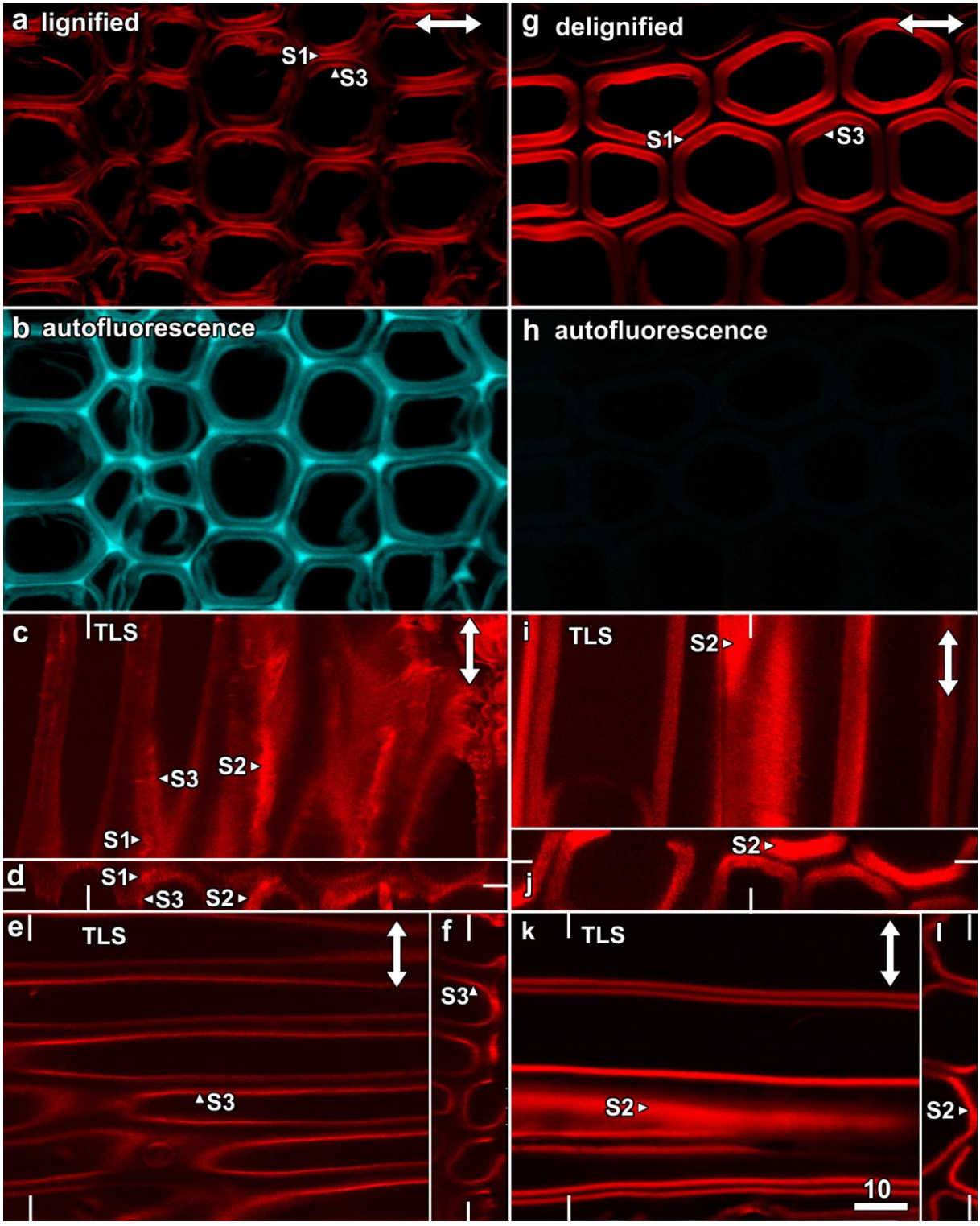

Figure 3.24 The effect of cell wall delignification on P4B labelling of the S2 layer in opposite wood. Delignification modified P4B labelling, but did this in a complex manner that was not directly visible in transverse sections (TS).

a. Opposite wood control TS, showing P4B fluorescence from the S1 and S3 layers.

b. Opposite wood control TS, showing lignin autofluorescence.

c. Tangential longitudinal section (TLS) where the tracheid axis and the S2 microfibrils were parallel to the laser excitation.

d. Reconstructed transverse section from optical stacks collected with 0.5 µm steps through the longitudinal sections shown in **c**. S1 and S2/S3 regions were visible.

e. TLS where the tracheid axis and the S2 microfibrils were perpendicular to the laser excitation by rotating the microscope stage 90^{o}.

f. Reconstructed transverse section from optical stacks collected with 0.5 µm steps through the longitudinal sections shown in **e**. The S3 and / or some part of the inner S2 layer were also visible. The S1 layer was not, however, visible.

g. TS of delignified opposite wood, showing P4B fluorescence.

h. TS of delignified opposite wood, showing hardly any lignin autofluorescence. The image was collected concurrently with the same settings that showed lignin autofluorescence in panel **b**.

i. TLS of delignified opposite wood, where the tracheid axis (S2 layer) was nearly parallel to the laser excitation.

j. Reconstructed transverse section of delignified opposite wood, from optical stacks collected with 0.5 µm steps through the longitudinal sections shown in **i**. Strong S2 fluorescence was seen.

k. TLS of delignified opposite wood, where the tracheid axis (S2 layer) was nearly perpendicular to the laser excitation by rotating the microscope stage 90^{o}.

l. Reconstructed transverse section from optical stacks collected with 0.5 µm steps through the longitudinal sections of delignified opposite wood, shown in **k**. There S1 and S3 fluorescence were not resolvable from a strong S2 labelling.

Bar in **k** = 10 µm for all images. Double headed arrows show the laser polarisation direction. White bars at the edges of panels **c**, **e**, **i** and **k** show the relative locations of the reconstructed planes (**d**,**f**,**j**,**l**), whereas the white bars in the reconstructions show the relative locations of the optical sections shown (**c**,**e**,**i**,**k**).

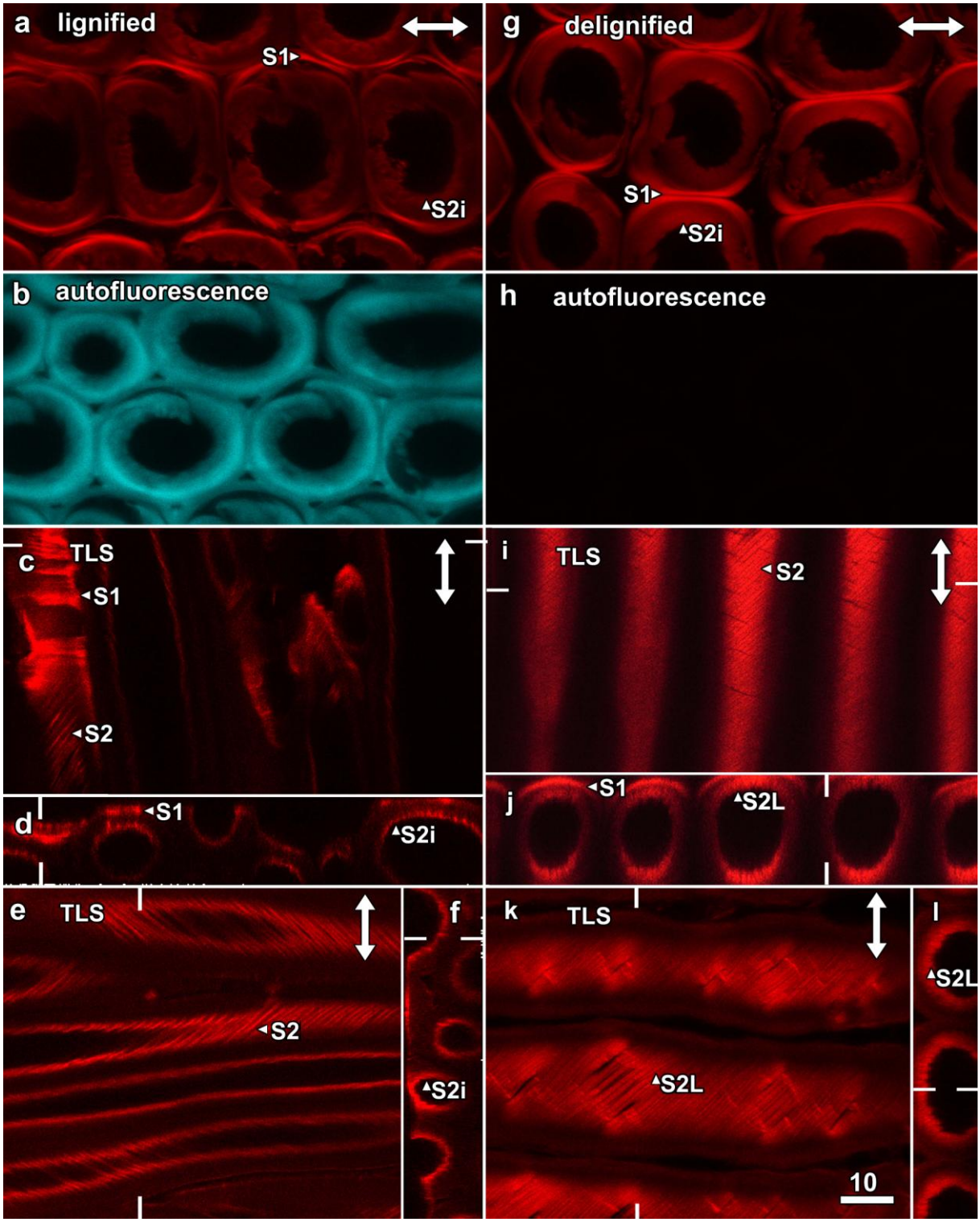

Figure 3.25 The effect of cell wall delignification on P4B labelling of the S2 layer of compression wood. Delignification modified P4B labelling, but did this in a complex manner that is not directly visible in transverse sections (TS).

a. Compression wood control TS showing P4B fluorescence from the S1 and inner S2 layers (S2i).

b. Compression wood control TS showing lignin autofluorescence.

c. Tangential longitudinal section (TLS) where the tracheid axis was nearly parallel to the laser excitation. S1 and S2 layers were visible.

d. Reconstructed transverse section from optical stacks collected with 0.5 µm steps through the longitudinal sections shown in **c**. S1 and S2i regions were visible.

e. TLS where the tracheid axis was nearly perpendicular to the laser excitation.

f. Reconstructed transverse section from optical stacks collected with 0.5 µm steps through the longitudinal sections shown in **e**. Only the S2i regions were visible.

g. TS of delignified compression wood, showing P4B fluorescence.

h. TS of delignified compression wood, showing hardly any lignin autofluorescence.

i. TLS of delignified compression wood, where the tracheid axis was nearly parallel to the laser excitation. The S2i striations were visible but were not as clear as in the non-delignified sample (**c**).

j. Reconstructed transverse section of delignified compression wood, from optical stacks collected with 0.5 µm steps through the longitudinal sections shown in **i**. Strong fluorescence from S1 and S2L regions were visible.

k. TLS of delignified compression wood, where the tracheid axis was nearly perpendicular to the laser excitation.

l. Reconstructed transverse section from optical stacks collected with 0.5 µm steps through the longitudinal sections of delignified compression wood, shown in **l**. Strong S2i and S2L fluorescence.

Bar in **k** = 10 µm for all images. Double headed arrows show the laser polarisation direction. White bars at the edges of panels **c**, **e**, **i** and **k** show the relative locations of the reconstructed planes (**d**,**f**,**j**,**l**), whereas the white bars in the reconstructions show the relative locations of the optical sections shown (**c**,**e**,**i**,**k**).

In compression wood transverse sections, P4B labelling (Figure 3.25a,g) and lignin autofluorescence (Figure 3.25b,h) patterns, both in control (Figure 3.25a,b) and delignified samples (Figure 3.25g,h) were similar to that of opposite wood, and demonstrated that delignification did not cause significant changes in S2 labelling. Longitudinal sections of both control and delignified samples in which the S2 layer was parallel to laser polarisation showed the classic S1 and inner S2 labelling pattern in the reconstructed transverse sections (Figure 3.25c,d,i,j). A similar but much weaker S1 labelling with a strong inner S2 labelling was seen in the reconstructions through cells of delignified samples where the S2 layer was perpendicular to the laser polarisation (Figure 3.25k,l). However, the control samples did not any S1 labelling (Figure 3.25 e,f).These results demonstrated that delignification allowed for S2 labelling, but does this in a highly complex manner that is not directly visible in regular transverse section because of the longitudinal orientation of the cellulose microfibrils in the S2 layer.

3.3.10 Can S2 labelling be improved?

Keeping in mind the question as to why the S2 layer does not fluoresce in transverse sections, it was tested whether higher temperatures or dramatically increased staining times would promote better penetration of P4B into the S2 layer. Experiments were conducted in transverse (TS) sections of opposite (Figure 3.26 - 3.28) and compression wood (Figure 3.29). It was found that increased staining time and delignification greatly improved the P4B labelling of the wall layers (Figure 3.28). However, the standardised staining time (5 min) was found optimum as the appearance of samples stained for longer time was found similar. Apart from the improved P4B labelling, the dye was found penetrated to greater depths (labelling deeper into the wood) with temperature, time and delignification. Considerable improvement in dye penetration was observed with higher staining time and delignification (Figure 3.28b,d). In transverse sections of opposite wood, delignification improved the dye penetration to the S1 and S3 layers, as evident from the increased labelling of S1 at great depth and better S2 fluorescence (Figure 3.28d). Temperature had less influence on dye penetration compared to increased staining time or delignification (Figure 3.28c). Lignin autofluorescence was found unaffected by higher temperature or longer staining time (Figure 3.27).

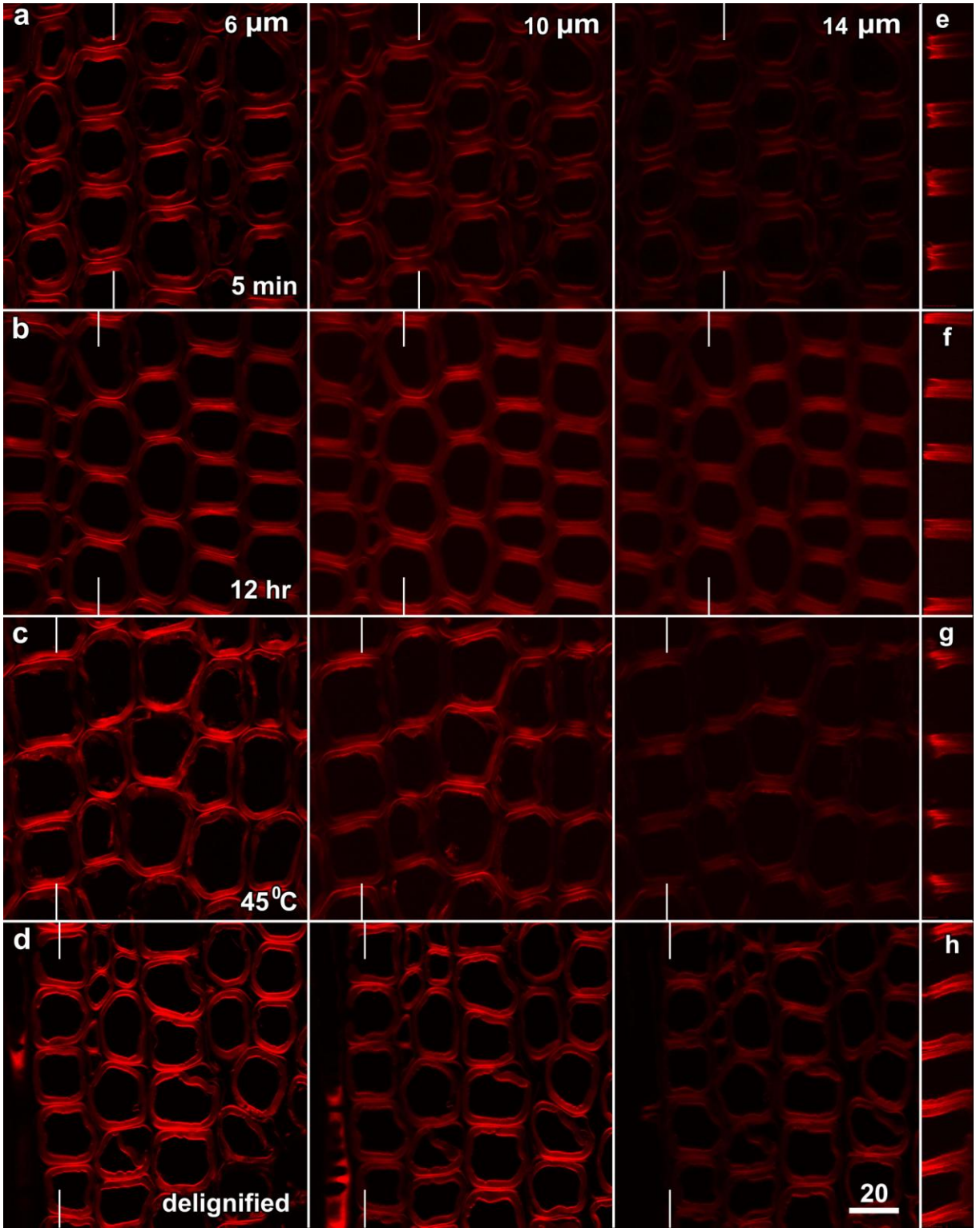

Figure 3.26 Increased staining time, temperature and delignification all improved P4B labelling in opposite wood. Stacks of confocal optical sections were collected, and are shown at 3 different depths into the wood (6, 10 and 14 µm), along with vertical reconstructions in the radial longitudinal plane.

a. 5 min staining with P4B using the standard procedure.

b. 12 h staining with P4B.

c. Staining for 5 min at 45^0C.

d. Staining for 5 min after delignification of the wood blocks.

e-h. Reconstructed radial longitudinal sections showing improved dye penetration (labelling deeper into the wood) with temperature, time and delignification.

Bar in **d** = 20 µm for all images. White bars in panels **a**-**d** show the relative locations of the reconstructed images.

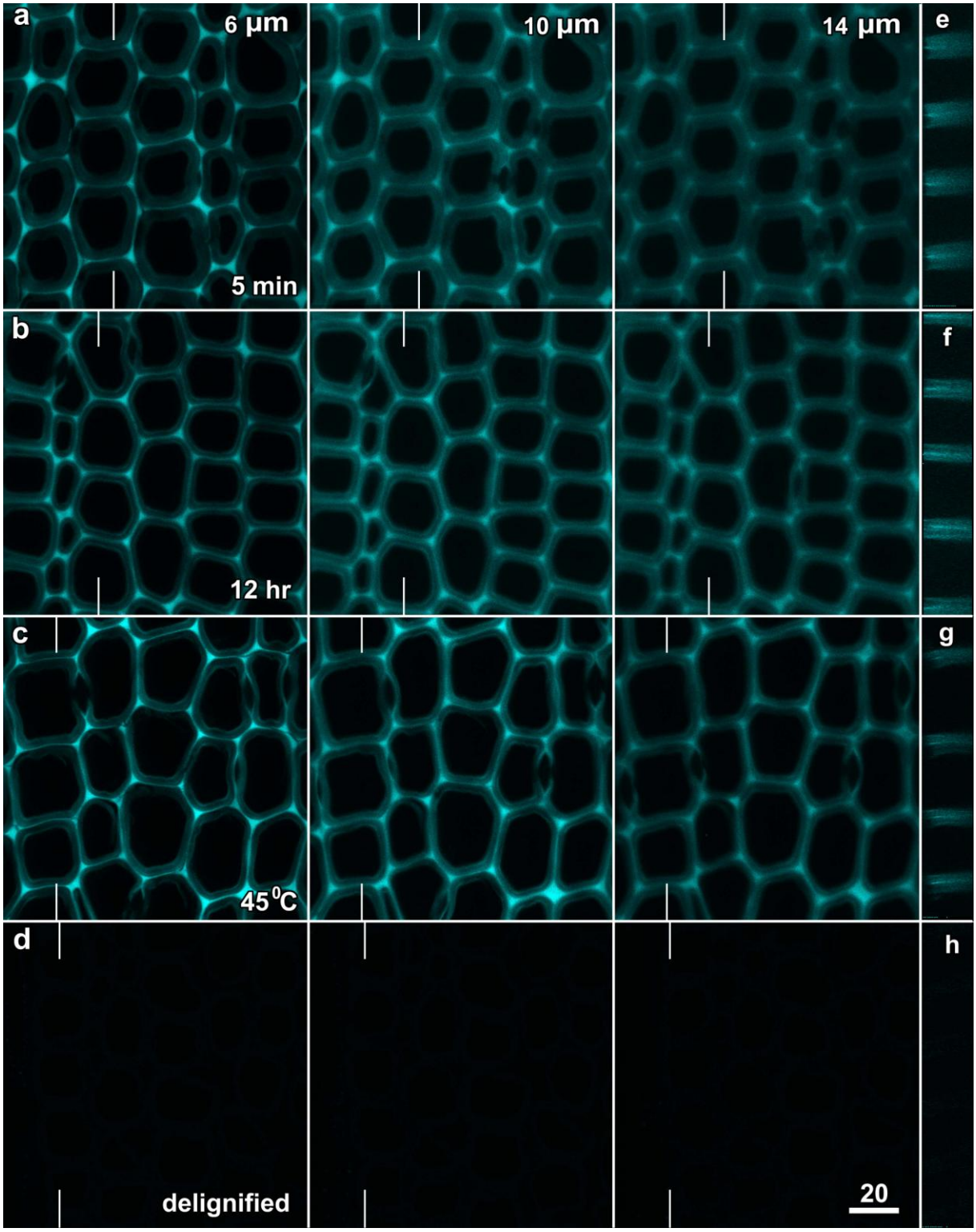

Figure 3.27 Lignin autofluorescence collected for the images shown in Figure 3.26. Stacks of confocal optical sections were collected, and are shown at 3 different depths into the wood (6, 10 and 14 µm), along with vertical reconstructions in the radial longitudinal plane.

a. Sample stained for 5 min with P4B using the standard procedure.

b. Sample stained for 12 h with P4B.

c. Sample stained with P4B for 5 min at 45^0C.

d. Sample stained with P4B for 5 min after delignification of the wood blocks. No fluorescence was observed using the standardised image collection settings.

e-h. Reconstructed radial longitudinal sections showing that lignin autofluorescence was unaffected by higher temperatures or longer staining times. As lignin autofluorescence was similar at all depths, the increased P4B fluorescence at depth in the different treatments can be confirmed as improved dye penetration.

Bar in **d** = 20 µm for all images. White bars in panels **a**-**d** show the relative locations of the reconstructed images.

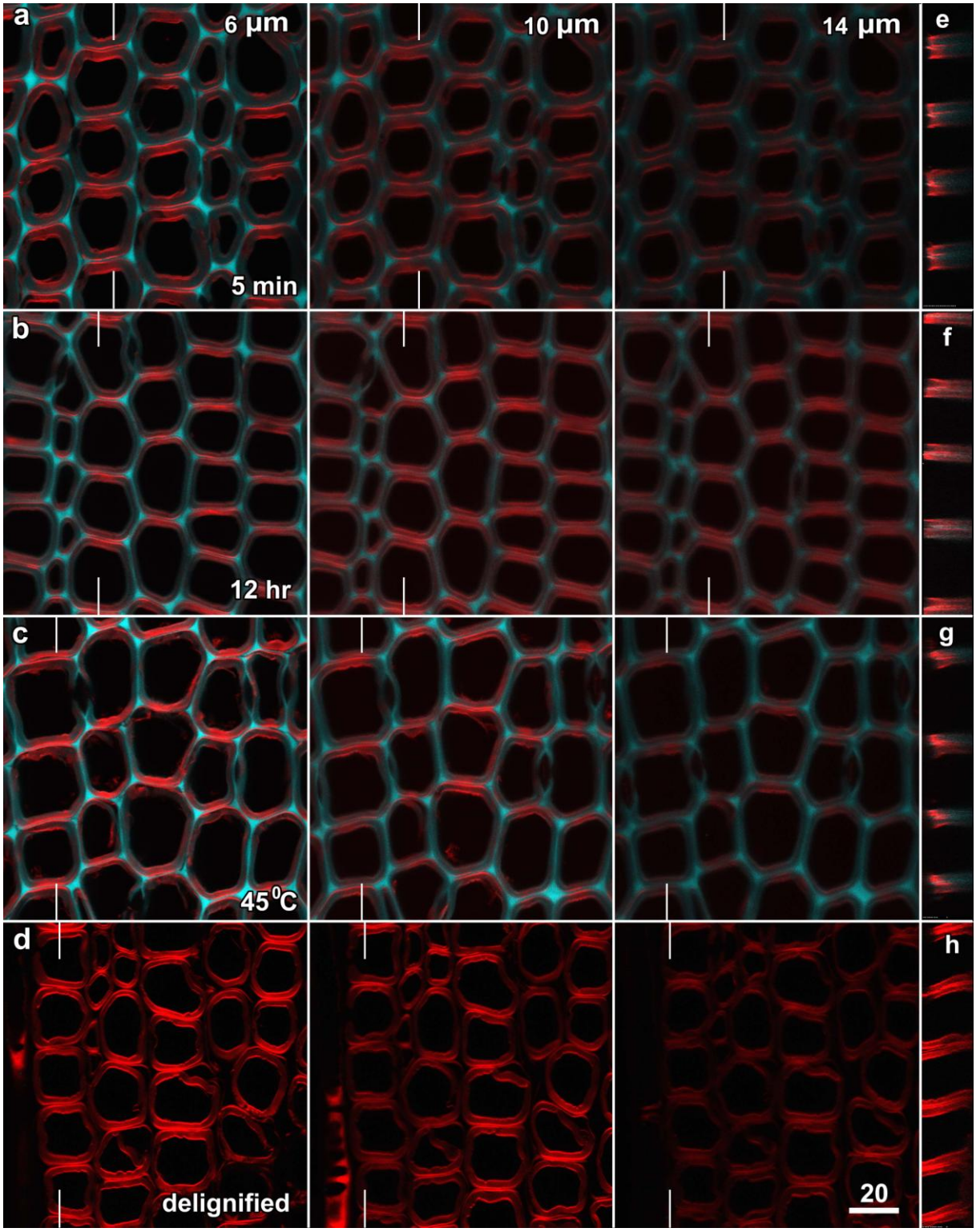

Figure 3.28 Overlay of the images shown in Figure 3.26 and Figure 3.27, with P4B shown in red and lignin autofluorescence in cyan. Stacks of confocal optical sections were collected, and are shown at 3 different depths into the wood (6, 10 and 14 µm), along with vertical reconstructions in the radial longitudinal plane.

a. 5 min P4B staining using the standard procedure.

b. 12 h staining.

c. Staining for 5 min at 45^0C.

d. Staining for 5 min after delignification of the wood blocks.

e-h. Reconstructed radial longitudinal sections showing improved dye penetration.

Bar in **d** = 20 µm for all images. White bars in panels **a**-**d** show the relative locations of the reconstructed images.

As lignin autofluorescence was similar at all depths, the increased P4B fluorescence at depth in the different treatments can be confirmed as improved dye penetration. As with opposite wood, increased staining time, temperature and delignification improved P4B labelling in compression wood (Figure 3.29). At some depth into samples, it was also observed that ray cells would show P4B fluorescence whereas surrounding tracheids did not (Figure 3.30). This demonstrated that the dye could penetrate the less well organised walls of the ray cell but was not entering the more packed secondary walls of the tracheids. In these longitudinal sections of P4B treated compression wood samples, P4B penetrated to a depth of up to 20 μm and P4B labelling from S1 and S2 regions were visible (Figure 3.30c). However, a notable feature was that the less lignified walls of a ray cell showed much better P4B labelling than the nearby S2 microfibrils. Lack of lignification was evident from absence of lignin autofluorescence from the walls of the ray cell (Figure 3.30b). Moreover the concurrently collected transmitted light image (Figure 3.30d) showed many more S2 striations which were not seen labelled with P4B. The deeper P4B labelling on some parts of the ray cell was due to less lignification on those walls, which in other way showed that penetration was not the only issue for less fluorescence from S2 region.

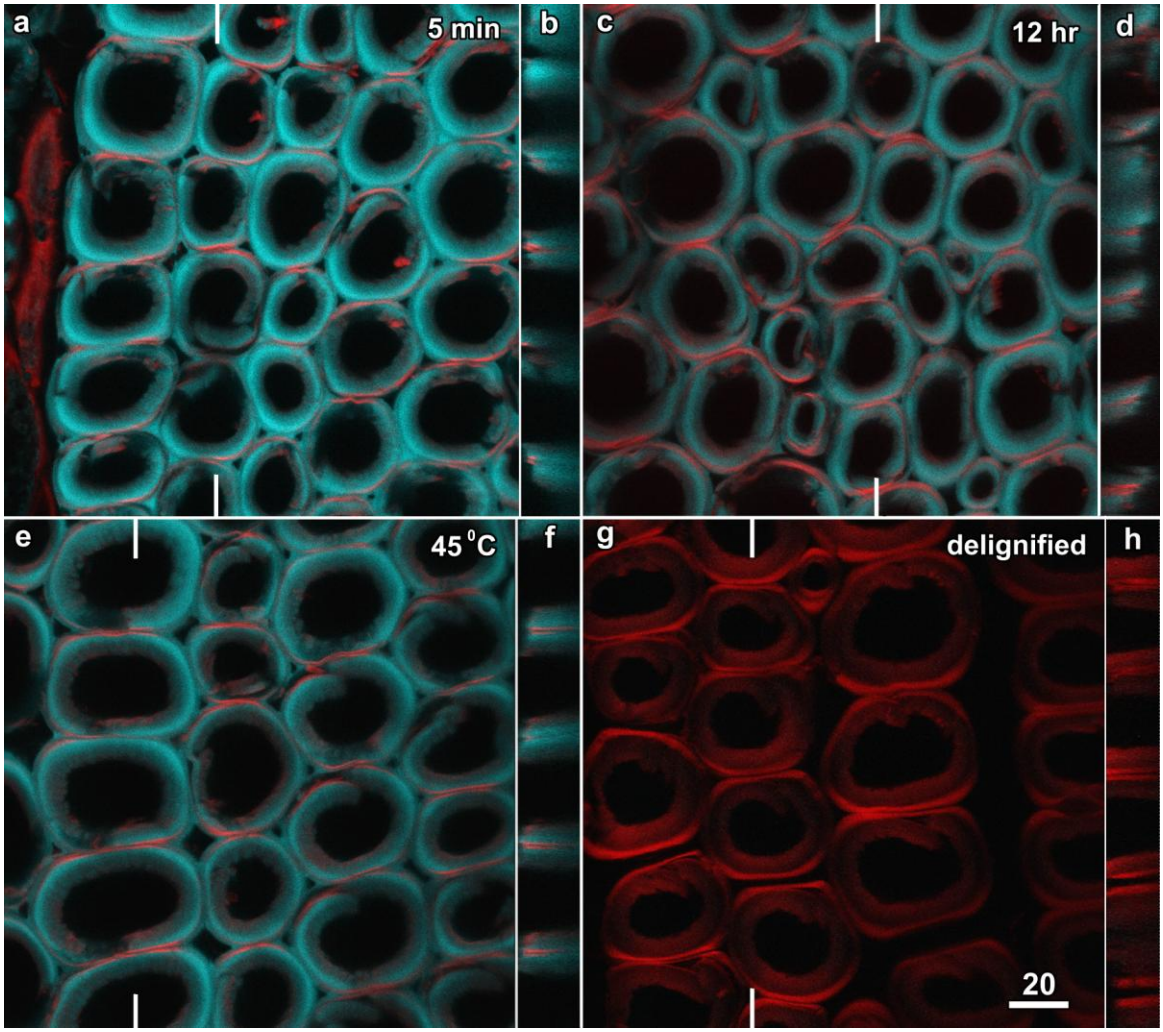

Figure 3.29 Increased staining time, temperature and delignification improved P4B labelling in compression wood. Stacks of confocal optical sections were collected and used to generate reconstructions in the radial longitudinal plane. P4B fluorescence is shown in red and lignin autofluorescence in cyan.

a. 5 min staining using the standard procedure.

b. Reconstructed longitudinal view of the sample in **a** showing limited dye penetration.

c. 12 h staining.

d. Reconstructed longitudinal view of the sample in **c** showing much improved P4B penetration.

e. Staining for 5 min at 45^{0}C.

f. Reconstructed longitudinal view of the sample in **e** showing improved dye penetration.

g. Stained for 5 min after delignifying the wood blocks.

h. Reconstructed longitudinal section showing improved dye penetration.

Bar in **d** = 20 µm for all images. White bars in panels **a**, **c**, **e** and **g** show the relative locations of the reconstructed images.

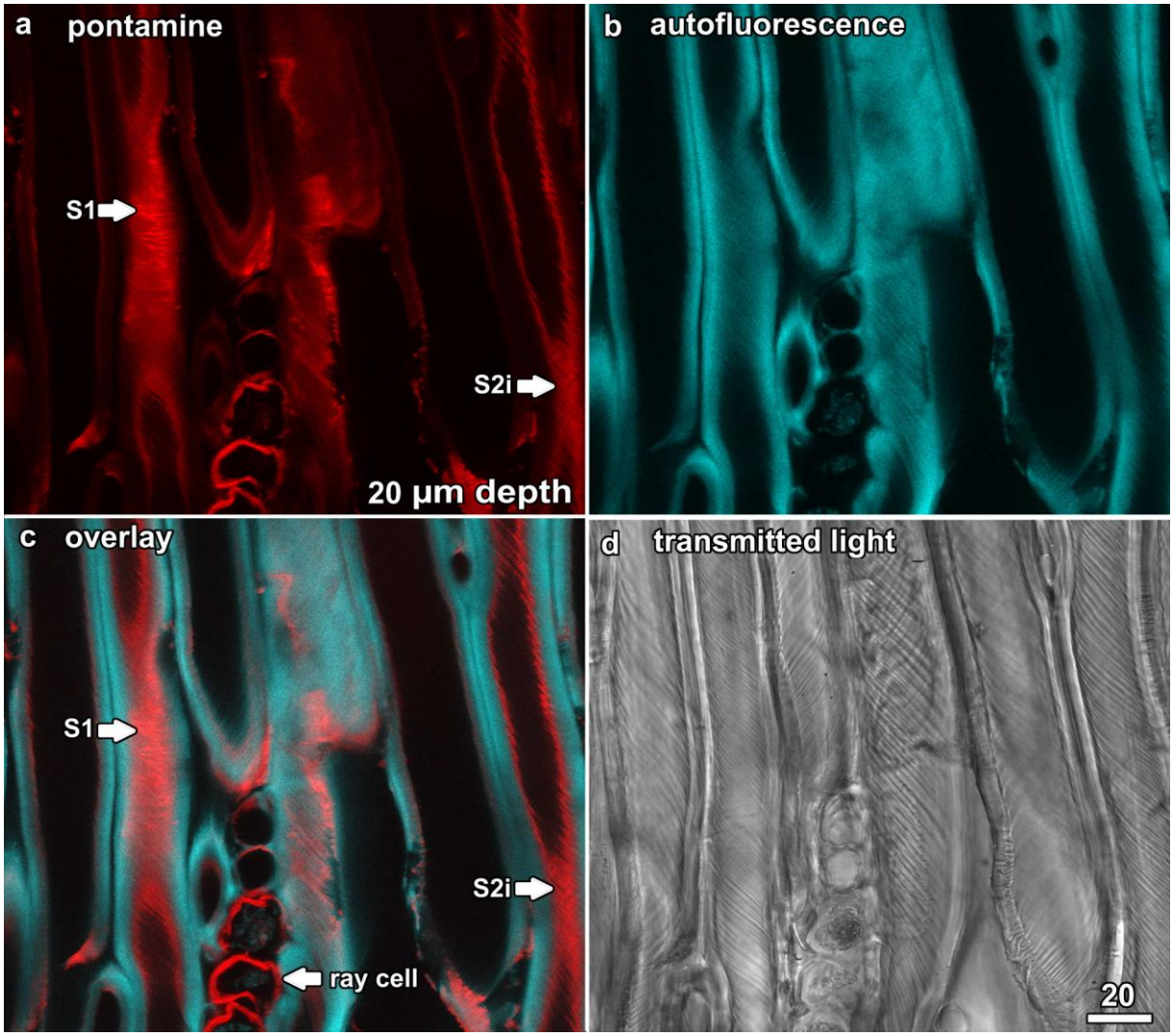

Figure 3.30 Lower lignification enhanced P4B labelling even at great depths. P4B fluorescence is shown in red and lignin autofluorescence in cyan.

a. P4B labelled on to S1 and some microfibrils of the S2 regions.

b. Lignin autofluorescence collected concurrently for the image in **a**.

c. Overlay image showing higher P4B labelling on to less lignified walls of the ray cell and lack of P4B fluorescence from lignified S2 layer.

d. Concurrent transmitted light image showing the bundled microfibrils as striations which were neither labelled nor detected in the P4B image, **a**.

Bar in **d** = 20 µm for all images.

3.4 Discussion

3.4.1 Cell wall fluorescence observed by traditional dyes

Being well known 'traditional dyes,' safranin, Congo red and calcofluor white, along with autofluorescence, were used to study the nature of cell wall fluorescence from tracheids in two year old radiata pine. These dyes and autofluorescence were compared and contrasted to the hitherto unknown dye, P4B fast scarlet 4B. Safranin was used to label lignin and segregate the non-lignified cellulosic regions of the wall whereas Congo red and calcofluor white were used to label cellulose specifically. However, both calcofluor white and Congo red were found less specific to cellulose, in agreement with previous studies (Anderson et al. 2010), and safranin did not provide clear distinctions between different wood types so their use was discontinued after the initial characterisation of P4B. This information on P4B gained through its comparative characterisation has generated new insights in to the cell wall studies.

3.4.2 The advantages of P4B

P4B has several advantages over other conventional "cellulose" stains such as calcofluor white and Congo red. Unlike calcofluor, it is excited by green light (561 nm) rather than UV light, and thus can be readily discriminated from lignin autofluorescence. It is also less prone to fading than calcofluor. And unlike both calcofluor and Congo red, it is more specific towards cellulose than to xyloglucan and other wall components (Anderson et al., 2010). Spectral analysis also confirmed that inclusion of 150 mM NaCl in the staining solution markedly improved P4B fluorescence, as previously reported (Anderson et al., 2010). There were, however, some specific differences between the spectral data measured in pine and *Arabidopsis*. In this analysis, excitation with 405, 488 and 561 nm light (violet, blue and green) produced a P4B emission maxima at 575 nm in both opposite and compression wood, similar to the emission maximum measured in fungi and oomycetes (Hoch et al., 2005). In contrast, Anderson's experiments, which visualised microfibril bundles in growing *Arabidopsis* roots, reported an emission peak at approximately 630 nm (Figure 1B,C in Anderson et al. (2010)). This difference cannot be explained, except to note that the spectra measured by Anderson and colleagues were collected *in vitro*, and these pine data were collected *in vivo*. In more recent studies of P4B labelling in *Arabidopsis* and other plants, 561 nm excitation has also been used to generate fluorescence in the 570-600 nm range (Lampugnani et al., 2013; Landrein et al., 2013; Liu et al., 2013; Park et al., 2011; Voiniciuc et al., 2013; Wang et al., 2011).

P4B is a cellulose-specific cell wall stain, unlike Congo red and calcofluor white. The higher specificity of P4B for cellulose was borne out in the improved axiality ratios (Table 3.4) which indicates that the P4B fluorescence was fourfold or more higher when light was polarised in a parallel orientation compared to the orthogonal. Lower axiality ratios were measured for both calcofluor white and Congo red, and published values for Congo red are also lower. For example, axiality ratio of between 1.5 and 2.5 have been measured in expanding primary walls of onion epidermal cells (Suslov et al., 2009) and the S2 layer of compression wood in pine and spruce (Bergander et al., 2002; Sedighi-Gilani et al., 2005), although values as high as 4 have been recorded (Jang, 1998). Even though it is highly likely that measurements of axiality ratio will vary depending on equipment and measurement conditions, the higher values recorded for P4B are consistent with the dye binding to ordered cellulose and not to the less ordered hemicellulose. Nevertheless, P4B is not a 'pure' cellulose stain as its binding to cellulose is compromised in the presence of xyloglucan. This was demonstrated by the improved labelling of microfibril bundles in roots of the *Arabidopsis* XXT1/XXT2 mutant that lacks xyloglucan (Anderson et al., 2010).

3.4.3 P4B localises to the S1 and S3 layers in the secondary wall

P4B staining gave differing fluorescence intensities across the cell wall in both opposite and compression wood, typically characterised by a pair of bright bands around each tracheid. Calcofluor white and Congo red also gave a similar labelling pattern but their fluorescence was not as sharp as P4B. On the basis of the correlative microscopy images (Figure 3.15), this was attributed to the S1 and S3 layers in opposite wood and the S1 and inner S2 layers in compression wood. The observed dimensions of the fluorescent bands of approximately 0.5 to 1 µm in width were consistent with this attribution. The data are comparable to previous observations of the radiata pine tracheid wall with polarised light microscopy (Frey-Wissling, 1976; Wardrop and Dadswell, 1953), transmission electron microscopy (Donaldson, 2002), scanning electron microscopy (Butterfield and Meylan, 1980; Maurer and Fengel, 1991) and fluorescence microscopy where immunolabelled mannan epitopes were also attributed to the S1 layer (Marcus et al., 2010).

3.4.4 Microfibrils did not fluoresce in cross sections for multiple reasons

The preferential fluorescence of P4B and, to a lesser extent calcofluor white and Congo red, from the S1 and S3 layers might have several causes. In confocal microscopy, excitation laser light is plane polarised. Although all microfibrils might bind to bifluorescent dyes, only those microfibrils that run parallel to the polarisation plane of the excitation light can absorb energy and thus fluoresce. However, the dye-bound microfibrils perpendicular to the excitation light

will not absorb and thus cannot fluoresce. The microfibrils oriented in between will absorb and fluoresce partially. The observations on the bordered pits (section 3.3.6), in which a bordered pit, lying at almost 45^0 (arrow) had lower fluorescence compared to the ones parallel to the excitation light, also suggest the importance of the incident angle.

In transverse sections, the bifluorescent nature of P4B labelling demonstrates that the dye binds along the cellulose microfibrils. In the S1 and S3 layers, where cellulose is roughly transverse to the cell's axis (Donaldson, 2008; Donaldson and Xu, 2005), only microfibrils that are parallel to the polarisation plane of the confocal excitation laser will fluoresce forming the observed pair of bright bands on opposing sides of the cell. In the S2 layer, however, microfibril orientation varies from oblique in compression wood to running along the length of the cell in normal wood. In cross sections, P4B fluorescence from these microfibrils would, therefore, be limited especially in the case of opposite wood. This lack of fluorescence is explained graphically in Figure 3.31.

Microfibril orientation is, however, only one of several reasons why S2 microfibrils did not fluoresce in cross sections, as detailed in section 3.3.10. P4B labels the cellulose microfibrils made up of cellulose and sheathed with various amount of lignin and hemicellulose. Even though the total quantity of lignin is high, its concentration is lower in the S2 region (20%) compared to the S1 and S3 regions (nearly 50-70%) (Donaldson, 1987; Walker and Butterfield, 1993). This higher concentration of lignin in the S1 and S3 layers explains their low porosity and reduced flow of extraneous materials like dyes to the S2 region especially from the lumen through which majority of liquid flow takes place. In many instances, the dye could get into the S3 layer through the lumen. The S1 layer, however, is buried beneath the S2 layer so the dye has limited access to it. This might then suggest that dye penetrated into some samples (Figure 3.25 d,j,f,l) in which the highly lignified inner S2 regions (S2i) of compression wood fluoresced more strongly than the S1 layer. Furthermore, in cross sections, the cut allows direct access for the dye.

The dense lignin-hemicellulose matrix in the S2 region could also have hindered the access to the binding sites of the dye. As previously noted by Jang (1998) for Congo red dyeing of pulped wood fibres, dense lignification can explain the lack of fluorescence from the S2 wall regions. It is also known that the microfibrils in S1 and S3 are not very closely packed (Booker and Sell, 1998; Walker and Butterfield, 1993) unlike the thickly packed S2 region especially in compression wood suggesting that there could not be any flexibility or room available for other molecules to penetrate.

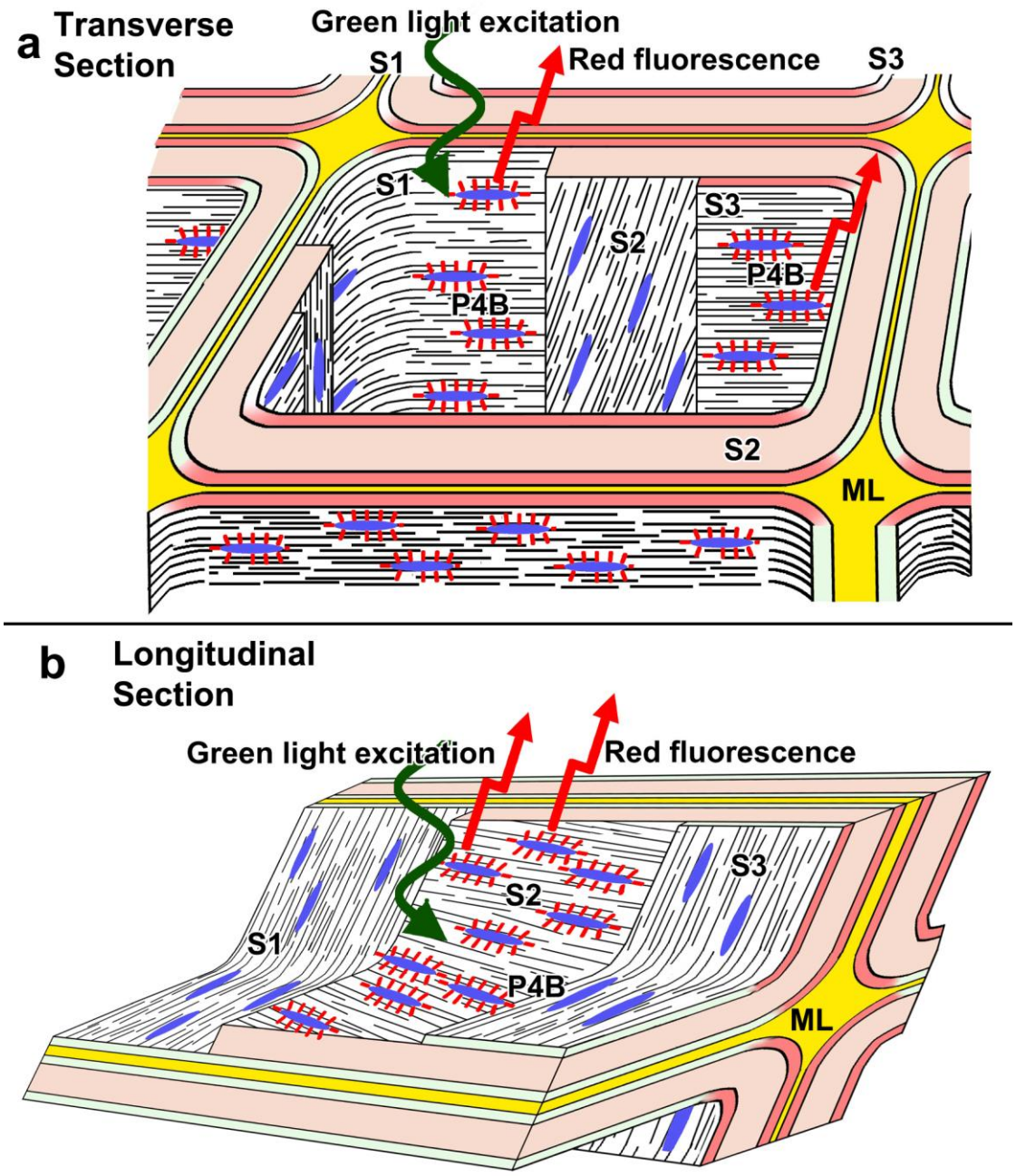

Figure 3.31 Graphical explanations for differential P4B fluorescence from various cell wall regions.

a. P4B fluoresced from opposite walls of the S1 and S3 regions in transverse section.

b. In longitudinal section S2 microfibrils running along the line of excitation fluoresced with lack of fluorescence from the S1 and S3 regions.

3.4.5 Observing and measuring microfibril angle in the tracheid wall

In this study, measurements of microfibril angle within the tracheid wall were demonstrated through two different approaches. These were the direct observation of microfibrils, in transmitted light and fluorescence images showing the bundled microfibrils as striations, possible in both the S1 and S3 layers, and measurements of P4B bifluorescence, a phenomenon not previously documented. The direct observation approach has been used previously with P4B. In the primary wall of elongating *Arabidopsis* roots, P4B labelled individual microfibrils bundles (Anderson et al. 2010) and it was possible to confirm similar structures present in the different layers of the tracheid cell wall. As it was possible to directly observe microfibril orientation in the S1 and S3 layers, P4B provides marked improvement of previous observation systems. Direct observations of microfibril angles by light microscopy have been limited to the S2 layer in compression wood, where the heavy striations of the inner S2 layer make measurements directly possible, and through a range of other light microscopy methods (Donaldson, 2008).

The second approach through which P4B can be used to measure microfibril angle is based on measurements of fluorescence polarisation effects (bifluorescence This followed work using Congo red in primary walls by Verbelen and Stickens (1995), Verbelen and Kerstens (2000) and Suslov et al. (2009) and in secondary walls by Jang (1998), Bergander et al. (2002) and Sedighi-Gilani et al. (2005). This later, indirect approach would work even if individual microfibrils bundles were not resolved, although it has not previously been attempted for P4B for until now.

For more accurate and easy indirect measurements of microfibril angle, a confocal system in which the excitation polarisation could be accurately and directly modulated would be ideal. In the absence of this system on the confocal microscope used in these experiments, it was necessary to make do with rotating the sample with respect to a constant excitation polarisation. This was less accurate and considerably more troublesome, thus limiting the use of this indirect approach.

Some consideration must also be given to the nature of previous experiments in which bifluorescence have been measured using Congo red, especially when applied to secondary walls. Exactly what was being measured with this dye? As this dye is less specific for cellulose than P4B, and secondary wall structure is less than ideal for making observations especially in cross sections, perhaps the polarisation dependent asymmetries in fluorescence reflect patterns in hemicellulose as well as cellulose.

3.5 Conclusions

These observations demonstrate that P4B is a dye that can be used effectively to investigate cell wall architecture in the wood of radiata pine. Moreover, its binding specificity, spectral properties and bifluorescence demonstrate that it is an improvement over conventional cell wall stains such as Congo red and calcofluor white. These characteristics suggest that P4B should be useful in observing the organisation of cellulose microfibrils in the different layers of the tracheid cell wall, and make it suitable for measuring microfibril angle in both the S1 and S3 layers, structures previously difficult to investigate without the use of electron microscopy.

In this study, the applicability of P4B labelling for observing and measuring cellulose and cellulose orientation in the radiata pine tracheid has been demonstrated. While the organisation of cellulose microfibrils within the S2 layer has been well studied by many researchers (reviewed in Donaldson 2008), organisation of the S1 and S3 layers has received less attention. There has not been a detailed investigation of microfibril angle and its variation in the S1 and S3 layers between early and latewood, up and down the tree and across growth rings, and associated with timber defects such as compression wood and spiral grain. These methods, nevertheless, demonstrate that such studies are now feasible.

These observations of microfibril orientation in the fluorescent bands are also consistent with these being the S1 and S3 layers. In compression wood, the S1 layer was observed to be transverse (Figure 3.21) while in opposite wood, cellulose in the S1 and S3 layers was also oriented transverse to the S2 layer (Figure 3.24). These observations are consistent with previously published observations for radiata pine (Donaldson and Xu 2005, Donaldson 2008).

It is, therefore, concluded that the possible reasons for the characteristic P4B fluorescence patterns can be due to any or all of the following reasons:

1) The orientation of the cellulose microfibrils and the direction of the incident laser light.

2) Microfibrils are closely arranged in S2 where as they are more or less loosely arranged in S1 and S3 and hence the dye could not penetrate / adhere to the target substratum.

3) Because of the dense lignification in the S2 layer, the complex lignin cellulose hemicellulose matrix hinders any binding of cellulose with the dye molecule.

Chapter 4

Detection and mapping of resin canals by image analysis in transverse sections of mechanically-perturbed, young *Pinus radiata* trees

4.1 Introduction

This chapter describes a novel, semi-automatic quantitative method for the detection and visualisation of axially-oriented resin canals in transverse sections of 8 month-old *Pinus radiata* (radiata pine) trees. Sections were imaged with a flatbed scanner using circularly polarised transmitted light and were processed with digital image analysis. This novel imaging of the resin canals paved the way to the automatic detection of the canals by image analysis followed by the 3D visualisation of spiral grain.

4.1.1 Resin canals

Resin canals are the tubular intercellular ducts that occur in most conifers and which serve as the repositories for the resins in the wood (IAWA Committee et al., 2004; Rao and Juneja, 1992). A typical resin canal is composed of a tubular duct that is lined by a single layer of resin-secreting epithelial cells which are themselves surrounded by parenchyma cells. Included or strand tracheids surround the parenchyma cells. The entities, as a whole, are known as resin canal complexes, resin ducts or simply as resin canals (IAWA Committee et al., 2004; Wiedenhoeft and Miller, 2002) (Figure 4.1). Resin canal epithelial and parenchyma cells have unlignified cell walls while associated strand tracheids are lignified to the same extent as axial tracheids (Bamber, 1972).

In the family Pinaceae, the ducts in resin canals form through the separation of the canal's parenchyma cells from each other, and thus form a series of linked intercellular spaces. Resin canals run both vertically and horizontally. Vertical (or axial) resin canals run parallel to the tracheids and, in transverse sections, are scattered, either solitary or in groups of 2 to 6. They are larger in size than the radial (or horizontal) canals that lie amongst fusiform ray cells (Bamber and Burley, 1983; Cown et al., 2011; IAWA Committee et al., 2004; Rao and Juneja, 1992). The radial canals are interconnected with the vertical canals to form a three dimensional network (IAWA Committee et al., 2004; Rao and Juneja, 1992).

Resin canals are taxonomically important, and their structure and organisation can be of diagnostic value in identifying several genera of the Pinaceae (Bamber, 1976; Wu and Hu, 1997). Resin canals are present in the secondary xylem of *Pinus* (pines) (Lin et al., 2002), and in radiata pine they are widely distributed in the latewood and in the early to latewood transition zone (Cown et al., 2011). However, in some other genera including *Abies* (firs) and *Tsuga* (hemlocks), canals are produced only as a result of an injury or external stimuli. Such canals are known as traumatic resin canals (Wu and Hu, 1997) and occur in tangential series(an arrangement in arcs concentric to the growth rings) (Esau, 1977; Nagy et al., 2000).

Resin canals are absent from some gymnosperms such as *Juniperus* and *Cupressus* (Fahn and Zamski, 1970; Wimmer et al., 1999).

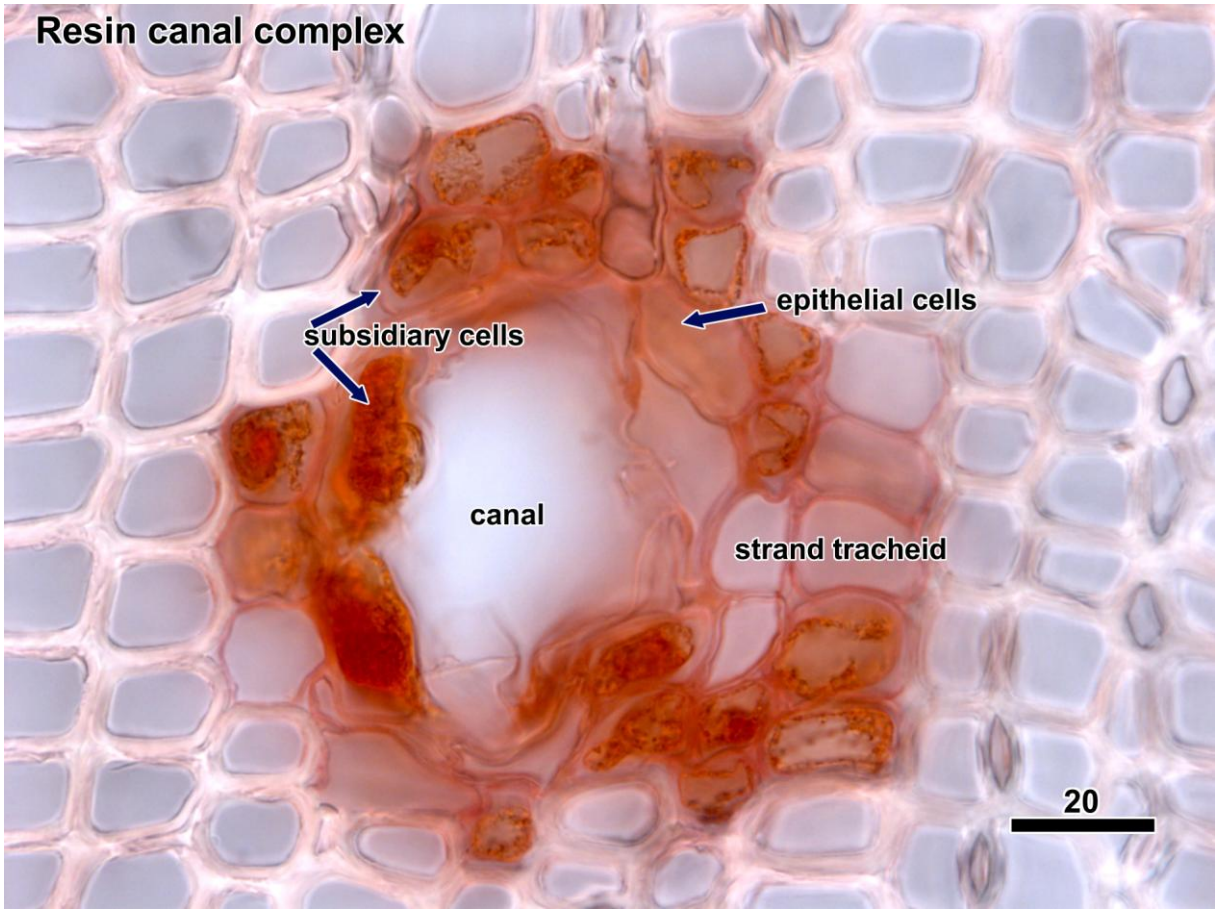

Figure 4.1 Transverse section through radiata pine wood showing a resin canal complex containing subsidiary cells, epithelial cells, strand tracheids and the main canal in the centre. The tissue was stained with pontamine and the labelling was more evident in the unlignified primary walls of the duct cells.

Bar = 20 µm.

Resin canals play a key role in a tree's defence against insect attacks, various infections and diseases and also function in injury healing (Berryman, 1988; LaPasha and Wheeler, 1990; Nagy et al., 2000). O'Neill et al. (2002) found a large increase in the size of normal resin canals, and in the number and frequency of traumatic resin canals, as a result of wounding experiments on *Picea sitchensis* (Sitka spruce). Wimmer and Grabner (1997) found that the vertical resin canal density was a useful variable for dendroclimatology studies on Norway spruce. Resin canals also affect the processing of timber (LaPasha and Wheeler, 1990). In a study to find the flow paths for the wood preservatives under vacuum impregnation in radiata pine, Matsumura et al. (1998) found an increase in preservative uptake through radial surfaces after pre-steaming the wood. This higher preservative intake was due to the opening of resin canals allowing more liquid to flow, and confirmed the role of resin canals can play in wood processing.

Experiments previously conducted within the School of Forestry at the University of Canterbury aimed to investigate the effect of wind on wood properties in radiata pine. Young trees were mechanically and intermittently rocked for six months to simulate wind (Apiolaza et al., 2011; Apiolaza et al., 2008). These studies were aimed at evaluating clones for inclusion in or exclusion from future breeding experiments and commercial planting. On the basis of a pilot study on a small number of transverse sections taken from limited regions of the rocked trees, Apiolaza et al. (2011) reported a significantly higher number of resin canals in rocked trees, and suggested that this observation warranted a more comprehensive investigation of the distribution of resin canals.

The presence of resin canals is a regular growth feature in most of gymnosperms including radiata pine. However, their presence in excessive numbers or the formation of bands of resin canals resulting from some trauma will result in weaker regions within the wood. These are referred to as resin pockets. The presence of many resin pockets on or near the surface of timber significantly reduces its value because of the difficulties that the resin causes for painting and polishing..

4.1.2 Observing resin canals

Traditional methods of studying resin canal characteristics involved serial sectioning and reconstructions, and to process a large number of samples might require months of work. In a systematic study of the resin canals in *Pinus taeda* (loblolly pine), LaPasha and Wheeler (1990) determined the length and interconnection between the vertical and radial resin canals by direct measurement and imaging 4000 transverse serial sections. They also observed that the orientation of the vertical resin canals is straight relative to the axis of the trunk.

Such manual counting of resin canals, often difficult to see in sections, is subjective, time consuming, tedious and prone to operator bias. However, use of image analysis tools to detect wood elements such as resin canals in transverse sections has become more widely accepted with the availability of modern image capturing equipment, and processing and analysing software (Chen et al., 2008). Therefore, to study the size, shape, area and other properties of resin canals in radiata pine wood transverse section, an automated image processing technique was developed using a combination of simple imaging and processing tools based on the freeware programme ImageJ (Rasband, 1997-2009).

4.1.3 Objectives

The two main objectives of this study were:

1) To develop a simple image acquisition technique, and to devise a rapid, reliable and reproducible image processing method that detects, counts and analyses resin canals in wood transverse sections.

2) To study the characteristics of resin canals in transverse sections of young radiata pine trees that had been subjected to tilting and rocking treatments, and to determine the potential of using these data for evaluating the trees at the sapling stage.

4.2 Materials & methods

4.2.1 Tree growth

In an experiment run by the School of Forestry, nursery seedlings of radiata pine were potted in specially-made rigid plastic pots and grown in a glasshouse. After two months, these trees were subjected to one of the three different treatments. One group of trees were allowed to grow straight without any constraints (control trees) (Figure 4.2a). A second set of trees were tilted and tied on to garden stakes to create a leaning angle of between 30^{o} and 45^{o} to the vertical (tilted trees) (Figure 4.2a). A third set of trees (rocked trees) were clamped above ground level in order to prevent stem rocking below that level and also to avoid any stress on the roots while rocking. These trees were rocked intermittently on a purpose built seesaw frame (Figure 4.2b) at 24 cycles per minute over an arc of 44^{0} ($\pm$ 22^{0} to the vertical) to simulate 10 km/h wind (Movie 1). Rocking was for 15 min every hour (Apiolaza et al., 2008). After 6 months, I collected small stem sections of about 25 mm in length from about 10 cm above and below clamp positions of the rocked trees, and from a similar location in the tilted and control plants. A small wedge was scored along the length of the rocked samples to indicate the direction of rocking. The remaining wood samples were processed for analysis of physical, chemical and mechanical wood properties at the School of Forestry, University of Canterbury and at the Chemistry Department, University of Auckland.

4.2.2 Sample Preparation

Small stem sections (25 mm in length) were cut from the trees and preserved in formaldehyde / acetic acid / alcohol fixative (FAA; 10% (v/v) formaldehyde, 5% (v/v) acetic acid, 50% (v/v) ethanol). Segments were thoroughly washed in warm water (30^{o}C, 15 min) and 60 µm-thick transverse sections were cut with a sliding microtome (HM400, Microm, Walldorf, Germany). During sectioning, the wood sample was kept wet. Complete transverse sections (up to 10 mm in diameter) were washed in warm distilled water and blotted on a filter paper for few seconds. Three sets of slides were prepared. Unstained transverse sections were compared to sections stained with pontamine fast scarlet 4B (P4B, Sigma-Aldrich Rare Chemical Library) (5 min in 0.1% (w/v) P4B in 150 mM NaCl) (Thomas et al., 2013) and safranin (Nice Microscopy, Cochin, India) (momentary dipping, 2% (w/v) in distilled water containing 5% (w/v) ferric alum and 14% (v/v) glycerol). Stained samples were blotted on filter paper for a few seconds to remove excess stain and carefully transferred to a microscopic slide and mounted in glycerol.

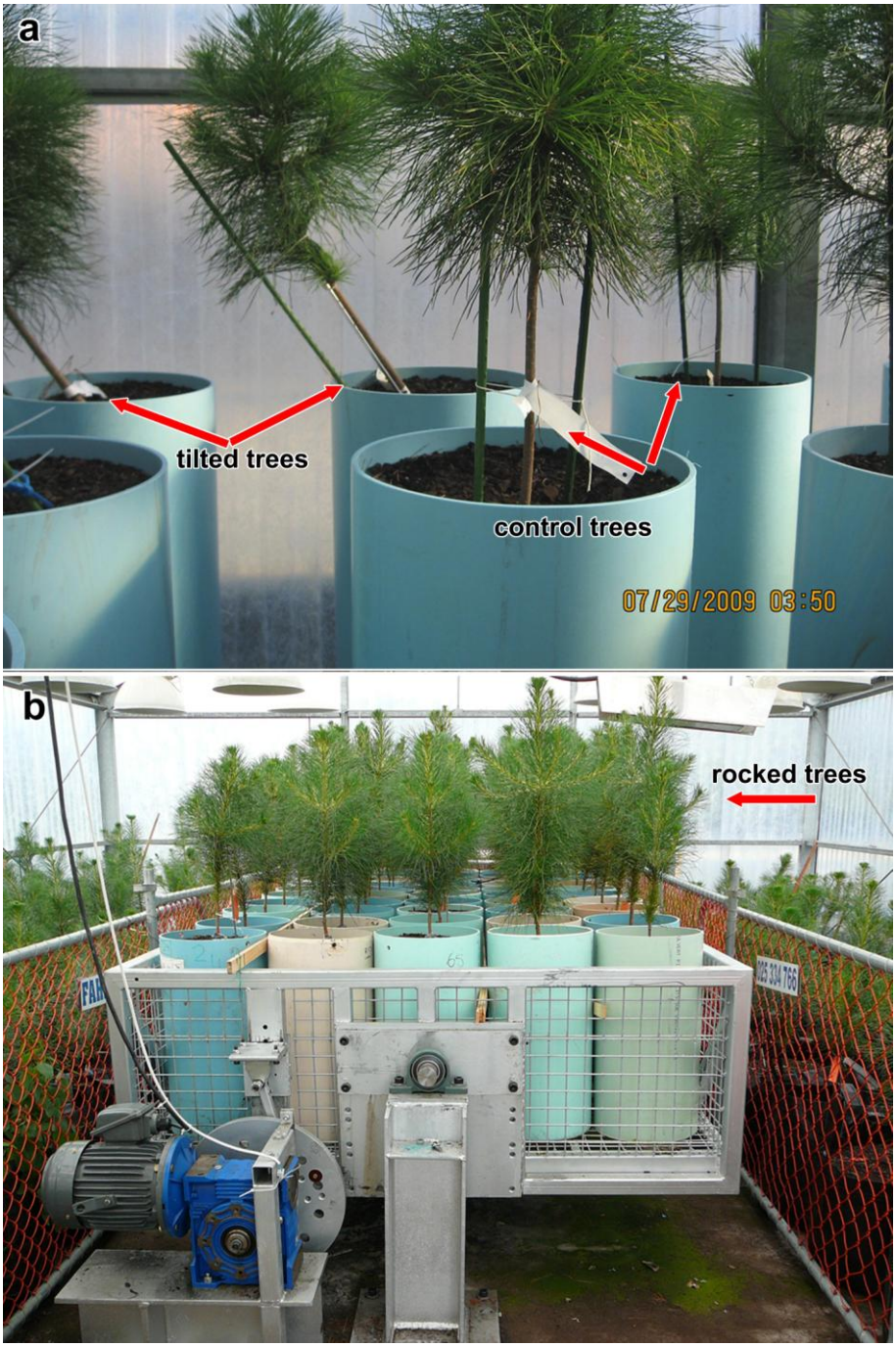

Figure 4.2 The set-up for rocking the trees at 24 cycles per minute to simulate wind. Plants to the left and right are the controls and tilted trees. Both photographs provided courtesy of Dr Luis Apiolaza, School of Forestry, University of Canterbury.

a. Control and tilted trees.

b. Rocking trees undergoing the simulated wind treatment on a purpose-built rocking mechanism.

4.2.3 Image capture

The complete stem transverse sections were imaged using transmitted light (Figure 4.3a) with a professional flatbed scanner (Epson Perfection V700 Photo) (24 bit colour, 2400 dpi) and saved as TIFF images. Professional grade scanners of this type can run in either transmitted or reflected light modes: the transmitted light mode used for these experiments was once often used to image film negatives.

Slides were placed on a sheet of linear polarising film (polariser) (catalogue number NT38-491, Edmund Optics, Singapore) on the scanner bed and then scanned either in the absence or presence of a second sheet of linear polarising film oriented at right angles (analyser) to create linear polarised light (Figure 4.3b) (Arpin et al., 2002). The presence of the crossed polarisers meant that in the scanned image, any linearly polarised background light whose polarity remained unmodified would be eliminated from the image. In some experiments, two sheets of quarter wave-retarder film (catalogue number NT27-344, Edmund Optics) were added to the optical path on either side of the microscope slides, and at an angle of 45^0 to the linear polarising sheets. This meant that the wood sections were imaged with circularly polarised light (Figure 4.3c) (Foster, 1997; Higgins, 2010; Patselt, 1985). Schematic representations of these optical paths are in Figure 4.3d-f.

4.2.4 Image analysis

Unlike most previous studies on resin canal properties, which have been based on small fractions of the complete stem transverse section, this study used the entire wood transverse sections. This enabled analyses that were not distorted by variations in canal frequency across the stem. This new resin canal detection technique had three important stages.

1) Image pre-processing gave individual tree cross section images by copying from the large scanned images that contained many slides that had been scanned together. The background of each image was carefully tidied by removing noise and particles (dust and lint) from the image using Photoshop CS4 (version 11.0.1, Adobe Systems, San Jose, CA, USA).

2) The shape of the transverse section was detected and its area measured.

3) Resin canals were detected, counted and their areas measured.

These second and third stages were completed with macros written in ImageJ (version 1.46m, National Institutes of Health, Bethesda, MD USA) (Appendix 1).

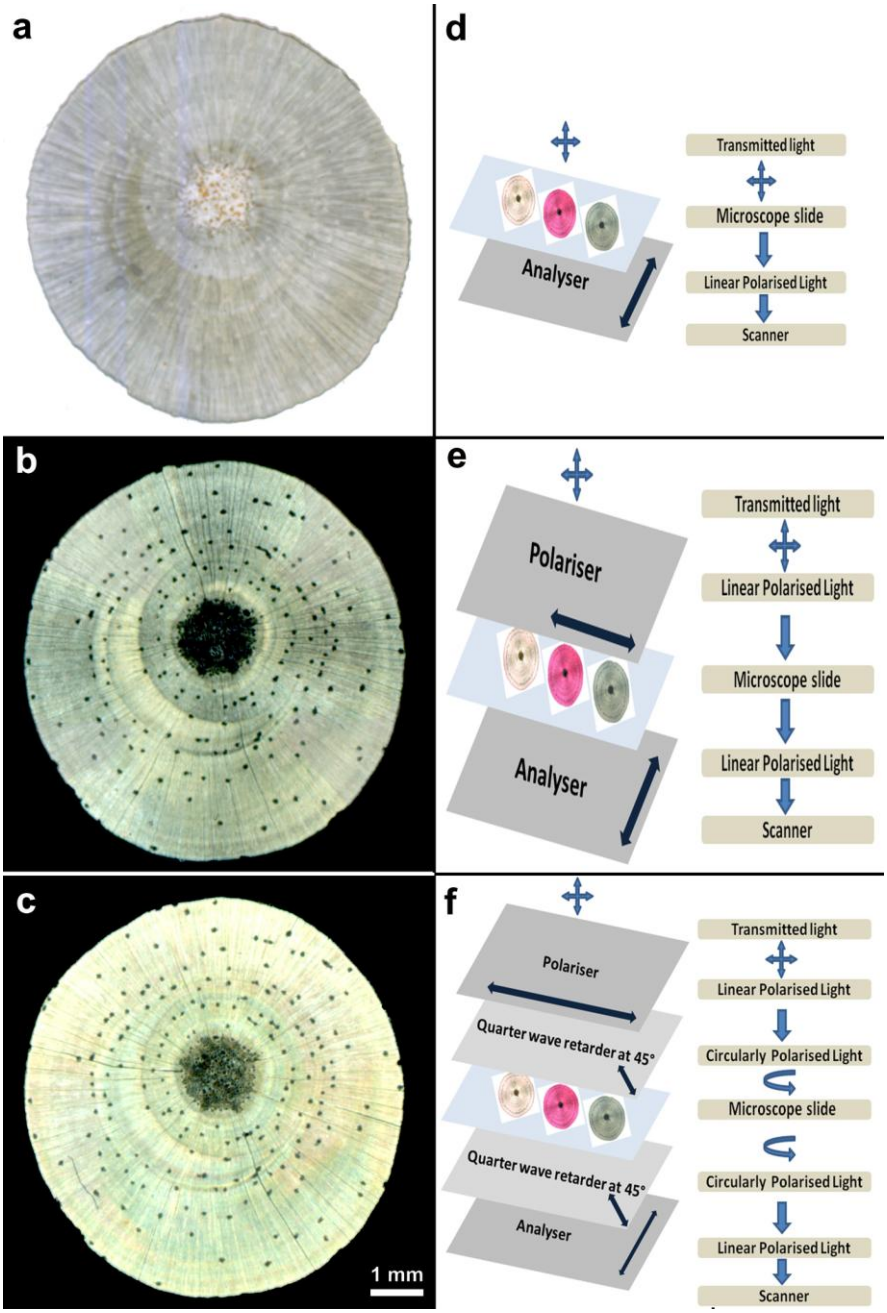

Figure 4.3 Use of crossed polarisers substantially improved the visibility of resin canals. Sections were stained with Pontamine fast scarlet 4B.

a. Transmitted light image.

b. Imaged with linear polarised light. The scan show the 'Maltese cross' effect, being slightly darker in the vertical and horizontal parts of the image.

c. Imaged with circular polarised light, demonstrating even lighting across the sample.

d. Schematic representation of the imaging technique with transmitted light.

e. Schematic representation of the imaging technique with linear polarised light.

f. Schematic representation of the imaging technique with crossed polarised light.

Bar in **c** = 1 mm for **a**, **b**, and **c**

4.2.5 Correlative imaging

To get a better understanding of the resin canal structure, and to confirm that the dark holes that appeared with the polarised light scanning were resin canals, correlative imaging of the resin canals was conducted. Resin canals, either unstained or P4B-stained, were initially imaged with the scanner using transmitted light and under crossed polars with and without the quarter wave-retarder films. Randomly-selected resin canals were then imaged with transmitted light, and linear and circular polarised light with a Leica DFC 310 FX digital camera connected to either a stereomicroscope (model MZ 10F Fluo, Leica Microsystems, Heerbrugg, Switzerland) or an inverted compound microscope (model DMI6000, Leica, Wetzlar, Germany).

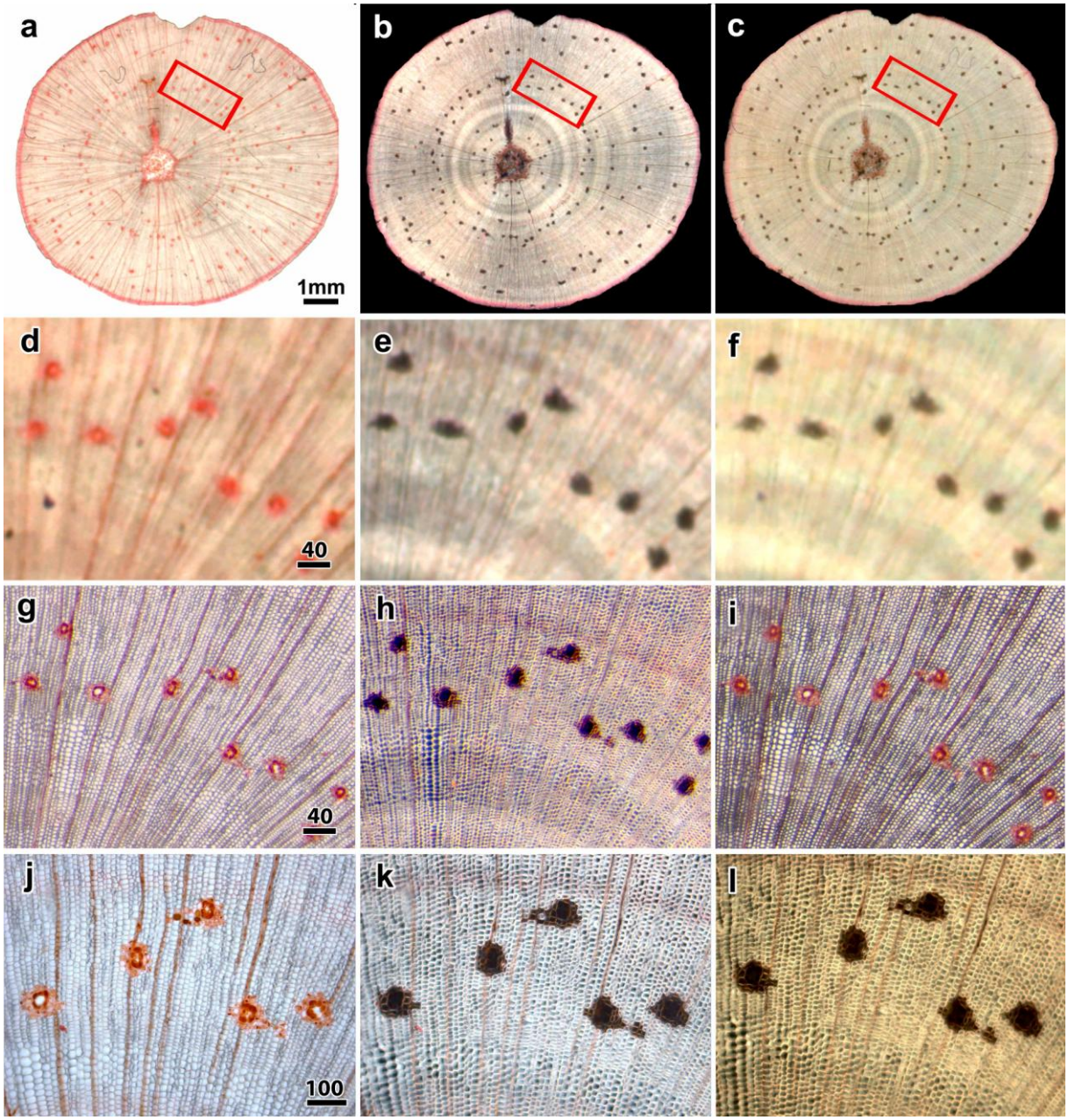

Figure 4.4 Correlative imaging with scanner, stereo-fluorescence microscope and compound microscope confirmed the dark dots as resin canals.

a-c. Imaging with a flatbed scanner using transmitted light (**a**), linear polarised light (**b**) and circular polarised light (**c**).

d-f. Enlarged view of the boxed location in **a**-**c**.

g-i. Imaging with a stereomicroscope using transmitted light (**g**), linear polarised light (**h**) and circular polarised light (**i**).

j-l. Imaging the area with a compound microscope using transmitted light (**j**), linear polarised light (**k**) and circular polarised light (**l**).

Bar in **a** = 1 mm for **a**, **b**, and **c**; bar in **d**= 40 µm for **d**, **e**, and **f**; bar in **g**= 40 µm for **g**, **h**, and **i,** bar in **j**= 100 µm for **j**, **k**, and **l.**

4.3 Results

4.3.1 Imaging stem transverse sections with a flatbed scanner

Three different methods were considered for imaging wood transverse sections in order to detect the resin canals. When slides with wood transverse sections were scanned at high resolution on a flatbed scanner with transmitted light, the images obtained failed to give any useful information about the distribution of resin canals as these were not clearly visible (Figure 4.3a,d). The same slides were then imaged with crossed polarisers. With this arrangement, background light was eliminated by the polariser-analyser duo. However, the presence of an anisotropic, birefringent material (the thin section of wood) between the crossed polarisers rotated the plane of polarised light and allowed some light to pass through the analyser. Thus, the cross sections through the stem, being composed primarily of cellulose, rotated the light and appeared bright against a dark background. Resin canals, however, being composed of a wall-free duct and parenchyma cells that contain only a thin, unlignified cell wall, did not rotate the light as much as the surrounding wood and appeared dark (Figure 4.3b,e). Subtle variations in secondary wall brightness were apparent, with both ring patterns and darker fringes running horizontally and vertically. This later 'Maltese cross' pattern, is typical of polarised light images (Foster, 1997). However, its presence in the images complicated automated image analysis based on thresholding. To overcome this, a pair of quarter wave retarder-films were added to the light path to give circular polarised light (Foster, 1997; Higgins, 2010) (Figure 4.3c,f). Their addition substantially improved the visibility of the resin canals, removed the Maltese cross effect and gave more even contrast across image. This made the images suitable for automated analysis.

4.3.2 Correlative imaging

Successful imaging of wood cross sections using circular polarised transmitted light and a scanner required that the dark structures visible in Figure 4.3 be conclusively shown to be resin canals. Correlative imaging of the same resin canals using the scanner (Figure 4.4a-c and Figure 4.4d-f at a higher magnification), stereomicroscope (Figure 4.4g-i) and compound microscope (Figure 4.4j-l) confirmed that the dark spots in the polarised light scanning were resin canals.

The scanner images collected using crossed polarisers, both with (Figure 4.4 right column) and without (Figure 4.4 - middle column) quarter wave-retarder films, were compared and found to match images collected under similar conditions using the stereo and compound

microscopes. Importantly, these images revealed the structure of the canals. In transmitted light, they appeared in this case as reddish dots, due to the staining with the pontamine (Figure 4.4, - left column) (Thomas et al., 2013). With linear and circular polarised light, the canals appeared as dark dots (Figure 4.4, - middle and right columns). However, with the higher resolution available with the compound microscope the pontamine-stained parenchyma cells in the resin canal complex were weakly visible with linear and circular polarised light (Figure 4.4k,l).

4.3.3 Detection of the wood transverse section area by Image J

After image pre-processing, an ImageJ macro was used to measure the wood transverse section area (Figure 4.5). The colour image (Figure 4.5a) was converted to a black and white image (Figure 4.5b) and binarised for separating the wood cross section from the background (Figure 4.5c). The threshold for binarisation was not critical in this macro. The '*Fill holes*' function was applied which completely filled the gaps in the transverse section (typically resin canals, ray cells and the pith) (Figure 4.5d). The scale for the image was then converted from Imperial units (2400 pixels per inch) into metric units (94.49 pixels per mm) using '*Set the scale'*, and the area of the filled section measured using the '*Analyse particles*' function (Figure 4.5e). Sections were batch processed with this macro, and the results saved as an Excel file. A detailed procedure on the use of the macro is given in the Appendix 1.

4.3.4 Detecting and counting resin canals with ImageJ

Another macro was written to detect and count the resin canals, and to measure their area (Figure 4.6). After the conversion of the original colour image (Figure 4.6a) to a black and white image (Figure 4.6b), the next step was '*Binarising*' in which the ImageJ software thresholded the image automatically (Figure 4.6c). Several problems were encountered at this stage as the automatic thresholding did not provide accurate detection of all the resin canals in the image. In initial scans, which were run with linearly polarised light, the variations in intensity at different angles (brighter on the diagonals, see Figure 4.3b) meant that correct automatic thresholding of the images was not possible. A second problem was that during these initial scanning runs, stained and unstained slides were scanned together. Again, variations in image intensity required manual thresholding. These difficulties were overcome by the use of circular polarised light and by grouping similarly treated slides for rescanning. During initial macro development, however, these issues were overcome by manually thresholding each image to accommodate the maximum number of resin canals (Figure 4.6c). After thresholding, the '*Erode*' function was used to smooth the edges (Figure 4.6d) and '*Find edges'* (Figure 4.6e) to detect the resin canals.

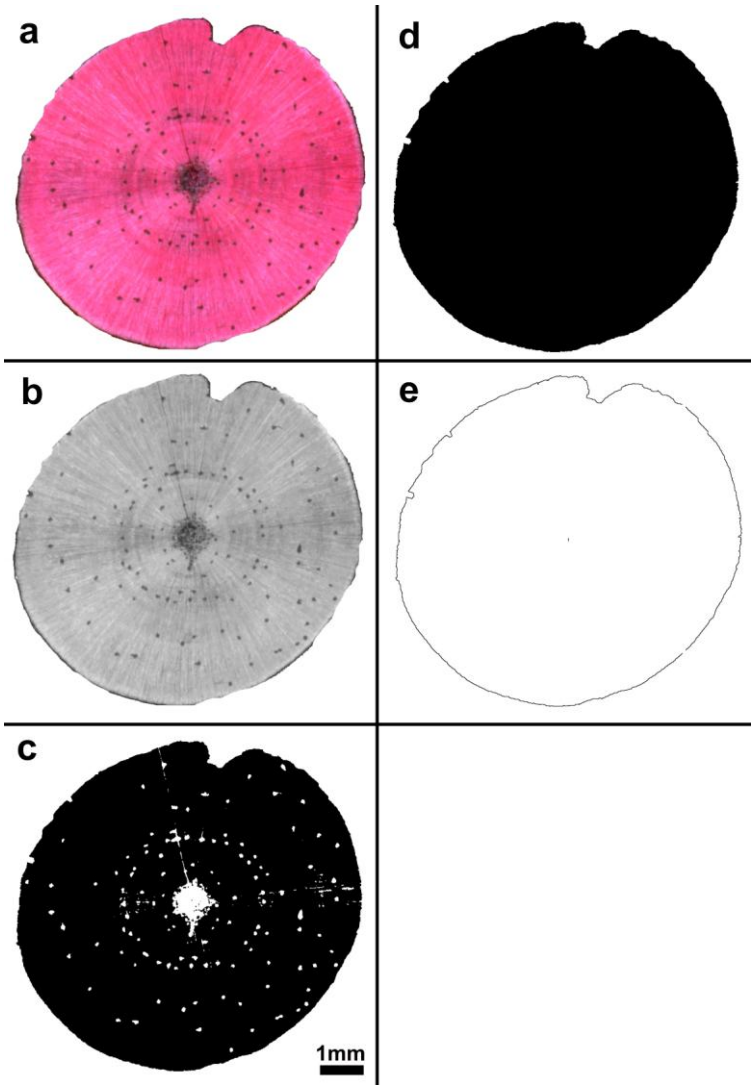

Figure 4.5 Images resulting from each processing step to detect the wood transverse section and area by the macro function in ImageJ. The notch in the transverse section is the score that delineates the direction of rocking.

a. Scanned image.

b. 8bit image.

c. Binarised image.

d. Filled holes.

e. Transverse section detected and area measured.

Bar in **c** = 1 mm for all images.

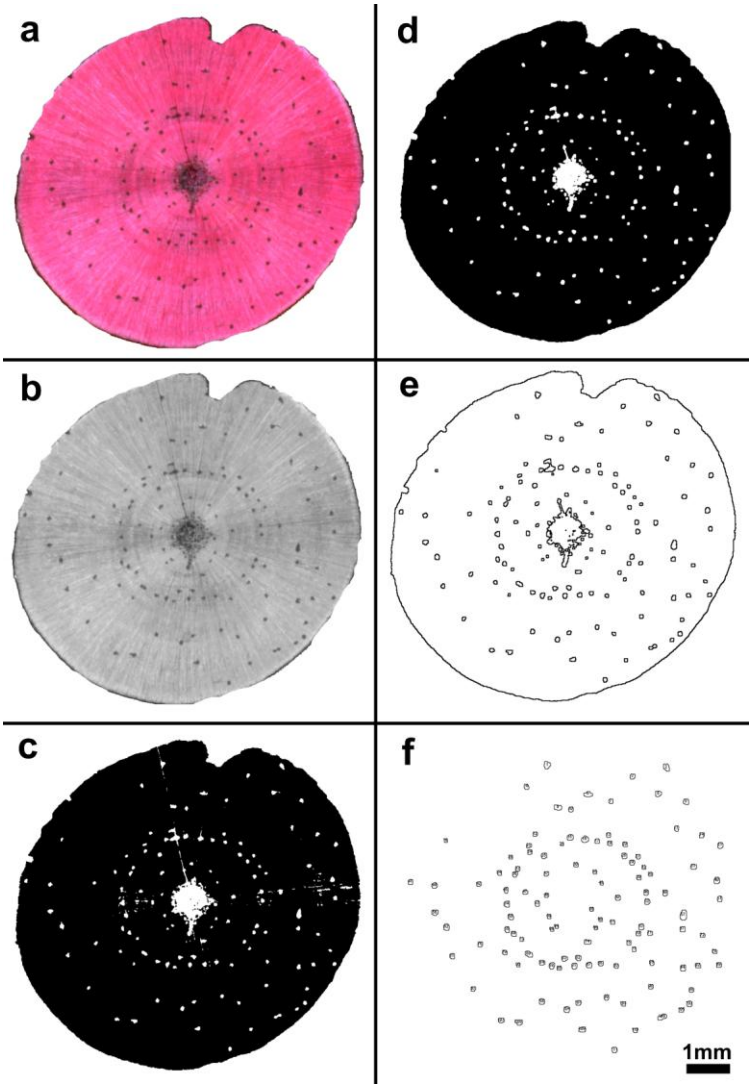

Figure 4.6 Images resulting from each processing step to detect the resin canals and map their distribution by the macro function in ImageJ. The notch in the transverse section is the score that delineates the direction of rocking.

a. Scanned image.

b. 8bit image.

c. Binarised image.

d. Eroded to smooth the detected canals.

e. Transverse section and the resin canals detected.

f. Resin canals detected, counted and their area measured.

Bar in **f** = 1 mm for all images.

After that, the scale was converted to metric units with '*Set the scale'* and the '*Analyse particles'* function was run to measure the area and count of resin canals. The resultant image was saved as a TIFF image (Figure 4.6f) and the calculations as an Excel file. This automated batch processing using the ImageJ software substantially reduced the time required to process and analyse images and also eliminated manual error in detection. Overlay image of the original and the resultant image was in good agreement verifying the detection technique (Figure 4.7a-c). A flow diagram summarising the different analysis steps involved in the processing of the images is shown in Figure 4.8.

4.3.5 Resin canals characteristics

Both the tilting and rocking treatments were found very effective in stimulating growth. Tilting induced pronounced eccentric growth on the lower side of the lean as compression wood was formed (Figure 4.9c,d) while rocking also created significantly more wood (Figure 4.9e,f) compared to the control samples (Figure 4.9a,b). The staining of sections with pontamine fast scarlet 4B (Figure 4.9 - middle column) and safranin (Figure 4.9 - right column) enhanced the visibility of resin canals in the images compared to the unstained controls (Figure 4.9 - left column). Also, wood formed before (Figure 4.9b,d,f) and after (Figure 4.9a,c,e) the commencement of the treatments showed considerable difference in number, frequency and arrangement of resin canals in the transverse section. Wood formation around the pith was more or less equally distributed in rocked and control trees. However in tilted wood, as expected, the wood formation became elliptical and more wood was formed on the leaned side (lower side) as a consequence of compression wood formation (Figure 4.9d).

4.3.5.1 Cross section areas

The rocking treatment significantly increased the transverse section area compared to the controls both above and below clamp positions (Table 4.1). The average transverse section area of these tress were 54.3 mm^2 (above clamp) compared to 32.5 mm^2 in the controls. A similar trend was observed in the stem sections below clamp with rocked samples having a mean area of 54.9 mm^2 against 40.0 mm^2 in controls. It may be noted that the transverse section area in the 'above' position of the controls was significantly lower than the corresponding area in the 'below' position. This is the natural way of plant growth with gradually reducing stem diameter along the shoot. Unlike this general pattern, the stems of rocked trees were notably cylindrical in shape with no significant difference in cross sectional area between the lower and upper locations. In tilted trees, the average transverse section areas above and below clamp positions were higher than the controls due to the formation of compression wood.

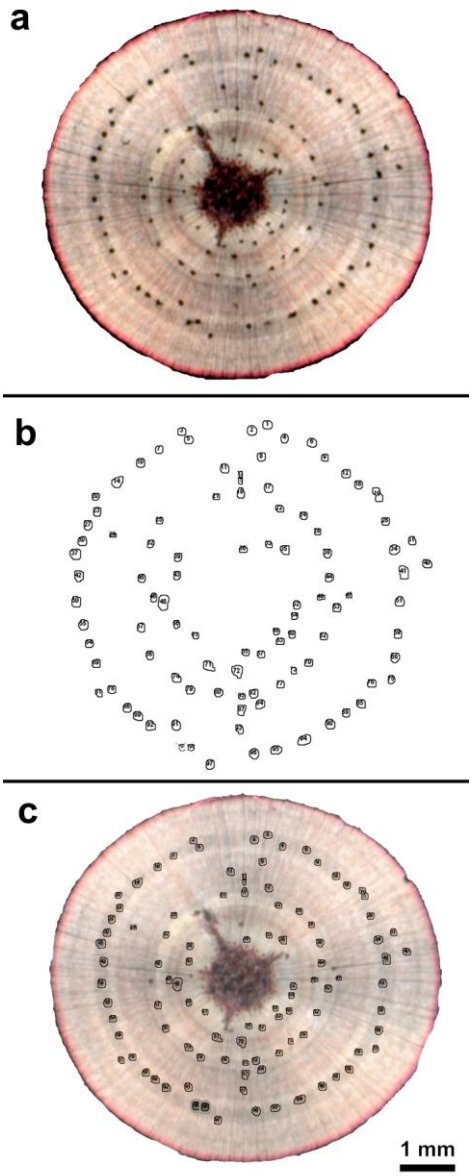

Figure 4.7 Overlay of the original and the resultant images were in good agreement verifying the detection technique.

a. Polarised light imaging improved visibility of resin canals.

b. Resin canals detected with ImageJ.

c. Overlay of images **a** and **b** showed congruent canals.

Bar in **c** = 1 mm for all images.

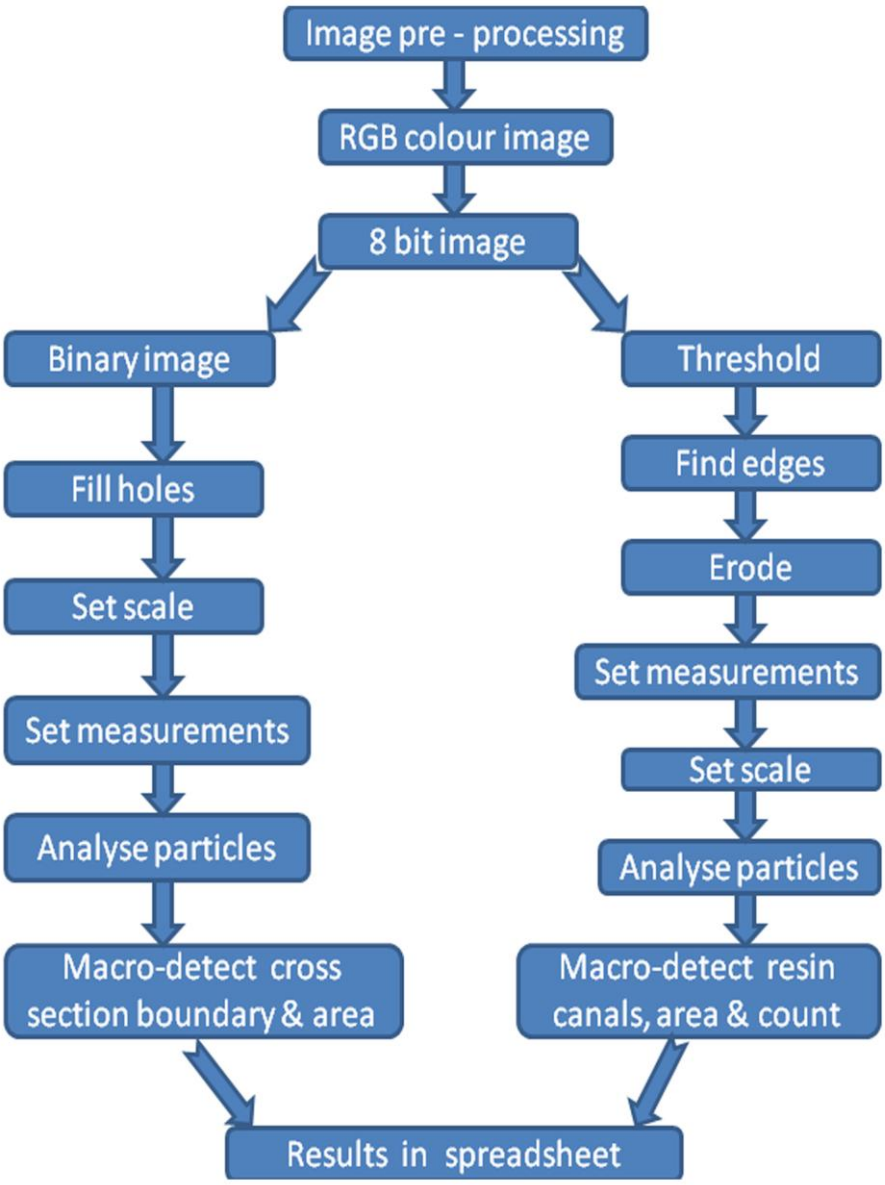

Figure 4.8 Flow diagram showing the important analysis steps involved in the processing of images to detect the cross sectional area and the number of resin canals.

Table 4.1. The relative occurrence of resin canals in rocked and tilted wood.

Treatment		Stem area (mm^2)	Resin canals (number)	Canal frequency (mm^{-2})	Canal area (mm^2)	Relative area (%)
Control	above	32.5 ± 1.6#	105 ± 10	3.26 ± 0.30	0.88 ± 0.09#	2.75 ± 0.25
(n = 10)	below	40.0 ± 1.9	131 ± 8	3.32 ± 0.23	1.13 ± 0.08	2.86 ± 0.22
Tilted	above	39.7 ± 3.7	97 ± 10#	2.49 ± 0.19*	0.82 ± 0.08#	2.08 ± 0.16*
(n =10)	below	49.7 ± 4.3	135 ± 12	2.73 ± 0.14*	1.15 ± 0.11	2.33 ± 0.11*
Rocked	above	54.3 ± 3.8*	145 ± 5*	2.78 ± 0.21	1.22 ± 0.05*	2.35 ± 0.19
(n = 10)	below	54.9 ± 4.0*	144 ± 6	2.74 ± 0.22	1.26 ± 0.07	2.38 ± 0.19

Values are means ± standard errors. Canal area is the total area of all canals in a cross section, and relative area is the percentage of the resin canal area to the total wood cross sectional area.

values significantly different in the above and below positions; T-test; $P < 0.05$.

* values significantly different from the vertical control; T-test; $P < 0.05$.

4.3.5.2 Resin canal number, frequency and area

While rocked trees showed significantly more resin canals than tilted or control trees, their relatively larger increase in cross sectional area meant that rocking caused a decrease in resin canal frequency (Table 4.1). One of the prominent features found in the rocked trees is the formation of significantly more resin canals. In the samples from above the clamp position (Figure 4.9a,c,e), the number of resin canals was highest in the rocked trees (145) and lowest in tilted trees (97). For the samples from near ground level, the highest number of resin canals was again observed in the rocking wood (144), a value similar to above the clamp. The number of canals in the 'above' position in tilted trees was significantly lower than both the rocked and control trees However, their canal number in the 'below' position was significantly higher than the above clamp position (135) which was also very close to their number in the control samples (131). This showed that the tilting treatment has considerably reduced the number of resin canals formed.

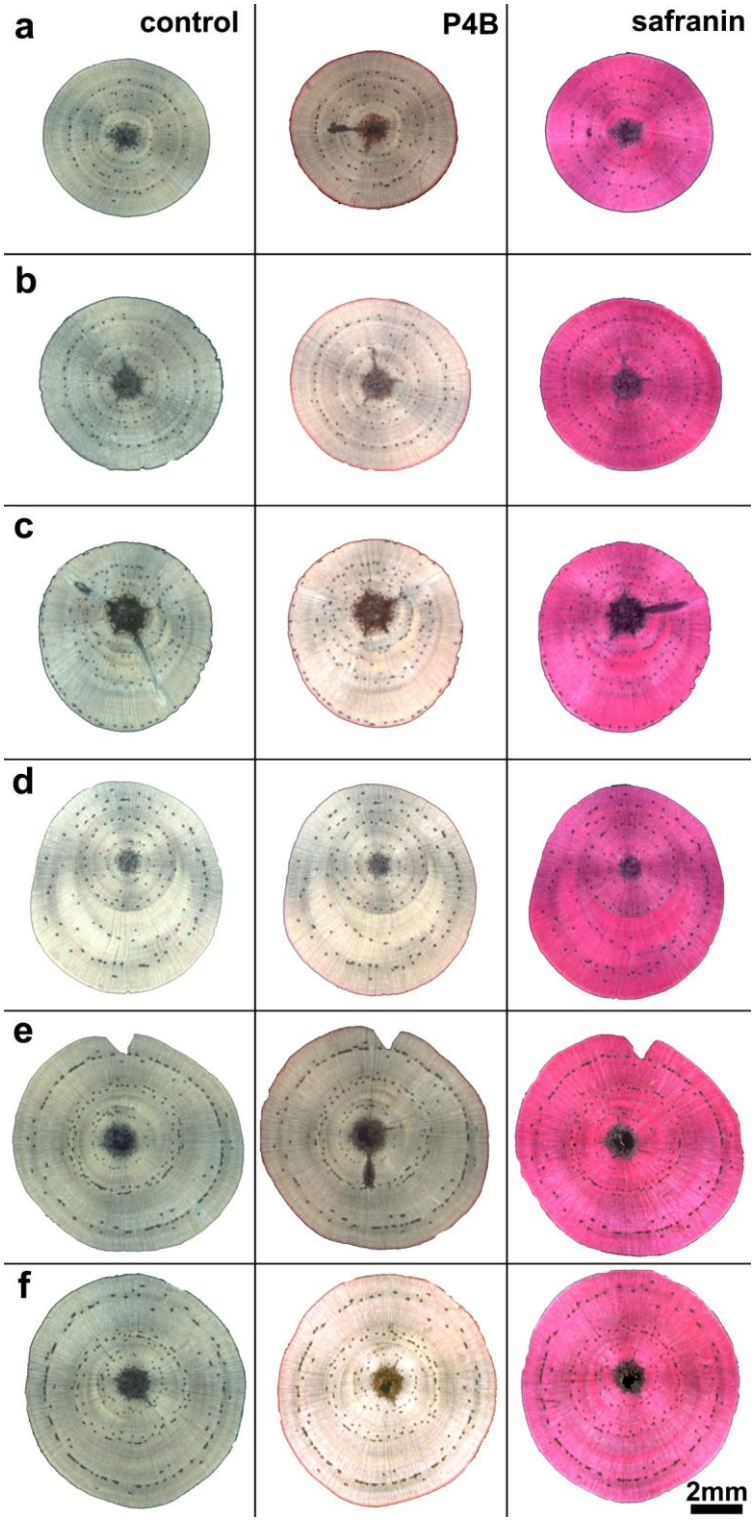

Figure 4.9 Rocking and tilting treatments enhanced wood formation compared to the freely/vertically grown controls. Transverse sections were imaged and produced at same scale to show the comparative difference in wood formation. While the left column is unstained,

middle column was stained with Pontamine fast scarlet 4B and the right column was stained with safranin for improving the visibility of resin canals.

a. Transverse section of a control (vertical) tree from above clamp position.
b. Transverse section of the same control tree from below clamp position.
c. Transverse section of a tilted tree from above clamp position.
b. Transverse section of the same tilted tree from below clamp position.
e. Transverse section of a rocked tree from above clamp position.
f. Transverse section of the same rocked tree from below clamp position.

Bar in **f** = 2 mm for all images.

Resin canal frequency, which is the number of resin canals per square millimetre of the wood, was highest in the control trees and significantly lower in the tilted trees. The higher frequency in control trees was due to their lower transverse section area. In rocked trees, however the canal frequency was the same both above and below the clamp, and the respective values were lower than in controls. Although not significant, the *P* values of 0.204 and 0.083 were tending towards significance. When the resin canal frequencies from above and below the clamp positions were pooled, then the respective *P* value was 0.03 which was significant.

The aggregate area of resin canals in rocked wood (1.22 mm^2) was significantly higher than the controls (0.88 mm^2) but comprised only 2.3% of the total transverse section area. The corresponding values at 'below' clamp positions were also higher than controls, and occupied a similar relative area. In tilted trees, however, the total area of resin canals at both positions was very close to the controls but because of he increased wood area, these canals formed a significantly lower relative area.

4.3.5.3 Arrangement and size of resin canals

There was no arrangement of the resin canals that was specific to any one of the three treatments examined, although some general trends were evident.

1) Resin canals were mainly solitary but occasionally were arranged into groups of twos and threes.

2) The highest density of canals was observed near to the pith.

3) In the tilted trees (Figure 4.9c,d), canals were almost always absent in areas with compression wood and they were found segregated to the normal wood – compression wood transition zone (see section 5.3.3).

4) While their organisation was often random, in many of the control and rocked trees, canals showed a circular arrangement.

There was no notable difference in the size or shape of resin canals across the treatments. With an average area of 8000 μm^2, canals were mostly circular and elliptical in shape except when multiple units were grouped together. Average diameter of these canals was 104 µm ranging from 46 to 186 µm. This is in agreement with the previous findings of Cown et al. (2011) (100 – 200 µm) and Cown et al. (2004) (60 – 300 µm).

4.3.6 Differential staining with pontamine and safranin

Wood transverse sections were stained with pontamine (Figure 4.9 - middle column) and safranin (Figure 4.9 - right column) and compared with an unstained control (Figure 4.9 - left column) to find whether staining can improve resin canal detection in any way. In transmitted light images, both safranin and, notably, pontamine improved the visualisation of resin canals although these stains had no effect on polarised light images. As expected, safranin has an affinity to stain the compression wood parts owing to the higher lignin content in these areas (Figure 4.9 c,d).

4.4 Discussion

4.4.1 Imaging stem transverse sections with a flatbed scanner

The imaging technique employed in this study, using a combination of the polariser films (Arpin et al., 2002) and quarter wave-retarder films (Foster, 1997; Higgins, 2010), is a novel approach to create high-contrast images suitable for any modern image analysis programme. The approach replicates the combination of polariser and the analyser films used in polarised light microscopy but is particularly useful for imaging large areas which can be difficult with conventional microscopy.

The addition of correctly-oriented quarter wave-retarder films to the optical path generated circular polarised light and substantially improved the quality of images produced by eliminating the 'Maltese cross' effect in which the image is brightest on the diagonals, and darkest in the vertical and horizontal directions. Circular polarised light has previously been suggested as a way in which to overcome these image asymmetries. (Foster, 1997; Higgins, 2010). However the use of circular polarised light with automatic image analysis is novel. This new imaging technique is simple to create, convenient to operate and provides better quality images.

4.4.2 Detection and counting of the resin canals by Image J

ImageJ has become a standard for low-cost scientific image processing. The newly written macros contain simple but powerful image analysing steps to process single or multiple images. Even though the macros were written for batch processing of 2400 dpi images, they can easily be edited to process images of other resolutions or types. For example, the time required for the computer to process the 180 images (twenty images from three different treatments, run in triplicate), and to detect and count around 28,000 resin canals was just under 1 minute.

4.4.3 Resin canal frequency and organisation

This study was designed to test the preliminary report (Apiolaza et al., 2011) that suggested an increase in the frequency of resin canals in young radiata pine saplings subjected to rocking. In this previous analysis, resin canals were manually counted in small samples of wood from only a few trees. The number of resin canals found in the rocked trees was 34.9 per mm^2, an increase from the frequency in control trees of 28.4 per mm^2. In the current study, automated counting of full cross sections of larger sample of trees, both from above and below the clamp positions, was performed. This demonstrated that there was a 15% reduction in

canal frequency from 3.3 per mm^2 in control trees to 2.8 per mm^2 in rocked trees. Although the values from above and below the clamp were not significantly different from their respective controls on their own, when pooled the data showed a significant decrease in canal frequency (P = 0.03). The reduction in canal frequency in newly formed wood from the rocked samples is likely to be greater than this 15% value, which is the reduction in frequency over the entire cross sectional area and which includes wood formed before the rocking began. Thus, the preliminary report of Apiolaza et al. (2011) is incorrect, both in the frequency of the resin canals and in the direction of changes in canal frequency induced by rocking.

An increase in canal number, but a reduction in canal frequency caused by rocking, has not previously been reported. These observations are linked, however, by the increased cross sectional areas of the trees. This may be due to the increased physiological activity owing to continued rocking, and it is evident that the rocking treatment has increased the transverse section area and the volume of wood produced substantially. This is well matched with the pioneering study by Telewski (1989) on the effect of stem flexing on one year old *Abies fraseri* (Fraser fir) trees in which he found the formation of more xylem as a result of stem flexing.

With the exception of the Apiolaza et al. (2011) report, the results of this present study match with reports in the literature on measurements of canal densities, and with observations about how canal densities can be changed. In a recent study on 14 year old radiata pine trees grown in Chile, Ananías et al. (2010) found that the resin canal frequency decreases both axially and radially and varies between 1.5 to 0.8 per mm^2 depending upon the planting density and resin tapping. Kuroda and Shimaji (1983); Mickovski and Ennos (2003); O'Neill et al. (2002) also found significant increases in the number and size of traumatic resin canals formed as a result of the wounding treatment. Similarly, Tomlin and Borden (1997) found a higher number of resin canals in high weevil resistant clones of Sitka spruce, suggesting the formation of more resin canals as a natural mechanism to resist the weevil attack by producing more resin. Nagy et al. (2000) also described how the Norway spruce trees create resistance mechanism by developing new traumatic resin canals against pathogens that may come through a newly formed wound. External stimuli, including the application of ethrel which is metabolised into the hormone ethylene, can also induce increased radial growth and formation of resin canals (Telewski et al. 1983). Hence, it is inferred that the higher area of wood produced and the formation of significantly more resin canals as a result of the stem rocking treatment can be considered as a counter mechanism of the trees to sustain against the external factors which affected their normal growth.

Resin canal formation also depends on other factors. The low number of resin canals in tilted trees can be explained by the presence of compression wood. The limited number of resin canals formed in these trees contributed to their lowest frequency rates at both positions. This concept will be returned to in Chapter 5. And the commonly observed, circular arrangement of traumatic resin canals in many of the rocked and control trees is believed to be a response to the pruning of those trees which was conducted, in part, to facilitate their placement onto the rocking cradle (Figure 4.2b) (personal discussions with Professor John Walker, School of Forestry, University of Canterbury).

4.5 Conclusions

This chapter addressed two important objectives

A new, simple and inexpensive technique has been presented to acquire high resolution images of complete wood transverse sections without the need of any sophisticated instruments or materials to visualise anatomical structures. This was achieved by creating circularly polarised light using a combination of polariser films and the quarter wave retarder plates placed on the scanner bed on either side of the microscopic slide. This novel use of the polarisers and the quarter wave retarder plates provided a better way of image acquisition for the subsequent image analysis. The possibility of scanning several slides/ samples together contributed a substantial saving in the total time of image acquisition This imaging technique was confirmed by replication with a stereo and compound microscopes on which circularly polarised light was not originally available

A semiautomatic technique was developed in ImageJ to detect, count and map the arrangement / distribution of the resin canals in wood transverse section images obtained from the flatbed scanner. The newly developed macros detect and measure the wood transverse section area, and counted and mapped the distribution of resin canals. The new method is quick and easy to operate, and gives reproducible results.

These techniques were used to test the effects of tilting and rocking trees on the formation of resin canals. Both the tilting and rocking treatments were found very effective in stimulating growth, with the former inducing pronounced eccentric growth on the lower side of the lean (compression wood) and the later also created significantly more wood compared to the control samples. The number of resin canals formed as result of the rocking treatment was significantly higher both at above and below clamp positions, but because of the increase in wood formed, their frequency was lower. The number and frequency of resin canals was significantly lower in the tilted trees most likely due to the formation of compression wood.

Chapter 5

3-dimensional visualisations and measurements of spiral grain in young *Pinus radiata* wood by image reconstruction

5.1 Introduction

This chapter describes a series of novel image analysis techniques to create 3-dimensional (3D) visualisations and measurements of spiral grain in *Pinus radiata* (radiata pine). These 3D visualisations were made possible by two different techniques. These are reconstructions of serial transverse sections in which resin canals were imaged with a flatbed scanner using circular polarised light, based on the procedure described in Chapter 4, and the use of X-ray microtomography. A simple image analysis routine has been developed in Matlab (version 2008a) (Mathworks, Natick MA, USA) that takes these 3D reconstructions and converts them into measurements of the grain in wood samples. These methods, notably the analysis of resin canals, have been used to investigate the possible link between the occurrence of spiral grain and compression wood. Confocal microscopy, using techniques described initially in Chapter 3, proved to be unsuitable for extensive and large-scale reconstructions of radiata pine grain.

5.1.1 Spiral grain and compression wood in radiata pine

The presence of compression wood and spiral grain in radiata pine timber could be described as a tree's natural mechanism to counter the biological and physiological triggers which cause their propagation. A detailed description on the deleterious effects of compression wood (see section 1.7.5) and spiral grain (see section 1.8.1) on the strength and wood working properties were given in the introduction to this thesis.

5.1.2 Biological aspects of spiral grain formation

The occurrence of spiral grain, mechanism of its formation, its causative factors, and the possible functions that spiral grain might have in trees, have fascinated researchers for more than a century. Early works suggested environmental, silvicultural and physiological factors as contributors to the formation of spiral grain (Eklund and Sall, 2000; Harris, 1989; Mattheck, 1991; Noskowiak, 1963). Subsequently, many researchers have suggested that prevailing winds may be the causative agent of spiral grain (Eklund and Sall, 2000; Skatter and Kucera, 1997; Skatter and Kucera, 1998). Other investigations have shown a strong genetic control in spiral grain formation (Hansen and Roulund, 1997; Hansen and Roulund, 1998; Harris, 1989; Kubler, 1991; Pape, 1999; Tian et al., 1996). Thus, there remain many counter arguments and alternative theories as to what factors cause a tree to develop spiral grain.

The cellular mechanisms through which spiral grain develops have also been a subject of extensive debate. Most researchers have suggested that spiral grain develops during cell division and maturation within the vascular cambium, the meristematic tissue from which wood

develops. This seems most likely, for the presence of the thick secondary wall around mature tracheids would preclude any subsequent cell movements and realignments.

As described in section 1.8 of the introduction to this thesis, the most widely accepted view of spiral grain formation has three different cell division processes which are believed to cause spiral grain development either alone or in combination (Eklund et al., 2003; Hejnowicz and Marek, 1974). They are:

1) Spiral grain angle is related to the frequency of pseudo-transverse divisions of the vertically aligned cambial cells and the subsequent intrusive growth of the daughter cells (Bannan, 1966; Hejnowicz, 1980; Kohl, 1933; Kubler, 1991; Larson, 1994).
2) Intrusive growth alone without pseudo-transverse division. This means that the pointed tips of the elongating cambial derivatives grow past one another, changing the overall cellular orientation. Both the ends of the cells need to grow in opposite directions to create a slight rotation of the cell which results in a change in the angle between the stem axis and the cell.
3) Another process involved is the imperfect periclinal divisions and the cell differentiations that accompanies those divisions (Savidge and Farrar, 1984).

There is, however, no evidence that one of the above possibilities is more likely or unlikely than others, and the mechanisms are not mutually exclusive (Eklund et al., 2003).

5.1.3 Spiral grain and compression wood in radiata pine - the unknown link

Compression wood and spiral grain are both notorious for their effects in devaluing the wood of radiata pine by adversely affecting the wood properties. Their occurrence and influence on wood properties have been well documented and reviewed (Chapter 1). However, their inter-relationship in radiata pine and other species is not understood, and has only rarely been investigated. In Chapter 2, experiments were described in which compression wood was measured in 3 year old pine samples that had been subjected to tilting. These experiments, along with extensive mechanical testing of the upper and lower halves of stem segments by Dr Shakti Chauhan and colleagues (School of Forestry, University of Canterbury), analysed whether young clones were suitable for screening in breeding programmes (Apiolaza et al., 2011; Chauhan and Entwistle, 2010; Chauhan et al., 2013; Sharma, 2013). It was observed that in some samples, the wood opposite to the compression wood had visible spiral grain on its surface and had a strong tendency to twist. The compression wood regions, however, lacked spiral grain and twist, and instead warped and bent consistent with the presence of compression wood (Figure 5.1a, b). This suggests that there may be as yet unexplored links between spiral grain and compression wood.

There is only very limited information available on the link between compression wood and spiral grain in trees, and the information that exists is often contradictory. Misra (1939, 1943a, 1943b) was the first to observe strong positive correlations between spiral grain and stem eccentricity, with the eccentricity in radial growth and the inclination of the twisted fibres correlated to one another. He also found both the degree of stem eccentricity and spiral grain angle diminish upwards in young *Pinus longifolia* trees. Misra also made several further, intriguing observations. In wood transverse sections of a normal stem, growth rings are concentric and the ray cells appear like radii running straight from pith to periphery (Figure 5.1c). In transverse sections with eccentric growth rings, due to the presence of compression wood, a sudden change of orientation of ray cells when they leave or enter compression wood was often seen (Figure 5.1d,e,f). This deviation of ray cells from its straightness seems to be associated with the change in grain. This pattern was observed within the samples collected from the School of Forestry which showed spiral grain on one side of the stem only (Figure 5.1b).

Not all research has indicated a link between compression wood and spiral grain. Both Pawsey (1974) and Zobel et al. (1965) observed less spirality in compression wood compared to normal wood of the same tree, but the difference in spirality was not statistically significant. Harris (1989) quoted Pawsey (1974); Zobel et al. (1965) as saying that “spiral grain in markedly eccentric logs abruptly becomes straight in that sector containing compression wood”. And, without elaborating further on the topic, Fielding (1967) also mentioned that ”the occurrence of compression wood can strongly affect the angle of the grain at a particular position”. However, Sleigh (1996) found more spiral grain in compression wood in radiata pine although again, the difference in grain angles was not significant. Hence, it is believed that there could be an unknown link and interaction between the formation and presence of compression wood and spiral grain in trees.

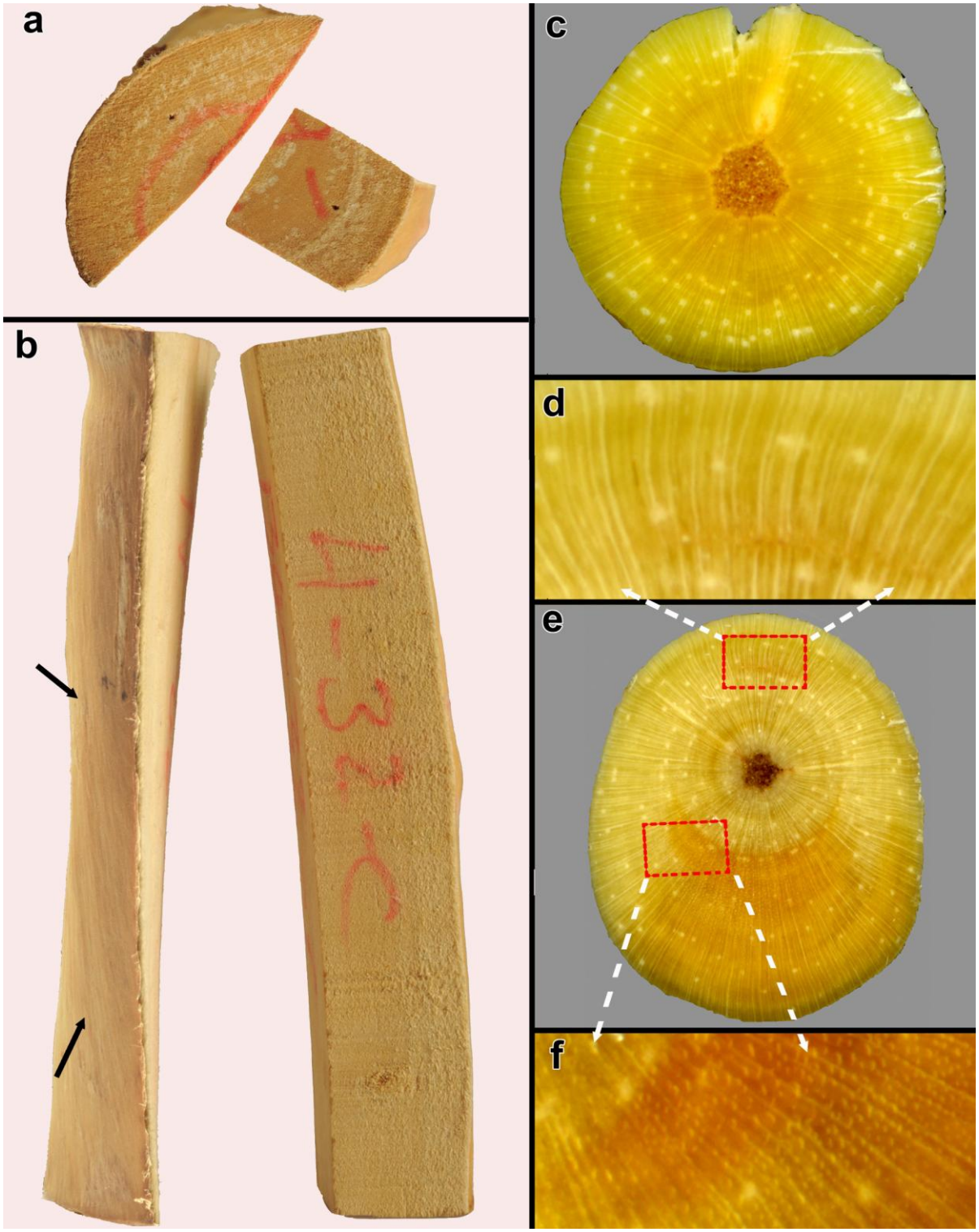

Figure 5.1 Wood samples from a leaned tree. When samples were split along their length, the lower side would show compression wood while the upper side could exhibit spiral grain.

a. Transverse sections of the splits shown in **b**.

b. When split longitudinally and dried, regions with compression wood showed bending (right) while opposite wood, which was straight while green, developed severe

twisting (left). Visible spiral grain was present on the upper surface, as shown by the traces of the resin canals (arrows).

c. Transverse section of normal wood showing ray cells running straight from pith to periphery.

d-f. Enlarged view of the transverse section showing sudden shift in orientation of ray cells.

e. Transverse section of a leaned tree showing majority of ray cells running straight from the pith to periphery with deviations potentially associated with the grain direction.

5.1.4 Methods for observing and measuring spiral grain in pine and other trees

To understand how spiral grain forms, and how spiral grain might be linked to compression wood, it is necessary to investigate grain at the cellular level. In this section, only microscopic level investigations and / or use of automated techniques including image analysis and modelling to detect spiral grain in wood will be discussed. Other methods of spiral grain detection were described in more detail in Chapter 1.

Traditionally, spiral grain has been measured either by the scribe test (Northcott, 1957) or by using destructive techniques like the radial splitting (Brazier, 1965) and serial sectioning (Bannan, 1966; Hejnowicz, 1961; Włoch et al., 2002). Remarkable studies on the mechanism of formation of spiral and wavy grain in the cambial zone of a variety of angiosperms and gymnosperms were completed by Hejnowicz and co-workers (Hejnowicz, 1961; Hejnowicz and Marek, 1974; Hejnowicz and Romberger, 1973; Hejnowicz and Romberger, 1979). These experiments used serial transverse and tangential sectioning followed by imaging with light microscopy, and subsequent manual image reconstruction to reveal the spatial arrangement of the cells. Subsequently, similar studies have also been conducted (Bannan, 1966; Harris, 1973; Jura et al., 2006; Kojs et al., 2004; Włoch et al., 2002; Włoch et al., 2001).

Recent technological advances and the availability of sophisticated software have enabled researchers to investigate spiral grain with various new techniques. These modern approaches include confocal microscopy, computed tomography and digital imaging coupled with image analysis. Notable among these has been the use of confocal microscopy for measuring interlocked grain in a tropical hardwood, *Hopea odorata* (Ogata and Fujita, 2005). By measuring the tangential lag between two optical cross sections of different depths obtained, grain angle was measured using image cross-correlation and the results compared to data generated by splitting and scoring. It was suggested that confocal microscopy might be an easier and more accurate method for measuring spiral grain than traditional methods.

Following on from Chapter 3 in which confocal microscopy was used to investigate the organisation of the cell wall in radiata pine; attempts were made to see changes in grain angle due to spiral grain by microscopy, using approaches similar to Ogata and Fujita (2005). Several fundamental limitations were found with using confocal microscopy. First, even though confocal microscopy is an excellent tool to create 2D image stacks, as wood is only partially translucent, 3D observation is limited to just a several tens of micrometers in the Z-direction (Trtik et al., 2007). Even under ideal imaging conditions, excitation light only penetrates about 100 µm into a piece of wood, and the fluorescence from the wood is attenuated according to depth. Thus, although measurements of grain angle can be made, based on the orientations

of individual tracheids, this is difficult. More importantly, however, are limitations imposed by scale. Even using a low magnification lens (10x), the field of view resolved by the confocal microscope is only a 1.5 mm square. Because an optical series (z-stack) needs to be collected for measurements of grain, and because this would require high resolution imaging (images of 2048 pixels or more) to see the tracheids with sufficient resolution, and because images would need to be taken across the entire stem, the process would be extremely slow. The time taken to make confocal observations of grain, even in a tree that was only 10 mm wide, would be significant.

Because of these limitations, other approaches were investigated to see whether they would provide better tools with which to analyse spiral grain. Several ideas have been described in the literature. Ogata et al. (2003) devised an 'inclinable soft X-ray photography' method that used soft X-rays to evaluate the individual vessel orientation in *Acacia mangium*. Using serial tangential sections, they favourably compared measurements of fibres and vessel orientation made by microscopy and Fast Fourier transforms of their X-ray images.

Other approaches to spiral grain detection are also varied. Spiral grain was measured by Saren et al. (2006) in Norway spruce using X-ray diffraction and laser scattering, by Nyström (2003) utilising the light transmitting properties of the tracheids (tracheid effect), by Ekevad (2004) using the CT direction method in which a series of computed tomography (CT) images were used to calculate the tracheid directions in 3 dimension, by Buksnowitz et al. (2008) who verified the potential of Silviscan technology that uses X- ray diffraction with a rapid assessment of spiral grain on Norway spruce logs. Sepúlveda used X- ray tomography as a tool to verify models that predict spiral grain in Norway spruce logs and sawn timber (Sepúlveda (2001); Sepúlveda et al. (2002a); (2002b). Mavrou (2007) attempted to develop a mathematical model to predict spiral grain in Sitka spruce trees with partial success while Tong et al. (2003) also successfully modelled and simulated the sawing pattern of sugar maple trees by the application of CT images and Tian et al. (1996) created a whole tree model for calculating the spiral grain in radiata pine using multiple non-linear regression analysis.

The use of image analysis by segmentation of digital colour camera images by Lu and Tan (2004), however, produced only grain information on the surface of walnut timber. Other non-destructive methods to find spiral grain include use of microwaves (Schajer and Orhan, 2006) and visible- and near infra-red-spectroscopy for lumber (Gindl and Teischinger, 2002).

5.1.5 Possible experimental approaches to image reconstructions

In this chapter, several different approaches will be compared for observing and measuring spiral grain in radiata pine. The logic behind these approaches is described in the following sections.

5.1.5.1 Using resin canals as a proxy for grain angle

Noskowiak (1963), in his classic review on the spiral grain formation in trees, mentioned the various techniques used by researchers such as Koehler (1955) for the detection of spiral grain on wood surfaces by measuring the alignment of seasoning checks, resin canals and rays which gave an early indication that the resin canals can be useful in studying grain direction. In his review on spiral grain formation in trees (Harris, 1989) also described this. Subsequently, in a study to determine the length of the resin canals in loblolly pine (*Pinus taeda*), LaPasha and Wheeler (1990) observed that the orientation of the vertical resin canals is straight relative to the axis of the trunk. Because of their large size and length, resin canals are much easier to track than tracheids (Sections 4.3.5.3, 5.4.2.2).

In *Pinus,* canals near to the pith are shorter (average length 10 cm) compared to the outer ones having average length up to 50 cm (Bannan, 1936). Furthermore, they have different cell wall characteristics, as shown by their differential staining with pontamine (Chapter 3, section 3.3.8) and reduced birefringence (Chapter 4).

There is, however, a dearth of information on the formation of resin canals in trees. Bannan (1936), through serial sections, demonstrated that the parenchymatous epithelial cells around the resin canals were formed by segmentation of fusiform elements from which the tracheids were also formed. Werker and Fahn (1969), after careful examination through cross and longitudinal sections of *Pinus halepensis* shoots, found that the pattern and development of the vascular tissues and resin canals were closely related. It is hypothesised, therefore, that the vertical resin canals in radiata pine follow the grain of the wood and that by measuring their angle of orientation, the spiral grain angle of wood can be assessed. Thus, to study the grain orientation in radiata pine wood a novel technique involving imaging the transverse sections with circular polarised light followed by 3D reconstruction of the images, using simple image processing tools available in the freeware programme ImageJ was developed (Rasband, 1997-2009).

5.1.5.2 X-ray tomography

Non-destructive evaluation of wood properties is gaining wider acceptance and computed X-ray tomography (CT) scanning is an emerging technique for obtaining internal log characteristics of standing trees, logs and converted timber. It provides an alternative technique to deal with larger pieces of wood in which sectioning is not possible. The word 'tomography' derives from Greek '*tomos*' (slice) and '*graphein*' (to write), and since its introduction in the 1970s, CT imaging has become one of the most important tools in the medical diagnosis. CT is a non-invasive technique for the 3D imaging of the internal structure of opaque material like wood (Trtik et al., 2007) and allows for the non-destructive generation of cross sections (Wei et al., 2008).

The CT system consists of a micro-focus X-ray source, an X-ray sensitive CCD camera and a precise goniometer (Bielecki et al., 2004) (Figure 5.2). The development of high-resolution CCD detectors and micro-focus X-ray tubes that provide a fine focal spot size in the micrometers range have revolutionised the CT technique in the recent past. As the pixel size of the reconstructed images is now in micrometer range, this technique is now also known as micro-computed tomography (µCT). The most important factors affecting the CT image quality (spatial resolution) are the focal spot size of the X-ray tube and the characteristics of the detector including pixel size.

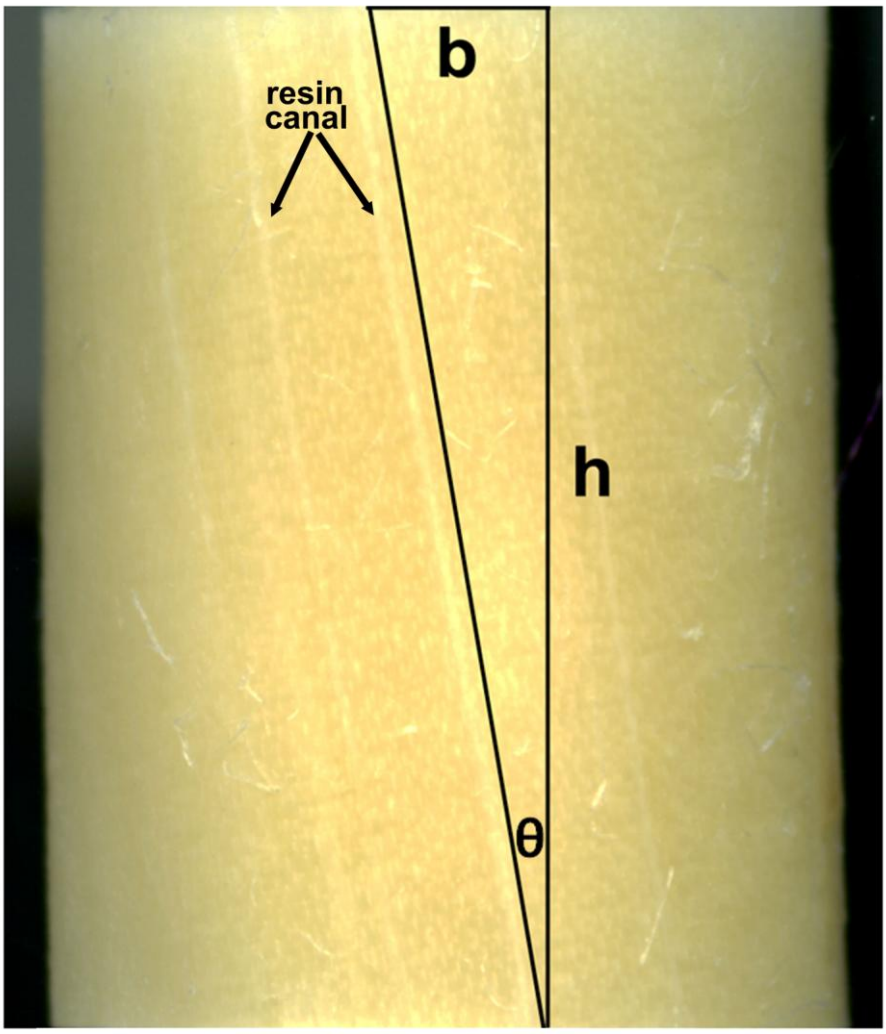

Figure 5.2 Measurement of surface grain angle, based on visible resin canals. The spiral grain angle could be calculated with the equation:

$$\Theta = \tan^{-1} (b / h)$$

where ‘h’ is the length of the resin canal visible on the surface and ‘b’ is the horizontal displacement along this length.

CT has several advantages over the traditional 2D X-ray analysis. Very small samples (1 mm x 1 mm x 1 mm) can be scanned without the need of any laborious sample preparation which avoids any damage to the sample and artefacts due to sample preparation process. The entire imaging process is fast and non-destructive, and capable of creating high-contrast images with high resolution. This enables reconstruction of images to visualise internal structures in 3D using suitable rendering software. Significant disadvantages, however, include the high experimental cost involved and the problems associated with the processing of exceptionally large computer files. Being a powerful tool to investigate the 3D structure of materials, usage of CT has increased dramatically over the past two decades. The use of CT has been widely accepted in many scientific applications including non-destructive material testing, industrial log scanning, archaeology, textiles, hydrology, entomology, plant physiology, soil science and geology (Steppe et al., 2004; van den Bulcke et al., 2009).

Besides internal log scanning, CT is being used for a variety of applications in wood processing. These include detecting defects on standing trees, wood drying and quality control (Pang and Wiberg, 1998), locating defects, knots, heartwood, and sapwood (Wei et al., 2008), sawing optimisation and determining density (Fromm et al., 2001). Schmoldt et al. (2000) and Nordmark (2002) have also studied the feasibility of identifying clear wood, and knots in oak and Scots pine, while CT has also been used for studying fibre boards under compression (Badel et al., 2008), micro-structure and resin distribution in medium density fibre boards (Walther and Thoemen, 2009) and wood plastic composites (Wang et al., 2007), and for detecting organo-silicon compounds (De Vetter et al., 2006), structural analysis of spruce wood (Trtik et al., 2007) and wood anatomy (Ekevad, 2004; Steppe et al., 2004). van den Bulcke et al. (2009) illustrated the power of X-ray computed tomography as a tool for three-dimensional wood anatomical analysis by reconstructions without labour-intensive sample preparation, whereas Wei et al. (2009) demonstrated how to create 3D images of internal log features from 2D images. Illman and Dowd (1999) were the first to successfully use µCT for characterising the 3D geometry of pine wood, whereas Sepúlveda (2001); Sepúlveda et al. (2002a); (2002b) utilised X-ray tomography as a tool to verify his model to predict spiral grain in Norway spruce timber. Bhandarkar et al. (1996); (1999) developed a new system for the detection and rendering of internal log defects using computer tomography. Investigation of these published reports concerning novel approaches for detecting spiral grain shows that most detected the grain at a “macro” level, describing the overall grain deviation.

There is, however, a dearth of a suitable method for studying changes in grain at the cellular level. Information at cellular level is essential to understand the incremental changes in tracheid orientation that contribute to the formation of spiral grain.

5.1.6. Objectives

The major objectives of this chapter were:

1) To devise an image processing method to create the 3D visualisation of the organisation of resin canals from wood transverse sections, based on the newly developed image acquisition techniques (Section 4.2.3) using circular polarised light, and to correlate this to 3D visualisation of compression wood determined from images collected with a stereo fluorescence microscope.

2) To verify the potential of computed X-ray tomography as a tool to study spiral grain in wood.

3) To determine which of the preceding approaches is / are most suitable for studying spiral grain at a cellular level.

4) To make mathematical measurements of change in grain, and investigate the possible links between compression wood and spiral grain.

5.2 Materials & methods

5.2.1 Sample preparation

Eight month old stems from rocked, tilted and control trees (Section 4.2.1) were analysed in this study. The tilted trees had produced compression wood on their lower side of the lean. Stem sections preserved in FAA (approximately 25 mm long) were washed and a vertical line scored along the surface as a baseline from which to measure grain angle, and also to act as a reference mark during image reconstructions.

5.2.2 Calculating the visible grain angle

Ten stem samples each from control, rocked and tilted trees were imaged using reflected light with a professional flatbed scanner (Epson Perfection V700 Photo) (24 bit colour, 2400 dpi). Resin canals visible on the wood surface enabled the calculation of the spiral grain angle. From the tilted samples, the compression wood and the opposite wood surfaces were scanned separately. Measurements ('b' and 'h') of 3 separate resin canals each were obtained from every sample surface directly by Photoshop. Spiral grain angle on the sample surface was calculated using the simple formula,

$$\textbf{Spiral grain angle, } \theta = \tan^{-1}(b / h)$$

where 'h' is the length of the resin canal visible on the surface and 'b' is the horizontal displacement along this length (Figure 5.2).

5.2.3 Sectioning

Samples from five trees from each of the vertical, rocked and tilted samples were randomly selected. After levelling the surface, a sledge microtome (Reichert, Vienna, Austria) was used to cut 60 µm-thick, complete (8 to 10 mm in diameter) transverse sections. A minimum of 72 sections, covering at least 4.5 mm of the stem, were generated for each stem. Sections were transferred in to serially numbered culture dishes, washed in warm distilled water and blotted on a filter paper for few seconds. They were carefully transferred to serially numbered slides and mounted in glycerol.

5.2.4 Image capture

To study the spatial variation in the orientation of resin canals, serial cross sections were imaged using circular polarised light as described in section 4.2.3 (Foster, 1997; Higgins, 2010; Patselt, 1985).

Lignin autofluorescence from compression wood was also imaged in these transverse sections with a Leica DFC 310 FX digital camera connected to a stereo-fluorescence microscope (model MZ 10F Fluo, Leica Microsystems, Heerbrugg, Switzerland), using blue excitation and green fluorescence under constant imaging conditions.

To ascertain the suitability of tracing resin canals as a means through which the orientation of the grain might be studied, transverse sections from a single vertical tree were photographed at two locations adjacent to resin canals with a Leica compound microscope (DMI6000 CS, Leica Microsystems, Wetzlar, Germany) and a Leica DFC 310 FX digital camera.

5.2.5 X-ray tomography

A high-resolution X-ray microtomography system, SkyScan 1172, (SkyScan, Kontich, Belgium) located at the Otago Centre for Electron Microscopy (Department of Anatomy, University of Otago, Dunedin, New Zealand) was used to acquire X-ray tomography images (tomograms) of the wood specimens with resolutions as low as 2-3 µm (Figure 5.3). Stems from which serial sections had been cut were imaged so that direct comparisons could be made between X-ray tomography and serial sectioning approaches. Two vertical and two tilted trees were used for this analysis.

Beyond drying the specimens, no specific sample preparation was required for the X-ray tomography imaging. The sample was mounted vertically on the specimen holder with Blutack (Bostik, Australia) (Figure 5.3b). The specimen was rotated at 0.3^{o} increments through an X-ray beam which produced a series of images that were collected with a high sensitivity (10 megapixel) digital CCD camera, Hamamatsu HRF (Hamamatsu Photonics, Hamamatsu City, Japan) (Figure 5.3c). These images were processed through specialised software (SkyScan 1172 µCT Control program, version 1.5A, build 1) and an image reconstruction package (NRecon, version 1.5.1.4) to produce a series of transverse sections from the raw X-ray images. Further processing of these transverse section images was completed with Photoshop and ImageJ to create the 3-dimensional reconstructions that visualised resin canal organisation.

5.2.6 3D visualisation of spiral grain from scanned images

3-dimensional reconstruction of the resin canals imaged with the circular polarised light resulted in the visualisation of spiral grain. For these polarised light scanner images, the background of each image was filled with white to enable a uniform thresholding and images were partially aligned manually in Photoshop. Subsequent image processing was completed using ImageJ.

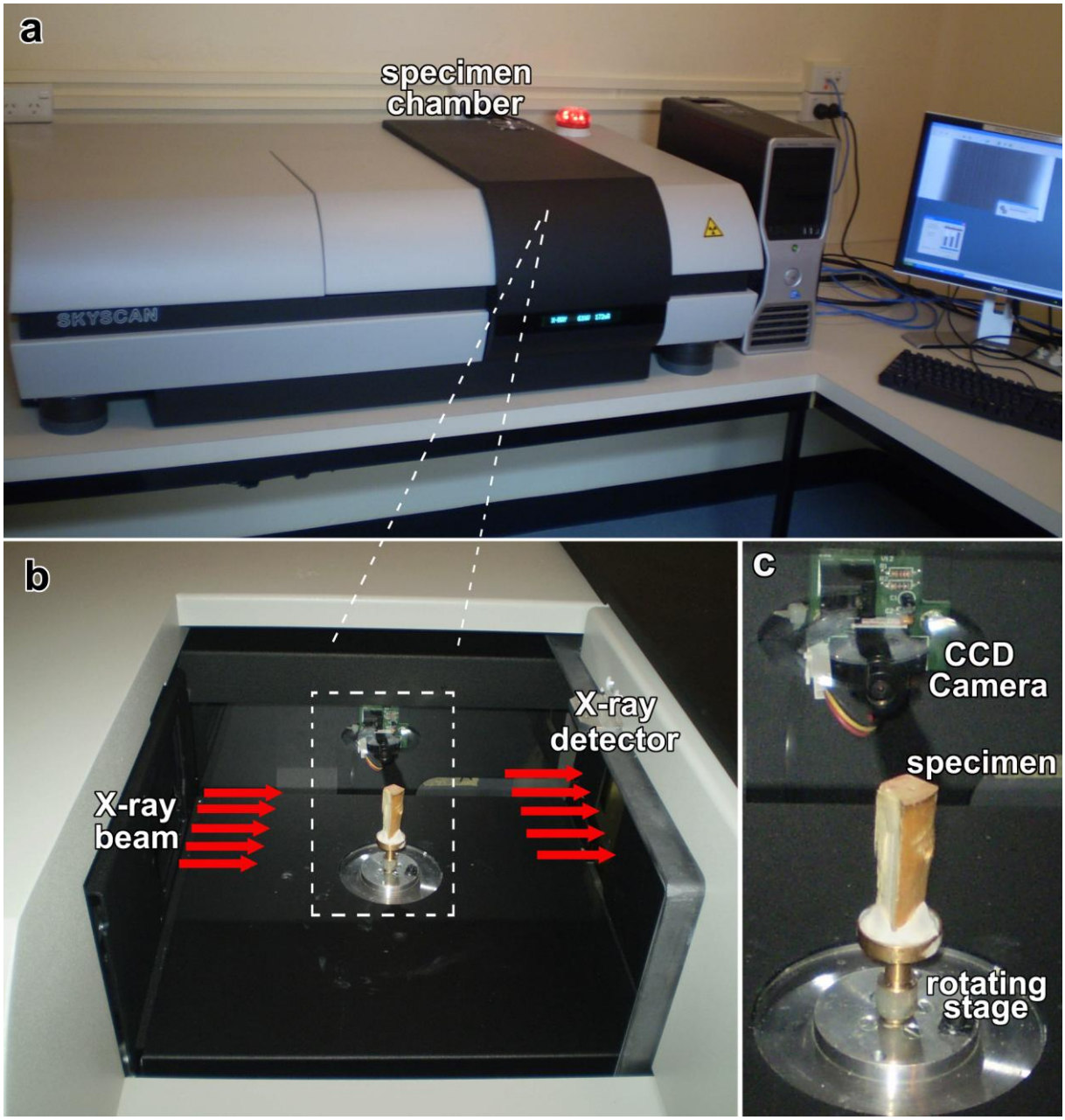

Figure 5.3 X-ray microtomography using SkyScan 1172 system.

a. The system consists of a SkyScan 1172 machine and a controlling computer at right.

b. A view of specimen chamber. A micro-focused, air-cooled X-ray beam passed through the specimen and images were collected at the detector.

c. A 10 megapixel digital CCD camera captured images of the specimen that was mounted onto the specimen holder with Blutack as it was rotated at incremental angles. These images were converted into transverse section images using the software.

Individual images were converted to 8 bit images and combined into an image stack. Brightness and contrast were standardised within the stack by '*Image'* – '*Adjust*' – '*Brightness/ Contrast.'* The canvas size was then made square by '*Image'* – '*Adjus*t' – '*Canvas size'* and the images were aligned using an ImageJ plugin named '*StackReg*'. Because this plugin defaults to aligning items within the image, and because the non-birefringent resin canals dominate the image, the '*StackReg*' plugin gave straight resin canals and induced a twist within the stem, as judged by the rotation of the vertical score mark. A custom plugin, '*Cumulative Rotation'* (see Appendix 5.1) was used to correct this rotation, and to make the score mark straight within the image stack. Once the stack was aligned, uniform thresholding was applied by '*Image*' – *'Adjust'* – '*Threshold*' and the scale converted from imperial units into metric units (94.49 pixels per mm for a 2400 dpi scanner image).

The '*Analyse particles'* function was run to detect and measure the location of the resin canals with the following settings: size= 25 - 500 square pixels, circularity= 0.5 to 1.0, and with the '*Show Masks*' selected. The measurements to be collected from the image were set with the '*Analyze'* – '*Set measurements'* function, and were '*Area'*, '*Centroid*' (that is, where the centre of the object was) and '*Stack position*'. The output from the 'Show masks' option was a file that showed the location of all the resin canals detected, with non-measured objects excluded, and this was used to generate a 3D image of spiral grain using the plug-in '*3D Viewer.*'

In the 3D reconstructions shown, either as a figure or as a movie the z direction has been compressed 6-fold. This comes about because ImageJ has made the reconstruction with cubic voxels, whereas the horizontal (xy) resolution is 10 um, and the vertical resolution in the z direction is 60 um (the slice thickness). This makes the angles appear steeper than they really are, but it allows our eye to see the differences. Stretching the figure 6-fold in the z direction does not actually work unfortunately. The important steps involved in this image processing are indicated in the flow chart shown in Figure 5.4a.

5.2.7 3D visualisation of compression wood

Similar to the reconstruction of the resin canals to show the spiral grain, compression wood was visualised from the stereo fluorescence microscope images. The lignin autofluorescence images collected from the stereo fluorescence microscope had their background adjusted to black to enable uniform processing, and were partially aligned with Photoshop. Blue and green channels of these RGB images were removed by '*Curves*' function. The brightness / contrast were adjusted such that only the compression wood parts were visible. Subsequent image processing was completed in ImageJ. The canvas size was made square, and the images were aligned using a plugin named '*StackReg*'. A 3D projection of this image stack

was made to visualise compression wood, using 'Plugins' - '*3D*' - '*3D Viewer*' plugin. The important steps involved in this image processing are shown in Figure 5.4b.

5.2.8 3D visualisation of spiral grain and compression wood

Another 3D image reconstruction was made to visualise both spiral grain from scanned images and compression wood from fluorescence images. This was achieved by creating a new stack of images using both Photoshop and ImageJ.

From the fluorescence microscope images, the red channel was separated as detailed in the previous section. Similarly, resin canals were identified from the circular polarised light scanned images as detailed in 5.2.5.1. Overlay of these images was made by Photoshop and saved as TIFF images with subsequent image processing completed in ImageJ. An image stack of the overlays was made, and a 3D projection of this image stack was made to visualise compression wood using '*Plugins*' - '*3D*' - '*3D Viewer*' plugin. The flowchart (Figure 5.4c) depicts all the important image processing steps involved in the 3D reconstructions and visualisation of spiral grain and or compression wood.

5.2.9 3D visualisations from X-ray tomograms

A protocol similar to that described in section 5.2.6 was followed to process images to visualise spiral grain in wood. However the plugins '*Stackreg*' and '*Cumulative rotation'* were not required for these reconstructions as the individual tomograms were aligned by the SkyScan software itself. After thresholding and applying the '*Analyze particles*', on the image stack, its 3D view was reconstructed with the '*3D viewer*' function.

5.2.10 Calculation of grain angle using Matlab

An image processing protocol was developed by writing suitable algorithms in Matlab to detect the change in orientation of the resin canals which showed the spiral grain in these circular polarised light scan images (Appendix 3). The same protocol was used to process the X-ray tomograms.

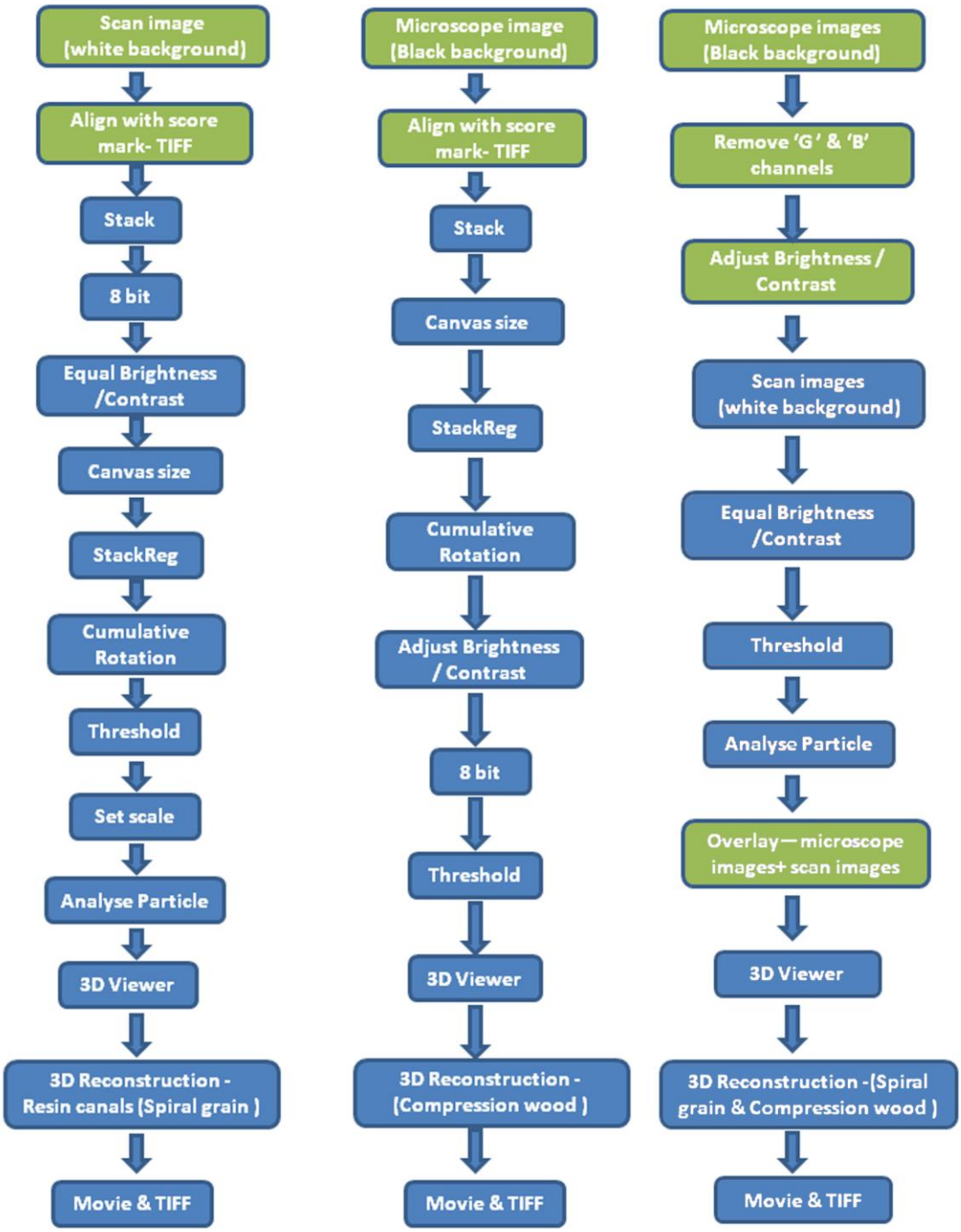

Figure 5.4 Flowchart for the 3D visualisation of compression wood and spiral grain by processing of circular polarised light images. Green and blue colours denote the steps completed by Photoshop and ImageJ respectively. Image processing steps for visualising the spiral grain is given in the left column.

While the middle column represents the steps for visualising compression wood and the steps for visualising both compression wood and spiral grain are given in the right column.

5.3 Results

5.3.1 Calculating the visible spiral grain angle

Using scanned images and Photoshop (Figure 5.5), spiral grain was measured on the surface of 10 replicates each from vertical controls, rocked trees and trees that had been artificially leaned. Spiral grain angle was found highest on the surface of the control trees and, although the difference was not statistically significant, was lower in the rocked trees (Table 5.1). As the rocking treatment itself was meant to re-create the action of the wind, this result was a surprise as it was contrary to the existing wind theory on generation of spiral grain. Opposite wood samples in the tilted trees showed similar angles to vertical controls and rocked wood. However, the spiral grain present in compression wood was significantly lower than both the vertical control and the opposite wood value.

Table 5.1. Variation of spiral grain among rocked, tilted and control trees.

Treatment	n	Surface spiral grain angle (degrees)
Control trees	10	8.6 ± 1.0
Rocked trees	10	7.6 ± 0.7
Tilted trees		
upper surface (normal wood)	10	7.6 ± 0.6
lower surface (compression wood)	10	6.3* ± 0.4

Values are means ± standard errors.

* values significantly different from the vertical control; T-test; $P < 0.05$.

5.3.2 Resin canals run parallel to tracheids

Analysis of serial transverse section images confirmed that tracheids run parallel to resin canals (Figure 5.6). Serial transverse sections were imaged with a compound microscope at an identical location at depths from zero to 900 µm. Images were then converted to 8 bit and by '*Process'- 'Find Edges'* function in ImageJ to outline the tracheids in transverse sections. These images showed several tracheids, highlighted with white dots, that stayed at identical

locations with respect to the resin canal indicating that they are traceable as long as their length permits and that the canals can be used as a proxy for grain.

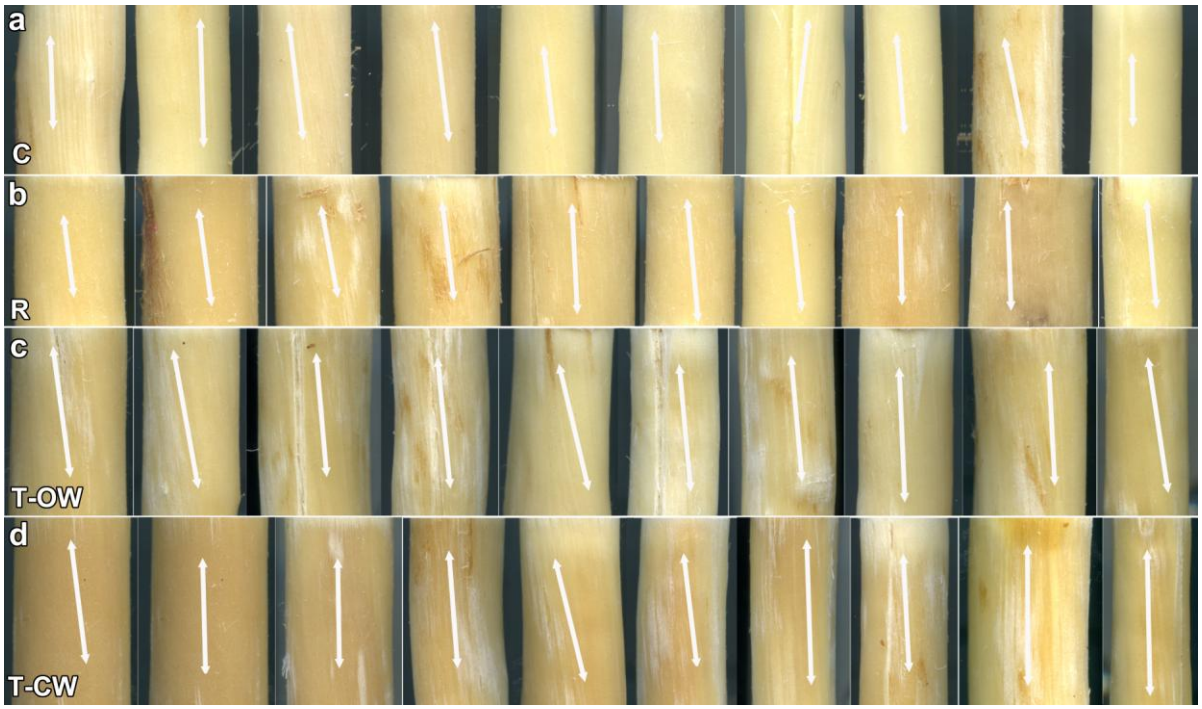

Figure 5.5 The surfaces of 30 trees were scanned with reflected light to measure the visible surface grain angle.

a. Vertical controls (C).

b. Rocked trees (R).

c. Opposite wood in the tilted trees (T-OW).

d. Compression wood in the tilted trees (T-CW).

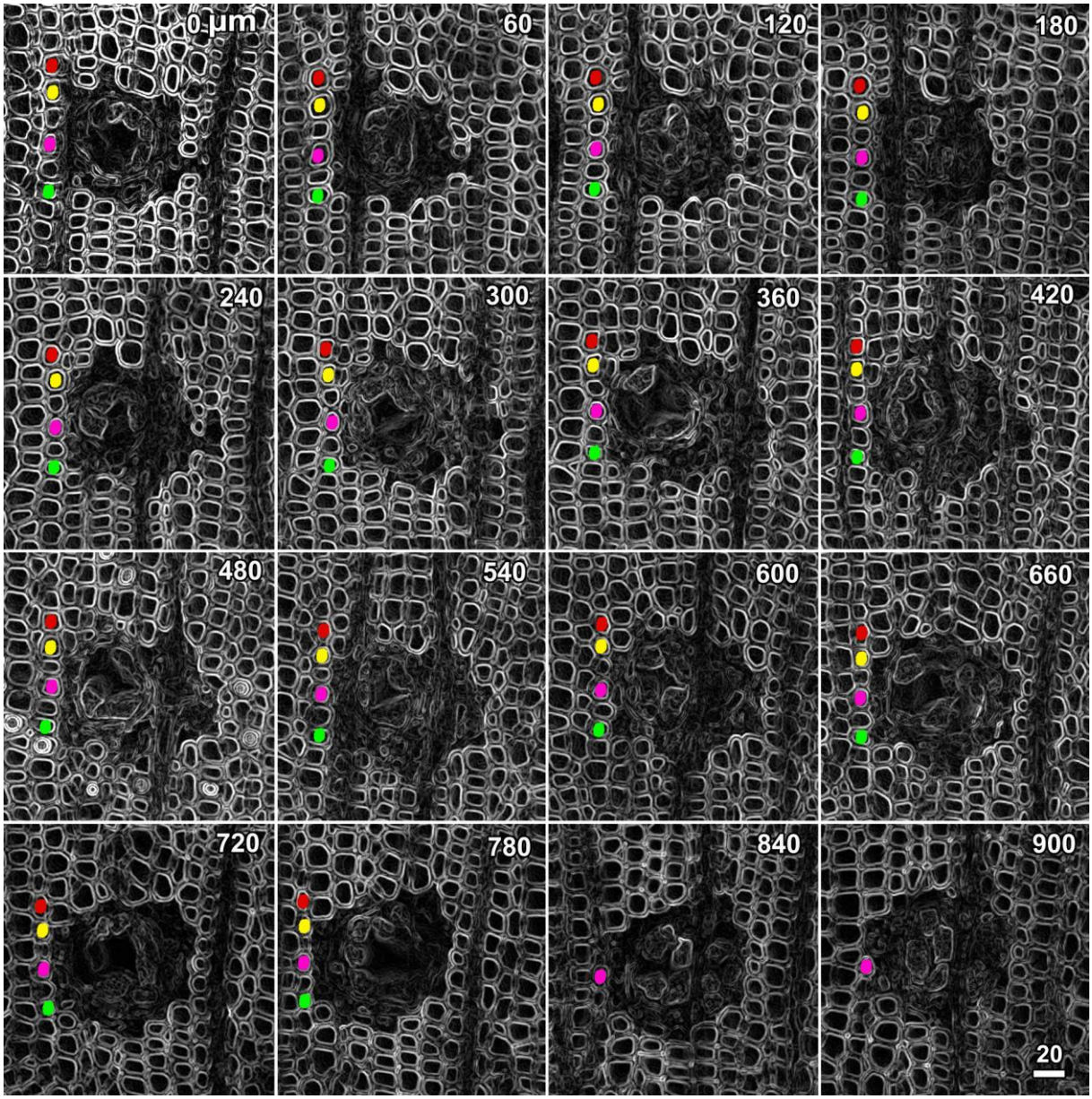

Figure 5.6 Resin canals run parallel to tracheids indicating the change in grain. Serial cross section images were collected (zero to 900 µm) with a compound microscope. Images were then converted to 8 bit and by '*Process'- 'Find Edges'* function in ImageJ tracheids' cross sections were outlined. Images showed several tracheids (a few of them are shown as coloured dots) staying at identical locations indicating that they are traceable as long as their length permits.

Bar = 20 µm for all images.

5.3.3 3-dimensional image reconstructions and analysis of grain orientation

The first approach to analysing spiral grain was to use serial sectioning. Unlike previously published studies in which the area analysed was limited, 60 µm-thick whole cross sections (8 to 10 mm stem diameter) were analysed, and resin canals were used as a proxy for grain as these cells form from the same fusiform initials as the tracheids and run parallel to them (Bannan, 1936; Werker and Fahn, 1969). In the initial experiment, 192 sections were collected from over 10 mm of the stem from a straight grown tree. These were scanned in colour at 2400 dpi with circular polarised light (see section 4.2.3). After the individual images had been converted into a stack, they were centred and aligned based on the vertical score mark that was visible within the sections. The resin canals were identified by thresholding, and a 3D model generated with ImageJ.

Resin canals were arranged in concentric bands around the pith with the canals nearest to the pith nearly straight and those in the outer regions twisted leftwards (Figure 5.7, movie 2). As the resin canals follow the tracheids in radiata pine, this twisting of the resin canals demonstrated the rapid and early onset of spiral grain within the first several millimetres of wood formation outside the pith. The angles of the resin canals were calculated in Matlab by joining the centres of the resin canals measured in ImageJ into chains. When plotted as a function of the distance from the centre of the stem, an increasingly left-handed twist to the grain was evident (Figure 5.8a). The angular distribution of these canals was symmetric around the centre of the stem (Figure 5.8b). However, observation of this grain pattern and the measured grain angles demonstrated that the changes in grain were not uniform, with a slight decrease in grain twisting present between the inner and outer parts of the wood. Comparisons were made to the fluorescence images of the sections (Figure 5.8c). The arcs of compression wood were relatively constant over the distance measured (see below for a more in depth analysis of this). Those resin canals formed before the compression wood formation had less spiralling than the canals formed immediately after the compression wood formation. These observations suggesting a possible link between the formation of compression wood and spiral grain in radiata pine (Figure 5.8c,d).

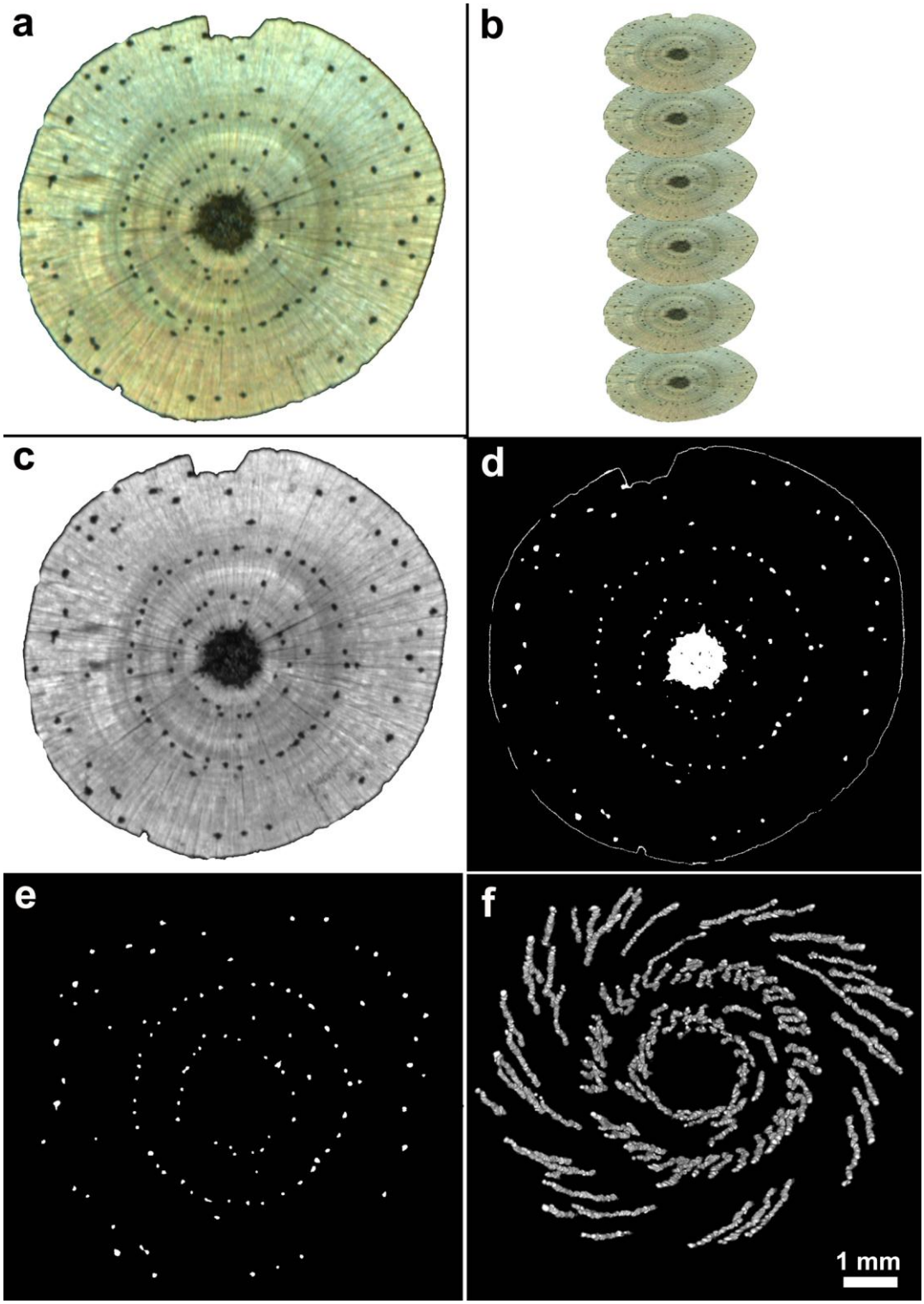

Figure 5.7 3-dimensional visualisation of resin canals and spiral grain from a vertical tree. In this 3D reconstruction shown, the z direction has been compressed 6-fold. This is because ImageJ made the reconstruction with cubic voxels, whereas the horizontal (xy) resolution is 10 um, and the vertical resolution in the z direction is 60 um (the slice thickness). This made the

angles appear steeper than they really were, but it allowed our eye to see the differences. Stretching the figure 6-fold in the z direction did not actually work unfortunately.

a. Circular polarised light scan image of the transverse section.

b. Stack of images created with ImageJ.

c. Image converted to '*8 bit.'*

d. Image thresholded.

e. '*Analyse particles'* was applied to detect resin canals which are shown as white dots.

f. 3-dimesional visualisation of resin canals and spiral grain using the entire stack.

Bar = 1 mm for all images.

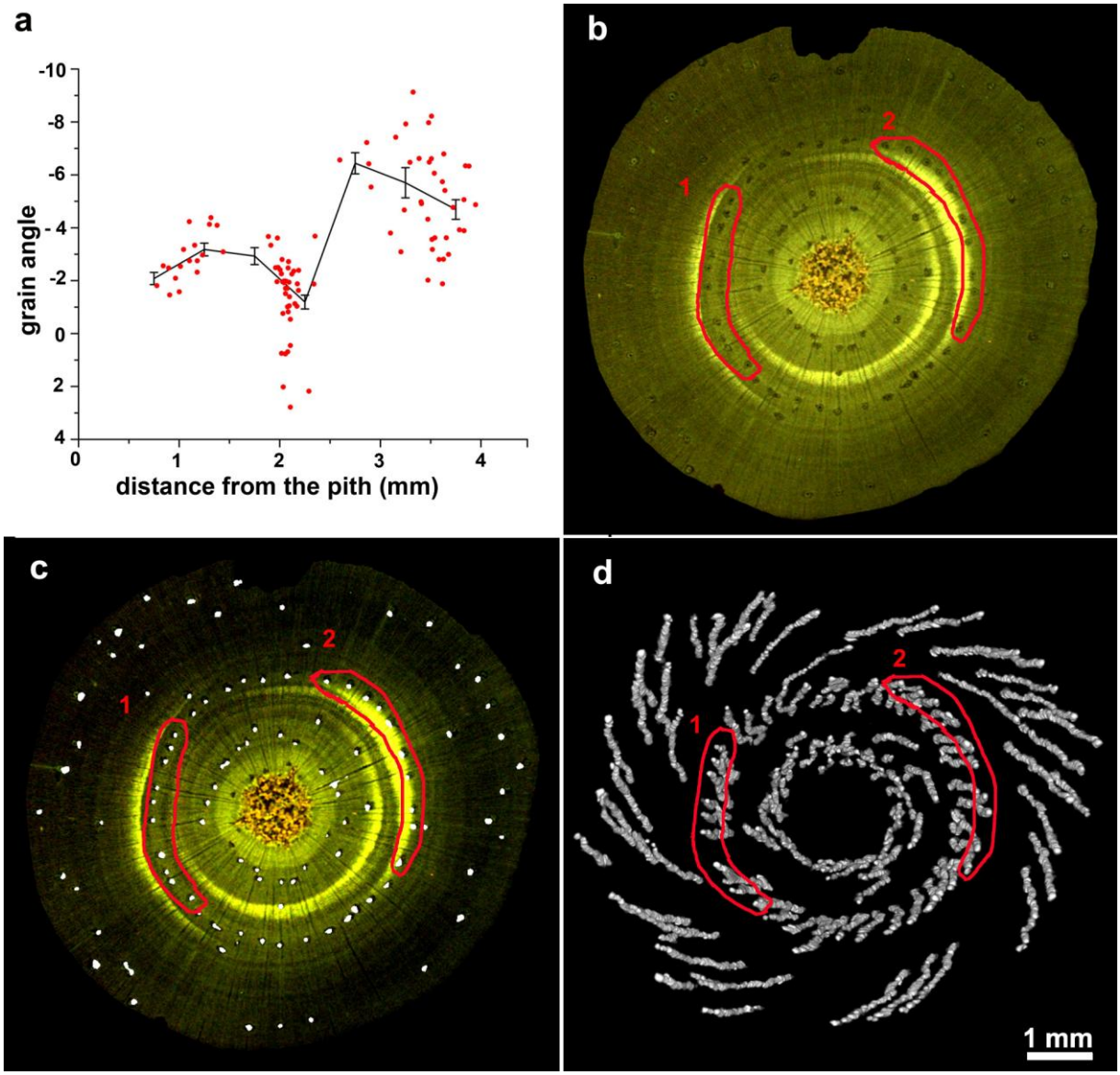

Figure 5.8 The effect of compression wood on the orientation of resin canals.

a. Measurements of grain angle at different distances from the centre of the stem and how grain angle progressively left-handed.

b. Fluorescence microscope image collected using blue excitation and green fluorescence with a compound microscope showing compression wood arcs.

c. Overlay of a fluorescence microscope image and the corresponding polarised light scan image in which resin canals were detected. Two regions are highlighted. Region (1) shows resin canals formed prior to the formation of a compression wood band whereas region (2) shows resin canals formed after the formation of a similar band of compression wood on the opposite side. These resin canals show less leftward twisting.

d. 3d reconstruction of the resin canals over a length of 10 mm showing the change in grain in regions before and after the formation of compression wood. In region (1), resin canals formed before compression wood formation spiralled less compared to the canals formed after the formation of compression wood in region (2).

Bar in **d** = 1 mm for **b**-**d**.

A similar analysis of serial sections from a tilted tree was also conducted. Sections were imaged with circular polarised light and subsequently with a stereo-fluorescence microscope. 3D reconstruction of the circular polarised light images revealed the organisation of the resin canals in these tilted trees. These trees formed compression wood in their lower halves and the organisation of the canals around the pith showed a remarkable asymmetry, as previously discussed in Chapter 4 (section 4.3.5.3). There were fewer canals in the compression wood region and these appeared to be much straighter than the twisted canals found elsewhere. Those canals in the opposite wood regions showed similar characteristics of canals in the control trees described earlier.

Fluorescence microscopy demonstrated its capability to detect compression wood in wood cross section images. The serial sections collected over 4.5 mm revealed that the pattern of compression wood looked similar at different depths (Figure 5.9a-c). 3D reconstructions of the fluorescence microscope images demonstrated this showing that the formation of compression wood was uniform (Figure 5.9d-f). When fluorescence images were analysed to compare the locations of the resin canals and the grain orientation (Figure 5.10a-c), it was found that the number and amount of twisting of the canals in the compression wood regions were less than in opposite wood (Figure 5.10d-f).

Because of the apparent interplay between compression wood and spiral grain, a more extensive analysis was initiated. Fortunately, and fortuitously, the experimental material used for the analysis of resin canals in Chapter 4 proved to be ideal experimental material, and the serial sectioning approach was extended to 13 more trees covering control, rocked and tilted trees. However, in these experiments, only 72 sections covering a stem length of nearly 4.5 mm were sectioned and reconstructed. Circular polarised light images of the transverse sections of all the sample stems studied are shown in Figure 5.11. 3D reconstructions of images collected with circular polarised light comparing orientation of resin canals (an indication of spiral grain) of all the fifteen trees studied are shown in Figure 5.12. The image in Figure 5.12c shows the same tree that was shown in Figures 5.7 and 5.8, but in this case the number of sections has been limited to 72 (rather than 192) to match the other samples.

In general, the resin canals were arranged circularly around the pith with much less twisting. In both the control and rocked trees, canals further away from the pith had more twisting towards left. However, in the tilted trees there were fewer canals in the compression wood and these were straighter than the twisted canals. This is consistent with Cown et al. (2003) who observed few or no canals in radiata pine compression wood. Even though the pattern of resin canal orientation and grain change had some consistency, there were large variations among the different trees in the amount of twisting present.

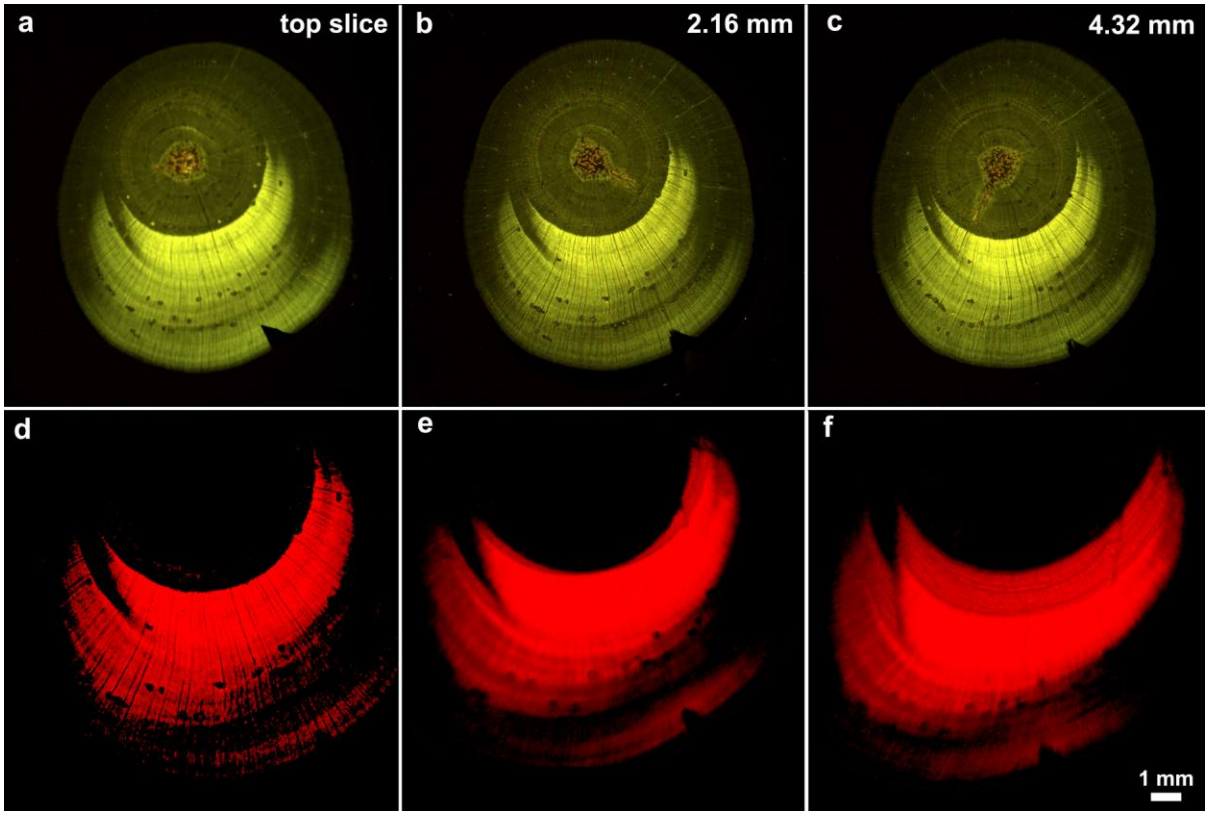

Figure 5.9 3-dimensional visualisation of compression wood which was relatively similar along the length of stem. Fluorescence microscope images of the serial cross sections were processed to generate the 3D views.

a. Fluorescence microscope image of transverse section of a leaned tree.

b. A similar image collected at 2.16 mm from the section in **a.**

c. Another image collected at 4.32 mm from the section in **a** demonstrating the uniform pattern of compression wood along the length.

d. Stack of fluorescence images whose blue and green channels were removed and brightness/contrast adjusted to show only compression wood.

e. Top view of the 3D reconstruction.

f. Side view of the 3D reconstruction.

Bar in **f** = 1 mm for **a**-**f**.

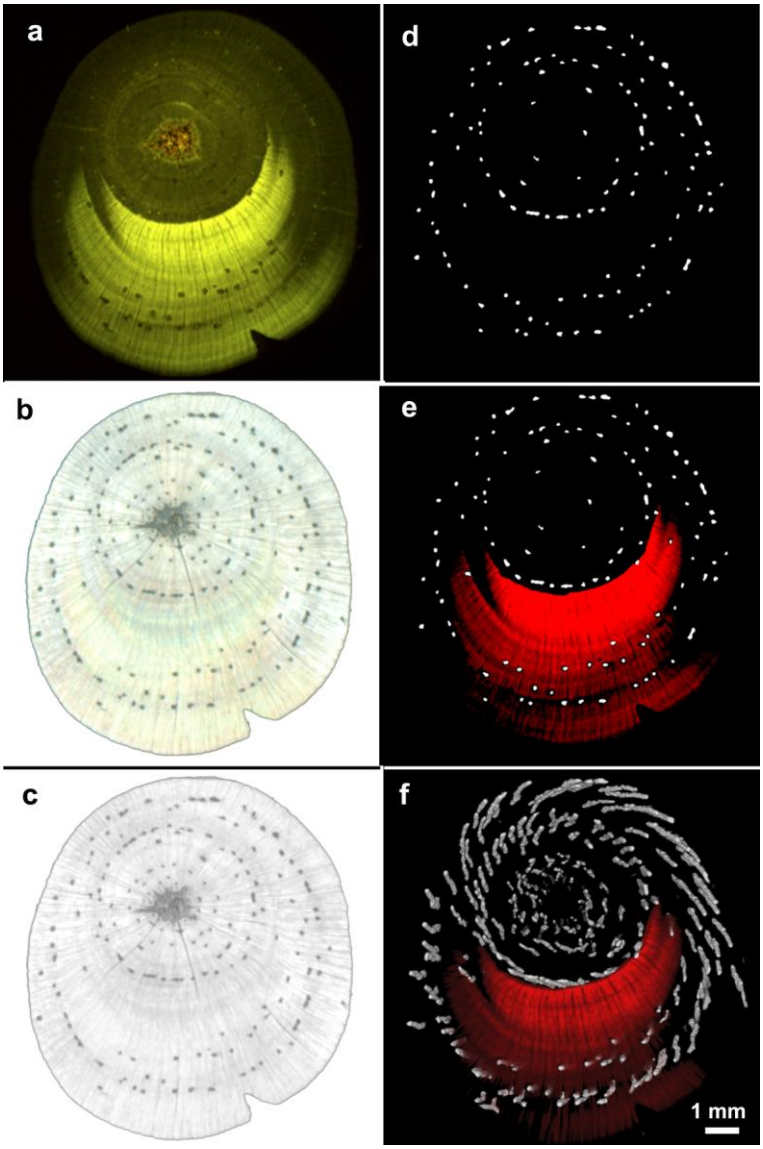

Figure 5.10 A 3-dimensional visualisation of the link between compression wood and spiral grain.

a. Fluorescence microscope image of the transverse section of a leaned tree.

b. Circular polarised light scan image of the same transverse section.

c. Image converted to '*8 bit'.*

d. The '*Analyse particles'* function was applied to detect resin canals, shown as white dots.

e. Overlay stack of fluorescence images **(a)** whose blue and green channels were removed and corresponding images in which resin canals were detected **(d)**.

f. 3-Dimesional visualisation of compression wood and spiral grain.

Bar in **f** = 1 mm for **a**-**f**.

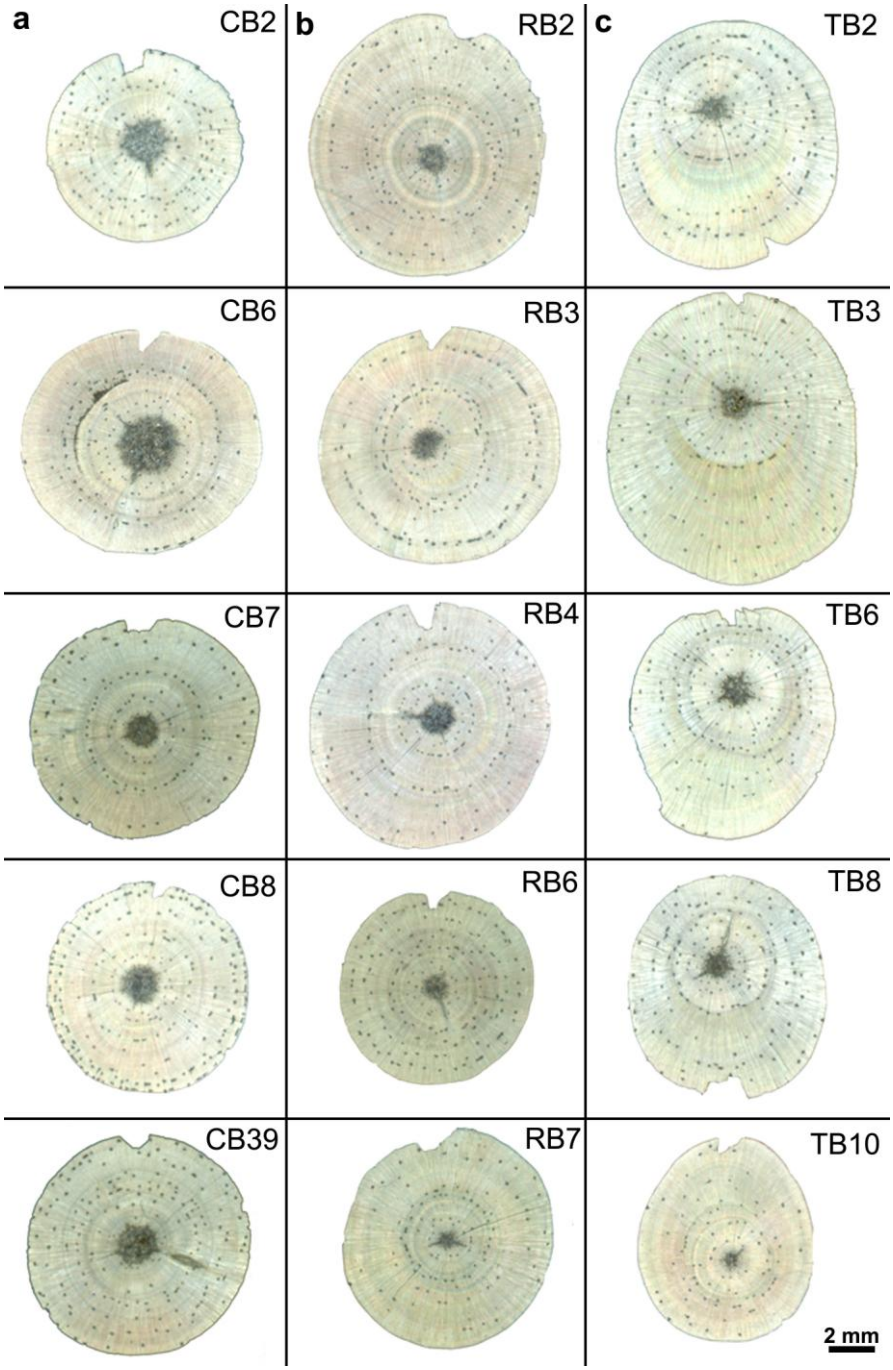

Figure 5.11 Circular polarised light images of the transverse sections of all the samples studied.

Bar = 1 mm for all images.

5.3.4 Numeric analysis and quantification of spiral grain using Matlab

As the link between compression wood and spiral grain was visually conspicuous, a numerical analysis to find the angular variation of grain was conducted. The location of resin canals was identified in each section using ImageJ, using the protocols described in Chapter 4. These locations were then 'strung together' into chains using algorithms developed in Matlab by Dr Jonathan Harrington (Scion, Rotorua, New Zealand). A detailed protocol for this analysis, along with the 'm' files is given in Appendix 3). Matlab calculated the location and angle of these chains of identified resin canals with the angular variation in grain change represented as arrows as recorded by Matlab (Figure 5.13c). The arrowheads represent the canal at the top of the stem while the beginning of arrow is the canal at other end of the stem. Thus, the arrow lengths indicate the magnitude of the grain, and the arrow direction the grain handedness. In all the controls and rocked trees, the grain was nearly straight or right-handed near the pith while the grain became more left-handed away from the pith, which was expected.

From these measurements, graphs were developed showing grain angle of the resin canals, indicated by red dots, plotted against distance from the approximate centre of the section for each tree (Figure 5.13, 5.14 and 5.15). Four of the control trees (CB2, CB7, CB8 and probably CB39) showed a gradual increase in twisting towards being more left-handed (more negative angles) the further away the canal is from the centre of the stem (Figure 5.13a-c). In rocked samples, RB2, RB3, RB4 and maybe RB6 and RB7, showed the same pattern (Figure 5.14a-c). In control trees, the average grain angle determined by the orientation of the resin canals was 'positive' near the pith (0 to 4^0) which meant a right-handed grain existed in that area (Figure 5.13a). The average grain angle progressively decreased to zero at the middle of the stem and reversal of grain was observed near the periphery. The left-handed angle near the stem surface ranged between zero to 6^0. A similar pattern was seen for the average angles in the rocked trees.

To measure the asymmetry of canal angles, the cross section of the stem was divided into 4 zones, described as upper and lower, left and right for the leaned trees (Figure 5.16b) and similarly for the vertical and rocked trees (Figure 5.16a) with the designations based on the orientation of the sections when scanned. Average angles were then compared for the upper and lower zones for each tree. For the control and rocked samples, the red and blue lines in Figure 5.13b and 5.14b show the 'upper' and 'lower' regions and, in most cases, these were similar which indicated that the grain was symmetric around the stem.

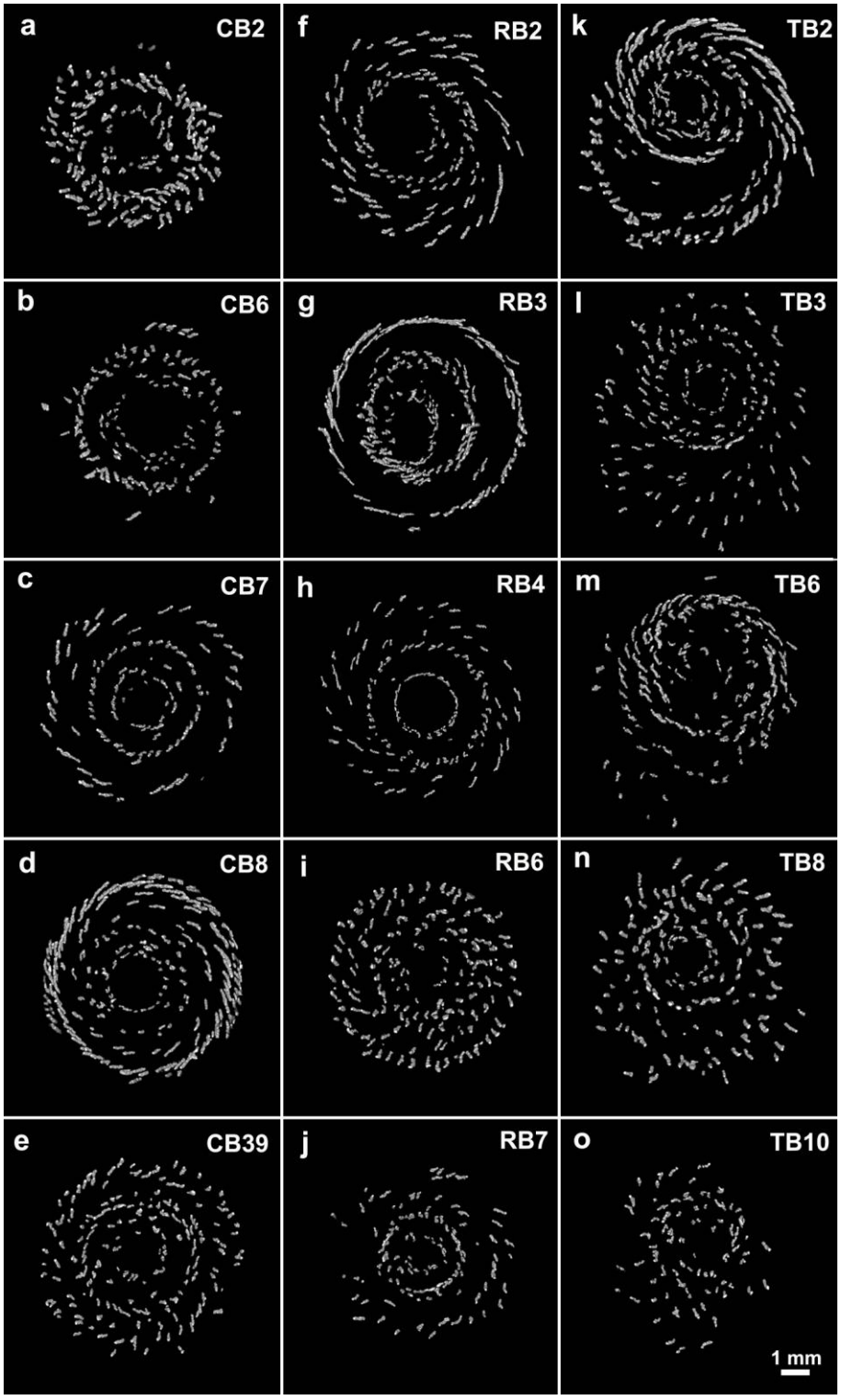

Figure 5.12 3D reconstructions of images collected with circular polarised light comparing orientation of resin canals - an indication of spiral grain, in 5 each of control, rocked and tilted trees. These reconstructions used 72 images covering 4.5 mm of the stem length.

a-e. Control trees.

f-j. Rocked trees.

k-o. tilted trees.

Image in 5.12c differs from similar previous appearances in 5.7**f** and 5.8**d** in which 3D reconstruction of 192 sections covering 10 mm of stem length was shown.

Scale bar in **o** = 1 mm for all images.

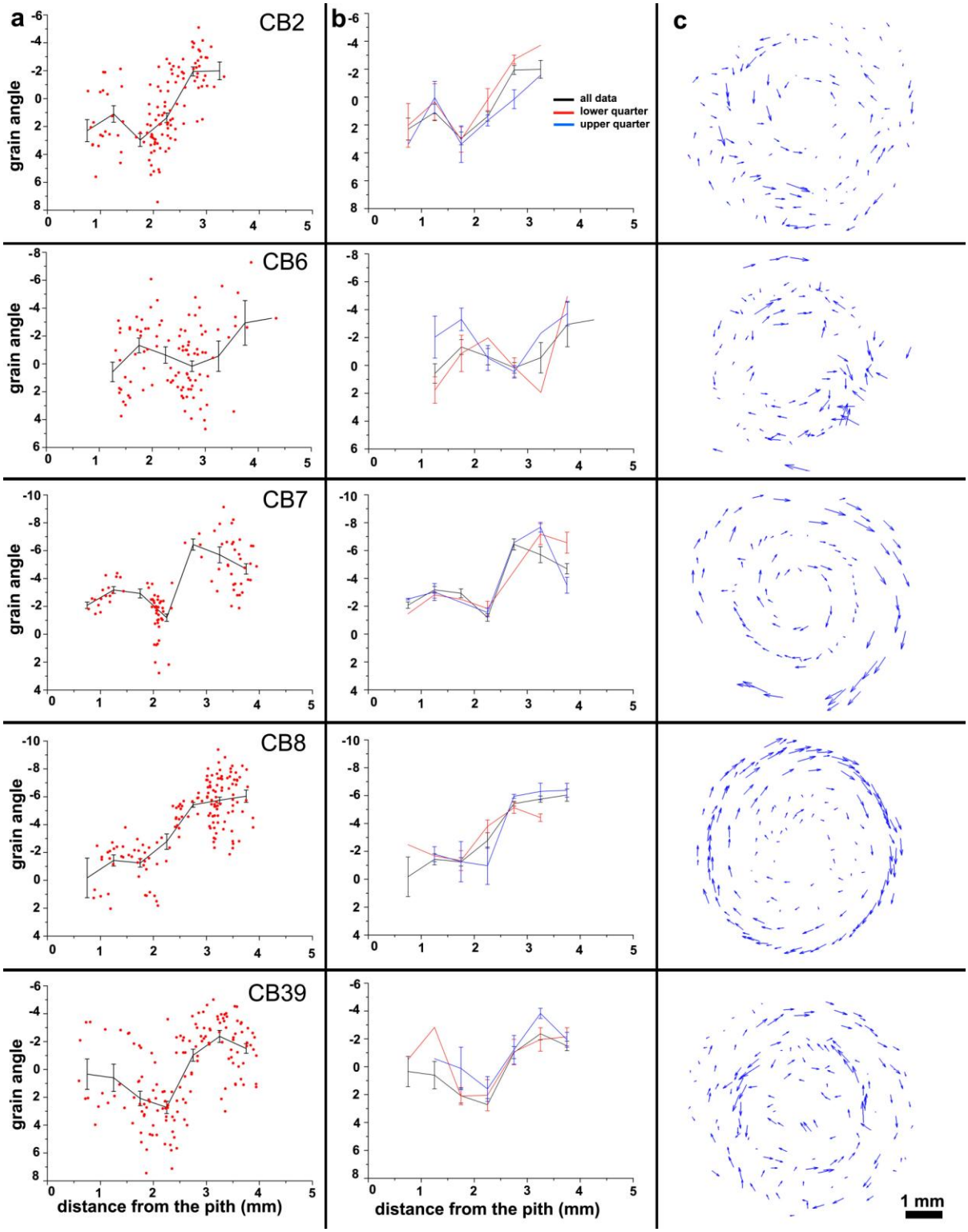

Figure 5.13 Numeric analysis of spiral grain in control trees. The designations 'upper' and 'lower' reflect randomly assigned opposite halves of the cross section from the vertical trees.

a. Individual measurements for resin canal angles (red dots) and average grain angle from pith to periphery.

b. Average grain angles for entire trees (black line), along with randomly assigned 'upper' and 'lower' halves (blue and red lines respectively).

c. Output from the Matlab programme showing grain maps from the detected resin canals.

Scale bar in **c** = 1 mm for all images.

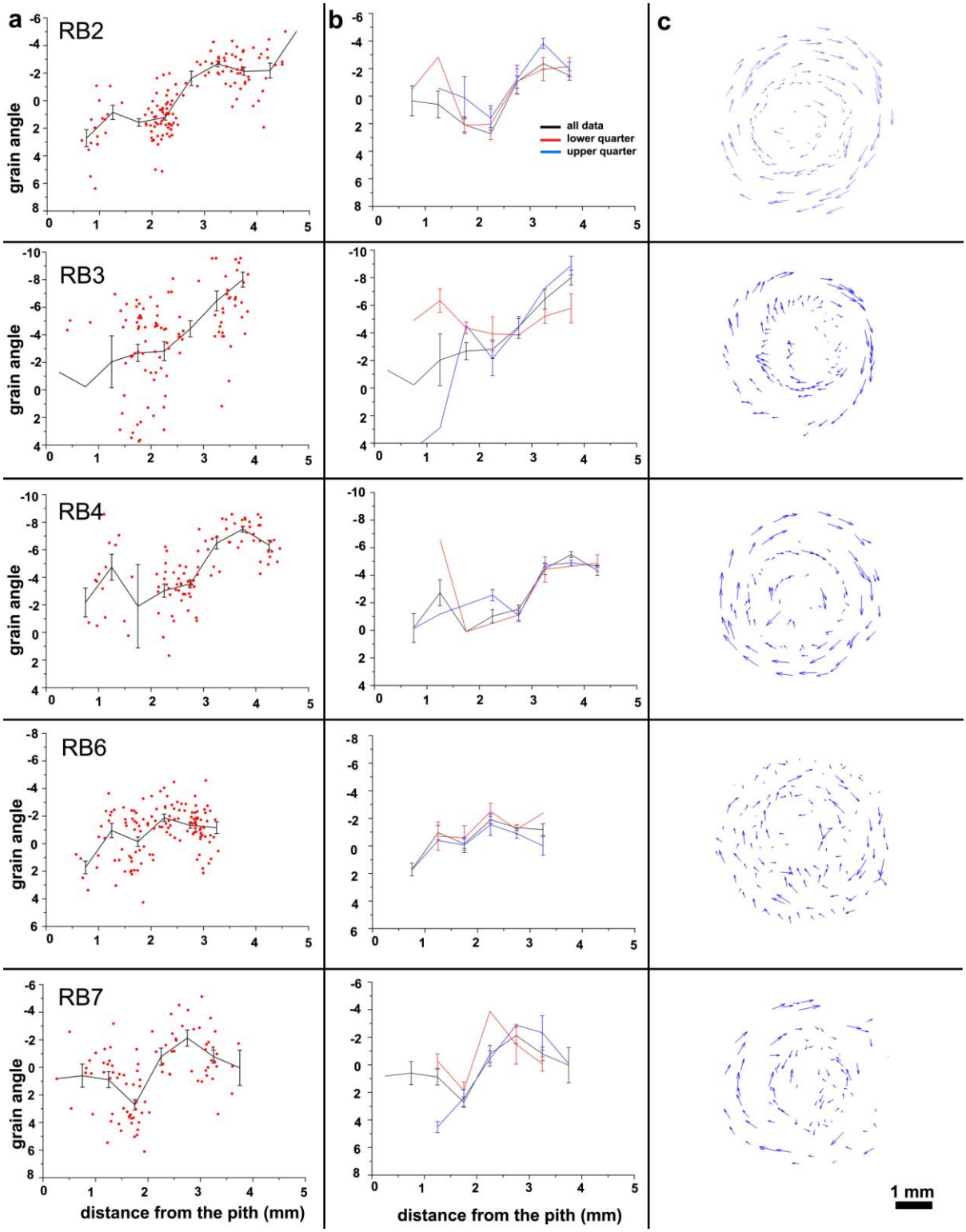

Figure 5.14 Numeric analysis of spiral grain in rocked trees. The designations ‘upper’ and ‘lower’ reflect randomly assigned opposite halves of the cross section from the vertical trees.

a. Individual measurements for resin canal angles (red dots) and average grain angle from pith to periphery.

b. Average grain angles for entire trees (black line), along with randomly assigned ‘upper’ and ‘lower’ halves (blue and red lines respectively).

c. Output from the Matlab programme showing grain maps from the detected resin canals.

Scale bar in **c** = 1 mm for all images.

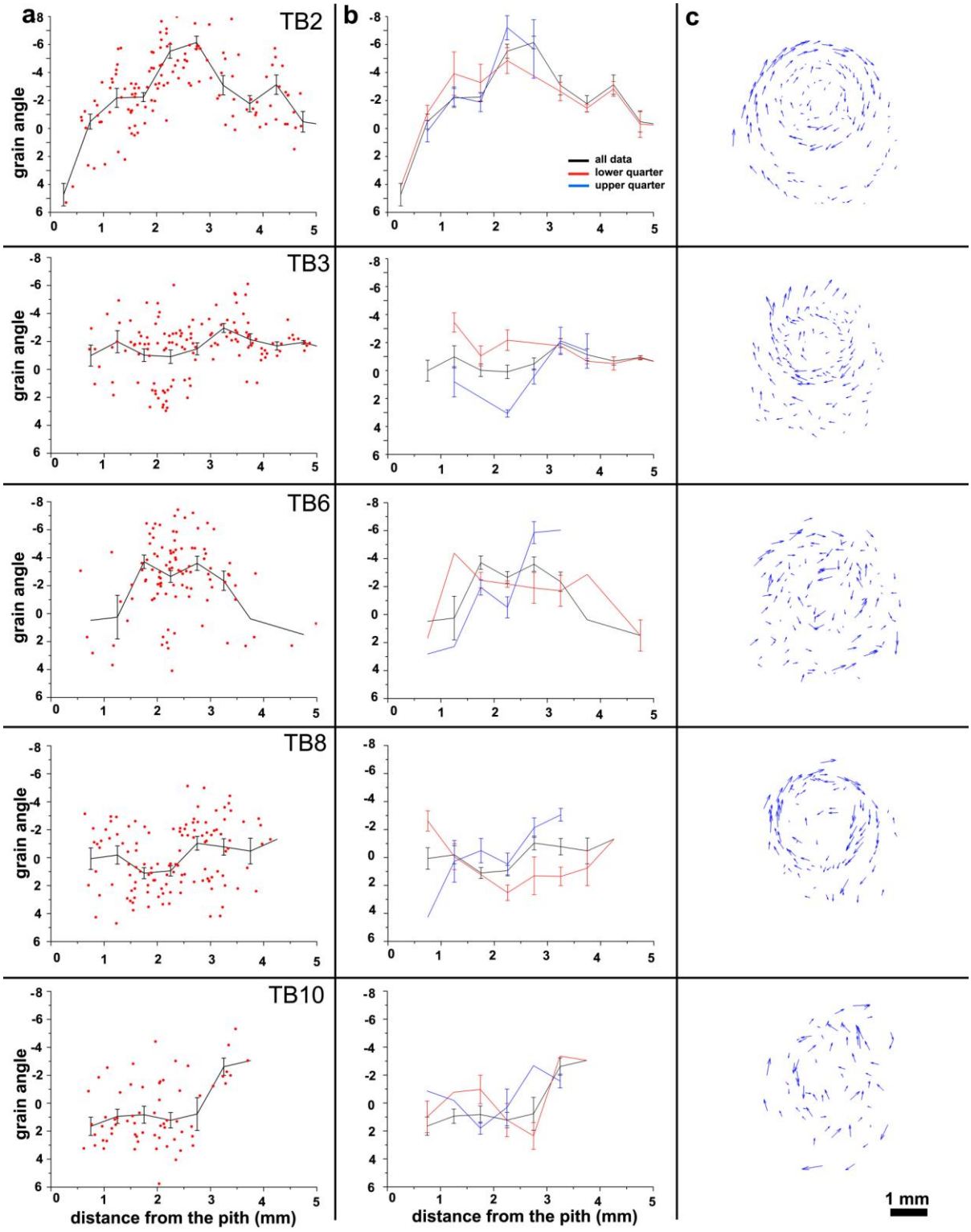

Figure 5.15 Numeric analysis of spiral grain in a tilted tree. The designations ‘upper’ and ‘lower’ reflect the real variations in orientation of the leaned tree.

a. Individual measurements for resin canal angles (red dots) and average grain angle from pith to periphery.

b. Average grain angles for entire trees (black line), along with averages for the 'upper' and 'lower' halves (blue and red lines respectively).

c. Output from the Matlab programme showing grain maps from the detected resin canals.

Scale bar in **c** = 1 mm for all images.

In the tilted samples, however, the two zones represented the real upper and lower halves of the cross section (Figure 5.15a-c). In general, the gradual increase in left-handed grain observed in vertical and rocked trees was not observed, and grain did not follow the trend to become more left-handed, except in TB10. In fact, it began to go back the other direction or showed straightness throughout the length. In TB2 and TB6 the grain showed the trend of going back to right-handed after reaching a left-handed peak of -7^{o} and -4^{o} respectively. However, in TB3 and TB8 the grain remained straight throughout the length with a very little change in their left-handed angle ($+1^{o}$ to -2^{o}).

Analysis of the tilted samples, which required a comparison of the compression wood (red line) with opposite wood (blue line), was complex because more compression wood formed below the stem made the stem asymmetric. This meant that the red line typically extended further to the right along the X axis (Figure 5.15b). The blue line also lies above the red line, notably from about 2.25 mm. This is consistent with there being a change in grain formation on the lower side relative to the upper side.

It is possible that in all of the samples, the average grain angle in the normal wood was more left-handed than the average angle in compression wood, although several cases were not clear. The fundamental difference between the control and tilted trees was that there were fewer canals in the lower side of the tilted trees and more wood formation. The analysis of these leaned trees suggested that the grain is affected by the presence of compression wood, and is consistent with the interplay between spiral grain and compression wood that the initial observations suggested.

5.3.5 X-ray microtomography visualisation of resin canal angles

X-ray microtomography produced raw images of the scans which were processed through specialised software (SkyScan 1172 µCT Control program, version 1.5A, build 1) and an image reconstruction package (NRecon, version 1.5.1.4) to produce a series of transverse sections from the raw X-ray images (Figure 5.17a). These images compared well with the images collected with the circular polarised light (Figure 5.17b) and the fluorescence stereo-microscope (Figure 5.17c). The tomograms looked similar to a low magnification light microscopy image, with the advantage that they cover the entire transverse section area. Anatomical details such as the resin canals, ray cells and bands of compression wood were clearly visible. In these tomograms, denser objects were brightly visible whereas objects with low density had reduced brightness. Void spaces, such as the tracheid lumen and cell cavities, appeared dark. Brighter areas showed the presence of compression wood due to the higher density of the compression wood tracheids owing to their increased lignification and thicker cell walls.

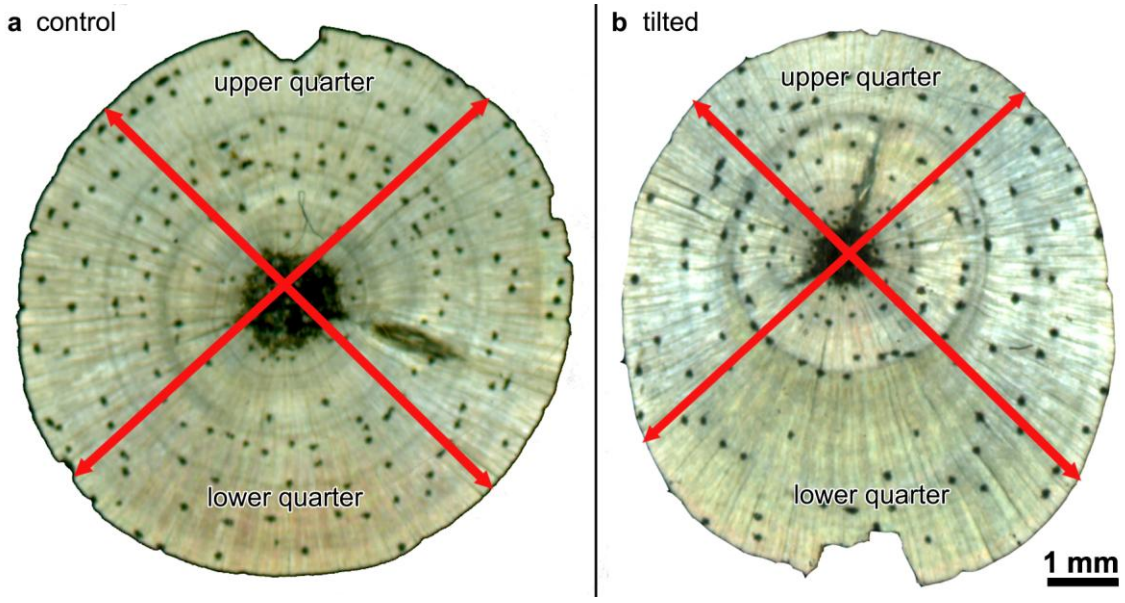

Figure 5.16 Sampling pattern for the numeric analysis of spiral grain in control trees.

a. A typical example of control or rocked tree with four equal quadrants.

b. Frequency and number of canals in the compression wood region was much lower in the lower quarter. Note the relatively higher area of the lower quarter due to compression wood formation.

Scale bar in **b** = 1 mm for all images.

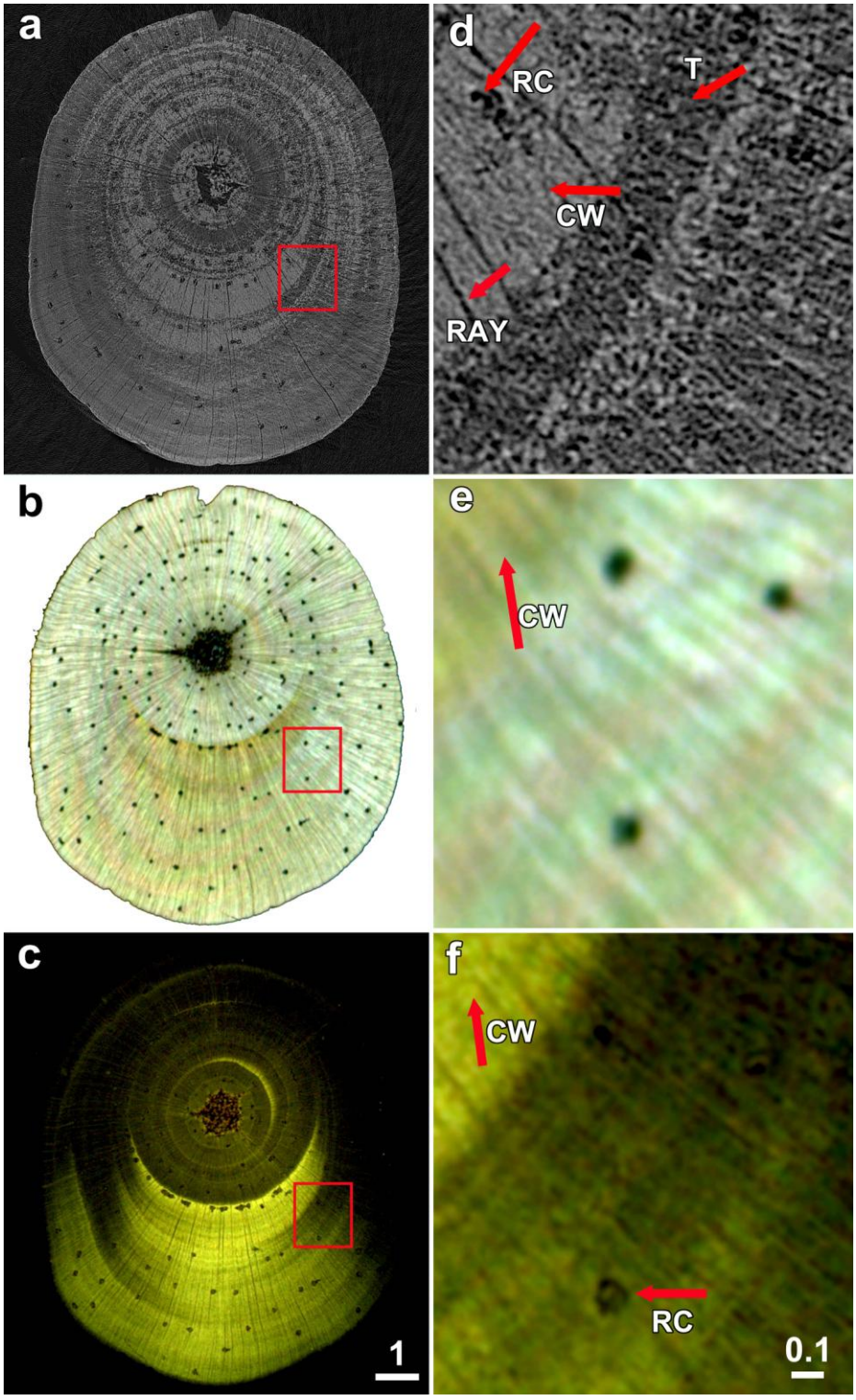

Figure 5.17 Comparison of imaging techniques using polarised light, fluorescence microscopy and X-ray tomography.

a. An X-ray tomogram of the transverse section of a leaned tree.

b. Circular polarised light scan image of a similar transverse section. This section would have been up to 1 mm away from the section shown in **a**, and therefore the resin canals are in slightly different locations.

c. Fluorescence microscopy image of the same transverse section as shown in **b**.

d. Enlarged view of the boxed region in **a,** showing resin canals, ray cells, compression wood and, more importantly, the tracheids.

e. Enlarged view of the boxed region in **b,** showing resin canals, ray cells and the compression wood. Tracheids were not clearly visible.

f. Enlarged view of the boxed region in **c,** showing resin canals, ray cells and the compression wood. Tracheids were not clearly visible.

RC = resin canal, CW = compression wood, T = tracheid and RAY = ray cell.

Scale bar in **c** = 1 mm for **a**-**c;** bar in **f** = 0.1 mm for **d**-**f**.

In enlarged views of tomograms, individual tracheids with their dark lumens were visible (Figure 5.17d), with the cellular-level resolution better than the other two methods. Comparison between the fluorescence (Figure 5.17f), polarised light (Figure 5.17e) and the X-ray tomography images (Figure 7.17d) from the same tree, demonstrated that they show similar patterns although the locations of the resin canals were not identical between the tomograms and the traditional microscopy images because the later were cut from a slightly different location within the stem.

Further processing of these transverse section images was completed with Photoshop and ImageJ to create the 3-dimensional reconstructions that visualised resin canal organisation using approaches that were similar to those used for circular polarised light. The resin canals could be reconstructed by this method to show the grain pattern inside the wood and, moreover, the resulting pattern was similar to that found by polarised light in the same tree (Figure 5.18). Most of the resin canals identified in reconstructions from the polarised light images could also be identified in reconstructions from the tomograms (Figure 5.18a, d). In 3D reconstructions of the resin canals, viewed from side on, the left-handed twist exhibited by the resin canals in both the samples was clearly visible (Figure 5.18b, e). These images represent 4.5 and 3.9 mm of stem tissue (for the polarised light and tomography images respectively) but the tomography image appears slightly longer with lower canal angles. This arises from the fact that to load the entire 20 GB image stack into ImageJ was not possible, with only every tenth image loaded and that with a 50% reduction in size. Thus, while the polarised light image is compressed 6-fold, the tomography image is only compressed 5-fold. Processing with the Matlab routine also demonstrated the chains of resin canals showing left-handed twist (Figure 5.18c, f)

5.3.6 X-ray microtomography visualisation of tracheid angles

In the circular polarised light imaging technique, the canals were considered as proxies for the grain of the tracheids. However, X-ray tomography can begin to show the tracheids themselves (Figure 5.17) and the grain angles at which they run (Figure 5.18f). This provides another, independent and direct way to analyse the grain. As the computing resources available to run full analyses of these image stacks (each about 20 GB) was limited, image processing and reconstructions were completed for only selected, 600 µm cubic subsets of the entire image set (250 pixels in each direction). However, even this approach demonstrated the exciting possibilities of X-ray tomography as a powerful tool to study the internal structure of wood.

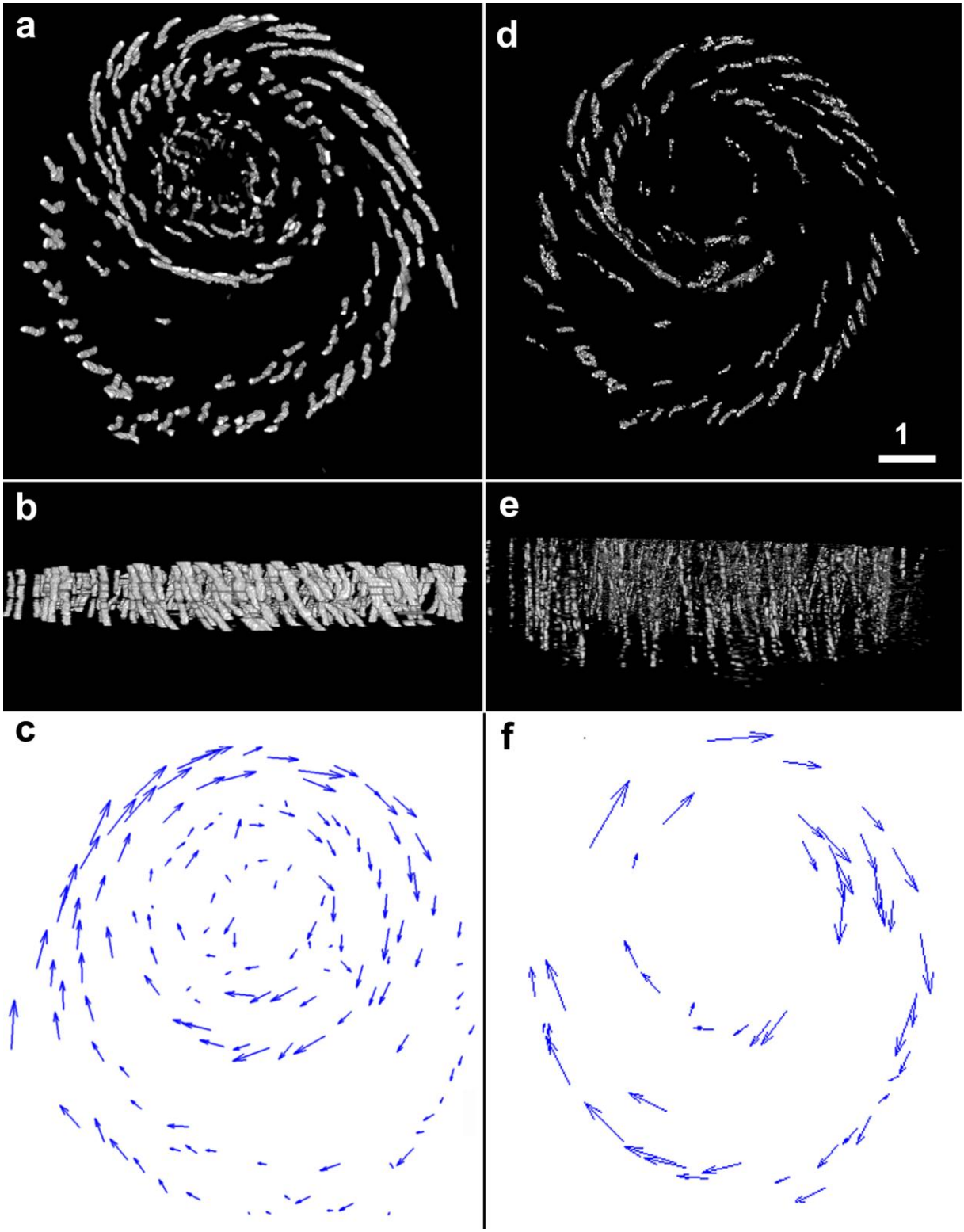

Figure 5.18 Comparison of grain angle measurements from adjacent sections of the same vertical tree using polarised light scan and X-ray tomography.

a. 3-D reconstruction of resin canals using the circular polarised light.

b. A side view of the 3-D reconstruction in **a** showing left-handed resin canals.

c. Grain map derived from the resin canals detected in **a**.

d. 3-D reconstruction of resin canals using the X-ray tomography. The overall pattern is very similar to the pattern found in the adjacent part of the stem shown in **a**.

e. A side view of the 3-D reconstruction in **d** showing left-handed resin canals.

f. Grain map derived from the resin canals detected in **d**. Not as many resin canals were detected by X-ray tomography compared to circular polarised light.

Scale bar in **d** = 1 mm for **a** and **d**.

Four different, highly-enlarged regions on an image stack from a tilted sample were processed with ImageJ (Figure 5.19a). These regions appeared relatively similar in structure (Figure 5.19b-e). Tracheids were visible as their walls were bright and lumen dark. Other softwood anatomical features like resin canals and ray cells were also visible in these transverse sections.

Tangential and radial longitudinal sections through these subsets were then reconstructed using the image '*reslice*' function in ImageJ (*Image* / *stacks* / *reslice*) and by using the following settings:

~ output spacing = 1

~ the 'avoid interpolation' box checked

~ for tangential longitudinal sections, regions b and c in the upper half of the stem, 'start at' used 'top' whereas for regions d and e in the lower half of the stem, 'bottom' was selected. This meant that all the reconstructions were viewed from the outside of the stem inwards, and with a consistent orientation. Images were then selected from locations 1, 84, 167 and 250.

~ for radial longitudinal sections, 'start at' used 'left' and four images were then selected from locations 1, 84, 167 and 250. In this case, the order of the slice did not make any different in grain orientation.

Anatomical features visible in the tangential sections were spindle-shaped rays, comprising several cells, and vertical or near vertical tracheids. In region b towards the upper edge of the leaned tree, these tracheids were visible with a leftward orientation, consistent with a left-handed grain (Figure 5.19f). This high leftward orientation decreased in tangential slices closer to the pith (Figure 5.19g), and was also not visible on the lower side of the stem where compression wood had formed (Figure 5.19h,i). This is exactly what was showed previously, as the grain orientation near the pith is much straighter than the grain away from the pith. Radial longitudinal sections were also reconstructed using the same image stacks and the brick-like organisation of the ray cells, typical of the radial section, was visible as in low resolution light microscope images (Figure 5.19j-m).

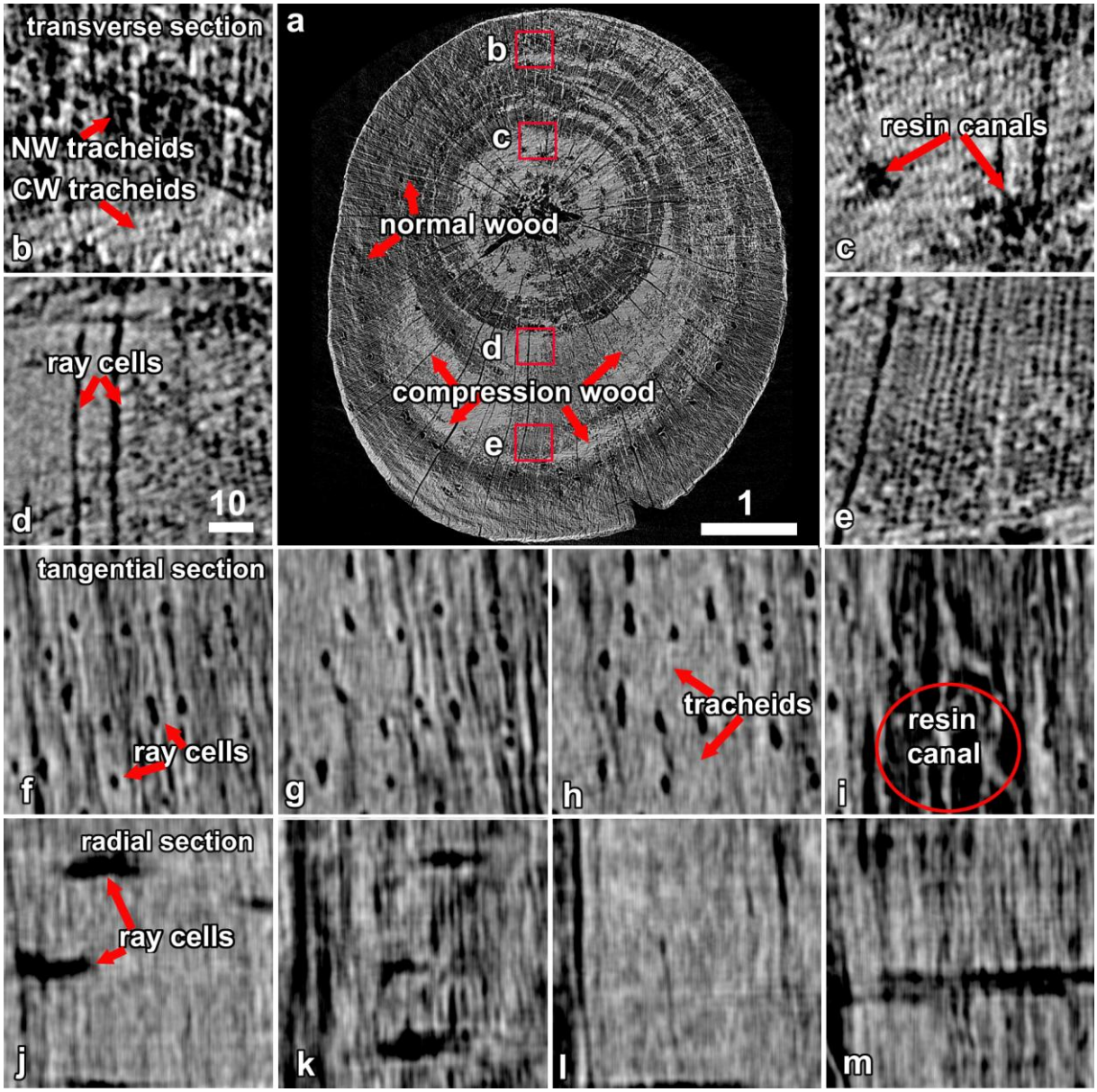

Figure 5.19 Anatomical organisation of the wood was visible at a cellular level with X-ray tomography.

a. An X-ray tomogram of the transverse section of a leaned tree. Compression wood (brighter) and normal wood (dull) areas were clearly visible.

b-e. Magnified view of the regions boxed in **a**, corresponding to an area of 607 x 607 µm. Transverse section from four regions showing different cell elements. Compression wood (brighter) and normal wood (dull) tracheids were clearly visible.

f-i. Tangential longitudinal sections through the image stack showing leftward oriented tracheids and ray cells, notably in **f** but less so in the other locations. Dark voids in a resin canal complex were also seen.

j-m. Radial longitudinal sections through the image stack showing tracheids and ray cells.

Scale bar in **d** = 10 µm for **b**-**m**; bar in **a** = 1 mm for **a**.

5.3.7 A comparison of spiral grain measurements using 3 different approaches

A comparison of grain measurements carried out by the 3 different approaches was made (Table 5.2). These approaches were measurements made on the surface by tracing the orientation of the visible resin canals for the 10 trees each under 3 growth conditions, spiral angle values measured with the Matlab routine on the polarised light images (5 trees each), and on images collected with the X-ray tomography (2 tilted trees and a control).

Correlations between surface measurements and internal grain as detected by polarised light were poor (Figure 5.20). While the correlation coefficient for angle measurements in the rocked trees was reasonable (R^2 = 0.76), for control trees the value was low (R^2 = 0.47). Moreover, the correlation was actually negative, with trees showing a high surface grain having a low internal grain and vice versa. Correlations for tilted trees were also very poor, as the R^2 values were 0.23 for opposite wood and 0.20 for compression wood. The Matlab calculated angles neither among the three wood types nor between the opposite and the compression wood sides of the tilted trees (p = 0.06) were significant among them or with the control trees (0.08).

The same Matlab routine was used to measure grain angles in the polarised light scan and the tomography images. Detection of resin canals and their angle measurements worked well in the case of polarised scan images. Processing of the images with the Matlab routine resulted in numerical angle measurements (an Excel file) and the graphical representations of the orientation of resin canals (Figures 5.13 - 5.15). Matlab calculated the location and angle of these chains of identified resin canals with the angular variation in grain change was represented as arrows as recorded by Matlab (Figure 5.18 and 5.21). Visual comparison of the orientation of resin canals reconstructed (Figure 5.18a and 5.21a) and the strings formed by the Matlab (Figure 5.18c and 5.21b) based on the canal detection of the polarised light scan images was excellent. However, detection of the canals in the tomograms was poor due to the artefacts in the tomography imaging technique (Figure 5.21d). Many resin canals were not detected as a result and the 3D reconstruction and their numerical analysis were not impressive. Therefore, the Matlab routine did not perform as expected and angular values for the resin canals were not measureable. The precise causes of these problems, and how they might be remedied, remain unknown.

Table 5.2. Comparison of spiral grain measurements with 3 different methods.

Treatment	surface grain angle (^{o}) (n =10)	Grain angle - polarised light (^{o}) (n = 5)	Grain angle - X-ray tomography (^{o}) (n = 2)
Control trees	8.6 ± 1.0	3.43 ± 0.7	not measurable
Rocked trees	7.6 ± 0.7	4.33 ± 0.7	---
Tilted trees			
normal wood	7.6 ± 0.6	3.91 ± 1.0	not measurable
compression wood	6.3* ± 0.4	0.74 ± 1.3	not measurable

Values are means ± standard errors.

* values significantly different from the vertical control; T-test; $P < 0.05$.

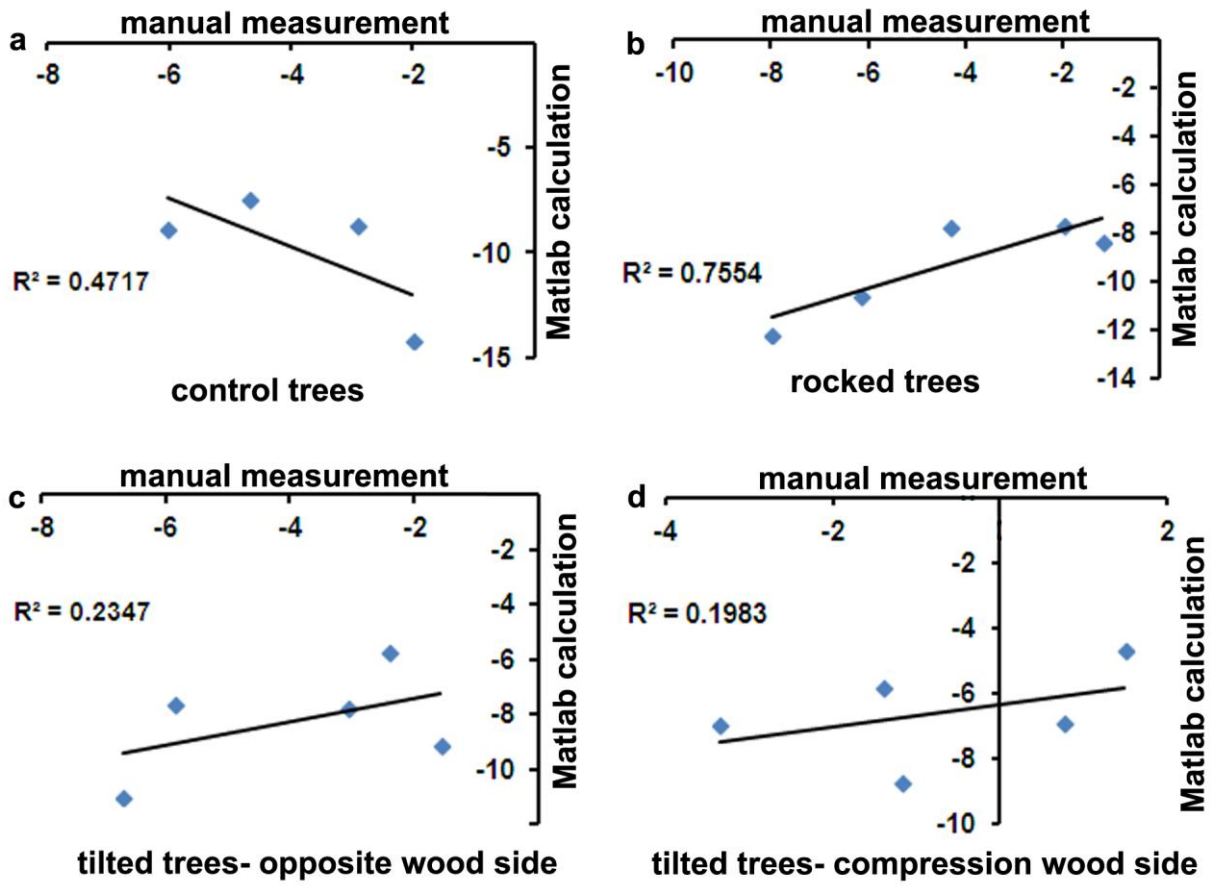

Figure 5.20 Comparison of grain angle measurements with direct measurement of orientation of the resin canals on the sample surface and by Matlab routine on the polarised light images. Negative values showed a left-handed twist. N = 4 or 5 trees for each condition.

a. Measurements made in control trees.

b. Measurements made in rocked trees.

c. Measurements made in the opposite wood side of the tilted trees.

d. Measurements made in the compression wood side of the tilted trees.

5.4 Discussion

LaPasha and Wheeler (1990) reported that the orientation of the vertical resin canals is quite straight relative to the long axis of the trunk, which opened an opportunity for exploring resin canals as a tool to study the spiralling of grain in radiata pine. Zobel et al. (1965) observed that the pith could be the best reference plane for obtaining the angle of grain deviation and use of stem axis might be better for larger trees. These observations coupled with our own observations on the twisted wood samples paved the basis of this new technique. Moreover the imaging technique employed in this study (section 4.4.1), using circularly polarised light and a scanner, provided the basis of the initial image analysis and 3D reconstructions. These reconstructions were subsequently confirmed using X-ray microtomography.

5.4.1 Resin canals as an indicator of grain

Resin canals have often previously been used as markers for spiral grain orientation (Harris, 1989; Koehler, 1955; Noskowiak, 1963). Measurements of the deviation of a tree's grain based on 3D visualisation of the resin canals was only possible because the resin canals followed the grain and were much bigger, longer and more visible than tracheids. Literature reports suggest that resin canals in *Pinus* are formed from the same cambial cells that form the tracheids (Bannan, 1936), and thus are parallel to the grain, and observations from serial sections and X-ray tomography confirmed this.

For imaging grain across an entire stem, even one as small as 10 mm in diameter as used in this study, tracheids as visualised by light microscopy make a poor target by comparison with resin canals. This is because the tracheids are much shorter by comparison (2-4 mm long, depending on position and age of the tree) and have smaller cross sectional dimensions (average diameter 20-30 µm). The larger dimensions of the canals, with an average diameter of about 104 µm (see Section 4.3.5.3), makes the canals visible even to the naked eye, and they were easy to track along the length of the stem through the serial cross sections when viewed with circular polarised light. This meant that the resin canals provided a much superior target to track changes in grain pattern by image processing and 3D visualisation.

More importantly, although the length of the resin canals was not measured in this study, not being a primary objective, as visualised through the reconstructed images, they were typically seen to be continuous all the way through the length of the stem segment sectioned. This suggests that the resin canals in an 8 month old radiata pine tree are not less than 6 mm in length, and that they are likely considerably longer. LaPasha and Wheeler (1990) reported that the vertical resin canals in loblolly pine were relatively straight, compared to the long axis

of the trunk, and had mean canal lengths of 57 to 196 mm. Their analysis did not, however, consider the use of the resin canals to study grain within the tree.

5.4.2 Spiral grain develops rapidly in young trees

Radiata pine shows the typical LR pattern of northern hemisphere pine trees, with the rapid development of left-handed grain in the corewood, followed by a reduction in the angle of the grain and sometimes the formation of right-handed wood. This pattern has been shown to develop early in the formation of the tree. In replicating earlier work (Chattaway, 1959), Cown and his colleagues demonstrated that grain near the pith is aligned almost vertically, but that left-handed spiral grain develops in the youngest growth ring, subsequently reaching a maximum in the second or third ring (Cown et al., 1991). This study confirmed the early onset of left-handed spiral grain in vertical (and rocked) trees. In general, the resin canals near to the pith showed lower spiralling, being either vertical or sometimes even weakly right-handed, whereas the canals near to the cambium were highly spiralled in a left-handed direction (Figure 5.8).

The 3D reconstruction of the stem sections imaged with polarised light and reconstructed with ImageJ was a highly novel way of looking inside whole stems. From the reconstructions, it was apparent that nearby resin canals can have differing orientations. They were seen running along the length of the stem with curves / bends to adjust their orientation to allow the needles, ray cells or radial resin canals to pass. Moreover, they were sometimes observed to split and subsequently rejoin to pass around a needle. All these observations indicated that the resin canals were matching the grain orientation by following the major xylem element in conifers, the tracheids.

5.4.3 The unknown link between compression wood and spiral grain

In initial wood quality experiments run with leaned trees by Dr John Walker and Dr Shakti Chauhan from the School of Forestry at the University of Canterbury, samples from the upper side of trees which contained opposite wood, where no compression wood was present, showed severe twisting consistent with the presence of spiral grain. However, the compression wood from the lower side of the trees showed warping and bending and did not twist (Figure 5.1b). The organisation of resin canals, and thus the deduced grain orientation, that was observed by 3D reconstructions in these samples, was consistent with the shape and dimensional instability of the wood samples as noted earlier. Moreover, the direct observations of tracheids in a tilted tree were also consistent with there being a difference in grain between normal and compression wood. These observations strongly suggest a link between the

formation of compression wood and spiral grain in radiata pine. There is, however, a lack of information on this very important wood quality issue in this available literature. While exploring the correlation between the stem eccentricity and spiral grain formation in *Pinus longifoli*a cross sections, Misra (1939, 1943a, 1943b) observed a sudden change in orientation of ray cells when entering or leaving the compression wood areas and suggested this deviation could be due to the change in grain. Similar grain changes were observed in the samples in this study.

The role of plant hormones, including IAA/auxin and ethylene, has been investigated in the formation of spiral grain (Eklund et al., 2003; Zagorska-Marek and Little, 1986) and compression wood (Cown et al., 2003; Funada et al., 1990; Wilson et al., 1989) (see sections 1.7.4 and 1.8.5). These studies, however, have focussed on either compression wood or spiral grain formation alone, and have not considered any link between the two. It is worth noting that the presence of excess levels of endogenous and exogenous auxin has been reported in both cases. For example, application of exogenous auxin induces compression wood formation in radiata pine (Cown et al., 2003), and also stimulates compression wood formation in vertical stems that would not otherwise form compression wood (Timell, 1986), while endogenous auxin levels have been associated with the formation of compression wood in Douglas fir (Christopher and Phelps, 1986; Wilson et al., 1989) and Japanese cedar (Funada et al., 1990). Similarly, Zagorska-Marek (1986) concluded that auxin was important for spiral grain formation based on experiments that showed the orientation of fusiform parallel to auxin flow. The development of spiral grain and compression wood on opposite sides of a leaned tree is, however, a much more complex situation than these experiments have investigated, because the changes in grain are occurring differently on opposite sides of the stem.

Both spiral grain (Ormarsson et al., 2000; Sepúlveda, 2001) and compression wood (Donaldson and Turner, 2001; Johanson, 2002; Nyström, 2002) are associated with growth stresses, and result in degradation of dried timber. Spiral grain is associated with stresses which result in twist in the wood whereas the stresses associated with compression wood are relieved in the form of bending and warping (Figure 5.1). It might, therefore, be wise to consider the formation of compression wood and spiral grain in wood as two sides of the same coin, and that wherever both compression wood and spiral grain are present in opposite sides of a stem, it may be to contain the stress developed due to each other.

By the reconstruction of the stereo-fluorescence microscope images using Photoshop and ImageJ, a 3-dimensional view of the compression wood was made (Figure 5.9). Stereo-fluorescence images were good enough to clearly show the compression wood in them

compared to the polarisation scan images. By combining the polarisation scan images and the stereo-fluorescence microscope images, both compression wood and spiral grain were visible. This technique has provided a novel way to understand these wood quality issues. From the 3D views generated, it was observed that the number of resin canals in compression wood areas is very low and that, where they do occur, they are fairly straight compared to the resin canals elsewhere (Figure 5.10). Cown et al. (2003) reported fewer or no resin canals in compression wood. The low number of resin canals and their relatively straight orientation in compression wood areas are seemed to be related.

It is now obvious from the available literature that researchers have looked at the incidence of compression wood and spiral grain separately, and have made only very limited effort on approaching these issues together. In this study, visualisation of the internal structure of full cross sections of pine tree stems was successfully made for the first time. The orientation of the resin canals has shown the grain deviation along the length of the stem and hence this 3D reconstruction technique would give a great opportunity to study the generation and progression of spiral grain in wood.

5.4.4 X-Ray tomography and grain angle measurements

X-ray tomography has been used to investigate wood grain in several ways in previous studies (section 5.1.5.2). For example, Sepúlveda (2001); Sepúlveda et al. (2002a); (2002b) made attempts to measure spiral grain in Norway spruce logs using an industrial log scanner and successfully verified a model to predict spiral grain in logs. These analyses were not, however, studies at the cellular level. Alternatively, wood anatomical characteristics were investigated at a cellular level in several studies but not looked at over large areas (Steppe et al., 2004; van den Bulcke et al., 2009). The use of X-rays to investigate grain at a cellular level, and over large areas of tissue, has been limited to the soft X-ray investigations of interlocked grain in *Acacia*, but in that study, no 3-dimensional reconstructions were attempted (Ogata et al., 2003).

This study is, therefore, the first attempt to look at grain across an entire stem but considering patterns at a cellular level. Grain was investigated in several ways, and more importantly, the wood blocks that were X-rayed were the stubs of the stems that had been used for serial sectioning so that direct comparisons could be made between the techniques. In the first approach, resin canals were identified by image analysis and their orientations shown to match the orientations seen by serial sectioning (Figure 5.18a, d). Unfortunately, the analysis routine developed in Matlab to measure the angles of the canals failed to give reliable measurements of the orientations of the canals in the X-ray tomograms. There are several

possible reasons for this. First, this routine was optimised for the relatively large-sized canals identified by circular polarised light. These large canals contains several layers of parenchyma cells that have primary cell walls and which rotate the polarised light only weakly, thus appearing dark against the bright background of the tracheid secondary walls. By X-ray tomography, however, the cell walls of these parenchyma cells were still imaged which meant that the observed size of the canals seen was considerably smaller (Figure 5.18a, d) where the identified canals by microtoming were much larger than by tomography. This meant that the canals were harder to distinguish, with many canals not seen in the image analysis routine in ImageJ which meant that Matlab could not string the canals together and provide an overall grain angle (Figure 5.18c, f). Time and computer limitations precluded further analysis of the tomography samples, although the method has been verified as a convenient and powerful approach for investigating grain.

The second approach to measuring grain with the X-ray microtomography samples was the direct approach in which the tracheids are directly visualised in the tangential longitudinal sections reconstructed using the '*reslice*' function in ImageJ (figure 5.19f-i). Again, computer limitations precluded further analysis of these images, although routines available in ImageJ including the '*analyze direction*' plugin which uses a Fast Fourier Transform to measure the overall angle within an image, have shown some promise in grain analysis on hardwood samples (data not shown). Thus, with the development of these new image and 3D reconstruction techniques, studying the changes at the cellular level is now possible.

5.4.5 Comparison of grain angle measurements

In the ongoing discussion four different ways to image and visualise the grain pattern inside the wood are described. They were

1) direct measurement of resin canals orientation as grain angle,

2) imaging the transverse sections with fluorescence microscopy,

3) imaging the transverse sections with circular polarised light and subsequent 3-D reconstruction, and,

4) imaging the stem with X-ray tomography and the subsequent 3-D reconstruction.

Direct measurement of grain angle on the stem surface was good for a limited number of samples (Figure 5.2 and 5.5). However, this direct measurement was entirely dependent on the visibility of resin canals on the surface, and the measurement can be highly subjective. Imaging the serial transverse sections with the stereo fluorescence microscope and their 3-D

reconstruction provided the opportunity to visualise compression wood inside the wood (Figure 5.9). The third approach in which imaging the same sections with circular polarised light using a flatbed scanner, and subsequent reconstruction of the image stack to visualise the grain inside was a first of its kind (Figure 5.10 and 5.21a, b). This is a very inexpensive and reliable technique to image objects like the resin canals. Imaging the same wood stub with X-ray tomography provided another way to determine and compare the grain orientation in wood (Figure 5.21a-d). As X-ray tomography does not require any laborious sample preparation, unlike in the other methods, this technique has proved very easy and quick to generate quality images. Tomography gives relatively good discrimination of compression wood due to its higher than normal density and the thicker cell walls which provided extra contrast. Moreover, although it was harder to see the resin canals than was found with circular polarised light in several of the images due to imaging artefacts, tomography has its own merits as to which the entire wood structure in tangential or radial planes can be reconstructed through the reslice or similar options. The potential of using a suitable contrasting agents (Pauwels et al., 2013) might also be explored to further increase the usefulness of the tomography approach.

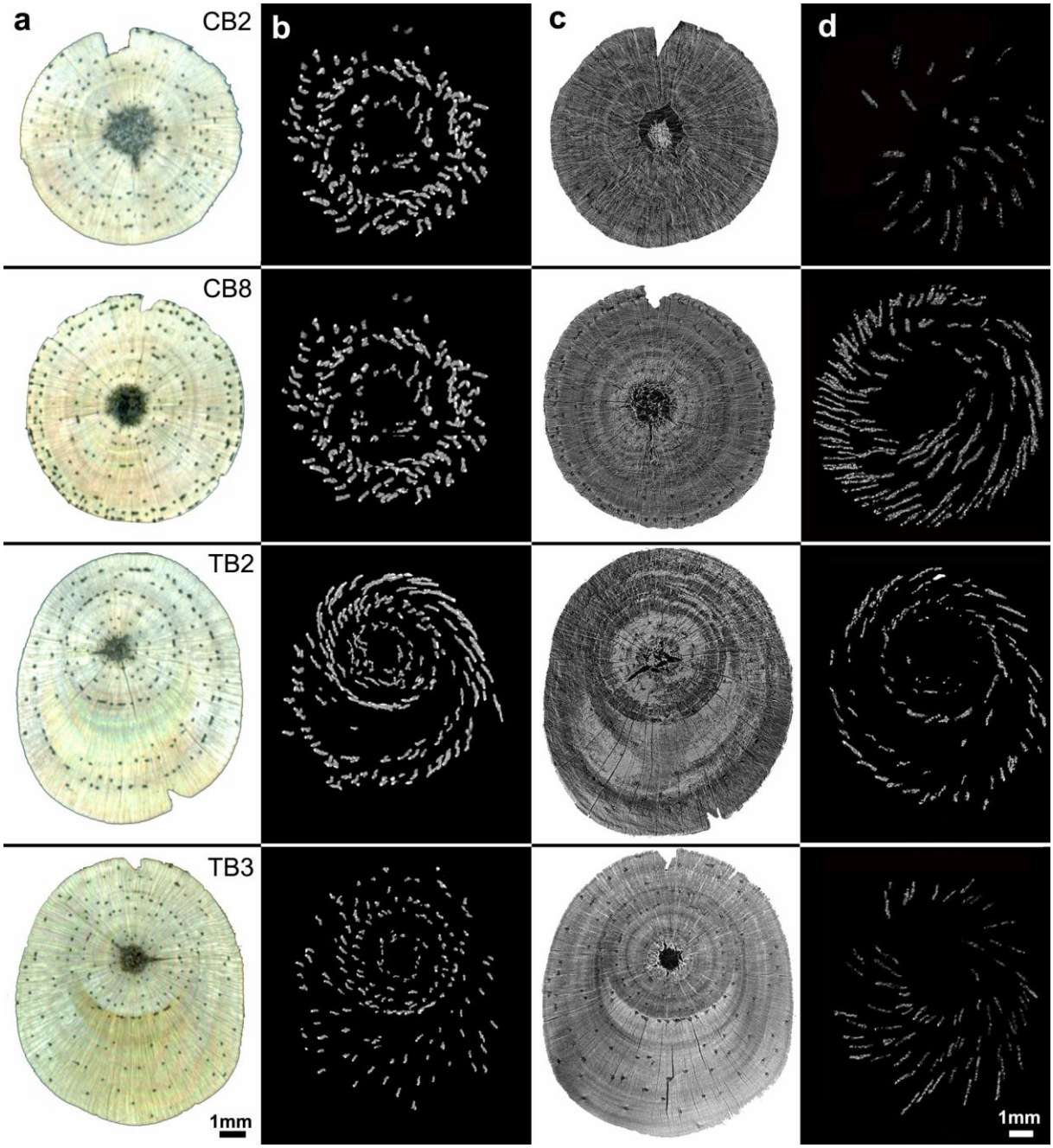

Figure 5.21 Spiral grain visualised from X-ray tomograms used a similar image processing protocol as with the circular polarised light scan images.

a. Circular polarised light scan images of control (CB2 and CB8) and tilted (TB2 and TB3) samples.

b. 3D reconstructed view of samples shown in **a**.

c. X-ray tomograms of control (CB2 and CB8) and tilted (TB2 and TB3) samples.

d. 3D reconstructed view of samples shown in **c**.

Scale bar in **a** = 1 mm for **a**-**b**; bar in **d** = 1 mm for **c**-**d**

5.5 Conclusions

This chapter addressed four important objectives.

1) A 3-dimensional (3D) visualisation of the organisation of resin canals in radiata pine wood was made possible by reconstructing the serially sectioned images using ImageJ. The orientation of resin canals near to the pith was less strongly spiralled whereas the canals near to the cambium spiralled in a left-handed helix. The visualised spiralling in the canals near to the cambium was well matched with the apparent grain angle measured on the stem section before microtoming.

2) As the visualisation of resin canals inside the wood is now possible, and their orientation was observed to follow the grain, studying the organisation and arrangement of resin canals is an excellent tool to study the occurrence of spiral grain. Being much longer and bigger than the tracheids, resin canals are easy to detect and track in serial images.

3) This method is good for visualising the internal structure, which was not possible earlier. It provides a better diagnostic tool to understand the real-time grain orientation at various positions inside the stem and the link between the spiral grain and compression wood .This new information could provide an insight into what is going on in trees in the formation of spiral grain.

4) X-ray tomography provided an excellent non-destructive tool to visualise and study the internal structure of the wood. Anatomical features inside a wood block can be studied without laborious sectioning or sample preparation. '*Reslice*' and '*3D viewer*' plugins in ImageJ are extremely useful in visualising the structure.

Chapter 6

Conclusions

Wood quality in radiata pine wood is a subject for intensive research because of the never ending human requirement of better quality timber, and higher economic returns on the timber that is grown. This species is the most common plantation tree in New Zealand, as well as in countires such as Australia and Chile, and it suffers from various wood quality issues like high longitudinal shrinkage and warping. The presence of spiral grain and compression wood, not only reduce the strength of timber but also devalues it and are very important for the forest industry due to the huge economic losses that they cause. Extensive research has been carried out at various levels to understand the formation, incidence and effects of both spiral grain and compression wood. Perhaps the most significant observation to be made within this thesis is the first strong demonstration that there exists a previously unknown link between the formation of spiral grain and compression wood in young radiata pine trees.

To improve radiata pine, and to increase the speed with which genetic material can be evaluated, tree breeders have been developing tools to select for wood quality at ages as young as 3 years old. By using simple image analysis tools available in Photoshop, I have demonstrated that RGB images collected from wood discs with a professional flatbed scanner can be processed with an easy, reliable and robust, fully automatic image analysis protocol to detect compression wood levels with a reasonable (81%) level of accuracy. The important advantage in this method is to use thresholding of the blue channel of the RGB image. Data from about 700 trees belonging to 20 different clones were used to verify this technique. The main aim of raising these trials was to generate normal wood so that the physical properties of different clones and families could be compared. Development of this new technique may reduce the waiting time for screening clonal planting materials based on compression wood content and potential winners and definite losers could be quickly selected for the future planting. Moreover, detection accuracy can be enhanced considerably by selecting a suitable threshold value manually. This approach works because of the variations in colour within the compression wood, and the fact that this most likely represents variations in the amount of blue-light-absorbing lignin within the wood. Initial results have also been obtained which suggest that improved detection of compression wood might be achieved using fluorescence. Results obtained by imaging of the stem cross sections with 450 nm excitation light using a fluorescence scanner suggested that fluorescence imaging can detect compression wood distribution in wood transverse sections. While limitations in

the available scanner technology prevented acquisition of high quality images suitable for image analysis and quantification of compression wood, subsequent scanning with more modern technology demonstrates that the principles of lignin fluorescence of dual channel fluorescence imaging might be more appropriate for compression wood detection. With the advent of strong LED light sources and sensitive cameras, it is not inconceivable that variations in fluorescence might also be usable for screening timber in commercial situations.

Cell wall fluorescence properties of a new cellulose-specific dye, pontamine fast scarlet 4B were investigated with different wood types (normal, opposite and compression wood). This dye was initially characterised in the *Arabidopsis* primary cell wall, and has previously been applied to research of the secondary wall. Using confocal and light microscopy, protocols for staining and characterisation of the dye were developed and optimised in radiata pine. It was found that pontamine is highly specific to cellulose labelling and its fluorescence properties are extremely useful in studying microfibril orientation and angle measurements, especially in the S1 and the S3 layers. Apart from its increased specificity to cellulose, the use of P4B has several advantages over the traditional dyes such as calcofluor white and Congo red as it is excited by green light and clearly discriminated from the autofluorescence, and does not bleach quickly. More interestingly, pontamine is strongly bifluorescent meaning that its excitation is dependent on the polarisation of the excitation lasers. As well as direct observations of the S1 and S3 layers, pontamine fluorescence can be investigated through this effect. In this study, such measurements were limited because the polarity of the excitation laser could not be directly modulated, with such experiments requiring the manual rotation of the sample.

While the confocal investigations of radiata pine where intended to develop methods by which spiral grain might be studied, confocal microscopy proved to be largely unsuitable for extensive and large-scale reconstructions of radiata pine grain. This is because although it provided cellular detail, imaging was limited to the surface layers of sections, and the area over which observations were required was prohibitive. New approaches were, therefore, required. Resin canals were used as a proxy to demonstrate the change in grain as both the tracheids and resin canals originate from the same cambium initials. Moreover, resin canals are much longer and wider than the tracheids and are therefore more easily tracked through serial sections. In a novel technique which has not previously been used for biological research, and which has only been used on several occasions for geological specimens, circular polarised light was used with the transmitted light mode of a professional scanner. This allowed the imaging at high (almost cellular) resolution of whole stem sections. Because the resin canal cells contain only a primary cell wall, they were weakly birefringent and

rotated the polarised light only weakly, unlike the strongly birefringent tracheids. Thus, the tracheids appeared dark against a bright background which meant that they could be easily distinguished and measured in ImageJ. In a comparison of purposefully tilted and rocked trees, the number and frequency of resin canals was lower in tilted trees, especially in compression wood, compared to the higher number of canals formed in the rocked trees and vertical controls. This experiment demonstrated that the use of circular polarised light for imaging samples on a scanner is a simple but powerful approach to quantifying biological specimens. More importantly, the use of commercial technology, for which the economies of scale have driven down the price much more than specialised scientific equipment, makes this high resolution approach feasible for most researchers even when expensive and specialised equipment is not available or affordable.

The value of the scanner approach was demonstrated by the investigations of spiral grain. A 3-dimensional view of the orientation of resin canals inside a stem could be re-created by analysing the locations of the resin canals in serial sections, using image analysis and reconstructions in ImageJ. The reconstructions of one year old trees showed that canals near to the pith were nearly straight but that resin canals near the wood surface showed a strongly developed left-handed spiral. This is consistent with the previous observation of grain in radiata pine, although the level of detail afforded by this approach is considerably higher than has previously been achieved. The grain angles in the samples were determined by a simple image analysis routine developed in Matlab, but there was little correlation between the angles measured from canals visible on the surface of the wood compared to the more detailed measurements of canals throughout the sample. The reasons for these differences remain unclear, but likely reflect inaccuracies in the observational measurements (based on only several canals visible on the surface) rather than the more detailed internal measurements.

While the grain in rocked samples behaved in a similar manner to vertical controls, perhaps suggesting that rocking is not a good proxy for wind treatments, tilting the trees and generating compression wood did significantly alter the grain. This result followed on from initial observations that in some tilted samples, the opposite wood had severe spiral grain visible through formation of twist whereas the compression wood had not twisting but warping. Grain measurements in Matlab confirmed this link - in tilted trees, there was reduced spiral grain on the lower side of the tree in association with the formation of compression wood.

This approach for the analysis of spiral grain has some major limitations. Stem sections with a diameter of more than 12 mm could not be reliably sectioned with the sledge microtome, and other cutting technologies did not generate thin enough sections for the circular polarised light scanning to work reliably. Thus, an alternative approach for larger stem sections was requied. X-ray microtomography fulfilled this requirement. Only small pieces of wood were processed in the course of this thesis research, with these being the stubs from which the serial sections had been cut so that direct comparisons could be made between the measurement technqiues. These showed not only that X-ray tomography could idenitfy the resin canals within wood sections, but that these could be reconstructed into patterns similar to those seen by serial sectioning. Technical issues prevented direct measurements of grain angles being collected from these reconstructions, but this problem should be solvable using a combination of altered image processing in ImageJ and calculations in Matlab. Tomographical approaches should also allow the tracheids of these small stems to be directly measured, with this providing further confirmation of how spiral grain develops within the stem.

Thus, it provides a better diagnostic tool to understand the real-time grain orientation at various positions inside the stem and the link between the spiral grain and compression wood .These new information could be an insight into what is going on in trees in case of formation of spiral grain.

In conclusion, this thesis has investigated wood quality issues in radiata pine in numerous different ways, and has provided a series of tools and experimental approaches that should allow considerably more research into these topics to be accomplished.

References

Abe H, Funada R. Review - The orientation of cellulose microfibrils in the cell walls of tracheids in conifers. IAWA Journal (2005) 26:161-174.

Anagnost SE, Mark RE, Hanna RB. Variation of microfibril angle within individual tracheids. Wood and Fiber Science (2002) 34:337-349.

Ananías RA, Lastra J, Salvo L, Contreras H, Barría C, Peredo M. Preliminary study of the resin canals in radiata pine. Maderas: Ciencia Y Tecnologia (2010) 12:135-142.

Anderson CT, Carroll A, Akhmetova L, Somerville C. Real-time imaging of cellulose reorientation during cell wall expansion in *Arabidopsis* roots. Plant Physiology (2010) 152:787-796.

Anderson CT, Wallace IS, Somerville CR. Metabolic click-labeling with a fucose analog reveals pectin delivery, architecture, and dynamics in *Arabidopsis* cell walls. Proceedings of the National Academy of Sciences of the USA (2012) 109:1329-1334.

Andersson C, Walter F. Classification of compression wood using digital image analysis. Forest Products Journal (1995) 45:87-92.

Apiolaza LA, Butterfield B, Chauhan SS, Walker JCF. Characterization of mechanically perturbed young stems: can it be used for wood quality screening? Annals of Forest Science (2011) 68:407-414.

Apiolaza LA, Walker JCF, Nair H, Butterfield B. Very early screening of wood quality for radiata pine: pushing the envelope. In: Proceedings of the 51st International Convention of Society of Wood Science and Technology, Concepción, Chile. (2008) 1-7.

Arpin TL, Mallol C, Goldberg P. Short Contribution: A new method of analyzing and documenting micromorphological thin sections using flatbed scanners: Applications in geoarchaeological studies. Geoarchaeology: An International Journal (2002) 17:305-313.

Atalla RH. The role of the hemicelluloses in the nanobiology of wood cell walls: a systems theoretic perspective. In: The Hemicelluloses Workshop, Entwistle K, Walker JCF, eds. Wood Technology Research Centre, University of Canterbury, Christchurch, New Zealand. (2005) 37-55.

Badel E, Delisee C, Lux J. 3D structural characterisation, deformation measurements and assessment of low-density wood fibreboard under compression: the use of X-ray microtomography. Composites Science and Technology (2008) 68:1654-1663.

Balodis V. Influence of grain angle on twist in seasoned boards. Wood Science (1972) 5:44-50.

Bamber RK. Properties of the cell walls of the resin canal tissue of the sapwood and heartwood of *Pinus lambertiana* and *Pinus radiata*. Journal of the Institute of Wood Science (1972) 6:32-35.

Bamber RK. The occurrence of secondary walls in resin canal tissue in genus *Pinus*. Journal of the Institute of Wood Science (1976) 7:15-17.

Bamber RK. A general theory for the origin of growth stresses in reaction wood - how trees stay upright. IAWA Journal (2001) 22:205-212.

Bamber RK, Burley J. The wood properties of radiata pine. Commonwealth Agricultural Bureaux, Slough, England. (1983)

Bannan MW. Vertical resin ducts in the secondary wood of the *Abietineae*. New Phytologist (1936) 35:11-46.

Bannan MW. Spiral grain and anticlinal division in the cambium of conifers. Canadian Journal of Botany (1966) 44:1515-1538.

Bedrick AE. Rapid one-solution differential staining with textile dyes: Pontacyl dark green B and Pontamine Fast Scarlet 4BA. Biotechnic & Histochemistry (1968) 43:321-325.

Bergander A, Brändström J, Daniel G, Salmen L. Fibril angle variability in earlywood of Norway spruce using soft rot cavities and polarization confocal microscopy. Journal of Wood Science (2002) 48:255-263.

Berryman AA. Towards a unified theory of plant defense. In: Mechanisms of woody plant defenses against insects-search for pattern. Mattson WJ, Levieux J, Bernard-Dagan C, eds. Springer-Verlag, New York, USA. (1988) 39-56.

Bhandarkar SM, Faust TD, Tang M. A system for detection of internal log defects by computer analysis of axial CT images. In: IEEE Workshop on Applications of Computer Vision, Sarasota, Florida, USA IEEE Computer Society Press, Los Alamitos, California, USA (1996) 258-263.

Bhandarkar SM, Faust TD, Tang M. CATALOG: a system for detection and rendering of internal log defects using computer tomography. Machine Vision and Applications (1999) 11:171-190.

Bielecki J, Bożek S, Lekki J, Stachura Z, Kwiatek W. X-ray computed micro tomography systems based on laboratory sources–possibilities and limitations. In: III rd International Conference of the European Society for Wood Mechanics, Universidade de Trás-os-Montes e Alto Douro, Vila Real, Portugal. European Society for Wood Mechanics (2004).

Bond J, Donaldson L, Hill S, Hitchcock K. Safranine fluorescent staining of wood cell walls. Biotechnic & Histochemistry (2008) 83:161-171.

Booker RE, Sell J. The nanostructure of the cell wall of softwoods and its functions in a living tree. Holz als Roh- und Werkstoff (1998) 56:1-8.

Boyd JD. Basic cause of differentiation of tensionwood and compression wood. Australian Forest Research (1977) 7:121-143.

Brändström J. Micro and ultrastructural aspects of Norway spruce tracheids - A review. IAWA Journal (2001) 22:333-353.

Brazier JD. An assessment of the incidence and significance of spiral grain in young conifer trees. Forest Products Journal (1965) 15:308-312.

Brazier JD. Timber Improvement 1. A study of the variation in wood characteristics in young Sitka spruce. Forestry (1967) 40:117-128.

Buksnowitz C, Muller U, Evans R, Teischinger A, Grabner M. The potential of SilviScan's X-ray diffractometry method for the rapid assessment of spiral grain in softwood, evaluated by goniometric measurements. Wood Science and Technology (2008) 42:95-102.

Burdon RD. Compression wood in *Pinus radiata* clones on four different sites. New Zealand Journal of Forestry Science (1975) 5:152-164.

Burdon RD, Kibblewhite RP, Walker JCF, Megraw RA, Evans R, Cown DJ. Juvenile versus mature wood: a new concept, orthogonal to corewood versus outer wood, with special reference to *Pinus radiata* and *P. taeda*. Forest Science (2004) 50:399-415.

Burgert I, Gierlinger N, Eder M, Fratzl P. The mechanical design of wood cell walls. Journal of Biomechanics (2006) 39:S351-S351.

Butterfield BG, Meylan BA. Three-dimensional structure of wood. An ultrastructural approach. Chapman and Hall, London, UK. (1980)

Cahn AR. Twisted trees. Science (1931) 73:561.

Cave I. The anisotropic elasticity of plant cell wall. Wood Science and Technology (1968) 2:268-278.

Cave ID. The longitudinal Young's modulus of *Pinus radiata*. Wood Science and Technology (1969) 3:40-48.

Chaffey N. Wood formation in trees - Cell and molecular biology techniques. Taylor & Francis, London, UK. (2002)

Champion HG. Contributions towards a knowledge of twisted fibre in trees. In: Indian Forest Records. Forest Research Institute, Dehradun, India. (1924) 11-80.

Chattaway MM. Spiral grain in *Pinus radiata*. In: CSIRO Forest Products Newsletter, Canberra, Australia. 250 (1959) 3-4.

Chauhan SS, Entwistle K. Measurement of surface growth stress in *Eucalyptus nitens* Maiden by splitting a log along its axis. Holzforschung (2010) 64:267-272.

Chauhan SS, Sharma M, Thomas J, Apiolaza LA, Collings DA, Walker JCF. Methods for the very early selection of *Pinus radiata* D. Don. for solid wood products. Annals of Forest Science (2013) 70:439-449.

Chauhan SS, Walker JCF. Variations in acoustic velocity and density with age and their interrelationsships in radiata pine. Forest Ecology and Management (2006) 229:388-394.

Chen FF, Yang JL, Downes G. A visual information assessment tool for resin canal identification and property measurement. IAWA Journal (2008) 29:397– 408.

Chiu CM, Lee CH. Wood bark grain spirality correlations in *Calocedrus formoasna*. IAWA Journal (1993) 14:29-34.

Christopher JS, Phelps JE. Induction of compression wood in rooted cuttings of *Pseudotsuga menziesii* (Mirb.) Franco by indole-3 acetic acid. IAWA Bulletin (1986) 7:13-16.

Cote WA, Day AC. Anatomy and ultrastructure of reaction wood. In: Cellular ultrastructure of woody plants Cote WA, ed. Syracuse University Press, New York, USA. (1965) 391-418.

Cown DJ. Effects of severe thinning and pruning treatments on the intrinsic wood properties of young radiata pine. New Zealand Journal of Forestry Science (1973) 3:379-389.

Cown DJ. Comparison of the effects of two thinning regimes on some wood properties of radiata pine. New Zealand Journal of Forestry Science (1974a) 4:540-551.

Cown DJ. Physical properties of Corsican pine grown in New Zealand. New Zealand Journal of Forestry Science (1974b) 4:76-93.

Cown DJ. New Zealand pine and Douglas fir - suitability for processing. Forest Research Bulletin 216 Forest Research Institute, Rotorua, New Zealand. (1999)

Cown DJ, Donaldson LA, Downes GM. A review of resin features in radiata pine. New Zealand Journal of Forestry Science (2011) 41:41-60

Cown DJ, Downes GM, Donaldson LA. Sources of variation in resin ducts - literature review WQI Report APP 36. (2004).

Cown DJ, Hanslett AN. The influence of wood quality on lumber drying distortion. Annals of Forestry Science (1996) 53:1177-1188.

Cown DJ, Haslett AN, Kimberley MO, McConchie DL. The influence of wood quality on lumber drying distortion. Annals of Forestry Science (1996) 53:1177-1188.

Cown DJ, Ilic J, Butterfield B. Compression wood in New Zealand radiata pine (2003). Wood Quality Initiative, Rotorua, New Zealand (unpublished).

Cown DJ, McConchie DL. Effects of thinning and fertiliser application on wood properties of *Pinus radiata*. New Zealand Journal of Forestry Science (1981) 11:79-91.

Cown DJ, Young GD, Kimberley MO. Spiral grain in plantation grown *Pinus radiata*. New Zealand Journal of Forestry Science (1991) 21:206-216.

Danborg F. Drying properties and visual grading of juvenile wood from fast grown *Picea abies* and *Picea sitchensis*. Scandinavian Journal of Forest Research (1994) 9:91-98.

De Vetter L, Cnudde V, Masschaele B, Jacobs PJS, Van Acker J. Detection and distribution analysis of organosilicon compounds in wood by means of SEM-EDX and micro-CT. Material Characterization (2006) 56:39-48.

Dhubhain AN, Evertsen JA, Gardiner JJ. The influence of compressionwood on the strength properties of Sitka spruce. Forest Products Journal (1988) 38:67-69.

Dinwoodie JM. Timber: Its nature and behaviour. 2 edn. E&FN Spon, New York, USA. (2000)

Donaldson LA. S3 lignin concentration in radiata pine tracheids. Wood Science and Technology (1987) 21:227-234.

Donaldson LA. Seasonal changes in lignin distribution during tracheid development in *Pinus radiata* D. Don. Wood Science and Technology (1991) 25:15-24.

Donaldson LA. Lignification and lignin topochemistry - an ultrastructural view. Phytochemistry (2001) 57:859-873.

Donaldson LA. Abnormal lignin distribution in wood from severely drought stressed *Pinus radiata* trees. IAWA Journal (2002) 23:161-178.

Donaldson LA. Microfibril angle - measurement, variation and relationships - A review. IAWA Journal (2008) 29:345-386.

Donaldson LA, Bond J. Fluorescence microscopy of wood. Scion, Rotorua, New Zealand (CD). (2005)

Donaldson LA, Burdon RD. Clonal variation and repeatability of microfibril angle in *Pinus radiata*. New Zealand Journal of Forest Science (1995) 25:164-174.

Donaldson LA, Grace J, Dowens GM. Within tree variation in anatomical properties of compression wood in radiata pine. IAWA Journal (2004) 25:253-271.

Donaldson LA, Lausberg MJF. Comparison of conventional transmitted light and confocal microscopy for measuring wood cell dimensions by image analysis. IAWA Journal (1998) 19:321-326.

Donaldson LA, Radotic K, Kalauzi A, Djikanovic D, Jeremic M. Quantification of compression wood severity in tracheids of *Pinus radiata* D. Don using confocal fluorescence imaging and spectral deconvolution. Journal of Structural Biology (2010) 169:106-115.

Donaldson LA, Singh AP, Yoshinaga A, Takabe K. Lignin distribution in mild compression wood of *Pinus radiata* D. Don. Canadian Journal of Botany (1999) 77:41-50.

Donaldson LA, Turner JCP. The influence of compression wood and microfibril angle on the occurrence of distortion in window frames made from radiata pine (*Pinus radiata*). Holz als Roh- und Werkstoff (2001) 59:163-168.

Donaldson LA, Xu P. Microfibril orientation across the secondary cell wall of radiata pine tracheids. Trees - Structure and Function (2005) 19:644-653.

Dumbrell IC, McGrath JF. Effect of fertiliser and growth rate on angle of spiral grain in young *Pinus radiata* in Western Australia. Australian Forestry (2000) 63:142-146.

Duncker P, Spiecker H. Detection and classification of Norway spruce compression wood in reflected light by means of hyperspectral image analysis. IAWA Journal (2009) 30:59-70.

Duncker P, Warensjö M. Detection of compression wood: literature review (2005): http://www.forestry.gov.uk/website/forestresearch.nsf/ByUnique/GGAE-5GGEAX Accessed 09/05/09.

Ekevad M. Method to compute fiber directions in wood from computed tomography images. Jounal of Wood Science (2004) 50:41-46.

Eklund L, Sall H. The influence of wind on spiral grain formation in conifer trees. Trees - Structure and Function (2000) 14:324-328.

Eklund L, Sall H, Linder S. Enhanced growth and ethylene increases spiral grain formation in *Picea abies* and *Abies balsamea* trees. Trees (2003) 17:81-86.

Elliott GK. Spiral grain in second growth Douglas fir and western hemlock. Forest Products Journal (1958) 8:91-98.

Esau K. Anatomy of seed plants. 2 edn. John Wiley & Sons, New York, USA. (1977)

Fahn A, Zamski E. The influence of pressure, wind, wounding and growth substances on the rate of resin duct formation in *Pinus halepensis* wood. Israel Journal of Botany (1970) 19:429-446.

Fielding JM. Spiral grain in *Pinus radiata* plantations in the Australian Capital Territorry. Forestry and Timber Bureau Comonwealth of Australia, Canberra, Australia (1967)

Foster B. Optimizing light microscopy for biological and clinincal laboratories. Dubuque, Iowa, USA. (1997)

Frey-Wissling A. The plant cell wall. Encyclopedia of plant anatomy. 3 edn. Gebruder Borntraeger, Berlin, Germany. (1976)

Fromm JH, Sautter I, Matthies D, Kremer J, Schumacher P, Ganter C. Xylem water content and wood density in spruce and oak trees detected by high-resolution computed tomography. Plant Physiology (2001) 127:416-425.

Fukushima K, Terashima N. Heterogeneity in formation of lignin. Part XV: Formation and structure of lignin in compression wood of *Pinus thunbergii* studied by microautoradiography. Wood Science and Technology (1991) 25:371-381.

Funada R, Mizukami E, Kubo T, Fushitani M, Sugiyama T. Distribution of indole-3-acetic acid and compression wood formation in the stems of inclined *Cryptomeria japonica*. Holzforschung (1990) 44:331-334.

Gapare W, Hathorn A, Kain D, Matheson C, Wu H. Inheritance of spiral grain in the juvenile core of *Pinus radiata*. Canadian Journal of Forest Research (2007) 37:116-127.

Gardiner BA, MacDonald EM. Compression wood in conifers - the characterisation of its formation and its relevance to timber quality. Final Report on the European Union Compression Wood Project QLK5-CT-2001-00177. QOL-2000-5.3: Sustainable and multi-purpose utilisation of forest resources: the integrated forestry-wood chain. Forest Research, Surrey UK. (2005)

Gindl W, Teischinger A. The potential of vis and NIR spectroscopy for the non-destructive evaluation of grain angle in wood. Wood and Fiber Science (2002) 34:651-656.

Gjerdrum P, Sall H, Storo HM. Spiral grain in Norway spruce: constant change rate in grain angle in Scandinavian sawlogs. Forestry (2002) 75:163-170.

Hansen JK, Roulund H. Genetic parameters for spiral grain, stem form, pilodyn and growth in 13 years old Sitka spruce (*Picea sitchensis*). Silva Genetica (1997) 46:107-113.

Hansen JK, Roulund H. Spiral grain in a clonal trial with Sitka spruce. Canadian Journal of Forest Research (1998) 28:911-919.

Harding K, Woolaston R. Genetic parameters for wood and growth properties in *Auraucaia cunninghamii*. Silva Genetica (1991) 40:232-237.

Harris JM. Preliminary studies of spiral grain in radiata pine. In: IUFRO Section 41 Melbourne, Australia. (1965) 23.

Harris JM. On the causes of spiral grain in corewood of radiata pine. New Zealand Journal of Botany (1969) 7:189-213.

Harris JM. Spiral grain and xylem polarity in radiata pine: microscopy of cambial reorientation. New Zealand Journal of Forestry Science (1973) 3:363-378.

Harris JM. Shrinkage and density of radiata pine compression wood in relation to its anatomy and mode of formation. New Zealand Journal of Forestry Science (1977) 7:91-106.

Harris JM. Spiral grain formation In: Xylem cell development. Barnett JR, ed. Castle House, Tunbridge Wells, UK. (1981) 256-274.

Harris JM. Spiral grain and wave phenomena in wood formation. Springer-Verlag, Berlin, Germany. (1989)

Haslett AN, Simpson IG, Kimberley MO. Utilisation of 25 year old *Pinus radiata*. Part 2- Warp of structural timber in drying. New Zealand Journal of Forestry Science (1991) 21:228-234.

Hejnowicz Z. Anticlinal division, intrusive growth, and loss of fusiform initials in nonstoried cambium. Acta Societatis Botanicorum Poloniae (1961) 30:729-748.

Hejnowicz Z. Tensional stress in the cambium and its developmental significance. American Journal of Botany (1980) 67:1-5.

Hejnowicz Z, Marek ZB. Mechanism of changes in grain inclination in wood produced by storeyed cambium. Acta Societatis Botanicorum Poloniae (1974) 43:381-398.

Hejnowicz Z, Romberger JA. Migrating cambial domains and the origin of wavy grain in xylem of broadleaved trees. American Journal of Botany (1973) 60:209-222.

Hejnowicz Z, Romberger JA. The common basis of wood grain figures in the systematically changing orientation of cambial fusiform cells. Wood Science and Technology (1979) 13:89-96.

Herrick EH. Further notes on twisted trees. Science (1932) 76:406-407.

Higgins MD. Imaging birefringent minerals without extinction using circularly polarised light. The Canadian Mineralogist (2010) 48:231-235.

Hoch HC, Galvani CD, Szarowski DH, Turner JN. Two new fluorescent dyes applicable for visualization of fungal cell walls. Mycologia (2005) 97:580-588.

Houkal D. Spiral grain in *Pinus oocarpa*. Wood Fiber (1982) 14:320-330.

Howard NF. Twisted trees. Science (1932) 75:132-133.

IAWACommittee, Richter HG, Grosser D, Heinz I, Gasson PE. IAWA List of microscopic features for softwood identification. IAWA Journal (2004) 25:1-70.

Illman BL, Dowd BA. High resolution microtomography for density and spatial information about wood structures. In: Proceedings of SPIE on Developments in X-ray Tomography II, Bonse U, ed. Society of Photo-Optical Instrumentation Engineers, Washington, USA. (1999) 198-204.

Ishida T, Kaneko Y, Iwano M, Hashimoto T. Helical microtubule arrays in a collection of twisting tubulin mutants of *Arabidopsis thaliana*. Proceedings of the National Academy of Sciences of the USA (2007) 104:8544-8549.

Jacobs MR. The occurrence and importance of spiral grain in *Pinus radiata* in the Federal Capital Territory, Leaflet No 50, Australia Commenwealth Forestry Bureau, Canberra, Australia. (1935)

Jacot AP. Tree twist. Science (1931) 73:567.

Jang HF. Measurement of fibril angle in wood fibres with polarization confocal microscopy. Journal of Pulp & Paper Science (1998) 24:224-230.

Johanson M. Moisture induced distortion in Norway spruce timber - experiments and models. PhD Thesis, Dept. of Structural Engineering, Chalmers University, Goeteborg, Sweden. (2002)

Johansson M, Perstorper M, Kliger R, Johansson G. Distortion of Norway spruce timber Part 2. Modelling twist. Holz als Roh- und Werkstoff (2001) 59:155-162.

Jura J, Kojs P, Iqbal M, Pulka JS, Włoch W. Apical intrusive growth of cambial fusiform initials along the tangential walls of adjacent fusiform initials - evidence for a new concept. Australian Journal of Botany (2006) 54:493-504.

Kadambi K, Dabral SN. On twist in chir (*Pinus longifolia* Roxb.). Indian Forester (1955) 81:58-64.

Kanai Y, Fujita M, Takabe K. Vessel network tracing by wire insertion and pigment injection. Bulletin of Kyoto University Forests (1996) 68:127-136.

Kliger RI. Spiral grain on logs under bark reveals twist-prone raw material. Forest Products Journal. (2001) 51:67-73.

Knight NL, Sutherland MW. A rapid differential staining technique for *Fusarium pseudograminearum* in cereal tissues during crown rot infections. Plant Pathology (2011) 60:1140-1143.

Koehler A. Guide to determining slope of grain in lumber and veneer. FPL-1585, US Forest Service Report, USA. (1955)

Kohl EJ. An explanation of the cause of spiral grain in trees. Science (1933) 78:58-59.

Kojs P, Włoch W, Rusin A. Rearrangement of cells in storeyed cambium of *Lonchocarpus sericeus* connected with formation of interlocked grain in the xylem. Trees (2004) 18:136-144.

Kollmann FFP, Cote WA. Principles of wood science and technology. Volume I, Solid Wood. Springer Verlag, Berlin, Germany. (1984)

Koslowski TT, Winget CH. Patterns of water movement in forest trees. Botanical Gazette (1963) 124:301-311.

Kubler H. Function of spiral grain in trees. Trees (1991) 5:125-135.

Kukkola E, Saranpaa P, Fagerstedt K. Juvenile and compressionwood cell wall layers differ in lignin structure in Norway spruce and Scots pine. IAWA Journal (2008) 29:47-54.

Kuroda K, Shimaji K. Traumatic resin canal formation as a marker of xylem growth. Forest Science (1983) 29:653-659.

Lampugnani ER, Moller IE, Cassin A, Jones DF, Koh PL, Ratnayake S, Beahan CT, Wilson SM, Bacic A, Newbigin E. *In vitro* grown pollen tubes of *Nicotiana alata* actively synthesise a fucosylated xyloglucan. PLoS ONE (2013) 8:1-10.

Landrein B, Lathe R, Bringmann M, Vouillot C, Ivakov A, Boudaoud A, Persson S, Hamant O. Impaired cellulose synthase guidance leads to stem torsion and twists phyllotactic patterns in *Arabidopsis*. Current Biology (2013) 23:895-900.

LaPasha CA, Wheeler EA. Resin canals in *Pinus taeda*: longitudinal canal lengths and interconnections between longitudinal and radial canals. IAWA Journal (1990) 11:227-238.

Larson PR. The vascular cambium: development and structure. Springer, Berlin, Germany. (1994)

Lausberg MJF. Developing a non-destructive method for measuring spiral grain in radiata pine. In: Wood Quality Workshop '95, Klitscher K, ed. Rotorua, New Zealand. (1997) 6-10.

Leelavanichkul S, Cherkaev A. Why the grain in tree trunks spirals: A mechanical perspective. Structural & Multidisciplinary Optimization (2004) 28:127-135.

Li X, Chapple C. Understanding lignification: challenges beyond monolignol biosynthesis. Plant Physiology (2010) 154:449-452.

Liang BM, Dennings AM, Sharp RE, Baskin TI. Consistent handedness of microtubule helical arrays in maize and *Arabidopsis* primary roots. Protoplasma (1996) 190:8-15.

Lin J, Hu Y, He X, Ceulemans R. Systematic survey of resin canals in Pinaceae. Belgian Journal of Botany (2002) 135:3-14.

Liu L, Shang-Guan K, Zhang B, Liu X, Yan M, Zhang L, Shi Y, Zhang M, Qian Q, Li J, Zhou Y. Brittle Culm1, a COBRA-like protein, functions in cellulose assembly through binding cellulose microfibrils. PLoS Genetics (2013) 9:1-15.

Low AJ. Compression wood in conifers - A review of literature. Part 1. Forestry Abstracts (1964) 25:35-43.

Lowery DP. A spiral grain classification system and its application. Forest Products Journal (1966) 16:47-50.

Lu W, Tan J. Grain pattern characterization and classification of walnut by image processing. Wood and Fiber Science (2004) 36:311-318.

Marcus SE, Blake AW, Benians TAS, Lee KJD, Poyser C, Donaldson LA, Leroux O, Rogowski A, Petersen HL, Boraston A, Gilbert HJ, Willats WGT, Knox JP. Restricted access of proteins to mannan polysaccharides in intact plant cell walls. Plant Journal (2010) 64:191-203.

Matsumura J, Booker RE, Donaldson LA, Ridout BG. Impregnation of radiata pine wood by vacuum treatment -identification of flow paths using fluorescent dye and confocal microscopy. IAWA Journal (1998) 19:25-33.

Mattheck C. Trees - the mechanical design. Springer, Berlin, Germany. (1991)

Maurer A, Fengel D. Electron microscopic representation of structural details in softwood cell walls by very thin ultramicrotome sections. Holz als Roh- und Werkstoff (1991) 49:53-56.

Mavrou I. Modelling spiral angle in *Picea sitchensis*. MSc Thesis, University of York, York, United Kingdom. (2007)

McDonald KA, Bendsten BA. Measuring localized slope of grain by electrical capacitance. Forest Products Journal (1986) 36:75-78.

McLaren P. Internal wood quality of radiata pine on farm sites - a review of the issues. New Zealand Journal of Forestry (2002) November:24-28.

McLauchlan TA, Norton JA, Kusec DJ. Slope-of-grain indicator. Forest Products Journal (1973) 23:50-55.

Michels J, Büntzow M. Assessment of Congo red as a fluorescence marker for the exoskeleton of small crustaceans and the cuticle of polychaetes. Journal of Microscopy (2010) 238:95-101.

Mickovski SB, Ennos AR. The effect of unidirectional stem flexing on shoot and root morphology and architecture in young *Pinus sylvestris* trees. Canadian Journal of Forest Research (2003) 33:2202-2209.

Misra P. Observations on spiral grain in the wood of *Pinus longifolia,* Roxb. Forestry (1939) 13:118-133.

Misra P. Correlation between eccentricity and spiral grain in the wood of *Pinus longifolia*. Forestry (1943a) 17:67-80.

Misra P. Xylem rays in relation to the eccentric rings and the spiral grain in the wood of *Pinus longifolia*, Roxb. Jounal of Indian Botanical Society (1943b) 21:327-331.

Moell MK, Fujita M. Fourier transform methods in image analysis of compression wood at the cellular level. IAWA Journal (2004) 25:311-324.

Nagy NE, Franceschi VR, Solheim H, Krekling T, Christiansen E. Wound-induced traumatic resin duct development in stems of Norway spruce (Pinaceae): anatomy and cytochemical traits. American Journal of Botany (2000) 87:302-313.

Nanayakkara B, Manley-Harris M, Suckling ID, Donaldson LA. Chemical characterization of compression wood in *Pinus radiata*. In: 59th Appita Annual Conference, Carlton, Australia. Appita (2005) 585–592.

Nanayakkara B, Manley-Harris M, Suckling ID, Donaldson LA. Quantitative chemical indicators to assess the gradation of compression wood. Holzforschung (2009) 63:431-439.

Nicholls JWP. Wind action, leaning trees and compression wood in *Pinus radiata* D.Don. Australian Forest Research (1982) 12:75-91.

Nordmark U. Knot identification from CT images of young *Pinus sylvestris* sawlogs using artificial neural networks. Scandinavian Journal of Forest Research (2002) 17:72-78.

Northcott PL. Is spiral grain the normal growth pattern? Forestry Chronicle (1957) 33:335-352.

Noskowiak AF. Spiral grain in trees - A review. Forest Products Journal (1963) 13:266-275.

Nyström J. Automatic measurement of compression wood and spiral grain for the prediction of distortion in sawn wood products. Doctoral Thesis, Division of Wood Technology, Lulea University of Technology, Skelleftea, Sweden. (2002)

Nyström J. Automatic measurement of fiber orientation in softwoods by using the tracheid effect. Computers and Electronics in Agriculture (2003) 41:91-99.

Nyström J, Grundberg S. Real- time non contact measurements of spiral grain on debarked saw logs. In: 13th International symposium on non-destructive testing of wood, University of California, Berkeley, California, USA. (2002) 43-47.

Nyström J, Kline DE. Automatic classification of compression wood in green southern yellow pine. Wood and Fiber Scince (2000) 32:301-310.

O'Neill GA, Aitken SN, King JN, Alfaro RI. Geographic variation in resin canal defenses in seedlings from the Sitka spruce × white spruce introgression zone. Canadian Journal of Forest Research (2002) 32:390-400.

Ogata Y, Fujita M. New anatomical method of grain angles measurement using confocal microscopy and image cross correlation. Trees (2005) 19:73-80.

Ogata Y, Fujita M, Nobuchi T, Sahri MH. Macroscopic and anatomical investigation of interlocked grain in *Acacia mangium*. IAWA Journal (2003) 24:13-26.

Ormarsson S, Cown DJ. Moisture-related distortion of timber boards of radiata pine: comparison with Norway spruce. Wood and Fiber Science (2005) 37:424-436.

Ormarsson S, Dahlblom O, Petersson H. A numerical study of the shape stability of sawn timber subjected to moisture variation. Part 1: Theory. Wood Science and Technology (1998) 32:325-334.

Ormarsson S, Dahlblom O, Petersson H. A numerical study of the shape stability of sawn timber subjected to moisture variation. Part 2: Simulation of drying board. Wood Science and Technology (1999) 33:407-423.

Ormarsson S, Dahlblom O, Petersson H. A numerical study of the shape stability of sawn timber subjected to moisture variation Part 3: Influence of annual ring orientation. Wood Science and Technology (2000) 34: 207-219.

Pang S, Wiberg P. Model predicted and CT scanned moisture distributed in a *Pinus radiata* board during drying. Holz als Roh- und Werkstoff (1998) 56:9-14.

Pape R. Influence of thinning on spiral grain in Norway spruce grown on highly productive sites in southern Sweden. Silva Fennica (1999) 33:3-12.

Park S, Szumlanski AL, Gu F, Guo F, Nielsen E. A role for CSLD3 during cell-wall synthesis in apical plasma membranes of tip-growing root-hair cells. Nature Cell Biology (2011) 13:973-980.

Patselt WJ. Polarized light microscopy - principles, instruments, applications. 3 edn. Ernst Leitz, Wetzlar, Germany. (1985)

Pauwels E, Van Loo D, Cornillie P, Brabant L, Van Hoorebeke L. An exploratory study of contrast agents for soft tissue visualization by means of high resolution X-ray computed tomography imaging. Journal of Microscopy (2013) 250:21-31.

Pawsey CK. Development of grafts of radiata pine made with scions of various origins. New Zealand Journal of Forestry Science (1974) 4:371-372.

Perem E. The effect of compression wood on the mechanical properties of white spruce and red pine. Forest Products Journal (1958) 8:235-240.

Plomion C, Leprovost G, Stokes A. Wood formation in trees. Plant Physiology (2001) 127:1513-1523.

Pont D, Brownlie RK, Grace JC. Disc image processsing software for three dimensional mapping of stem ring width and compression wood. New Zealand Journal of Forestry Science (2007) 37:168-185.

Prentø P. Staining of macromolecules: possible mechanisms and examples. Biotechnic & Histochemistry (2009) 84:139-158.

Preston RD. Spiral structure and spiral growth- the development of spiral grain in conifers. Forestry (1949) 23:48-55.

Rao KR, Juneja KBS. Field identification of fifty important timbers of India. Indian Council of Forestry Research & Education, Dehradun, India. (1992)

Rasband WS. ImageJ Bethseda, MD: National Institute of Health, USA. (1997-2009)

Rauchfuss J, Speer JH. Age dependence of spiral grain in white oaks (*Quercus alba* L.) in south-western Illinois. Tree-Ring Research (2006) 62:13-24.

Rault JP, Marsh EK. The incidence and silvicultural implications of spiral grain in *Pinus longifolia* Roxb. in South Africa and its effect on converted timber. In: Proceedings of Commonwealth Forestry Conference Canada. Forest Products Institute, Pretoria, South Africa (1952) 1-21.

Raymond C. Genetics of *Eucalyptus* wood properties. Annals of Forestry Science (2002) 59:525-531.

Saito K, Fukushima K. Distribution of lignin inter-unit bonds in the differentiating xylem of compression wood and normal woods of *Pinus thurnbergii*. Journal of Wood Science (2005) 51:246-251.

Samson M. Measuring general slope of grain with the slope of grain indicator. Forest Products Journal (1984) 34:27-32.

Samson M, Tremblay C, Langlais PA. Measuring slope of grain by electrical capacitance at moisture contents above fiber saturation Forest Products Journal (1993) 43:58-60.

Saren MP, Serimaa R, Tolonen Y. Determination of fiber orientation in Norway spruce using X-ray diffraction and laser scattering. Holz als Roh- und Werkstoff (2006) 64:183-188.

Sauter M, Seagull RW, Kende H. Internodal elongation and orientation of cellulose microfibrils and microtubules in deepwater rice. Planta (1993) 190:354-362.

Savidge RA, Farrar JL. Cellular adjustments in the vascular cambium leading to spiral grain formation in conifers. Canadian Journal of Botany (1984) 62:2872–2879.

Schajer GS, Orhan FB. Measurement of wood grain angle, moisture content and density using microwaves. Holz als Roh- und Werkstoff (2006) 64:483-490.

Scheller H, Ulvskov P. Hemicelluloses. Annual Review of Plant Biology (2010) 61:263-289.

Schimleck LR, Evans R. Estimation of *Pinus radiata* D. Don tracheid morphological characteristics by near infrared spectroscopy. Holzforchung (2001) 58:66-73.

Schmoldt DL, He J, Abbott AL. Automated labeling of log features in CT imagery of multiple hardwood species. Wood and Fiber Science (2000) 32:287-300.

Schulgasser K, Witztum A. The mechanism of spiral grain formation in trees. Wood Science and Technology (2007) 41:133-156.

Sedighi-Gilani M, Sunderland H, Navi P. Microfibril angle non-uniformities within normal and compression wood tracheids. Wood Science and Technology (2005) 39:419-430.

Sedighi-Gilani M, Sunderland H, Navi P. Within-fibre non-uniformities of microfibril angle. Wood and Fiber Science (2006) 38:132-138.

Selig B, Hendriks CLL, Bardage S, Daniel G, Borgefors G. Automatic measurement of compression wood cell attributes in fluorescence microscopy images. Journal of Microscopy (2012) 246:298-308.

Sepúlveda P. Measurement of spiral grain with computed tomography. Journal of Wood Science (2001) 47:289-293.

Sepúlveda P, Oja J, Gronlund A. Modelling spiral grain in saw logs based on data from a simulated X-ray log scanner. In: Fourth workshop IUFRO S5.01.04, Harrison Hot Springs, British Columbia, Canada (2002a) 155-161.

Sepúlveda P, Oja J, Gronlund A. Predicting spiral grain by computed tomography of Norway spruce. Journal of Wood Science (2002b) 48:479-483.

Sharma M. New approaches to wood quality assessment. PhD Thesis, School of Forestry, University of Canterbury, Christchurch, New Zealand. (2013)

Shelbourne CJA. Relationships between degree of compression wood development and specific gravity and tracheid characteristics in loblolly pine (*Pinus taeda* L.). Holzforschung (1968) 22:185-190.

Skatter S, Kucera B. Spiral grain - An adaptation of trees to withstand stem breakage caused by wind induced torsion. Holz als Roh- und Werkstoff (1997) 55:207-213.

Skatter S, Kucera B. The cause of the prevalent directions of the spiral grain patterns in conifers. Trees (1998) 12:265-273.

Sleigh JA. An investigation in to the incidence of spiral grain and compression wood in selected peeler cores from two separate forests. B.For.Sci. Thesis, University of Canterbury, Christchurch, New Zealand. (1996)

Slifkin M, Cumbie R. Congo red as a fluorochrome for the rapid detection of fungi. Journal of Clinical Microbiology (1988) 26:827-830.

Sorensson CT, Burdon RD, Cown DJ, Jefferson PA, Shellbourne CJA. Incorporating spiral grain in to New Zealand's radiata pine breeding programme. In: IUFRO '97 Genetics of Radiata pine, Burdon RD, Moore JM, eds. Forest Research Institute, Rotorua, New Zealand (1997) 180-191.

Sorensson CT, Lausberg MJF. Towards genetic improvement of spiral grain. In: Tree improvement for sustainable tropical forestry :QFRI - IUFRO Conference, M. J. Dieters MJ, Nikles DG, Harwood CE and Walker SM, eds. Queensland Forestry Research Institute, Caloundra, Queensland. Australia (1996) 216.

Steppe K, Cnudde V, Girard C, Lemeur R, Cnudde J-P, Jacobs P. Use of X-ray computed microtomography for non-invasive determination of wood anatomical characteristics. Journal of Structural Biology (2004) 148:11-21.

Sun J, Phillips CM, Anderson CT, Beeson WT, Marletta MA, Glass NL. Expression and characterization of the *Neurospora crassa* endoglucanase GH5-1. Protein Expression and Purification (2011) 75:147-154.

Sundberg B, Tuominen H, Little CHA. Effects of the indole-3 acetic acid transport inhibitors N-1-N naphthylphthalamic acid and morphactin on endogenous IAA dynamics in relation to compression wood formation in 1 year old *Pinus sylvestris* shoots. Plant Physiology (1994) 106:469-476.

Suslov D, Verbelen J-P, Vissenberg K. Onion epidermis as a new model system to study the control of growth anisotropy in higher plants. Jounal of Experimental Botany (2009) 60:4175-4187.

Tarvainen V. Measures for improving quality and shape stability of sawn softwood timber during drying and under service conditions - Best practice manual to improve straightness of sawn timber. VTT Publications Otamedia Oy, Espoo, Finland. (2005)

Telewski FW. Structure and function of flexure wood in *Abies fraseri*. Tree Physiology (1989) 5:113-121.

Thinley C, Palmer G, Vanclay JK, Henson M. Spiral and interlocking grain in *Eucalyptus dunnii*. Holz als Roh- und Werkstoff (2005) 63:372-379.

Thitamadee S, Tuchihara K, Hashimoto T. Microtubule basis for left-handed helical growth in *Arabidopsis*. Nature (2002) 417:193-196.

Thomas J, Ingerfeld M, Nair H, Chauhan S, Collings DA. Pontamine fast scarlet 4B: a new fluorescent dye for visualising cell wall organisation in radiata pine tracheids. Wood Science and Technology (2013) 47:59-75.

Tian X, Cown DJ, Lousberg MJF. Modelling of *Pinus radiata* wood properties. Part 1 Spiral grain. New Zealand Journal of Forestry Science (1996) 25:200-213.

Timell TE. Origin and evolution of compression wood. Holzforschung (1983) 37:1-10.

Timell TE. Compression wood in gymnosperms. Springer Verlag, Heidelberg, Germany. (1986)

Toit AJD. A study of the influence of compression wood on the warping of *Pinus radiata* D.Don timber. South African Forestry Asscociation Journal (1963) 44:11-15.

Tomlin ES, Borden JH. Thin bark and high density of outer resin ducts - Interrelated resistance traits in Sitka spruce against the white pine weevil (Coleoptera: Curculionidae). Journal of Economic Entomology (1997) 90:235-239.

Tong QJ, Zhang SY, Levesque Y. Modeling and sawing simulation of sugar maple logs-application of computer tomography images In: International symposium on plant growth modeling, simulation, visualization and their applications. Tsinghua University Press, Beijing, China (2003) 349-359.

Trtik P, Dual J, Keunecke D, Mannes D, Niemz P, Stähli P, Kaestner A, Groso A, Stampanoni M. 3D imaging of microstructure of spruce wood. Journal of Structural Biology (2007) 159:46-55.

Tsehaye A. Within and between tree variation in the wood quality of radiata pine., PhD Thesis, University of Canterbury, Christchurch, New Zealand. (1995)

Tsehaye A, Walker JCF. Spiral grain in Canterbury *Pinus radiata* - Within and between tree variations and effect on mechanical properties. New Zealand Journal of Forestry Science (1996) 25:358-366.

van den Bulcke J, Boone M, Van Acker J, Stevens M, Van Hoorebeke L. X-ray tomography as a tool for detailed anatomical analysis. Annals of Forest Science (2009) 66:508.

Verbelen J-P, Kerstens S. Polarization confocal microscopy and Congo red fluorescence: a simple and rapid method to determine the mean cellulose fibril orientation in plants. Journal of Microscopy (2000) 198:101-107.

Verbelen J-P, Stickens D. *In vivo* determination of fibril orientation in plant-cell walls with polarization CSLM. Journal of Microscopy (1995) 177:1-6.

Voiniciuc C, Dean GH, Griffiths JS, Kirchsteiger K, Hwang YT, Gillett A, Dow G, Western TL, Estelle M, Haughn GW. Flying saucer1 is a transmembrane RING E3 ubiquitin ligase that regulates the degree of pectin methylesterification in *Arabidopsis* seed mucilage. Plant Cell. (2013) 25:944-959.

Walker JCF, Butterfield B. The importance of microfibril angle for the processing industries. New Zealand Forestry (1995) November 1995:34-40.

Walker JCF, Butterfield BG. Primary wood processing: Principles and practice. Chapman and Hall, London, UK. (1993)

Walther T, Thoemen H. Synchrotron X-ray microtomography and 3D image analysis of medium density fiberboard (MDF). Holzforschung (2009) 63:581-587.

Wang W, Wang L, Chen C, Xiong G, Tan X-Y, Yang K-Z, Wang Z-C, Zhou Y, DeYe, Chen L-Q. *Arabidopsis CSLD1* and *CSLD4* are required for cellulose deposition and normal growth of pollen tubes. Journal of Experimental Botany (2011) 62:5161-5177.

Wang Y, Muszynski L, Simonsen J. Gold as an X-ray CT scanning contrast agent: Effect on the mechanical properties of wood plastic composites. Holzforschung (2007) 61:723-730.

Wardrop AB, Dadswell HE. The development of the conifer tracheid. Holzforschung (1953) 7:33-39.

Warensjö M, Nylinder M, Walter F. Modelling compression wood using data from a 3D laser scanner. In: Fourth Workshop IUFRO S5.01.04, Nepveu G, ed. Harrison Hot Springs, British Columbia, Canada (2002) 178-185.

Wei Q, Chui YH, Leblon B, Zhang SY. Identification of log characteristics in computed tomography images using back-propagation neural networks with the resilient back-propagation training algorithm and textural analysis: Preliminary results. Wood and Fiber Science (2008) 40:620-633.

Wei Q, Chui YH, Leblon B, Zhang SY. Identification of selected internal wood characteristics in computed tomography images of black spruce - a comparison study. Journal of Wood Science (2009) 55:175-180

Wentworth CK. Twist in the grain of coniferous trees. Science (1931) 73:192.

Werker E, Fahn A. Resin ducts of *Pinus halepensis* Mill. - Their structure, development and pattern of arrangement. Botanical Journal of the Linnean Society (1969) 62:379-411.

Wernsdörfer H, Reck P, Seeling U, Becker G, Seifert T. Identifying and measuring compression wood of Norway Spruce (*Picea abies* (L.) Karst.) by using methods of digital image analysis. Holz als Roh- und Werkstoff (2004) 62:243-252.

Westing AH. Formation and function of compression wood in gymnosperms. Botanical Review (1965) 31:381-480.

Wiedenhoeft AC, Miller RB. Brief comments on the nomenclature of softwood axial resin canals and their associated cells. IAWA Journal (2002) 23 299-303.

Wiedenhoeft AC, Miller RB. Structure and function of wood. In: Handbook of wood chemistry and wood composites. Rowell RM, ed. CRC Press, Boca Raton, Florida, USA. (2005) 9-33.

Wilson BF, Chien CT, Zaerr JB. Distribution of endogenous indole-3 acetic acid and compression wood formation in reoriented branches of Douglas fir. Plant Physiology (1989) 91:338-344.

Wiltshire EJ, Collings DA. New dynamics in an old friend: dynamic tubular vacuoles radiate through the cortical cytoplasm of red onion epidermal cells. Plant Cell Physiology (2009) 50:1826-1839.

Wimmer R, Grabner M. Effects of climate on vertical resin duct density and radial growth of Norway spruce [*Picea abies* (L.) Karst.]. Trees (1997) 11:271-276.

Wimmer R, Grabner M, Strumia G, Sheppard PR. Significance of vertical resin ducts in the tree rings of spruce. In: Tree Ring Analysis. Biological, methodological and environmental aspects Wimmer R, Vetter RE, eds. CABI Publishing, Wallingford, UK (1999) 107-118.

Włoch W, Mazur E, Beltowski M. Formation of spiral grain in the wood of *Pinus sylvestris*. Trees (2002) 16:306-312.

Włoch W, Mazur E, Kojs P. Intensive change of inclination of cambial initials in *Picea abies* (L.) Karst. tumours. Trees (2001) 15:498-502.

Wood PJ. Specificity in the interaction of direct dyes with polysaccharides. Carbohydrate Research (1980) 85:271-287.

Wu H, Hu Z-H. Comparative anatomy of resin ducts of the Pinaceae. Trees (1997) 11:135-143.

Yamaguchi KY, Itoh T, Shimaji K. Compression wood induced by 1-N-naphthylphthalamic acid (NPA)- an IAA transport inhibitor. Wood Science and Technology (1980) 14:181-185.

Yeh T-F, Braun JL, Chang H-M, Kadla JF, Goldfarb B. Morphological and chemical variations between juvenile wood, mature wood, and compression wood of loblolly pine (*Pinus taeda* L.). Holzforschung (2006) 60:1-8.

Yeh T-F, Goldfarb B, Chang H-m, Peszlen I, Braun JL, Kadla JF. Comparison of morphological and chemical properties between juvenile wood and compression wood of loblolly pine. Holzforschung (2005) 59:669-674.

Yoshizawa N, Watanabe N, Yokota S, Idei T. Distribution of guaiacyl and syringyl lignins in normal and compression wood of *Buxus microphylla*. IAWA Journal (1993) 14:139-151.

Yumoto M, Ishida S, Fukazawa K. Studies on the formation and structure of the compression wood cells induced by artificial inclination in young trees of *Picea glauca*. Part IV Gradation of the severity of compression wood tracheids. Research Bulletins of the College Experiment Forests (1983) 40:409-452.

Zagorska-Marek B, Little, C.H.A. Control of fusiform initial orientation in the vascular cambium of *Abies balsamea* stems by indole-3-ylacetic acid. Canadian Journal of Botany (1986) 64:1120-1128.

Zobel B, Stonecypher RW, Browne C. Inheritance of spiral grain in young Loblolly pine. Forest Science (1965) 14:376-379.

Zobel BJ, Sprague JR. Juvenile wood in forest trees. Springer series in wood science Springer, Berlin, Germany. (1998).

Appendix -: 1

Macros used to find the number and area of resin canals in a wood transverse section image.

Prerequisites: Wood transverse section images scanned as an RGB image at, 2400 dpi are required.

Macro 1 - Measuring the area of wood transverse section

1) In ImageJ, open the macro window using the command sequence '*Process* / *batch* / *macro.*'

2) Select the input folder containing the images for analysing, and select an output folder or create a new folder to save the resultant images. Also select '*Output Format*' from the drop down menu as '*TIFF.*'

3) Use the following commands by copying them to the active window.

```
run("8-bit");
run("Make Binary");
run("Fill Holes");
run("Set Scale...", "distance = 2400”, known distance = 25.4”,
   “pixel aspect ratio = 1”, “unit of length” = mm");
run("Analyze Particles...", "size = 15-Infinity”, “circularity =
   0.40-1.00”, “show = Outlines display record in_situ");
close();
```

4) Click on '*Process*.'

5) All the images in the input folder will be processed and resultant images will be saved as TIFF images in the output folder.

Macro 2 - Conversion of all images to 8 bit black and white

1) In ImageJ, open the macro window using the command sequence '*Process* / *batch* / *macro.*'

2) Select the input folder containing the images for analysing, and select another output folder or create a new folder to save the resultant images. This should be different to the folder used for Macro 1. Also select '*Output Format*' from the drop down menu as '*TIFF.*'

3) Use the following commands by copying them to the active window.

```
run("8-bit");
```

4) Click on '*Process*.'

Macro 3 - Counting and measuring resin canals in a wood transverse section image

1) In ImageJ, open the macro window using the command sequence '*Process* / *batch* / *macro.*'

2) Select the input folder containing the images for analysing, and select another output folder or create a new folder to save the resultant images. This should be different to the folder used for Macros 1 and 2. Also select '*Output Format*' from the drop down menu as '*TIFF.*'

3) Use the following commands by copying them to the active window.

```
run("Erode");
run("Find Edges");
run("Set Scale...", "distance=2400 known=25.4 pixel=1 unit=mm");
run("Analyze Particles...", "size=30-Infinity pixel
   circularity=0.40-1.00 show=Outlines display clear summarize
   record in_situ");
close();
```

4) Click on '*Process*.'

5) All the images in the input folder will be processed and resultant images will be saved as TIFF images in the output folder.

Appendix - 2:

Cumulative rotation macro for ImageJ.

Notes

1) This macro was written by Will Armour at the University of Sydney (Sydney, Australia) and appears with permission.

2) This macro is used to rotate images within an image stack by incrementally larger amounts. It was necessary because the StackReg plug-in within ImageJ aligned stacks of serial sections using the dominant feature. In these stacks, this was the resin canals rather than the vertically-aligned scoring mark that had been made along the stems.

3) It as necessary to ensure that the centre of the stem was at the centre of the image prior to running this macro. This could be done by expanding the image size, and then cropping this new image so that the stem centre was correctly in the centre of the image.

Cumulative rotation

```
fway\n"+
"\n");
Dialog.addNumber("Choose the number
of degrees to rotate by (+ve or -ve): ", 1);//the value
for calibrated 288dpi images 8.806
Dialog.addString
("Specify how you would like the image rotated (None,
Bilinear, Bicubic): ", "Bicubic");
Dialog.addNumber
("Choose how much extra border you would like on your
image (%): ", 30);
Dialog.show();
//Gets the choices the user entered for how may degrees
to rotate the image by and what type of transformation
to use
rotateSlice=Dialog.getNumber();
rotateSliceCumulative=rotateSlice;//initiates the
cumulative value to be the same as the input rotation
amount
rotateType=Dialog.getString();
imageBorderIncrease=Dialog.getNumber();
//This part asks the user to open the image and then
removes the extension e.g. .tif so you can save it as
```

```
whatever
open("");
inputImageName=getTitle;//gets the image title
inputFolder=getDirectory("image");//Choose the
folder of where the image was opened as the place where
to save the output image
index=lastIndexOf(inputImageName, ".");//selects file
extension eg. .tif
if (index!=-1) truncImageName=substring(inputImageName, 0,
    index);
//removes file extension eg. .tif
rename(""+truncImageName);
//renames image to exclude the file extension
//Resizes the
image to ensure that bits are not cropped off
getDimensions(width, height, channels, slices, frames);
width=width*(1+(imageBorderIncrease/100));//increase
width by the percentage specified by user
height=height*(1+(imageBorderIncrease/100));//increase width
by the percentage specified by user
run("Canvas Size...",
"width="+width+" height="+height+" position=Center");//add
the border on as specified by the percentage the user gave
//This will iterately go through every slice
Page 1
CumulativeRotation_.ijm
and rotate each by the amount specified in the variable
    rotateSlice
for (i=1;i<nSlices;i++) {
setSlice(i+1);
run("Rotate... ", "angle="+rotateSliceCumulative+" grid=1
interpolation="+rotateType);
rotateSliceCumulative=rotateSliceCumulative+rotateSlice;
//This cumulates the amount to rotate the image by as it
goes through this loop
}
if ((isOpen(truncImageName)==1)) {
selectWindow(truncImageName);
saveAs("Tiff", inputFolder+truncImageName+"-Rotated.tif");
//Saves the output image with the same name except with -
    Rotated.tif
appended at the end
} else if (isOpen(truncImageName)!=1)
{ exit("Could not find any image to save");
}
close();
}
```

Appendix - 3

M-files used in Matlab to calculate grain angle from scanned images and X-ray tomography.

Notes

1) The Matlab algorithms used in this analysis ('m'-files) were written by Jonathan Harrington, Scion, Rotorua, New Zealand, whose assistance is gratefully acknowledged.

2) These instructions/protocols were originally written by David Collings, with subsequent modifications by Jimmy Thomas, to calculate the grain angle from identified resin canals in radiata pine wood transverse sections.

~~~~~~

1) A separate folder should be established for each set of Matlab calculations. The following files should be copied to this folder:

   ~ gchain.m

   ~ plotChain.m

   ~ chain2vec.m

2) In Matlab, change the directory so that you are working in the directory which has the different 'm' files, and in which the different subdirectories are located. In the COMMAND WINDOW of Matlab, use the following prompt, edited to the location on your computer. Note that the location needs to be in single quotes.

```
cd '[drive letter]:[string address for the folder]'
```

3) To run the first analysis, copy the appropriate set of ImageJ outputs (the CSV file) from its folder and paste this into the main directory. To analyse this data set, run the m-file *'gchain'* using appropriate inputs. This is done in the COMMAND WINDOW as follows:

```
[p,c,A] = gchain('*.csv',10.58,60,0)
```
~~~~~~

p = position of points along chains

c = chain to which each point belongs

A = transverse-sectional area at each point along a chain

*.csv is the file in which the centroid data from ImageJ is stored, listed between single quote marks.

* 10.58 = the X and Y pixel size in micrometres, to be adjusted for each file as appropriate. However, for the polarised light transverse sections, 10.58 corresponds to 2400 dpi. This variable is different for X-ray tomography images.

* 60 = the Z slice step in um, to be adjusted for each file. For the polarised light transverse sections, the value is 60 µm, but for the X-ray tomography the value will be the pixel size multiplied by the value in which the Z direction was reduced. For example, use a value of 2 if the calculations are based on every second plane. This variable is different for X-ray tomography images.

* 0 = a minimum area value in unknown units, but which can be left at 0 if minimum areas have been selected in ImageJ.

4) To further analyse this data set, two more m-files need to be run. In the COMMAND WINDOW, run the m-file *'plotChain'* using the command:

```
plotChain (p,c)
```

This m-file gives a 3D graphical output of the chains that the programme has identified, which can be saved if required.

5) A further m-file called '*chain2vec*' should also be run in the COMMAND WINDOW using the command:

```
chain2vec (p,c)
```

This gives a two dimensional view of the vectors identified by '*gchain*' looking down on the system from above, and can be saved if required.

6) These values must be processed and exported so that they can be analysed. The first step is to define specific values. In the COMMAND WINDOW, type

```
[psi,th,X,Y,U,V,rmse]=chain2vec(p,c)
```

This brings up a figure which is completely blank, and which can be ignored. Close the window. Then, export the data. Within the WORKSPACE window of Matlab, under the list of named files, click on X which will open the X position file in the Variable editor. Copy all the values, and past them into a new Excel file. Repeat this for the files listed as Y, PSI and TH. These should now form 4 lines in an Excel spreadsheet which should be saved as an appropriately named file in the appropriate subfolder.

x = the X coordinate where the resin canal was mapped to.

y = the Y coordinate where the resin canal was mapped to.

PSI = the angle of the canal away from the vertical, and is independent of the orientation of the canal. All values for this lie between 0 and 90^{o}, and no indication of left-handed or right-handed twisting is given in the initial outputs.

TH = the angle that the canal is orientated at when viewed from above, and is independent of the angle to the vertical. The zero angle is defined as horizontal and to the right, with a positive TH value indicating a rotation in an anticlockwise manner.

The 3 m files used in Matlab to calculate angles were written by Dr Jonathan Harrington. Their scripts are as follows.

gchain.m

```
function [p,c,A]=gchain('TB2.csv',10.58,60,0)
% [p,c,A]=gchain(csv_filename,pxl_size,section_thickness,min_area)
%
% Reads a set of results from image j and tries to build chains
 using a
% naive nearest neighbour-within-limits approach
%
% csv format: ,Area,X,Y,Slice,XStart,YStart,,,,
%
% p - position of points along chains
% c - chain to which each point belongs
% A - transverse-sectional area at each point along a chain
%
% e.g.  [p,c,A]=gchain('Results-192.csv',10.583,60,0);
%
% jh, Oct 2012

%%%%%%%%%%%%%%%%%%%%%%%%%%%%%%%%%%%%%%%%%%%%%%%%%%%%%%%%%%%%
%%%%%%%%%%%%%%%%%%%% NO USER SERVICEABLE PARTS BELOW
%%%%%%%%%%%%%%%%%%%%%%%%%%%%%%%%%%%%%%%%%%%%%%%%%%%%%%%%%%%%
fn=csv_filename;
dz=section_thickness;

if nargin<4 || isempty(min_area),
  min_area=0;
end

% load data and build point list
%%%  ,Area,X,Y,Slice,XStart,YStart,,,,
X=csvread(fn,1,0);
X=X(X(:,2)>=min_area,:); % filter small areas - they're artefacts
A=X(:,2)*pxl_size^2;
p=X(:,3:5);
% p=[x1, y1, z1; .... ]
islice=p(:,3);
nslices=max(islice);
p(:,1:2)=p(:,1:2)*pxl_size; % mm
p(:,3)=dz*(islice-1);

% compute a maximum allowed shift based on requiring, for a
 typically
```

```
% 'small' xsectn vessel, an overlap between vessel areas in
% consecutive slices
dia=sqrt(4*A/pi);
dmax=prctile(dia,10);
gamma_max=atan(dmax/dz)*180/pi;

% loop over slices looking for unchained points
c=0*p(:,1); % labels the chain to which this point belongs
currentchain=0;
for startslice = 1:(nslices-1)
  seeds=find(startslice==islice & c==0);
  fprintf('%i: %i seeds\n',startslice,length(seeds))
  for seed=seeds'
    % assign chain number to the seed
    currentchain = currentchain + 1;
    c(seed)=currentchain;
    x0=p(seed,1);
    y0=p(seed,2);
    for nextslice=(startslice+1):nslices
      % find the nearest point in the next slice
      ii=find(nextslice==islice);
      d=sqrt((p(ii,1)-x0).^2+(p(ii,2)-y0).^2);
      inext=ii(d==min(d));
      if length(inext)>1, inext=inext(1); end
      %fprintf('%i:                  %i:                  dmin=%f,
       dmax=%f\n',startslice,nextslice,min(d),dmax)
      if min(d)>dmax,
        % if the next point lies further than dmax from this
        % point terminate the chain
        continue
      elseif c(inext)~=0
        % if the next point already belongs to a chain,
        % reassign points int his chain and continue
        iii=find(c==currentchain);
        c(iii)=c(inext);
        %currentchain=currentchain-1;
        continue
      else
        c(inext)=currentchain;
        x0=p(inext,1);
        y0=p(inext,2);
      end
    end
  end
end

% prune chains with less than nslices/2 members
cpruned=c;
for ic=unique(c)'
  if length(find(c==ic))<nslices/2
    cpruned(c==ic)=0;
  end
end
c=cpruned;
```

```
%figure
%hist(sqrt(4*A*(25.4e3)^2/pi))
% some friendly output
ic=setdiff(unique(c),0);
fprintf('Found %i chains linking %i points\n',length(ic),sum(c~=0))
fprintf('%i     points     not     assigned     to     any     chain
(%0.1f%%)\n',sum(c==0),100*sum(c==0)/length(c))
```

plotChain.m

```
function plotChain(p,c,ic)

% plotChain(p,c,ic)
%
% plots points and chains coming from gchain
%
% ic (optional) - vector specifying id's of chains to follow. if
not given
% all chains are followed
%
% jh, Oct 2012

plot3(p(:,1),p(:,2),p(:,3),'.','markersize',1)
%if ~exist('ic','var'), return, end
if ~exist('ic','var'), ic=setdiff(unique(c),0); end
for ii=1:length(ic)
  ii=find(c==ic(ii));
  hold on
  plot3(p(ii,1),p(ii,2),p(ii,3),'r-','linewidth',2)
end
%axis equal
```

chain2vec.m

```
function [psi,th,X,Y,U,V,rmse,ERR]=chain2vec(p,c)

% [psi,th,X,Y,U,V,rmse]=chain2vec(p,c)
%
% fits a line to the points in a chain and then calculates the
% orientation of that line w.r.t. coordinate system
%
% psi - total grain angle (spiral + cone)
% th - azimuth angle
%
% jh, Oct 2012

zmid=(max(p(:,3))-min(p(:,3)))/2;
k=1;
ERR=[];
for ic=unique(c(c>0))'
  xx=p(c==ic,1);
  yy=p(c==ic,2);
  zz=p(c==ic,3);
  px=polyfit(zz,xx,1);
  py=polyfit(zz,yy,1);
  X(k)=polyval(px,zmid);
  Y(k)=polyval(py,zmid);
  W(k)=1;
  U(k)=polyval(px,zmid+W(k));
  V(k)=polyval(py,zmid+W(k));
  err=sqrt((xx-polyval(px,zz)).^2+(yy-polyval(py,zz)).^2);
  rmse(k)=sqrt(sum(err.^2)/length(xx));
  k=k+1;
  ERR=[ERR; err];
end
U=U-X;
V=V-Y;
th=atan2(V,U)*180/pi;
psi=atan2(1,sqrt(U.^2+V.^2))*180/pi;

if nargout<1
  quiver(X,Y,U,V)
end
axis equal
```

Appendix -: 4

Protocol for calculating angles in Excel

Notes

1) These instructions/protocols were originally written by David Collings, with subsequent modifications by Jimmy Thomas, and allow the re-calculation of actual resin canal angles based on Matlab outputs.

2) These calculation routines are aimed for calculating the local and overall grain angle/ pattern in serial transverse sections collected from radiata pine. They can also be used for calculations based on X-ray tomography images.

~~~~~~

1) Matlab generates a spreadsheet with four different variables. These are:

x = the X coordinate where the resin canal was mapped to.

y = the Y coordinate where the resin canal was mapped to.

PSI = the angle of the canal away from the vertical, and is independent of the orientation of the canal. All values for this lie between 0 and 90^{o}, and no indication of left-handed or right-handed twisting is given in the initial outputs.

TH = the angle that the canal is orientated at when viewed from above, and is independent of the angle to the vertical. The zero angle is defined as horizontal and to the right, with a positive TH value indicating a rotation in an anticlockwise manner.

2) In Excel, a calculation spreadsheet is set-up that will run the following calculations automatically. It is, however, necessary to first estimate the centre of the piece of wood from the output graphs generated from Matlab. The units for this will be in micrometres that run with standard Cartesian coordinates.

3) The distance of the resin canal from the centre of the stem is calculated using Pythagoras's theorem.
~~~~~~

4) It is necessary to know the relative location of the resin canal compared to the image centre, and to realise that Matlab and Excel run calculations slightly differently. Canals are defined as being in one of 4 different quadrants, based on the location of the stem centre. The conventions on angles and coordinates used in these comments and calculations are for quadrants 1 through 4:

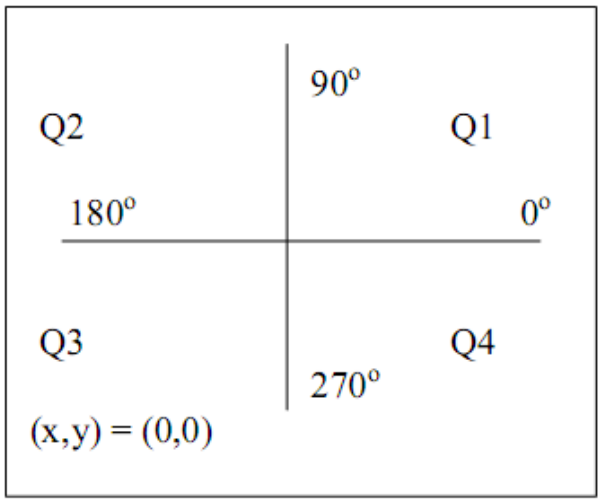

The conventions on locations and angles used by Matlab are different, and are as follows:

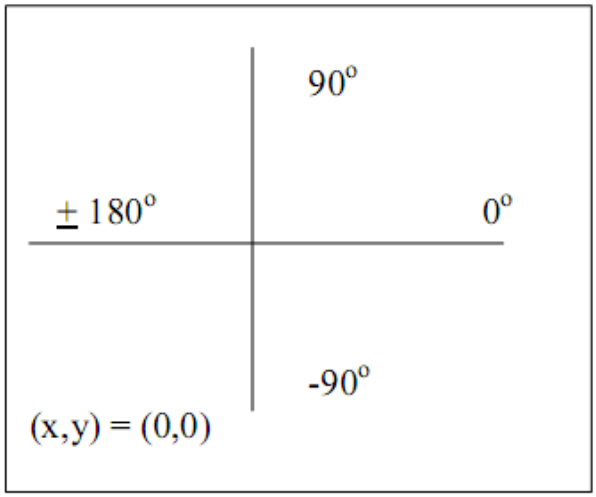

Simple mathematical equations can determine the quadrant that a canal lies in, based on whether the X and Y values for the canal location are larger or smaller than the values of the stem centre.

5) A raw angle is defined which is the relative position of the resin canal from the stem centre. This is calculated using the 'atan' function and the absolute value (that is, no negative numbers allowed) of the ratio (Y-Yc) / (X-Xc). The raw angle is simply the angle away from the horizontal where the resin canal occurs. The corrected angle is based on the quadrant in which the canal is located, with the raw angle converted to a real angle through a series of logic tests. Zero angle is defined as horizontal to right.

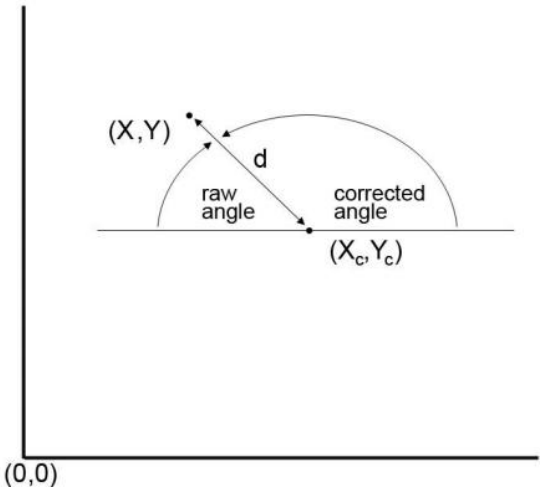

6) Excel calculates an angle difference. This calculation currently assumes that the azimuth value (TH) uses the same convention as the angle value, with the zero position is defined as horizontal to the right. Angle difference = the azimuth minus the corrected angle, and can range from almost -360^{o} to + 360^{o}. Values of angle difference that are + 90^{o} and + 270^{o} have the resin canal direction running at right angles to the location of the resin canal. These canals are running around the centre of the stem. Angle delta values of 0^{o}, + 180^{o} and + 360^{o} have the resin canals running parallel to the direction in which they are located, and are thus running radially either inwards or outwards.

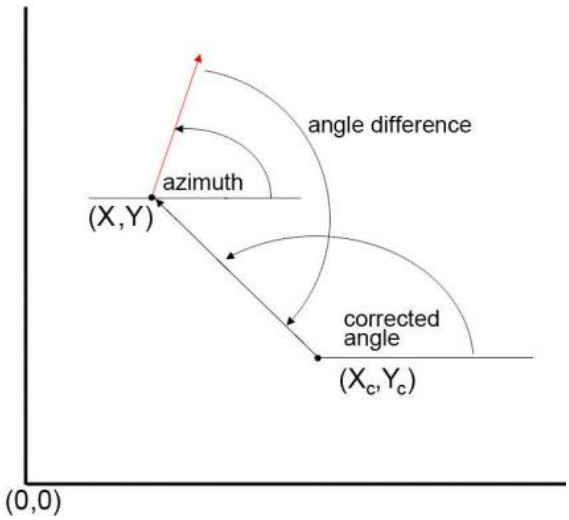

7) In the following example, the angle difference between the azimuth (in red) and the corrected angle is near 90°, which means that the grain element would be running tangential to the radial direction of the stem.

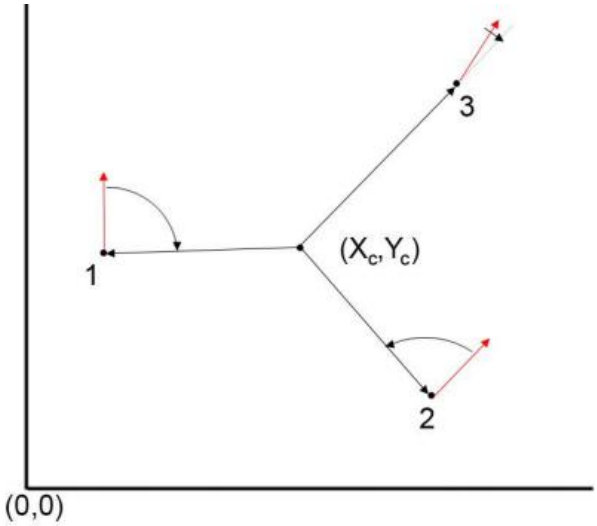

In the preceding example, 3 different grain elements are considered. At point 1, the difference between the azimuth and corrected angle equals -90o whereas at point 2 the difference is plus 90°. In both cases, the grain is wrapping around the stem but in opposite directions. At point 3, the azimuth is parallel to the corrected angle which means that the grain element is sloped inwards or outwards and not around the stem.

8) The two angle outputs from Matlab (PSI and TH) can then be modified based on the relative location of the resin canal to the centre of the stem. This spreadsheet calculates 3 different angle measurements for each grain element defined by Matlab. These are:

PSI with handedness which is simply the PSI value corrected for handedness with negative values being left-handed

PSIcorr: This value is a corrected PSI value, and describes the angle from the vertical of a resin canal tangential to its location. It is derived from the sine of angle difference multiplied by PSI. In other words, PSIcorr is a measure of how the resin canals are wrapped around the stem. More importantly, the sign of PSIcorr describes the handedness. When PSIcorr is negative, there is a left-handed spiral and when PSIcorr is positive the spiral is right-handed. Values are independent of the direction is which the calculations are conducted.

PSIradial: This value is related to PSIcorr but describes how much in or outwards there is in the winding of the resin canals around them stem. A value that is positive is defined as an outward lean and *vice versa*. However, unlike the values for PSIcorr, however, the terms inward and outward are relative terms only, and need to be defined in terms of the upward and downward growth of the tree. For a round stem, this value should average close to 0.

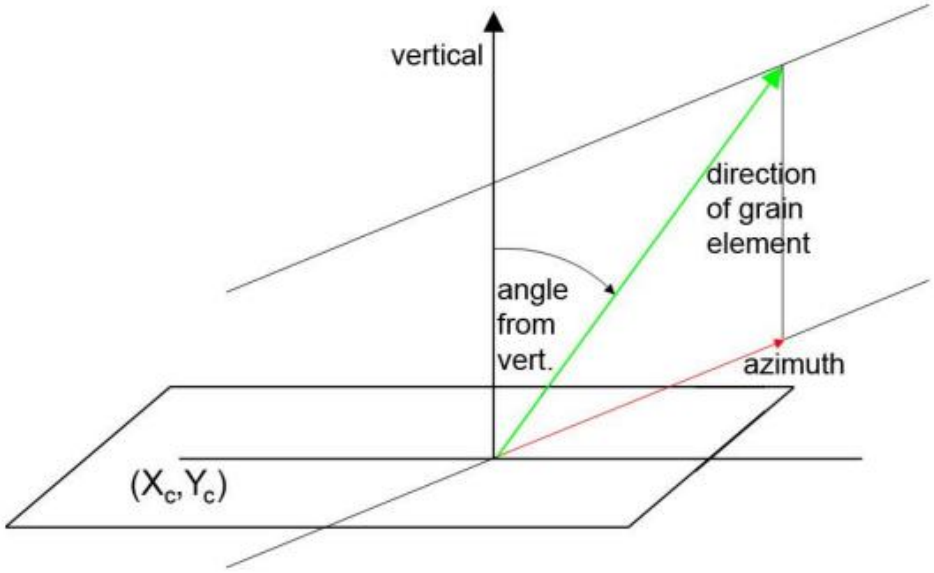

Expected outcomes

1) Vertical controls and rocking wood samples should have negative values for PSI with handedness corresponding to left-handed spiral grain.

2) Vertical controls and rocking wood samples have round stems. If the stem is round, then the average value for PSI with handedness should be similar to the average value of PSIcorr, and the average value for PSIradial should approach zero.

3) Vertical controls and rocking wood samples have round stems. There should be little correlation between corrected angle, which is angular coordinate of the location of the resin canal with respect to the manually identified stem centre, and the average values for PSI with handedness, PSIcorr and PSIradial. Systematic deviations from zero suggest that the stem might not be exactly round, and that transverse sections may have been cut slightly obliquely.

4) In leaning wood samples, the transverse section of the stem is not symmetric. This means that the growth rings on the lower side of the tree will not be tangential to lines drawn from the stem centre (or more specifically, the centre of the pith) to the different resin canals. Therefore, the distinction between PSIcorr and PSIradial will break down. There will be an apparent PSIradial component to any canal that is running in the growth ring.

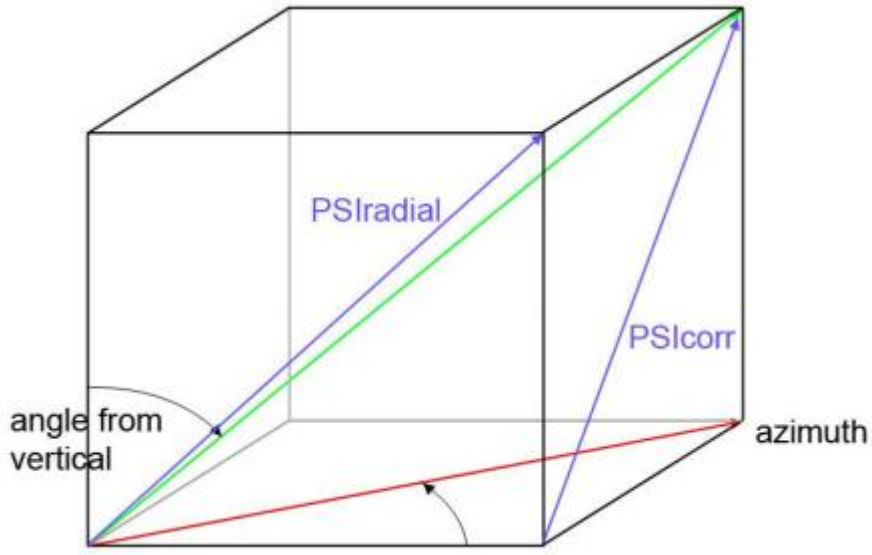

Analysing grain and compression wood

Preliminary analysis of leaned trees has suggested that the grain is affected by the presence of compression wood. Because compression wood can be imaged by fluorescence microscopy, it is possible to make direct comparisons on this linkage.

A simple comparison might involve dividing the stem into 4 (or more) different zones based on the central location. This would be easy enough to do, by adding 45 degrees to the 'corrected angle' column and then dividing by 90. The largest whole number (defined in Excel by the INT function) with the addition of 1, would give 4 zones, with zones 1 and 3 on the right and left hand sides, zone 2 on the upper side and zone 4 on the lower side. Angles could then be grouped into these zones. While there should be no significant differences between the zonal averages for vertical or rocked samples, it would be predicted that zone 4 would be lowest in the leaning wood.

In vertical and rocked sample, variations between the average of 'PSI with handedness' for opposite sides of the stem would likely be due to asymmetric or oblique cutting. Were this to be the case, the remaining two sides would likely be similar in their average values of 'PSI with handedness.